Synthesis and Characterisation of Iron-containing Perovskites



A thesis submitted for the degree of
Doctor of Philosophy
to the Division of Mathematical, Physical
and Life Sciences
at the University of Oxford

Yawei Tang
St Edmund Hall
Trinity Term 2018

A thesis submitted for the degree of Doctor of Philosophy to the Division of Mathematical, Physical and Life Sciences at the University of Oxford

Abstract

In this research project, iron-containing perovskites with the general formulae $A_3Fe_2B'O_9$, $A_2A'Fe_2B'O_9$ and $A_2A'FeB'B''O_9$ have been synthesised using conventional solid-state reactions. A combination of experimental techniques has been applied to characterise the samples. The main aspects studied include their crystal symmetry, cation ordering pattern and magnetic behaviour.

We have shown for the first time that $Sr_3Fe_2TeO_9$ can adopt a trigonal perovskite-like structure with the Fe^{3+} and Te^{6+} cations ordering in a 2:1 sequence. However, the trigonal structure is disrupted by both nano-twinning and regions where the cations order in a 1:1 sequence. These disruptions prevent full antiferromagnetic ordering throughout the sample and the unordered spins form a spin-glass phase that coexists below 80 K. The identification of this disorder has allowed us to account for inconsistencies in the existing literature.

$Ba_3Fe_2TeO_9$ is a 6*H* perovskite in which the cation sites in the face-sharing octahedra and the vertex-sharing octahedra are occupied by different fractions of Fe^{3+}. At a temperature close to 300 K the atomic moments begin to order in an antiferromagnetic manner, and the spins that are unable to take part in the long-range magnetic order form clusters that freeze at 18 K. In the series $Sr_xBa_{3-x}Fe_2TeO_9$ (x=1~2.5), as x decreases the crystal structure switches from purely pseudo-cubic to purely hexagonal via a biphasic region, illustrating the effect of the radius ratio r_A/r_B on crystal structure.

$A_2LaFe_2SbO_9$ (*A*=Ba, Sr, Ca) and $CaLa_2Fe_2SnO_9$ have cation disorder on their A sites. $Ca_2LaFe_2SbO_9$ and $CaLa_2Fe_2SnO_9$ both adopt a monoclinic $P2_1/n$ structure and $Sr_2LaFe_2SbO_9$ adopts a triclinic $P\bar{1}$ structure, all of which show different levels of B-cation ordering. $Ba_2LaFe_2SbO_9$ has a *Pbnm* structure with disordered B sites. These perovskites are not paramagnetic at 300 K, and they all adopt a G-type magnetic structure, which leads to long-range ferrimagnetic or weak ferromagnetic behaviour. The three antimony-containing compounds contain a minor spin-glass-like phase below 50 K, while $CaLa_2Fe_2SnO_9$ has a relatively well-developed magnetic backbone at 300 K.

We found that the six-coordinate cations in the $P2_1/n$ perovskite $SrLa_2FeCoSbO_9$ order in a previously-unreported manner. The observed cation distribution, with diamagnetic Sb^{5+} and magnetic Co^{2+} each partially occupying only one of the six-coordinate sites, results in ferrimagnetism below the Curie temperature of 215 K. $CaLa_2FeCoSbO_9$ and $ALa_2FeNiSbO_9$ (*A*=Ba, Sr, Ca) were prepared as analogues of $SrLa_2FeCoSbO_9$, and they have similar crystal structure and high Curie temperatures. However, TEM revealed the different levels of inhomogeneity present in these four compounds. The inhomogeneity is least significant in $CaLa_2FeCoSbO_9$, and it is most significant in $BaLa_2FeNiSbO_9$ where both primitive phase and body-centred phases have been observed in a single crystallite. Consequently, doubt has been cast on the interpretation of the diffraction data for these inhomogeneous samples.

$A_2LaFe_2NbO_9$ (*A*=Sr, Ca) and $CaLa_2Fe_2TaO_9$ were prepared with d^0 cations for comparison with the perovskites containing d^{10} B-cations. $Ca_2LaFe_2NbO_9$ and $CaLa_2Fe_2TaO_9$ adopt the $P2_1/n$ structure, and $Sr_2LaFe_2NbO_9$ adopts the $P\bar{1}$ structure. These three perovskites show less well-developed ordering pattern than their antimony analogues due to the smaller difference in size of B-cations. They are not simple paramagnets at 300 K, and they all adopt a G-type magnetic structure with long-range ferrimagnetism. However, the formation of magnetic backbone is significantly slowed down from that in the d^{10} compounds and the temperature for the paramagnetic spins to freeze is lowered below 20 K. We propose that in these materials a J_3 interaction occurs via the Fe^{3+} – O – Nb^{5+}/Ta^{5+} – O – Fe^{3+} pathway to compete with the dominant J_1 interaction. The J_3 interaction is more significant when d^0 cations are present because hybridisation of the empty *d* orbitals and the anion *p* orbitals facilitates virtual electron transfer.

Declaration

The work described in this thesis was carried out in the Inorganic Chemistry Laboratory at the University of Oxford between October 2014 and May 2018 under the supervision of Prof. P. D. Battle. All the work is my own, except where stated, and has not been submitted by the author for any other degree at this, or any other university.

Yawei Tang

May 2018

Acknowledgments

There are many people I would like to acknowledge for making the work described in this thesis able to be published, after three and a half years since I first stepped into the department of chemistry at University of Oxford.

First, I would like to thank to my supervisor, Prof. Peter Battle, for his input, patience and encouragement during my project. I am also grateful to Prof. Joke Hadermann and her group for doing all the TEM experiments on my samples, to Dr. M. Avdeev for his help on collecting neutron diffraction data from my samples, and to Prof. J. M. Cadogan for collecting Mössbauer spectra from my samples. My appreciation also goes to everyone at ISIS and the I.L.L for experimental assistance.

My time in the group would never have been so enjoyable without my fellow D.Phil. students and post-doc. Thanks to Emily, Andy and Diming for all the assistance and advice during my project, as well as for organising delicious group meals.

Finally, I would like to thank to my family and friends, especially my parents and Datuanzi, for all their support during these years. Without them it would be impossible for me to finish this work with a lovely memory. And, maybe I shall also say thank you to that voice in my heart: “Keep calm and carry on.”

Contents

Abstract i

Declaration ii

Acknowledgements iii

Contents iv

Chapter 1 Introduction 1

1.1 The perovskite structure 1

1.2 Cation ordering in perovskites 5

1.3 Magnetic properties of perovskites 9

1.3.1 Origin of magnetic moment 9

1.3.2 Common types of magnetic system 10

1.3.2.1 Paramagnetism 10

1.3.2.2 Ferromagnetism 11

1.3.2.3 Antiferromagnetism 11

1.3.2.4 Ferrimagnetism 12

1.3.2.5 Frustration and spin-glass behaviour 13

1.3.3 Exchange interactions 14

1.3.3.1 Origin of exchange interactions 14

1.3.3.2 Crystal field theory and superexchange interaction 14

1.4 Magnetism observed in iron-containing perovskites 17

1.5 An overview of the research 18

References 20

Chapter 2 Experimental Techniques 24

2.1 Solid-state synthesis 24

2.2 Powder diffraction techniques 25

2.2.1 General features of crystals and powder diffraction 25

2.2.2 X-ray powder diffraction (XRPD) 31

2.2.2.1 Laboratory Panalytical X'Pert Diffractometer 32

2.2.2.2 Laboratory Panalytical Empyrean Diffractometer 33

2.2.2.3 Diamond Light Source: national synchrotron science facility 33

2.2.3 Neutron diffraction (ND) 34

2.2.3.1 Constant wavelength neutron powder diffraction: I.L.L 37

2.2.3.1.1 D2B 37

2.2.3.1.2 D1B 38

2.2.3.2 Constant wavelength neutron powder diffraction – ANSTO 39

2.2.3.3 Time-of-flight neutron powder diffraction: ISIS 39

2.3 Rietveld analysis 42

2.3.1 General principle of the Rietveld method 42

2.3.2 Computer program used for Rietveld refinement 44

2.3.3 Modelling of Background 44

2.3.4 Description of peak shape 45

2.3.5 Goodness of fit 47

2.4 SQUID magnetometry 48

2.4.1 General principle of SQUID and sample preparation 48

2.4.2 DC magnetisation measurements 49

2.4.3 AC magnetisation measurements 50

2.5 Transmission electron microscopy (TEM) 51

2.6 Mössbauer spectroscopy 54

References 58

Chapter 3 Structural and Magnetic Properties of $Sr_3Fe_2TeO_9$ 60

3.1 Introduction 60

3.2 Experimental methods 62

3.3 Results 63

3.4 Discussion 77

3.5 Conclusions 81

References 81

Chapter 4 Structural and Magnetic Properties of $Ba_3Fe_2TeO_9$ and $Sr_xBa_{3-x}Fe_2TeO_9$ 83

4.1 Introduction 83

4.2 Experimental methods 84

4.3 Results 85

4.4 Discussion 98

4.5 Conclusions 102

References 102

Chapter 5 Structural and Magnetic Properties of the Perovskites: $A_2LaFe_2SbO_9$ (*A*=Ba, Sr, Ca) and $CaLa_2Fe_2SnO_9$ 104

5.1 Introduction 104

5.2 Experimental methods 105

5.3 Results 106

5.4 Discussion 130

5.5 Conclusions 135

References 135

Chapter 6 Structural and Magnetic Properties of $SrLa_2FeCoSbO_9$ 138

6.1 Introduction 138

6.2 Experimental methods 139

6.3 Results 140

6.4 Discussion 153

6.5 Conclusions 154

References 155

Chapter 7 Structural and Magnetic Properties of $CaLa_2FeCoSbO_9$ and $ALa_2FeNiSbO_9$ (*A* = Ba, Sr, Ca) 156

7.1 Introduction 156

7.2 Experimental methods 157

7.3 Results 158

7.4 Discussion 188

7.5 Conclusions 192

References 192

Chapter 8 Structural and Magnetic Properties of the Perovskites: $A_2LaFe_2NbO_9$ (*A*=Sr, Ca) and $Ca_2LaFe_2TaO_9$ 194

8.1 Introduction 194

8.2 Experimental methods 196

8.3 Results 197

8.4 Discussion 215

8.5 Conclusions 220

References 220

Chapter 9 Summary 222

Appendix 228

Chapter 1: Introduction

1.1 The perovskite structure

Oxides with crystal structures related to that of the mineral perovskite are among the most intensely studied compounds in solid-state chemistry because of the wide variety of physical properties they can display[1]. Their electrical behaviour ranges from insulating[2] to superconducting[3] and their magnetic properties show a comparable breadth, ranging from spin-glass behaviour[4] to ferromagnetism[5]. The extensive range of properties observed stems largely from the ability of the structure to accommodate a wide range of chemical compositions. The simplest oxide perovskites can be represented by the formula ABO_3, where *A* is a relatively large cation, usually an alkaline earth or rare earth element, that occupies the twelve-coordinate A site, and *B* is a smaller cation, usually a transition-metal or p-block element that occupies the octahedrally-coordinated B site. The ideal cubic ABO_3 perovskite structure (Figure 1.1) is thus formed by a network of corner-sharing BO_6 octahedra with *A* cations filling the twelve-coordinate interstices.

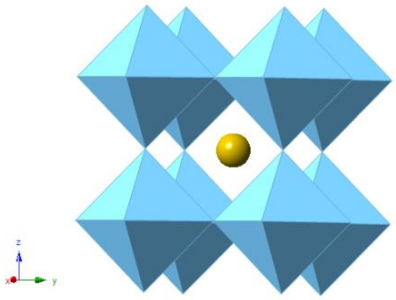

Figure 1.1 The ideal cubic ABO_3 perovskite structure. The BO_6 octahedra are shown in blue and the *A* cation is shown in yellow.

The structure of a cubic perovskite ABO_3 can also be considered to consist of pseudo-close-packed AO_3 layers stacked in a cubic-close-packed (ccp) sequence, with *B* cations occupying six-coordinate interstitial sites between the layers; the layers lie perpendicular to the [111] axis of the cubic unit cell. The [111] projection of the cubic cell is shown in Figure 1.2.

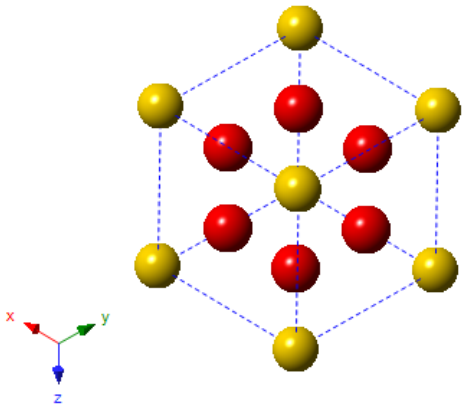

Figure 1.2 [111] projection of cubic ABO_3 unit cell. Cations on the A site are shown in yellow and oxygen atoms are shown in red. B cations are omitted for clarity.

In the ideal cubic perovskite, the *A*-O bond length is equal to the $\sqrt{2}$ * B-O bond length. However, the *A* and *B* cation radii usually do not match perfectly, and the perovskite structure is able to tolerate a significant strain by undergoing distortions that reduce the symmetry from the cubic ideal to orthorhombic or lower. The Goldschmidt tolerance factor[6] is often used to describe the mismatch of *A* and *B* cation size:

$$t = \frac{r_A + r_O}{\sqrt{2}(r_B + r_O)} \qquad \text{(Equation 1.1)}$$

where r_A, r_B and r_O are the ionic radii of A, B and O, respectively. If the *A* cation radius is smaller than ideal and $t < 1$, the BO_6 octahedra tilt to compensate for this cation size mismatch. For example, Figure 1.2 illustrates a distortion from cubic to orthorhombic symmetry, which is caused by tilting of the BO_6 octahedra.

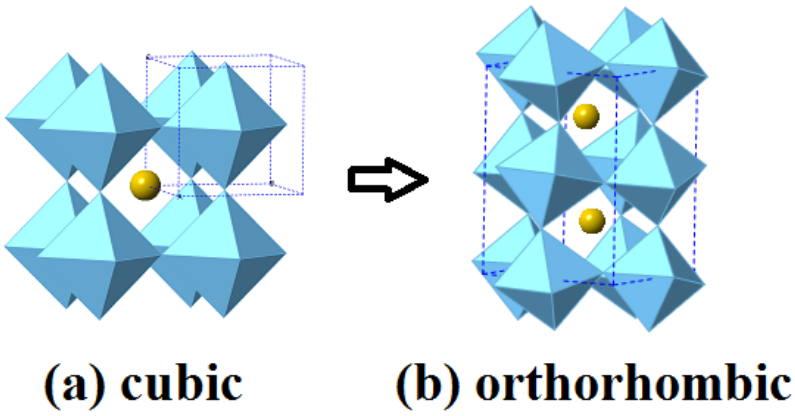

Figure 1.3 The transformation from ideal cubic unit cell to orthorhombic unit cell caused by tilting of octahetra.

$CaTiO_3$ is one of the compounds that undergoes the orthorhombic distortion shown in Figure 1.3[7]. If the cell parameter of the original cubic cell is *a*, then the orthorhombic unit cell will have cell parameters $a' \approx b' = \sqrt{2}a$ and $c' = 2a$, based on simple geometric considerations. It has an in-phase tilt about the [010] axes of the orthorhombic cell and equal out-of-phase tilts about [100] and [001], which is denoted at $a^-b^+a^-$ in the notation first described by Glazer[8]. In cases where $t < 1$, although the perovskite structure can have lower symmetries such as orthorhombic[7], monoclinic[9] and triclinic[10] with tilted octahetra, the crystal structures are still referred to as pseudo-cubic because they retain the network of corner-sharing octahedra that is present in the ideal structure.

When the tolerance factor $t > 1$, the A cation is too large and the structure cannot relieve the strain that arises from radius mismatch simply by tilting the octahedra. Instead of a pseudo-cubic structure, various hexagonal structures form. As the size of the cation *A* increases relative to that of the cation *B*, the stacking sequence of the AO_3 layers changes from ccp to hexagonal-close-packed (hcp), with the layers now lying perpendicular to the [001] axis of a hexagonal unit cell. The simplest hexagonal perovskite adopts the 2*H* structure shown in Figure 1.4.

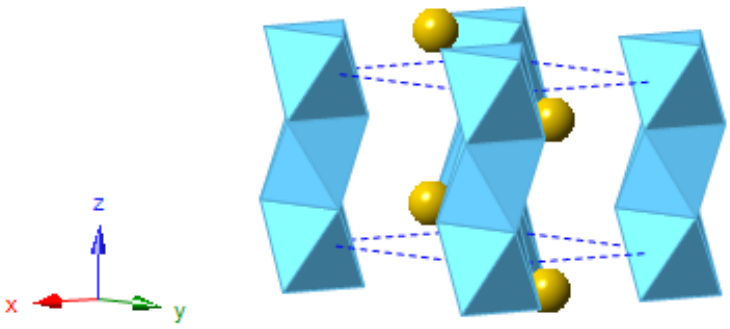

Figure 1.4 The 2*H* structure. The BO_6 octahetra are shown in blue and the *A* cations are shown in yellow.

The pure hcp stacking of AO_3 layers that occurs in the 2*H* structure results in infinite one-dimensional chains of face-sharing BO_6 octahedra parallel to the *c* axis which are separated by the *A* cations. Here "2" refers to the number of AO_3 layers in the unit cell, and "*H*" denotes the hexagonal symmetry. Due to the ability to readily expand in the *ab* plane relative to *c*, this hexagonal structure is able to accommodate larger *A* cations such as barium compared with pseudo-cubic perovskites. Although the short *B*-*B* distance will result in large interionic

repulsion between the octahedra if electrostatic forces are considered, an increase in the interlayer distance of the AO_3 layers decreases the repulsive force between the *B* cations and therefore stabilises the face-sharing octahedra[11]. $BaNiO_3$ and $BaMnO_3$ are two compounds that adopt the 2*H* structure[12, 13]. However, it is worth noting that not only the size of the *A* cation, but also other factors, for example the character of the bond can affect the transformation between pseudo-cubic and hexagonal perovskites. Under certain conditions, $SrCoO_3$ and $SrNiO_3$ both have SrO_3 layers stacked in a hexagonal sequence despite the presence of the smaller Sr^{2+} cation[14, 15]. This structure is stabilised by the increased covalency of the Co-O and Ni-O bonds, which counteracts the repulsive energy between the highly charged B^{4+} cations.

In addition to pure ccp and hcp stacking sequences, structures are known that are based on a mixed ccp and hcp sequence. The introduction of cubic stacking into a hexagonal stacking sequence has the effect of increasing the average separation of the *B* cations, and consequently reduces the electrostatic repulsions within the octahedral motifs. For this reason, this mixed stacking is seen more commonly than the 2*H* structure. The 4*H* structure adopted by $SrMnO_3$[16] and the 9*R* structure adopted by $BaRuO_3$[17] (Figure 1.5) exemplify a mixed stacking sequence, where B_2O_9 dimers and B_3O_{12} trimers, formed by face sharing BO_6 octahedra, are joined by corners. Here "*R*" stands for rhombohedral symmetry, which is closely related to hexagonal symmetry.

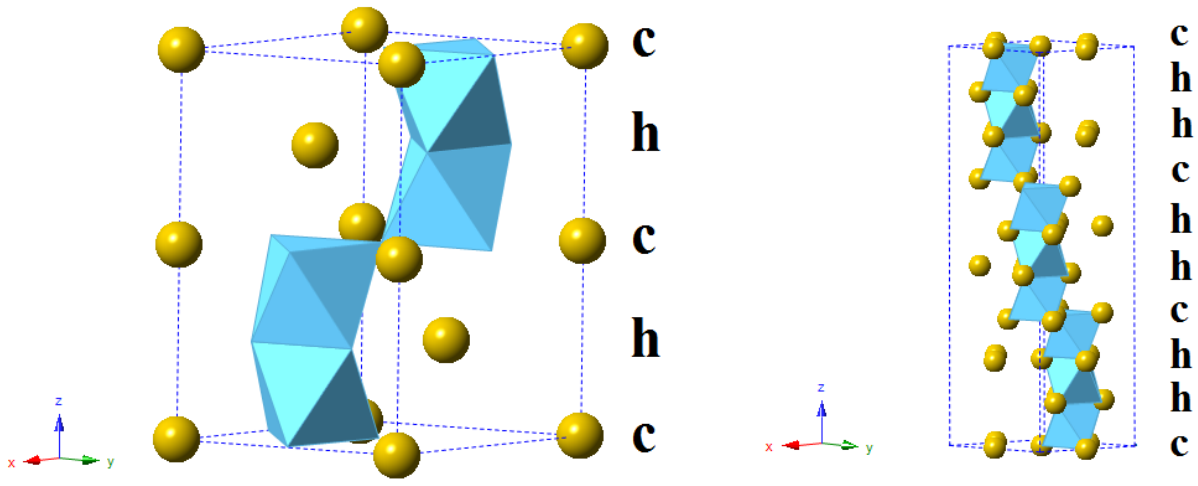

Figure 1.5 (Left) the 4*H* structure in which B_2O_9 dimers are shown in blue and *A* cations are shown in yellow. (Right) the 9*R* structure where B_3O_{12} trimers replace the dimers. Layers are labelled to show the mixed sequences.

Among all the possible mixed stacking sequences, the 6*H* structure (Figure 1.6) based on the six-layer *cchcch* sequence is particularly common. This structure contains B_2O_9 dimers which are linked together by single, vertex-sharing BO_6 octahedra. $BaTiO_3$[18] and $BaCrO_3$[19] are two compounds that can adopt this structure, and other 6*H* perovskites will be described in detail later in this thesis.

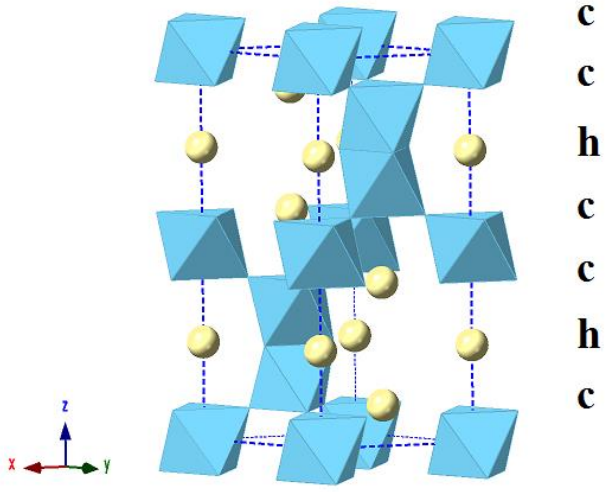

Figure 1.6 The 6*H* structure. The BO_6 octahetra are shown in blue and *A* cations are shown in yellow. Layers are labelled to show mixed sequence.

1.2 Cation ordering in perovskites

The formula ABO_3 represents the simplest form of oxide perovskite, in which there is only one cation species involved at the A site as well as the B site. Partial cation substitution at either the A site, the B site or both will however result in more complicated perovskites with formula such as $AA'BB'O_6$ and $A_2A'B_2B'O_9$. The cations in the pairs *AA*' and *BB*' can occupy their respective sites in an ordered, partially ordered or disordered manner and the physical properties of the resulting compound are very sensitive to the degree of ordering. Cation substitution is therefore an important strategy in the search for desirable properties[20, 21]. An ordered arrangement is usually stabilised when the cations in the pair differ significantly in their coordination preference, valence or size. Consequently, A-site ordering is relatively rare, and often involves vacancies as the second cation species[22], whereas B-site ordering is quite common.

Various types of B-site ordering pattern have been reported in literature, among which the 1:1 ordered $AA'BB'O_6$ systems are the simplest and most frequently encountered ordered

perovskites. The first oxide perovskites with a 1:1 ordering pattern at B site were the A_2ABO_6 (*A*=alkaline earth ion, *B*=Mo^{6+}, W^{6+}) systems described by Steward & Rooksby [23], and subsequently hundreds of 1:1 B-site ordered perovskites have been reported. Size and charge are usually the primary factors that control the ordering. A study of the $Ba^{2+}{}_2(B^{3+}Nb^{5+})O_6$ systems suggests that for a fixed charge difference of two, compounds with B-site order and those with a random cation distribution are separated by a threshold in ionic radii difference lying between 5% and 17%[24]. By far the most common 1:1 ordering pattern is the rock-salt arrangement, where the B cations alternate along three dimensions and the unit cell is doubled in all three crystallographic directions (Figure 1.7). The most symmetrical structure with this ordering type has no tilting of the octahedra and adopts a cubic crystal, as exemplified by Ba_2YRuO_6[25], although different tilting can occur to lower the symmetry from cubic to triclinic[21]. Other relatively rare ordering patterns have also been reported. For instance, the two B-cations in La_2CuSnO_6 alternate along [100], forming an unusual layered ordering pattern [26](Figure 1.7).

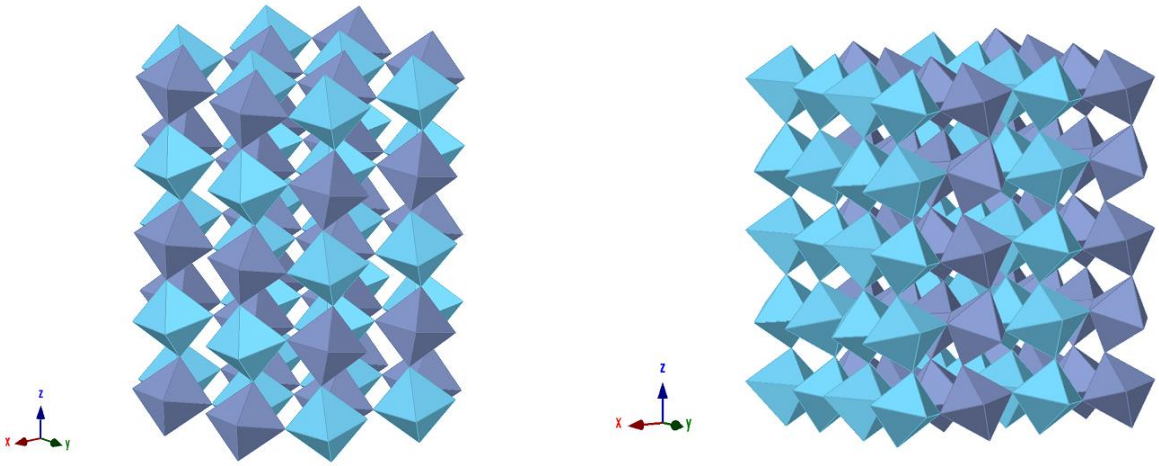

Figure 1.7 (Left) the rock-salt type arrangement of 1:1 ordering. (Right) the layered ordering pattern observed in compounds such as La_2CuSnO_6. Polyhedra shown in different colours are occupied by different B-cations, and A-cations are omitted for clarity.

It is noteworthy that the 1:1 ordered perovskite-type structure can accommodate not only a 1:1 B-cation stoichiometry, but other stoichiometries including $A_2A'B_2B'O_9$. One example in this family is $La_3Ni_2SbO_9$[27]. This compound adopts a monoclinic $P2_1/n$ structure (Figure 1.8) in which two crystallographically distinct B sites occur in a 1:1 ratio. One sublattice is occupied entirely by $3d^8$: Ni^{2+} cations and 2/3 of the sites on the second sublattice are occupied by Sb^{5+}, with the remaining 1/3 being occupied by Ni^{2+}.

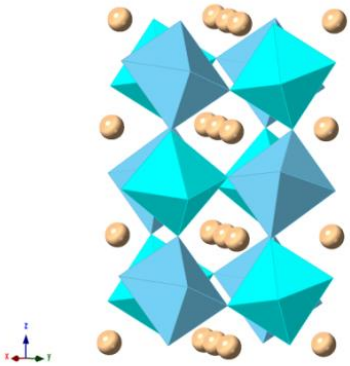

Figure 1.8 A monoclinic (space group $P2_1/n$) perovskite structure. The two distinct BO_6 octahetra are shown in different shades of blue and *A* cations are shown in yellow.

Besides the most common 1:1 B-site ordering, there are other relatively rare ordering types such as 1:2 and 1:3 ordering. $Ba_3SrTa_2O_9$, wherein Sr and Ta occur in a 1:2 sequence along the [111] direction of a trigonal unit cell to give a trigonal superstructure, was the first reported example of 1:2 ordering[28](Figure 1.9). Since then, other tantalates, niobates and ruthenates with similar stoichiometries which show 1:2 ordering have been found[29-32]. The limited occurrence of 1:2 ordering is believed to related to the resulting coordination environment of the oxygen anions, which leads to both overbonding and underbonding of the oxygen between different layers of the B-cations and usually requires the presence of a stable off-centred d^0 ion[33]. 1:3 ordering is even less frequently observed than 1:2 ordering. Examples include the recently-reported cubic perovskites $Ba_4BB'_3O_{12}$ (*B*=Li, Na, *B*'=Sb^{5+}, Bi^{5+})[34, 35].

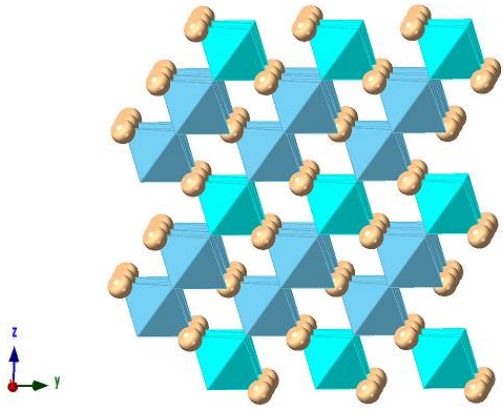

Figure 1.9 The 1:2 ordered perovskite structure viewed along [100] of a trigonal unit cell. The distinct BO_6 octahetra are shown in different shades of blue to highlight the 1:2 repeating pattern of different B-cations, and A-cations are shown in yellow.

Besides the pseudo-cubic perovskites, it is also possible for cation ordering to occur over the corner and face sharing sites in perovskites with 6*H* structure. For instance, in the study of the 6*H* perovskites $Ba_3LnIr_2O_9$ (*Ln* = Y, lanthanides), it has been reported that both hexagonal and monoclinically distorted unit cells are observed (Figure 1.10) with a 1:2 ordering pattern of the B-cations, which results from the distribution of distinct cation species over sites of different multiplicities[36]. $Ba_3Fe_2TeO_9$[37] is another 6*H* perovskite with a hexagonal cell and similar cation ordering pattern, and this compound will be discussed in another chapter.

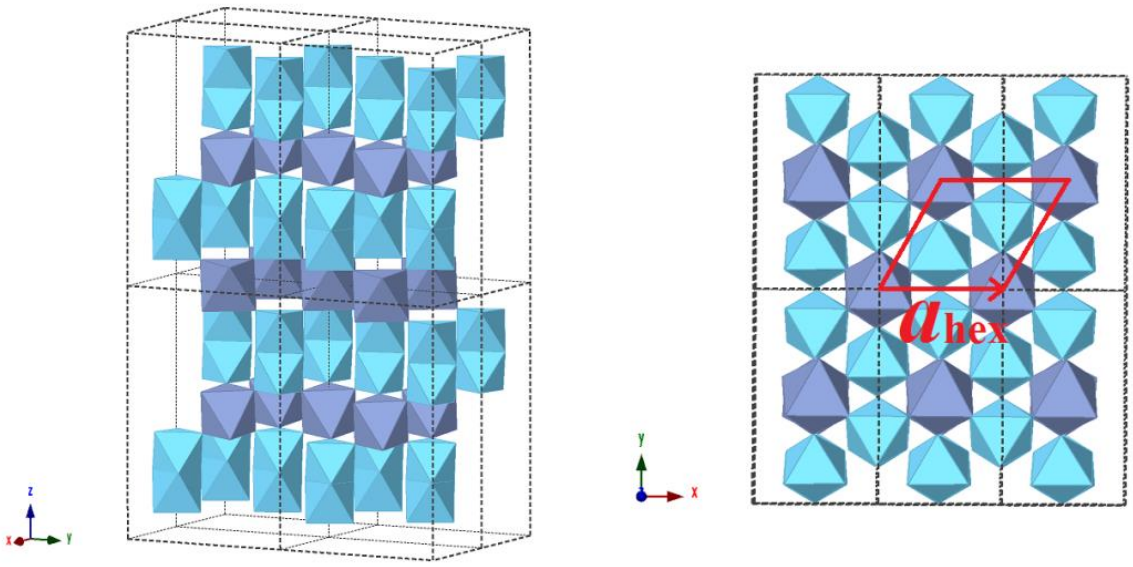

Figure 1.10 (Left) monoclinically distorted unit cells of 6*H* perovskite structure showing cation ordering over corner and face sharing sites. (Right) an illustration of the relationship between the hexagonal cell (red solid line) and monoclinic cell (black dashed line) viewing along *z* axis. Polyhedra shown in different colours are occupied by different B-cations, and A-cations are omitted for clarity.

It has been mentioned previously that while various types of B-site ordering have been observed, A-site ordering of different cation species are relatively rare due to the difficulty to create sufficient difference in size and charge of A-cations. However, under certain circumstances A-site and B-site ordering can coexist and correlate with each other. $NaLaMgWO_6$ is one example[38]. This perovskite adopts an ordered monoclinic structure, with B-cations in rock-salt-type arrangement and A-cations in layered arrangement along alternate *c*-planes. It is believed that in addition to the charge difference between Na^+ and La^{3+} which would potentially favour ordering, the particular displacement of the Mg^{2+} and W^{6+} ions in the *c* direction compensates the electrostatic imbalance due to the layer-like ordering of A-cations and thus helps to further stabilise this unusual structure.

1.3 Magnetic properties of perovskites

1.3.1 Origin of magnetic moment

Perovskites are particularly interesting not only for their various crystal structures, but also for their ability to exhibit novel magnetic properties. To understand various magnetic interactions observed in perovskites, we need to first understand the basic principles of magnetism.

The magnetic moment of an atom or ion originates from the presence of unpaired electrons with dipole moments in an atom or ion, and is most commonly associated with transition metal or rare earth elements. In the Bohr model of atom, the electron circulates around the nucleus and generates a current. The fundamental object in magnetism is the magnetic moment, μ. It is given by:

$$d\mu = I dS \text{ [39]} \qquad \text{(Equation 1.2),}$$

where I is the current surrounding an elementary oriented loop of area $|dS|$. If we consider the situation in an atom with a radius r, then

$$\mu = \pi r^2 I \qquad \text{(Equations 1.3).}$$

It can be derived that for an electron, the quantity $\pi r^2 I$ is equal to a constant, see reference[39]. The unit of electronic magnetism, Bohr magneton is thus defined by:

$$\mu_B = \frac{e\hbar}{2m_e} \qquad \text{(Equation 1.4) .}$$

The Bohr magneton is used as a convenient unit for describing the magnitude of atomic magnetic moments; it takes the value $9.274*10^{-24}$ Am^2. All the moments discussed in this thesis will be in this unit. In an atom, the magnetic moment is associated with the total angular momentum J, which is the sum of the orbital angular momentum L and the spin angular momentum S. The total magnetic moment is given by:

$$\mu = -g\mu_B J \qquad \text{(Equation 1.5),}$$

where g is the Landé constant. The effective moment, μ_{eff} is often quoted to characterise an atom:

$$\mu_{eff} = g_J\sqrt{J(J+1)} \qquad \text{(Equation 1.6),}$$

where $g_J = \frac{3}{2} + \frac{S(S+1)-L(L+1)}{2J(J+1)}$ (Equation 1.7).

1.3.2 Common types of magnetic system

1.3.2.1 Paramagnetism

Paramagnetism describes the behaviour of unpaired electrons when their orbital and/or spin-angular momentum interacts with an external field. In the absence of an applied magnetic field and interatomic interactions, magnetic moments of atoms align randomly due to thermal motion. However, in the presence of a strong field, the moments begin to change their alignment and finally point in the same direction as the field, acting like small magnets. For low levels of magnetisation, the magnetisation *M* is linearly related to the magnetic field *H*, and the solid is described as a linear material. We have the expression

$$M = \chi H \quad \text{(Equation 1.8)},$$

where χ is defined as the magnetic susceptibility. In practical cases magnetic susceptibilities are usually tabulated in terms of the molar magnetic susceptibility, χ_M. Curie's law can be used to describe the relationship between magnetic susceptibility and temperature for such paramagnetic system:

$$\chi = \frac{C}{T} \quad \text{(Equation 1.9)},$$

where *C* is the material-specific Curie constant. χ is proportional to 1/T, so that a graph of $1/\chi$ against T is linear. Curie's law is only valid when $\mu_B H \leq k_B T$, because at low temperatures or/and high field, the saturation of magnetisation occurs, and increasing the field will not lead to further alignment of moments. The Curie constant can be used to estimate the effective magnetic moment for a paramagnetic ion with non-interacting spins:

$$C = \frac{N_A}{3k_B}\mu_{\text{eff}}^2 \quad \text{(Equation 1.10)}.$$

In systems with interatomic interactions, the magnetic moments may show paramagnetic behaviour at high temperatures but start to order magnetically at low enough temperatures. In such cases the Curie law is amended, and the magnetic susceptibility can be fitted to the Curie Weiss law:

$$\chi = \frac{C}{T-\theta} \qquad \text{(Equation 1.11),}$$

where θ is the Weiss temperature. If θ is zero, then the material is ideally paramagnetic, while if θ > 0, the interatomic interactions are ferromagnetic and if θ < 0, they are antiferromagnetic. The meaning of these two terms is discussed below. Equation 1.9 can be easily rearranged into a linear function of 1/χ with respect to *T*, and it is often useful to plot 1/χ against *T* to examine the gradient and intercept of the resultant straight line to extract *C* and θ of the material (Figure 1.11).

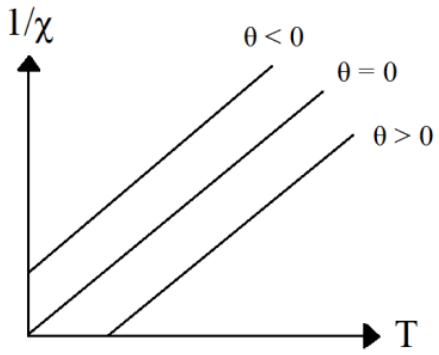

Figure 1.11 The Curie Weiss law shows linear plots of 1/χ against *T* for paramagnet, ferromagnet and antiferromagnet with intercepts of different signs.

1.3.2.2 Ferromagnetism

Ferromagnetism involves the spontaneous alignment of magnetic moments in the absence of an applied field. Ferromagnetism occurs below the Curie temperature T_C, at which point $\mu_B H = k_B T$ and the moment gained in the internal field *H* is just cancelled out by thermal motion energy. Below T_C, which equals the positive Weiss temperature, the *M*/*H* increases rapidly, while above T_C the material behaves as a paramagnet. Ferromagnetism can produce relatively strong forces, and is the mechanism by which well-known materials such as iron, nickel and cobalt form permanent magnets. These permanent magnets used in our daily life usually possess high Curie temperatures, far above room temperature. Ferromagnets also exist in the perovskite family; for example, $SrRuO_3$ was reported to order ferromagnetically below T_C ~ 160 K[40].

1.3.2.3 Antiferromagnetism

In contrast to ferromagnetism, in compounds exhibiting antiferromagnetism, neighbouring magnetic moments on different sublattices align in an antiparallel manner pointing in

opposite directions in the absence of an applied field. This should lead to a net magnetisation of zero. Above a transition temperature, which is referred to as the Néel temperature T_N, thermal energy breaks this magnetic ordering and the material becomes paramagnetic. Below T_N the susceptibility of the material is expected to decrease as the spins of two sublattices should begin to cancel each other out.

A complication with antiferromagnetism is that there are a number of ways to arrange the up and down spins in a lattice. Figure 1.12 displays a selection of possible arrangements of antiparallel spins in a cubic lattice. Either a single ordering pattern, or mixed ordering patterns can appear in one material. Among these arrangements, G-type ordering, which has all nearest-neighbour moments aligning in an antiparallel manner along all three axes, is very commonly found in perovskites[41, 42]. However there are exceptions such as $LaMnO_3$[43], where a distortion of the coordination geometry around the B-cation leads to a ferromagnetic interaction in the *ab* plane and an antiferromagnetic interaction along the *c* axis; this results in A-type ordering. C-type ordering with in-plane antiferromagnetic and out-of-plane ferromagnetic interactions has also been observed in perovskites, for instance, $ScCrO_3$ synthesised under high pressure and high temperature has been reported to adopt the C-type structure[44]. In another perovskite $Pr_{0.1}Sr_{0.9}MnO_3$, the intergrowth of G-type and C-type antiferromagnetically ordered layers has been reported[45].

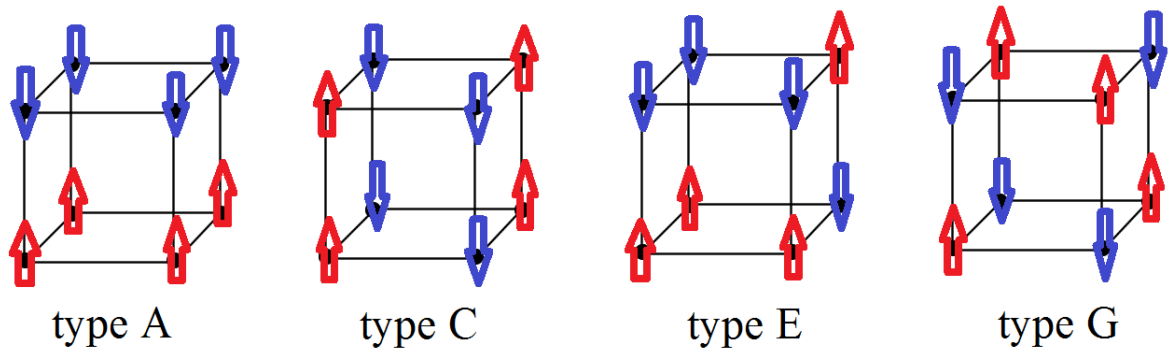

Figure 1.12 Four types of antiferromagnetic arrangement of spins in a cubic lattice.

1.3.2.4 Ferrimagnetism

In the above discussion of antiferromagnetism, we have assumed that the two sublattices are equivalent so that the net magnetisation is zero. However, it is also possible to have inequivalent sublattices and in this case the up and down spins will not cancel out, leading to a non-zero net magnetisation similar to ferromagnetism. This is known as ferrimagnetism.

The occurrence of ferrimagnetism is particularly common in ordered double perovskites with different concentrations of magnetic ion over distinct crystallographic sites[46, 47].

1.3.2.5 Frustration and spin-glass behaviour

For the magnetic systems described above, all magnetic moments align in a regular pattern and produce long-range magnetic ordering in the crystal. However, sometimes it is not possible to satisfy all the local magnetic interactions to achieve a single unique ground state, for example in the triangular lattice shown in Figure 1.13. In this case the system is referred to as being geometrically frustrated, and the material is called a spin glass. A spin glass is a random magnetic system involving mixed interactions. It is characterised by a random, yet cooperative freezing of spins at a well-defined temperature T_f, below which a variety of metastable frozen states with similar low energies could appear in the absence of magnetic long-range ordering[39]. Above T_f the material is paramagnetic. Spin-glass behaviour is most clearly seen in ac magnetisation measurements using an oscillating magnetic field, as the transition temperature shows a frequency-dependence.

There are many perovskites exhibiting spin-glass behaviour. For instance, Yb_2CoMnO_6 is a spin glass with disordered B site and a $T_f \sim 40$ K[48]. $La_3Ni_2NbO_9$ is a double perovskite with partial ordering of B-cations, however local fluctuations in composition lead to competition between different types of interaction and consequently frustration of the system[47]. Sr_2CaReO_6 is reported to be a fully ordered double perovskite, yet it behaves as a spin glass, and the mechanism involved is unclear[49].

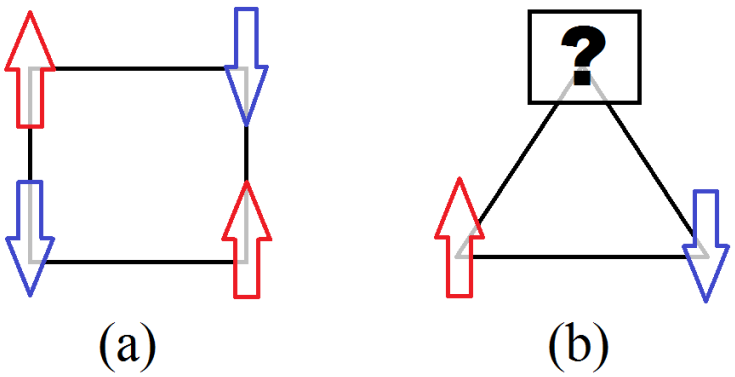

Figure 1.13 Antiferromagnetic arrangements of spins in (a) square lattice and (b) triangular lattice. In the triangular lattice the third spin cannot satisfy the requirement for antiferromagnetic interactions with the other two spins and frustration arises.

1.3.3 Exchange interactions

1.3.3.1 Origin of exchange interaction

At this stage we have shown various arrangements of magnetic moments in crystals, but for the moments to communicate with each other and potentially produce long-range order, some form of interaction must occur between the moments. The so-called exchange interaction is the key to the phenomenon of long-range magnetic order in solids. The exchange interaction is basically an electrostatic interaction, which results from the Coulomb repulsion of electrons. A series of wave functions deduced from quantum mechanics can be used to describe the effect of direct exchange, but they are not very relevant to this study so we will not go into details of them. For the metal oxide materials that we discuss in this thesis, it is indirect exchange responsible for the magnetic properties that they exhibit, and the mechanism involved is explained below.

1.3.3.2 Crystal field theory and superexchange interaction

In perovskites, the magnetic cations do not exist as free ions; there are significant interactions between each atom and its surroundings. For example, if we consider the B-cations, which control most of the magnetic properties of perovskites, they are six-coordinated, located in the centre of an octahedron formed by oxide ions. Therefore this octahedral coordination can impose effects on the electronic configuration and consequently the magnetic behaviour of the cation. Crystal field theory, which was developed in the 1930s[50], is a powerful tool to explain and predict such effects.

The crystal field is considered as an electric field arising from neighbouring atoms in the crystal, and the neighbouring orbitals are treated as negative point charges. The symmetry of the local environment largely controls the size and nature of the crystal field effects. The octahedral environment for the B-cations in perovskites is a common case. The d-orbitals of the metal cation are classified into two types, the t_{2g} orbitals that point between the *x*, *y* and *z* axes and the e_g orbitals that point along these axes, so that d_{xy}, d_{yz} and d_{xz} orbitals fall into the former type, and d_{z^2} and $d_{x^2-y^2}$ orbitals fall into the latter one. The two types of d-orbitals both rise in energy when put in a field, but are affected by the crystal field in different ways. For instance, Figure 1.14 shows the d_{xy} and $d_{x^2-y^2}$ orbitals in plan view, where we can see the $d_{x^2-y^2}$ orbital has a higher overlap with the neighbouring p-orbitals and consequently has a higher electrostatic energy.

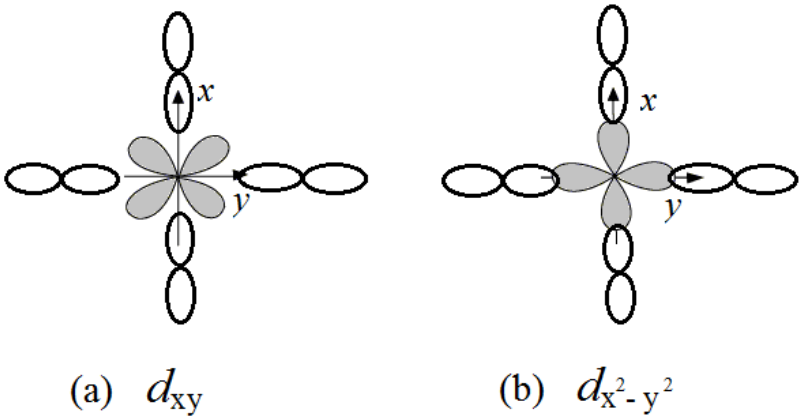

Figure 1.14 The crystal field originates from electrostatic interaction between the *d*-orbitals of the metal and the *p*-orbitals of the surrounding anions.

As in the octahedral environment, negative charges from the ligands are located at the points (±*r*, 0, 0), (0, ±*r*, 0) and (0, 0, ±*r*) pointing directly towards the e_g orbitals while between the t_{2g} orbitals, the t_{2g} orbitals are then lowered in energy and the e_g orbitals are raised in energy due to Coulomb repulsion. This effect breaks the degeneracy of the *d*-orbitals and results in the splitting of the five levels, with the field splitting energy to be Δ (Figure 1.15). For lighter atoms such as 3*d* ions where the crystal field interaction is the dominant interaction and the interaction between *L* and *S* is much smaller, the effective magnetic moment can be treated as a simple function of the spin angular momentum to a first approximation, and we can use the spin-only moment to estimate their magnetic moments such that *L* = 0:

$$\mu_{SO} = \sqrt{4S(S+1)}\mu_B \qquad \text{(Equation 1.12).}$$

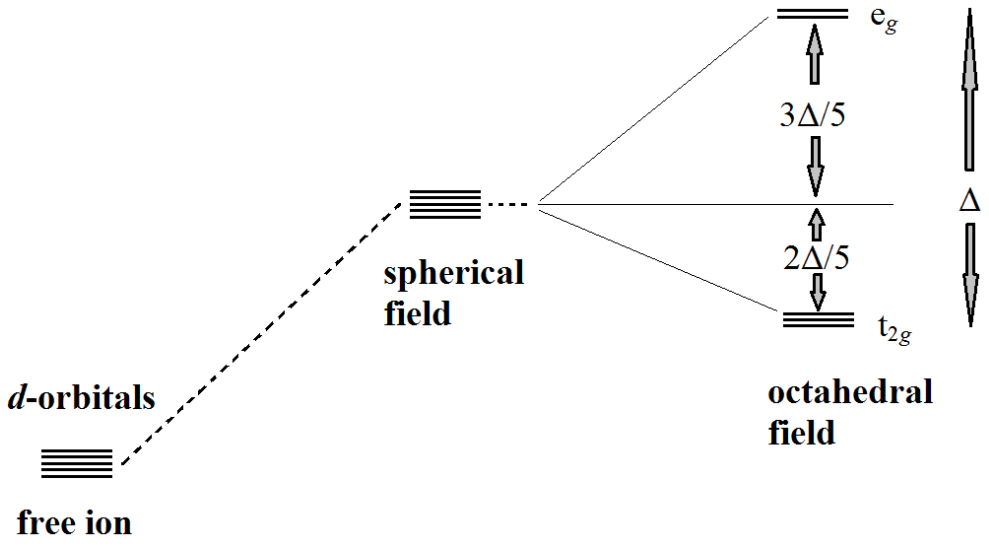

Figure 1.15 The crystal field in an octahedral environment.

The splitting of the energy levels by the crystal field influences the magnetic interactions between the cations. The exchange interaction in oxides usually occurs via a non-magnetic atom placed between the magnetic species as a bridge; this type of interaction is known as superexchange. The magnetic electrons are able to be delocalised over the *M*-O-*M* unit through mixing the ground state with an excited state, so that the kinetic energy can be lowered. Under some circumstances superexchange can also lead to ferromagnetism, for example, when an e_g electron from a magnetic atom hops onto the unoccupied e_g orbital of another magnetic atom, although this interaction is weaker and less common. Whether the material adopts antiferromagnetic or ferromagnetic superexchange interactions can be determined from the Goodenough rules[51]: virtual electron transfer between half-filled overlapping orbitals leads to antiferromagnetism, while transfer between a half-filled and an empty orbitals, or a filled and half-filled orbitals results in ferromagnetism.

The strength of the superexchange interaction largely depends of the degree of orbital overlap, and thus is strongly dependent on the angle of the *M*-O-*M* bond. Corner-sharing octahedra in an ideal cubic structure would produce an array of 180° *M*-O-*M* bonds, and the bond formed from orbital overlap along one axis is a σ bond; while an in-plane π bond has a bond angle of 90°. The strength of σ exchange and π exchange would depend upon the electronic configuration of the metal system, although generally σ exchange is stronger due to greater orbital overlap. These two types of exchange interactions can exist on their own, or take place simultaneously. Here we can use the exchange interactions between d^3 ions, d^5 ions and d^8 ions as examples to illustrate different situations. A d^3 ion has no electron in the e_g orbital so that σ exchange between two d^3 ions is not possible; any exchange interaction can only occur via a π bond. This π exchange interaction is thus responsible for the magnetic properties of some perovskites containing Cr^{3+} cations. A d^8 ion such as Ni^{2+} has fully occupied t_{2g} orbitals and half-filled e_g orbitals, and consequently only σ exchange operates between two d^8 ions. For two high-spin d^5 ions with both half-filled t_{2g} orbitals and e_g orbitals, both σ and π interactions can operate, leading to a great strength of exchange.

Below we consider the iron-containing perovskites. In most cases iron exists in perovskites as Fe^{3+} which has high-spin d^5 electronic configuration. With reference to the Goodenough rules, the neighbouring Fe^{3+} cations can then interact in an antiparallel manner through the half-filled orbitals, leading to both σ and π exchange. This superexchange interaction in the Fe-O-Fe unit is illustrated in Figure 1.16. The resulting antiferromagnetic coupling is usually a strong interaction which dominates the magnetic properties of iron-containing perovskites.

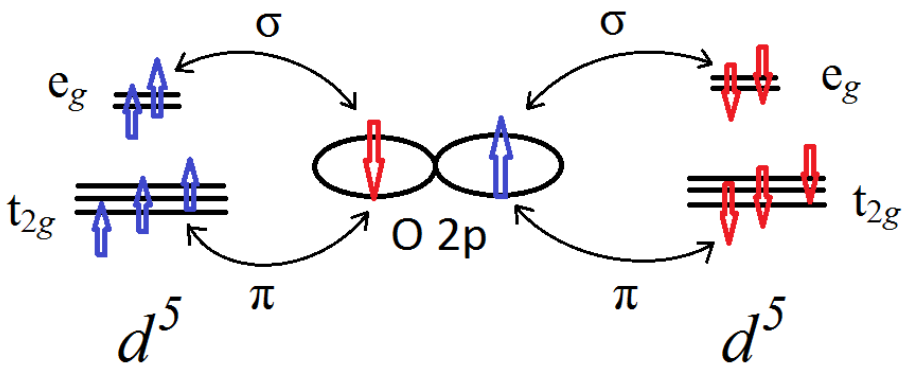

Figure 1.16 Superexchange interaction proposed for d^5 oxides which leads to antiferromagnetism.

1.4 Magnetism observed in iron-containing perovskites

There are a variety of magnetism types that can be observed in iron-containing perovskites. The simplest case is the perovskite with only one B site, such as orthoferrites with the primitive orthorhombic space group *Pbnm*. $LaFeO_3$ is one of these compounds. The number of the up-spin and down-spin atoms are equal to each other, so that they would be expected to be cancelled out and result in G-type antiferromagnetism. However, in reality weak ferromagnetism is reported for $LaFeO_3$[52], and this type of magnetism is often observed in other orthoferrites[53-57]. The behaviour of ferromagnetism arises from the exchange interaction between the excited state of one magnetic atom and the ground state of the other magnetic atom, which is known as the anisotropic exchange interaction and the Dzyaloshinsky-Moriya interaction[58, 59]. This interaction has the effect of canting the spins by a small angle and therefore produces a small ferromagnetic component of moment lying perpendicular to the spin-axis of the antiferromagnet (Figure 1.17).

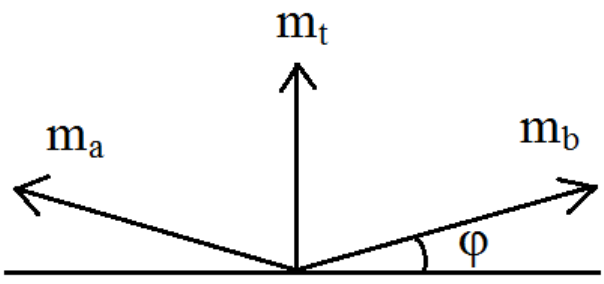

Figure 1.17 Two antiparallel spins m_a and m_b are canted by an angle φ and lead to a net moment of m_t pointing perpendicular to the G-type spin-axis.

Many iron-related perovskites that contain other transition metal elements on the same site as iron adopt the *Pbnm* structure as well, and in this case whether the overall magnetic property of the material is influenced by these species depends largely on the electronic configurations of the cations. For example, in the $LaFe_xCo_{1-x}O_3$ system, the magnetic properties can be explained by assuming a low-spin state of Co^{3+} with no unpaired electron, and the observed antiferromagetism comes purely from interactions between the Fe^{3+} ions[60]; while in the compound $LaFe_{0.5}Ni_{0.5}O_3$, no long-range magnetic order at low temperature is reported, and the material is a spin glass[61]. Spin-glass behaviour is common in iron-containing perovskites, especially when there are multiple magnetic species involved in the system, which makes the situation of interactions complex and competition between interactions arises. For example, in the cubic perovskite Sr_2FeTiO_6 mixed valence states: Ti^{4+}/Ti^{3+} and Fe^{4+}/Fe^{3+} are present and spin-glass-like state is observed below 16 K[62]. Sr_2FeRuO_6 is reported to have disordered B-cations in a monoclinic crystal structure and exhibits spin glass behaviour under 50 K[63]. Sr_2FeNbO_6 is a rather special case, which contains a disordered distribution of magnetic Fe^{3+} and non-magnetic Nb^{5+} ions and only antiferromagnetic interactions are expected; however the non-frustrated lattice shows spin glass behaviour under 32.5 K. It is believed that the competition between the nearest-neighbour interaction and the next-nearest-neighbour interaction is responsible for this unusual property[4]. Antiferromagnetic coupling through a superexchange mechanism is also often reported in the literature[41, 64, 65] for double perovskites containing iron, and many of these compounds actually have an overall ferrimagnetic structure due to different iron concentrations at crystallographically independent B sites. For instance, ferrimagnetism in a G-type magnetic structure is observed under 280 K in $Sr_3Fe_2MoO_9$[41], where one B site is fully occupied by Fe^{3+} and the other contains a random distribution of Fe^{3+} and Mo^{6+} cations.

1.5 An overview of the research

This research project is designed to investigate crystal structures and magnetic properties of iron-containing double perovskites with general formulae $A_3Fe_2B'O_9$, $A_2A'Fe_2B'O_9$ and $A_2A'FeB'B''O_9$. The main aspects to be studied include their crystal symmetry, cation ordering and magnetic behaviour.

As introduced earlier, our research group have previously described a double perovskite $La_3Ni_2SbO_9$. In $La_3Ni_2SbO_9$, the imbalance in the concentration of Ni^{2+} cations on the two B

sites of $La_3Ni_2SbO_9$ leads to ferrimagnetic behaviour with an ordering temperature of 105 K, although local variations in the composition cause the formation of small magnetic domains and thus eliminate magnetic Bragg scattering from the neutron diffraction pattern at low temperature due to a lack of long-range order. By analogy with relaxor ferroelectrics represented by some lead-based perovskites[66], this compound has been described as a relaxor ferromagnet[27, 67]. In another nickel-containing double perovskite $SrLa_2Ni_2TeO_9$, it has been reported that similar partial cation ordering also exists, while this compound is essentially a spin glass with regions of long-range magnetic ordering also present[68]. In the antimony-containing double perovskite $Sr_2LaCr_2SbO_9$ which involves the $3d^3$: Cr^{3+} cation[46], ferrimagnetic behaviour is observed below 150 K with the same G-type magnetic structure as $La_3Ni_2SbO_9$, but in a triclinic form of the perovskite structure. In this case magnetic Bragg peaks were observed in the neutron diffraction pattern at low temperature. However, the frequency dependence observed in the ac susceptibility of this compound indicates there are minor regions that are not fully ordered below the ordering temperature. It was proposed that, in contrast to $La_3Ni_2SbO_9$, strong π-mediated superexchange interactions are present in $Sr_2LaCr_2SbO_9$ and this increase in exchange strength facilitates the establishment of magnetic coherence despite the presence of low-level cation disorder. Thus $Sr_2LaCr_2SbO_9$ was described as a frustrated ferrimagnet rather than a relaxor ferromagnet. These variations show that the physical properties of double perovskites are closely related to the intrinsic properties of the cations as well as the crystal structures. The contrasting behaviour of these d^8 and d^3 systems, based on σ and π interactions respectively, prompted a comparative study of d^5 systems in which both types of interaction are operative. The work described below thus focussed on double perovskites containing Fe^{3+}. The first two compounds considered are $Sr_3Fe_2TeO_9$ and $Ba_3Fe_2TeO_9$, in which only the B site holds more than one species of cation. These two compounds are indeed very different from each other, both in crystal structures and magnetic properties. The change in crystal structure from the strontium compound to the barium analogue demonstrates how the size of A-cation affects stacking sequences in perovskites. The synthesis of the solid solution $Sr_xBa_{3-x}Fe_2TeO_9$ (x=2.5, 2.25, 2, 1.5, 1.25, 1) has been attempted and will be discussed.

The compounds $A_2LaFe_2SbO_9$ (A=Ba, Sr, Ca) which contain two different cation species on the A site were then successfully synthesised. Again as the radii of A-cations increase the crystal structures show obvious changes. Some compounds in the series $A_2LaFe_2B'O_9$ (A=Ba, Sr, Ca, B=Nb, Ta) with pentavalent transition-metal B-cations were selected for study. Three

compositions in the series $A La_2Fe_2SnO_9$ (*A*=Ba, Sr, Ca) have been synthesised, and the calcium compound will be discussed in detail. These compounds display various ordering patterns at the B site and therefore various physical properties, emphasising the possibility of manipulating the physical behaviour of perovskites by cation doping on the A site or B site.

In a continuation of the work on $La_3Ni_2SbO_9$, since the net magnetisation is expected to be larger in a compound containing a more strongly magnetic cation, and it is also likely that the transition temperature will increase above the value of 108 K seen in $La_3Ni_2SbO_9$, the consequence of introducing Fe^{3+} and Co^{2+} into the structure has been studied. Five double perovskites which contain three cation species at the B site: $A La_2FeCoSbO_9$ (*A*=Sr, Ca) and $A La_2FeNiSbO_9$ (*A*=Ba, Sr, Ca) will be described in detail.

All the samples discussed were synthesised using standard solid-state reactions under various conditions. A combination of techniques has been applied to characterise the samples, including X-ray diffraction, neutron diffraction, magnetometry measurements (both dc and ac), transmission electron microscopy and ^{57}Fe Mössbauer spectroscopy. These techniques are complementary to each other, and consequently it has proved possible to obtain a more integrated view of the sample by analysing data collected different techniques. These techniques are introduced in Chapter 2, and results and discussions are presented in the remaining chapters.

References

[1] S.A. Bhalla, R. Guo, R. Roy, Material Research Innovations 4 (2000) 3.

[2] E.V. Pannunzio-Miner, J.M. de Paoli, J.M. Alonso, M. Garcia Hernandez, R.D. Sanchez, R.E. Carbonio, Physica B, Condensed Matter 398 (2007) 397.

[3] H. Takei, N. Kobayashi, H. Yamauchi, T. Shishido, T. Fukase, Journal of the Less-Common Metals 125 (1986) 233.

[4] R. Rodriguez, A. Fernandez, A. Isalgue, J. Rodriguez, A. Labarta, J. Tejada, X. Obradors, J. Phys. C: Solid State Phys 18 (1985) L401.

[5] A. Callaghan, C.W. Moeller, R. Ward, Inorganic Chemistry 5 (1966) 1572.

[6] V.M. Goldschmidt, Naturwissenschaften 14 (1926) 477.

[7] S. Sasaki, C.T. Prewitt, J.D. Bass, Acta Crystallographica, Section C: Crystal Structure Communications 43 (1987) 1668.

[8] A.M. Glazer, Acta Crystallographica B28 (1972) 3384.

[9] H. Chen, T. Yu, P. Gao, J. Bai, J. Tao, T.A. Tyson, L. Wang, R. Lalancette, Inorganic Chemistry 52 (2013) 9692.

[10] S. Ishiwata, M. Azuma, M. Takano, E. Nishibori, M. Takata, M. Sakata, K. Kato, Journal of Materials Chemistry 12 (2002) 3733.

[11] Y. Takeda, F. Kanamaru, M. Shimada, M. Koizumi, Acta Crystallographica, Section B: Structural Science 32 (1976) 2464.

[12] H. Krischner, K. Torkar, B.O. Kolbesen, Journal of Solid State Chemistry 3 (1971) 349.

[13] E.J. Cussen, P.D. Battle, Chem. Mater. 12 (2000) 831.

[14] G. Zhang, Y. Liu, X. Yang, Y. Wei, S. Ouyang, H. Liu, Materials Chemistry and Physics 99 (2006) 88.

[15] Y. Takeda, T. Hashino, H. Miyamoto, F. Kanamaru, S. Kume, M. Koizumi, Journal of Inorganic and Nuclear Chemistry 34 (1972) 1599.

[16] P.D. Battle, T.C. Gibb, C.W. Jones, Journal of Solid State Chemistry 74 (1988) 60.

[17] P.C. Donohue, L. Katz, R. Ward, Inorganic Chemistry 4 (1965) 306.

[18] R.D. Burbank, H.T. Evans-Jr, Acta Crystallographica 1 (1948) 330.

[19] B.L. Chamberland, Journal of Solid State Chemistry 48 (1983) 318.

[20] M.T. Anderson, K.B. Greenwood, G.A. Taylor, K.R. Poeppelmeier, Progress in Solid State Chemistry 22 (1993) 197.

[21] S. Vasala, M. Karppinen, Progress in Solid State Chemistry 43 (2015) 1.

[22] M.A. Alario-Franco, I.E. Grey, J.C. Joubert, H. Vincent, M. Labeau, Acta Crystallographica, Section A: Foundations of Crystallography 38 (1982) 177.

[23] S.G. Steward, H.P. Rooksby, Acta Crystallographica 4 (1951) 503.

[24] F. Galasso, W. Darby, Journal of Physical Chemistry 66 (1962) 131.

[25] P.D. Battle, C.W. Jones, Journal of Solid State Chemistry 78 (1989) 108.

[26] M.T. Anderson, K.R. Poeppelmeier, Chemistry of Materials 3 (1991) 476.

[27] P.D. Battle, M. Avdeev, J. Hadermann, J. Solid State Chem. 220 (2014) 163.

[28] F. Galasso, J.R. Barrante, L. Katz, Journal of American Chemical Society 83 (1961) 2830.

[29] F. Galasso, J. Pyle, Journal of Physical Chemistry 67 (1963) 533.

[30] F. Galasso, J. Pyle, Inorganic Chemistry 2 (1963) 482.

[31] F. Galasso, J. Pyle, Journal of Physical Chemistry 67 (1963) 1561.

[32] J.T. Rijssenbeek, T. Saito, S. Malo, M. Azuma, M. Takano, K.R. Poeppelmeier, Journal of American Chemical Society 127 (2005) 675.

[33] P.K. Davies, H. Wu, A.Y. Borisevich, I.E. Molodetsky, L. Farber, Annual Review of Materials Research 38 (2008) 369.

[34] A. Alonso, E. Mzayek, I. Rasines, Materials Research Bulletin 22 (1987) 69.

[35] M.A. Subramanian, Journal of Solid State Chemistry 111 (1994) 134.

[36] Y. Doi, Y. Hinatsu, Journal of Physics: Condensed Matter 16 (2004) 2849.

[37] M.S. Augsburger, M.C. Viola, J.C. Pedregosa, R.E. Carbonio, J.A. Alonso, J. Mater. Chem. 16 (2006) 4235.

[38] T. Sekiya, T. Yamamoto, Y. Torii, Bull. Chem. Soc. Jpn. 57 (1984) 1859.

[39] S. Blundell, Magnetism in Condensed Matter, Oxford University Press, 2001.

[40] C.W. Jones, P.D. Battle, P. Lightfoot, W.T.A. Harrison, Acta Cryst. C 45 (1989) 365.

[41] M.C. Viola, J.A. Alonso, J.C. Pedregosa, R.E. Carbonio, Eur. J. Inorg. Chem. (2005) 1559.

[42] I. Sosnowska, P. Fischer, Journal of the Less-Common Metals 111 (1985) 109.

[43] T. Shimura, T. Hayashi, Y. Inaguma, M. Itoh, Journal of Solid State Chemistry 124 (1996) 250.

[44] L. Ding, P. Manuel, D.D. Khalyavin, F. Orlandi, Y. Kumagai, F. Oba, W. Yi, A.A. Belik, Physical Review B 95 (2017) 054432.

[45] C. Martin, A. Maignan, M. Hervieu, B. Raveau, Z. Jirak, M.M. Savosta, A. Kurbakov, V. Trounov, G. Andre, F. Bouree, Physical Review B 62 (2000) 6442.

[46] E.C. Hunter, P.D. Battle, R. Paria Sena, J. Hadermann, Journal of Solid State Chemistry 248 (2017) 96.

[47] C. Chin, P.D. Battle, S. Blundell, E.C. Hunter, F. Lang, M. Hendrickx, R. Paria Sena, J. Hadermann, Journal of Solid State Chemistry 258 (2018) 825.

[48] X. Wang, M. James, J. Horvat, F. Gao, A. Li, H. Liu, S. Dou, Journal of Magnetism and Magnetic Materials 246 (2002) 86.

[49] J.E. Greedan, S. Derakhshan, F. Ramezanipour, J. Siewenie, T. Proffen, Journal of Physics: Condensed Matter 23 (2011) 164213-1.

[50] J. Van Vleck, Physical Review 41 (1932) 208.

[51] J.B. Goodenough, Journal of Physics and Chemistry of Solids 6 (1958) 287.

[52] S. Chanda, S. Saha, A. Dutta, B. Irfan, R. Chatterjee, T.P. Sinha, Journal of Alloys and Compounds 649 (2015) 1260.

[53] M.P. Attfield, P.D. Battle, S.K. Bollen, T.C. Gibb, R.J. Whitehead, Journal of Solid State Chemistry 100 (1992) 37.

[54] J. Blasco, J. Garcia, Journal of Physics and Chemistry of Solids 55 (1994) 843.

[55] A. Ghosh, M.G. Masud, K. Dey, B.K. Chaudhuri, Journal of Physics and Chemistry of Solids 75 (2014) 374.

[56] Z. Zhou, L. Guo, H. Yang, Q. Liu, F. Ye, Journal of Alloys and Compounds 583 (2014) 21.

[57] R.M. Bozorth, Physical Review Letters 1 (1958) 362.

[58] I. Dzyaloshinski, Journal of Physics and Chemistry of Solids 4 (1958) 241.

[59] T. Moriya, Physical Review 120 (1960) 91.

[60] D.V. Karpinskii, I.O. Troyanchuk, K. Baerner, H. Szymczak, M. Tovar, Journal of Physics: Condensed Matter 17 (2005) 7219.

[61] M. Gateshki, L. Suescun, S. Kolesnik, J. Mais, K. Swierczek, S. Short, B. Dabrowski, Journal of Solid State Chemistry 181 (2008) 1833.

[62] P.N. Lekshimi, S.S. Pillai, K.G. Suresh, P.N. Santhosh, M.R. Varma, Journal of Alloys and Compounds 522 (2012) 90.

[63] P.D. Battle, T.C. Gibb, C.W. Jones, F. Studer, Journal of Solid State Chemistry 78 (1989) 281.

[64] S.A. Ivanov, P. Nordblad, S.G. Eriksson, R. Tellgren, H. Rundlof, Mater. Res. Bull. 42 (2007) 776.

[65] S.A. Ivanov, S.G. Eriksson, R. Tellgren, H. Rundlof, Materials Research Bulletin 36 (2001) 2585.

[66] S.A. Ivanov, R. Tellgren, H. Rundlof, N.W. Thomas, S. Ananta, Journal of Physics: Condensed Matter 12 (2000) 2393.

[67] P.D. Battle, S.I. Evers, E.C. Hunter, M. Westwood, Inorg. Chem. 52 (2013) 6648.

[68] R. Paria Sena, J. Hadermann, C. Chin, E.C. Hunter, P.D. Battle, Journal of Solid State Chemistry 243 (2016) 304.

Chapter 2: Experimental Techniques

2.1 Solid-state synthesis

Solid-state synthesis is one of the main routes to prepare inorganic materials[1]. The term is used to describe all the reactions that involve solids in a broad sense. The synthesis of oxide materials can be conducted in various ways, for example, using a flux method for single crystal growth, using a ceramic method to prepare polycrystalline solids, and using gel methods in the preparation of nanoparticle powders. The ceramic method involves mixing powdered starting materials in a stoichiometric ratio and annealing the mixture in a furnace under appropriate conditions until a single-phase product is formed. This is the technique that was used to synthesise the compounds described in the chapters that follow.

The mechanism of standard ceramic synthesis falls into three steps. First, rearrangements together with breaking and reforming of chemical bonds occur on the contact surface of the reactant particles to generate the crystal centre. In the second stage, the cations escape from their original positions and diffuse into a defect so as to trigger further reaction. The final stage requires the reactants to diffuse and grow around the crystal centre to form a single phase. Temperature, pressure, atmosphere, surface area, particle size and chemical composition can all affect the speed of reaction. Raising the temperature would increase both the reaction rate constant:

$$k = A\exp\left(-\frac{G}{RT}\right) \qquad \text{(Equation 2.1)}$$

and the diffusion constant:

$$D = D_0 \exp\left(-\frac{Q}{RT}\right) \qquad \text{(Equation 2.2).}$$

Pressing the loose reactant powders into a pellet can decrease the distance between particles, and thus increase the contact surface area as well as the diffusion area to maximise the possibility of reaction. The atmosphere might influence reactions that are sensitive to oxygen or nitrogen. Particle size is another important factor, as reaction rate is inversely proportional to the square of particle diameter. Also, the chemical compositions of the reactants need to be chosen carefully, since different reactants have different activities. For instance, Co_3O_4 is

used as a cobalt source instead of commercially available CoO, because the CoO formed on decomposition of Co_3O_4 has a higher reactivity.

All samples described in this thesis were prepared using the standard ceramic method under ambient atmosphere. The general reaction can be described as a combination reaction:

$$A_{(s)} + B_{(s)} \rightarrow C_{(s)} \qquad \text{(Equation 2.3).}$$

Reactants such as ACO_3 (A=Ba, Sr, Ca), La_2O_3, Fe_2O_3, and other starting materials (purity >99.95%) were weighed out in the appropriate stoichiometric ratio with an accuracy of ±0.1 mg and ground together in an agate mortar for 30 minutes to give a homogeneous mixture. When La_2O_3 was involved, it was heated at 800 °C for 24 hours prior to use to ensure it was completely dry. The mixture was then loaded into an alumina crucible and fired at 800 °C for 24 h for pre-heating, as well as for releasing CO_2 if carbonate was used as a starting material. It was then quenched to room temperature, reground and pressed into a pellet which was fired in air at high temperatures, typically between 1150 °C and 1300 °C. It was usually necessary for samples to undergo air-quenching to room temperature followed by regrinding and reheating to ensure homogeneity and help increase the reaction rate. The precise reaction time, firing temperatures and reaction schemes were different for each sample, and will be stated in detail in each chapter. Finally, the furnace was allowed to cool to 800 °C and then the sample was quenched to room temperature. Most of the products were obtained as deep-coloured powders. The progress of reactions was followed by laboratory X-ray powder diffraction, and the reactions were assumed to have completed when there was no apparent change in the X-ray diffraction profile upon further heating.

2.2 Powder diffraction techniques

2.2.1 General features of crystals and powder diffraction

Materials in the crystalline state are commonplace and important in our daily life[2], such as household chemicals, industrial materials and precious stones that we wear for decoration. The most obvious feature of crystals is the presence of their planar surfaces; and another readily observed feature is that the crystals of a specific material tend to be alike (Figure 2.1). This suggests that the microscopic form of a crystal depends strongly on structural arrangement at the atomic or molecular level.



Figure 2.1 A specimen of perovskite crystals on a matrix[3]. The shape of the crystal directly reflects the primitive cubic arrangement of atoms in unit cell, which was described in Chapter 1.

The symmetry of crystal as a whole is related to the symmetry of smaller subunits. The smallest subunit of a crystal is a unit cell, which confers translational symmetry and is the building block of the crystal structure. A unit cell is defined by six length and angle parameters *a*, *b*, *c*, *α*, *β*, *γ* (Figure 2.2). There are seven distinct types of subunit and we describe them as seven crystal systems: triclinic, monoclinic, orthorhombic, tetragonal, trigonal, hexagonal and cubic systems. Among them the cubic system is of the highest symmetry which has four triad axes, while the triclinic system is of the lowest symmetry with no essential symmetry element.

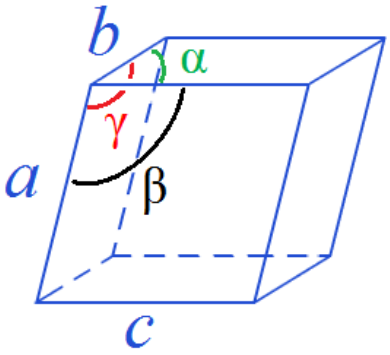

Figure 2.2 A general unit cell showing all the six cell parameters.

Lattice planes in unit cells can be described with Miller indices. If a set of parallel planes cuts the edges of the unit cell at regular intervals of *a*/*h*, *b*/*k* and *c*/*l*, where *h*, *k*, *l* are integers with a greatest common devisor to be one, the set of lattice planes can be written as (*hkl*). Figure 2.3 shows a set of (321) planes in a unit cell as an example. The perpendicular distance between two adjacent (*hkl*) planes is defined as the *d*-spacing, d_{hkl}.

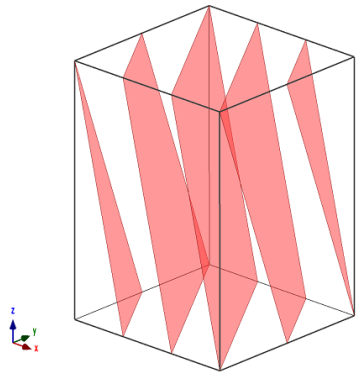

Figure 2.3 The (321) lattice planes determined by intercepts in a unit cell.

In terms of the arrangement of lattice points in the unit cell, there are three main types of unit cell (Figure 2.4). The most common one is the primitive unit cell, which contains one lattice point per unit cell. Other non-primitive unit cells containing additional lattice points include body centred unit cells and face centred unit cells, which have two lattice points and four lattice points per unit cell, respectively.

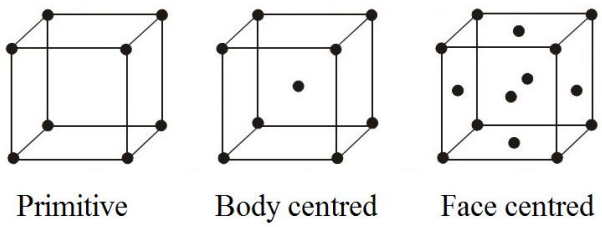

Figure 2.4 Three types of unit cell with distinct lattice point arrangements.

The unit cell of any compound may contain symmetry elements, e.g. rotations, reflections, screw axes (rotation plus translation) and glide planes (reflection plus translation). When symmetry elements are combined in groups, it has been shown that there are altogether 230 possible distinctive arrangements, and each one of them is called a space group with a unique symbol. For example, the primitive triclinic space group *P* -1, the primitive monoclinic space group $P2_1/n$ (where 2_1 is a screw axes and *n* stands for an *n*-glide plane) and body-centred tetragonal space group *I*4/*m*. All three-dimensional crystalline solids can be assigned to one of the 230 space groups. The determination of space group is the first step in studying the structure of a crystalline material. This can be usually achieved with diffraction techniques.

In the field of structure determination, diffraction techniques are one of the most common and important non-destructive tools. They include X-ray diffraction, neutron diffraction and electron diffraction. If classified by morphology of the sample being examined, they can be

divided into single crystal diffraction and powder diffraction. Examples of the instrument setups are shown in Figure 2.5.

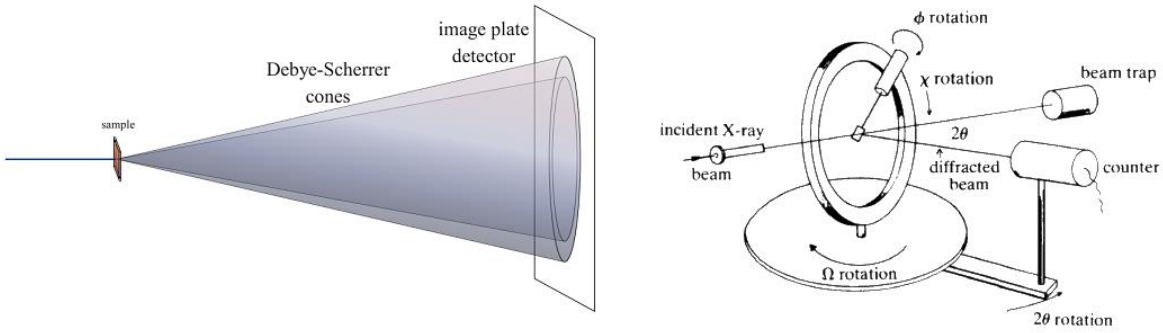

Figure 2.5 (Left) schematic of two-dimensional powder diffraction setup with flat plate detector[4]. (Right) schematic of 4-circle single crystal single crystal diffractometer[5].

Powder diffraction is carried out by a diffractometer that produces waves at a known wavelength. The wave source can be X-ray, neutron or electron. In a crystal there exists a periodic arrangement of scattering centres, i.e. atoms. When the wave reaches the sample, the atoms behave as a diffraction grating and produce maxima in the scattered intensity at particular angles. By measuring the angles at which the maxima occur, the separation of the scattering centres can be found.

The wavelength of the radiation must be comparable to atomic spacings. The incoming wave can be considered to be scattered by lattice planes that are separated by the interplanar distance *d*, see Figure 2.6. The difference in path length between waves scattered from neighbouring planes must be equal to an integer multiple of the wavelength for constructive interference to occur. The path difference is thus given by $2d\sin\theta$. If the scattered wave is collected on a flat plate detector like that shown in Figure 2.5, a smooth diffraction ring, or a cone results from the rotational averaging around the beam axis, and the angle between the cone and the beam axis is equal to 2θ, the scattering angle. The cumulative effect of reflections in successive planes of the crystalline lattice leads to the intensifying of the effect from the interference. Bragg's law describes the condition on θ for a maximum in the constructive interference to be observed:

$$2d_{hkl}\sin\theta_{hkl} = \lambda \qquad \text{(Equation 2.4)},$$

For moving particles such as electrons and neutrons, the associated wavelength is called the de Broglie wavelength, which can be determined by:

$$\lambda = \frac{h}{p} = \frac{h}{mv} \qquad \text{(Equation 2.5),}$$

where p is the momentum of the particle and h is the Plank constant.

A diffraction pattern is acquired by measuring the intensity of scattered waves as a function of scattering angle, and Bragg peaks with strong intensities appear in the diffraction pattern where the scattering angles satisfy the Bragg condition. This method is known as angle dispersive scattering, which is usually used in X-ray diffraction. However, it is also possible to conduct the experiment in another way. If we vary the wavelength instead and keep the angle constant, this is called energy dispersive scattering, or time-of-flight scattering. This technique is more commonly applied in neutron diffraction as neutron can travel at a range of speeds.

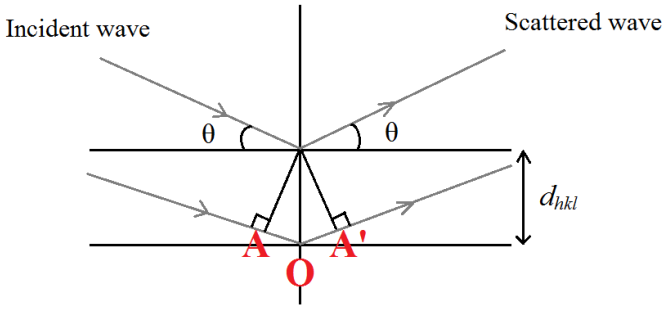

Figure 2.6 Diffraction process resulting from a set of lattice planes (*hkl*). The difference in path length between the two waves is equal to 2|OA|, and |OA| is equal to $d\sin\theta$.

The d-spacing is related to the Miller indices of the lattice planes in some way according to the crystal symmetry, therefore the diffraction pattern can be indexed, i.e. particular maxima can be associated with particular (*hkl*) planes. The simplest case is the primitive cubic crystal system, where we have the following equation and can usually index the pattern manually:

$$\frac{1}{d^2} = \frac{h^2+k^2+l^2}{a^2} \qquad \text{(Equation 2.6).}$$

Although manual indexing of cubic cells is a reasonably straightforward process, it is very time-consuming to deal with more complicated crystal systems such as tetragonal and hexagonal cells by hand. Fortunately there are computer auto-indexing programs available to help with data analysis, which will be discussed elsewhere.

Obviously the Bragg condition does not explain the intensity of each peak observed in the diffraction pattern. The intensity of the reflection from a certain set of lattice planes, I_{hkl}, is

proportional to the product of four parameters: the sample-independent Lorentz-polarisation factor *L*, the multiplicity of a reflection *m*, the absorption factor *A*, and square of the structure factor F_{hkl}. Among them the structure factor is probably the most interesting. It is given by:

$$F_{hkl} = \sum_n f_n \exp[2\pi i(hx_n + ky_n + lz_n)] \exp[\frac{-8\pi^2 U_{iso_n} \sin^2\theta_{hkl}}{\lambda^2}] \quad \text{(Equation 2.7)},$$

where f_n is the atomic scattering factor, and x_n, y_n and z_n are the fractional coordinates of the nth atom in the unit cell. In the equation the second exponential term makes a correction to the structure factor for the isotropic thermal displacements of the atoms, serving to reduce the intensity of a reflection when the scattering vector increases. A higher value of U_{iso} usually indicates stronger vibrational motion at higher temperatures, or larger uncertainty in coordinates of the atom. In addition, absorption of the incident wave and extinction phenomenon can effectively reduce the reflection intensity. An important observation resulting from the structure factor in diffraction patterns is the possibility of systematic absences. For primitive unit cells, a reflection from every set of Miller indices may be observed. However this is not the case for non-primitive unit cells. For example, if we have a face centred unit cell, it can be shown that F_{hkl} is equal to 4*f* when *h*, *k*, *l* are either all even or all odd, while it is equal to zero when *h*, *k*, *l* have mixed parity. This means some peaks in the pattern will be "missing". Similarly, in the diffraction pattern obtained from a body centred unit cell, the condition for allowed peaks is: $h + k + l = 2n$, with *n* being a natural number. Systematic absences can be very valuable in determining symmetry of crystals. When we index a diffraction pattern, one golden rule is that the conclusion should be always based on the observed peaks, but not the missing peaks. Allowed peaks could sometimes show very little intensity and be hard to identify; however the presence of any unallowed peak should help us rule out the related symmetry straightaway, even if all the other observed peaks are expected to appear in the pattern.

As stated previously, powder diffraction and single crystal diffraction are different in instrumental settings and they are complementary as diffraction techniques. The intensity of reflections is measured as a function of the Miller indices *hkl* in a single crystal diffraction experiment and three-dimensional data is acquired. If the space group is unknown, reflections can be compared with other possible symmetry equivalent reflections so that the correct Laue Class (point group) of the crystal can be determined. However in powder diffraction, all symmetry equivalent reflections have the same *d*-spacing, leading to the overlap of two-dimensional peaks which makes the measurement of individual peaks difficult. Moreover,

since we do not usually obtain a sufficient number of reliable intensities in powder diffraction to get the accurate normalised structure factor, which is statistically crucial in determining whether the structure is centrosymmetric or not, it is impossible to distinguish between centrosymmetric and non-centrosymmetric structures in terms of reflection conditions alone by powder diffraction. It is also worth noting that the operation of powder diffraction assumes that, in contrast to anisotropic single crystals, the powdered sample is completely isotropic with no texturing. Therefore sometimes rotation of the sample (by using rotating spinner sample stage, capillaries, etc.) is necessary to eliminate any texturing effect and achieve true randomness. These facts suggest powder diffraction may not be as powerful as single crystal diffraction in symmetry determination, however powder diffraction is widely used in the lab for the simplicity of sample preparation, rapidity of measurement and quick identification of mixed phases. Due to the extreme difficulty in growing single crystals of the compounds in this thesis, we will use powder diffraction methods to follow the progress of reactions and solve structures, and any problems met during the analysis of data will be discussed in appropriate chapter.

2.2.2 X-ray powder diffraction (XRPD)

X-ray diffraction is based on the fact that as waves of electromagnetic radiation, X-rays interact primarily with atoms' electrons when passing through the sample. For this reason, lighter atoms with fewer electrons, such as oxygen, are relatively hard to be detected by X-ray. Also, since we need to consider the interference effects from different electrons within an atom, there is a strong angular dependence of the scattering. The scattering power of an atom is expressed by its form factor, which drops rapidly as a function of $\sin\theta/\lambda$, leading to significant intensity loss at high angles in the diffraction pattern (Figure 2.7). This effect arises because the size of the scattering centre (the atom) is comparable to the wavelength of the radiation.

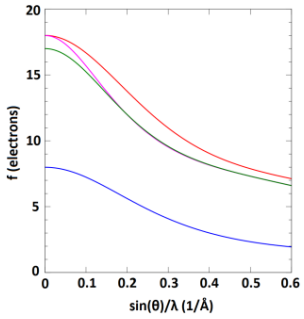

Figure 2.7 X-ray atomic form factors for: oxygen(blue), chlorine(green), Cl^-(magenta) and K^+(red)[6].

Collection of diffraction data is achieved by X-ray diffractometers. Laboratory X-ray diffractometers rely on the use of an X-ray tube, which serves to produce X-rays. A copper anode is most commonly used in such tubes, while cobalt and molybdenum are popular materials as well. Since X-ray sources produce $K\alpha_1$, $K\alpha_2$ and K_β radiations simultaneously, filters and monochromators are essential in order to eliminate the unwanted radiations as much as possible. For a copper radiation source, nickel with the appropriate absorption edge is chosen to be the material for the β-filter, and a silicon monochromator with a narrow band pass works best by reflecting only the $K\alpha_1$ wavelength that obeys Bragg's law for the particular *d*-spacings. The setting for most modern X-ray diffractometers is called the Bragg-Brentano geometry, which is illustrated in Figure 2.8. In this setting a constant sample-to-receiver distance is maintained, and the detector for counting photons moves around the diffractometer circle, with the sample being placed at the centre. Divergence slits are usually fitted in the beam path to control the equatorial divergence of the incident beam and thus the length of the sample being irradiated. Soller slits are used to limit the axial divergence of the beam so as to improve peak shape and resolution.

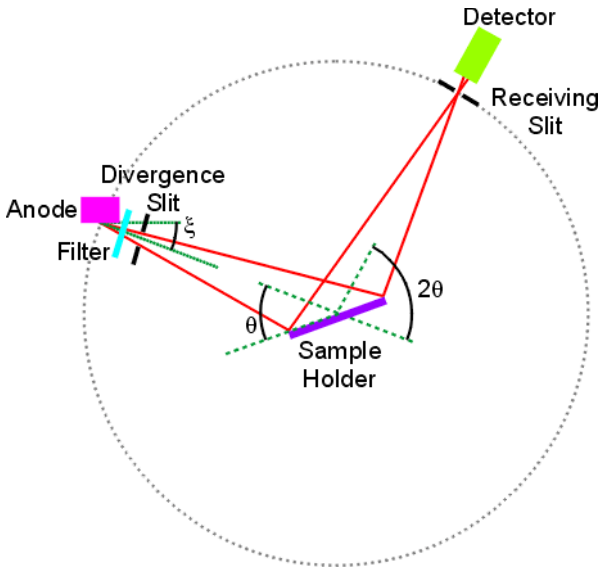

Figure 2.8 Setup of the Bragg-Brentano geometry in laboratory X-ray diffractometers[7].

2.2.2.1 Laboratory Panalytical X'Pert Diffractometer

The progress of reactions was routinely monitored with a laboratory Panalytical X'Pert Diffractometer using Cu $K\alpha_1$ radiation. Short 30-minute scans ($10 \leq 2\theta\,(^o) \leq 90$, $\Delta 2\theta = 0.05^o$) with flat sample stage were applied to initially access the synthesis progress and identify phases in the powders; longer three-hour scans ($5 \leq 2\theta\,(^o) \leq 125$, $\Delta 2\theta = 0.02^o$) with

spinner sample stage (which is for minimising the effects of preferred orientation) were used to check sample purity and acquire diffraction patterns for quantitative data analysis.

2.2.2.2 Laboratory Panalytical Empyrean Diffractometer

Progress of some reactions was also monitored by a Panalytical Empyrean Diffractometer using Cu $K\alpha_1$ radiation during the period when the Panalytical X'Pert Diffractometer was out of order. Similar short 30-minute scans were carried out on flat sample stage for rough phase identification, and longer overnight scans ($5 \leq 2\theta\,(^o) \leq 130$, $\Delta 2\theta = 0.02^o$) were recorded with the spinner sample stage in order to ensure phase purity and facilitate quantitative data analysis.

2.2.2.3 Diamond Light Source: national synchrotron science facility

Selected samples were taken to the Diamond Light Source located at the Harwell Science and Innovation Campus in Oxfordshire. The Diamond Light Source is the UK's national synchrotron source which produces a medium-energy electron beam for scientific research in various fields. The machine works by accelerating electrons from the electron gun through sequences of magnets until they reach almost the speed of light and are bent by the powerful magnetic field, so that they give off synchrotron light, which is millions of times brighter than light produced from conventional sources and 10 billion times brighter than the sun[8]. These bright beams are then directed off into laboratories known as beamlines. Beamlines use two different sources of synchrotron light: bending magnets and insertion devices. As the electron beam passes through a bending magnet, it emits a wide fan of synchrotron light, which is channelled into a beamline. Insertion device beamlines use special arrays of magnets inserted into the straight sections of the storage ring, which cause the electron beam to follow a wiggling, or undulating path and become even brighter. The schematic representation of the synchrotron facility is shown in Figure 2.9. Compared to the laboratory source, the most important advantage of synchrotron source is its brilliance, as higher brilliance enables us to see more details in the material with greater precision. In the case of the study in this thesis, it was found that the synchrotron source is particularly powerful at achieving high peak-to-background intensity, identifying weak impurity peaks and displaying detailed peak splitting. Moreover, the high-energy beam can penetrate deeper into the matter, and the wide spectrum of synchrotron radiation permits a wide range of scientific studies, such as bonds in molecules, nanoscale objects and short-time-scale chemical reactions.

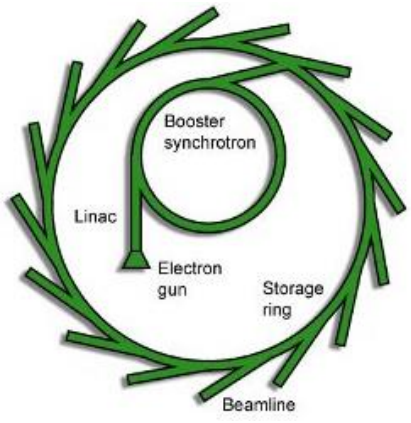

Figure 2.9 Setting of the synchrotron facility at the Diamond Light Source[8].

Powder diffraction data were collected from selected samples on instrument I11, which is a high resolution beamline for crystallography using an undulator source. Samples were loaded into borosilicate glass capillaries of 0.3mm diameter, and 30-minute constant-velocity scans ($0 \leq 2\theta\,(^{o}) \leq 150$) were conducted on the Multi-Analyser-Crystal (MAC) detector for purity and symmetry checking. The wavelength of the beam was determined to be 0.8259 Å by performing a measurement on a silicon standard.

2.2.3 Neutron diffraction (ND)

A complementary technique to X-ray diffraction, neutron diffraction involves the application of neutron scattering to the determination of the atomic coordinates, crystal symmetry and magnetic structure of a material. In contrast to X-ray, in neutron diffraction the fundamental scattering body is the nucleus of an atom instead of the electron cloud, except for magnetic materials. Most atoms have approximately equal scattering length, and any difference is within a factor of only two or three[9]. This means neutron diffraction is much more powerful in locating lighter atoms like oxygen. In general, there is a slight increase in scattering amplitude with atomic weight, with considerable irregular variations superimposed upon this being observed (Figure 2.10). This is because the scattering length is dependent on both potential scattering and resonance scattering. Potential scattering is always positive and increases slowly with atomic weight, while resonance scattering can impose random effects and sometimes even changes the scattering amplitude into negative values. It is worth noting that vanadium hardly scatters neutrons and therefore is often used as a container material in neutron diffraction experiments. There is also a sharp drop in scattering amplitude from Ni^{58} to Ni^{62}, reflecting the fact that scattering length of neutrons varies from isotope to isotope, and it is possible to mix isotopes of one element to give zero net scattering.

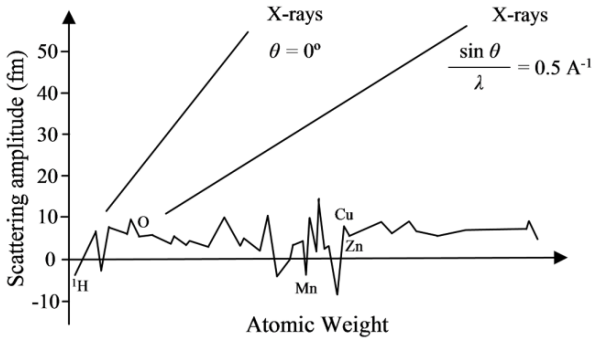

Figure 2.10 Irregular variation of neutron scattering amplitude with atomic weight. The regular increase for X-ray is shown for comparison[9].

Moreover, neutron scattering shows little variation with the angle θ, since unlike those of the electron cloud, the dimensions of nucleus are very small compared with the wavelength of 1 Å, and the form factor for neutron scattering is constant with θ. The additional information available at high angles in the diffraction pattern enables us to determine structural parameters of the material with great precision. Besides, with a penetration depth of several centimeters, neutron diffraction is suitable for analysing bulk samples, while even strong X-ray beams from synchrotron sources can only deal with thin specimens. The main disadvantage of neutron diffraction is that a relatively large quantity of sample is often needed, which might be challenging to prepare and, obviously, a nuclear reactor or spallation source is necessary for collecting data, which is unlikely to be seen in our standard laboratories. Various neutron sources around the world that have been used for this thesis will be introduced later.

One important application of neutron diffraction in materials science is the detection of long-range magnetic order and the determination of magnetic structure in solids. While neutrons mainly interact with the nucleus of an atom, additional scattering occurs when the neutron magnetic moment is scattered by the magnetic moment of the atom. Transition metals such as iron, cobalt and nickel possess unpaired electrons and resultant magnetic moment, which interacts with the magnetic moment of the neutron as the neutron has a spin quantum number of ½ with a magnetic moment of –1.9 nuclear magnetons. It may seem anomalous that as a neutral particle the neutron has a non-zero moment and is affected by magnetic fields. The existence of the magnetic moment is actually an indication of the neutron's quark substructure and internal charge distribution (Figure 2.11). It can be viewed as the consequence of the vector sum of the three quark magnetic moments plus the orbital moments arising from the movement of the charged quarks within the neutron.

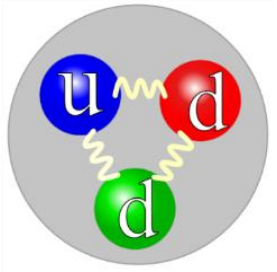

Figure 2.11 The quark model of the neutron. The neutron is composed of one up quark with charge of 2/3 *e* and two down quarks, each having charge of -1/3 *e*[10].

When the magnetic moments are ordered in a crystalline material, extra Bragg scattering will appear in the neutron diffraction pattern. Since the scattering body is the electron cloud with a size comparable to the neutron wavelength, magnetic form factors display a strong angular dependence similar to the case of X-ray diffraction, and intense magnetic Bragg reflections can only be observed at low angles (high *d*-spacings). If the moments are not ordered in a long-range manner such as in a spin glass, magnetic scattering will contribute to background intensity only. Neutron diffraction thus enables us to identify different arrangements of spins and magnetic architectures within the atomic structure of materials. Ferromagnetic structures and various types of antiferromagnetic structures, as well as the magnitudes of magnetic moments on ions in the crystal, can all be analysed with the aid of neutron diffraction data.

With magnetic scattering present, the total intensity of a Bragg peak in un-polarised neutron diffraction pattern is now the sum of nuclear intensity and magnetic intensity. The new structure factor F_{hkl} is related to both the nuclear term and the magnetic term:

$$|F_{hkl}|^2 = |\sum_n b_n \exp[2\pi i(hx_n + ky_n + lz_n)]|^2 + |\sum_n q_n p_n \exp[2\pi i(hx_n + ky_n + lz_n)]|^2$$ (Equation 2.8),

with b_n being the nuclear scattering length, p_n being the magnetic scattering length (which is proportional to both the magnitude of atomic moment and form factor):

$$p = \left(\frac{e^2\gamma}{2mc^2}\right) gJf$$ (Equation 2.9),

and q_n being the magnetic interaction vector. Unlike the nuclear structure factor, the magnetic structure factor is a vector quantity, and the observed intensity only results from the projection of the structure factor onto the scattering plane:

$$|q| = \sin\alpha$$ (Equation 2.10),

where α is the angle between the scattering vector and the spin direction. In practice, the intensity of magnetic Bragg peaks can be reduced from expected value by several factors, such as covalency, frustration and local variations in composition.

2.2.3.1 Constant wavelength neutron powder diffraction: I.L.L.

The Institut Laue-Langevin (I.L.L.) in Grenoble, France is an international research centre for neutron science and technology[11]. It provides scientists with the most intense continuous flux of neutrons in the world, feeding 40 instruments that are constantly being developed. During the four operating cycles every year, 1.5×10^{15} neutrons per second per cm^2 are produced from the high-flux reactor with a thermal power of 58.3 MW. The neutrons coming from the fission process are then passed through a large composite monochromator to select a narrow band of wavelengths desired by the user. Large multi-detectors and linear position-sensitive detectors covering a wide solid angle are equipped for maximum efficiency.

The ILL's diffraction instruments include two types: powder diffractometers and single-crystal diffractometers. These instruments use relatively short wavelengths ranging from 0.3 Å to 2.0 Å for resolving material structures to atomic resolution. The two-axis powder diffractometers used for this thesis, D2B and D1B, are described below.

2.2.3.1.1 D2B

D2B is a high-resolution powder diffractometer designed to achieve ultimate resolution for structural chemistry, and is particularly suitable for Rietveld analysis (see below). It is characterised by a very high take-off angle (135º) for the monochromator with a large mosaic spread. Recently the 2-D detector has been upgraded and the efficiency of D2B has been increased. A complete diffraction pattern is acquired with about 25 steps of 0.05° in 2θ, as the 128 detectors are spaced at 1.25° intervals. Such scans usually take 30 minutes and are repeated to improve statistics. A range of wavelengths are available, which can be easily changed by computer control. For this work the optimal wavelength is selected to be 1.594 Å. The schematic layout of the instrument is shown in Figure 2.12. In a typical experiment, the polychromatic beam is collimated before being diffracted by the monochromator to obtain high resolution. Powdered samples in a portion of 3 grams are enclosed in cylinder vanadium cans to ensure minimum container scattering, and measurements from 5 K to 300 K are carried out in the standard orange cryostat.

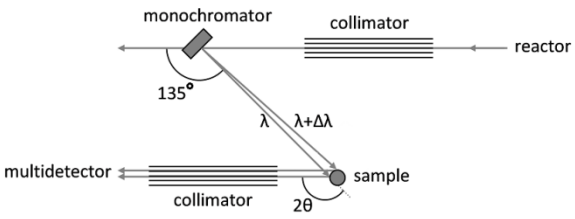

Figure 2.12 Instrumental layout of neutron diffractometer D2B[12].

2.2.3.1.2 D1B

D1B is a high intensity powder diffractometer with a take-off angle of 44° and equipped with a newly-installed position sensitive detector, covering the angular range from 0.8° to 128.8° using 1280 cells with a separation of 0.1°. It is in high demand for real time experiments and samples in relatively small portions for its sensitive detector. It is also particularly suitable for determination of magnetic structures, since the additional intensity caused by magnetic scattering will be more obvious in the pattern collected from D1B than any other instrument, and at small angles where magnetic peaks are expected to appear, a high spatial resolution can be achieved. Seven pyrolytic graphite monochromator crystals provide a wavelength of 2.52 Å, which is the wavelength used for the experiments in this thesis. A second wavelength of 1.28 Å is available by using a germanium monochromator. Its specially designed cryostat produces low background, which is crucial for detecting small intensity changes. Diffraction patterns with sufficient statistics can be collected in minutes, and patterns across a wide temperature range can be obtained in a few hours. For comparison with the diffraction patterns collected from D2B, measurements are carried out from 5 K to 300 K as well. A schematic diagram of D1B is shown in Figure 2.13.

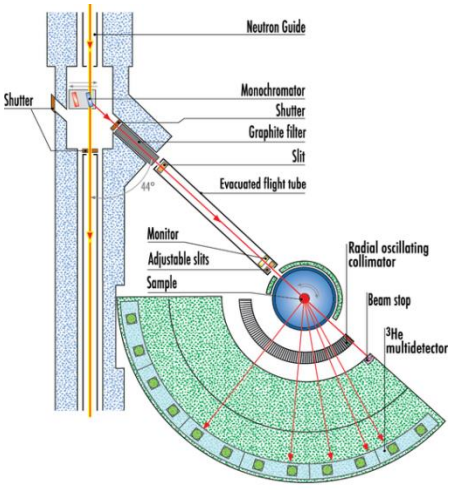

Figure 2.13 Colourful diagram of the layout of neutron diffractometer D1B[11].

2.2.3.2 Constant wavelength neutron powder diffraction – ANSTO

The Australian Nuclear Science and Technology Organisation (ANSTO) located at Lucas Heights, south-west of Sydney, is Australia's national centre for nuclear science. Some of the neutron diffraction experiments described in this thesis were executed in the Bragg Institute of ANSTO on the diffractometer Echidna by Dr. Maxim Avdeev.

Echidna (Figure 2.14) is a neutron powder diffractometer equipped with germanium monochromators and variable take-off angles (90° to 140°), using a wavelength from 1 Å to 3 Å and a highly collimated neutron beam to achieve high resolution for structural determination. A typical scan takes two to three hours, and data are collected by 128 ^{3}He position-sensitive detectors. In our experiments wavelengths were chosen to be 1.6215(5) Å and 2.4395(5) Å, and the angular region from 10° to 162.5° was scanned in steps of 0.05° at temperatures of 300, 250, 200, 150, 100, 50 and 3 K.

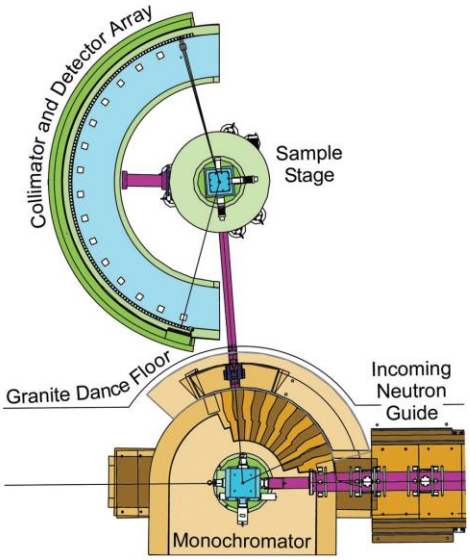

Figure 2.14 Diagram of the neutron powder diffractometer Echidna[13].

2.2.3.3 Time-of-flight neutron powder diffraction: ISIS

ISIS, located at the Rutherford Appleton Laboratory in Oxfordshire, is the UK's neutron and muon facility[14]. It is a world-leading research centre for physical and life science, producing the world's brightest pulsed beam of neutrons that allows scientists to study materials at the atomic level. In contrast to the previous neutron sources, neutrons come from a spallation process at ISIS. A beam of H^- ion is accelerated into a synchrotron and passed through an aluminium oxide stripping foil which converts the H^- ions to protons. This proton

beam is accelerated in the synchrotron before being directed to a heavy metal target made of tantalum. Protons hit the nuclei in the target metal and trigger an intranuclear cascade, which forces the nuclei into a highly excited state. The nuclei then release energy by expelling neutrons, some of which leave the target metal while others continue to trigger further reactions. The neutrons produced during this spallation process tend to have very high energies and velocities so that they must be slowed down for studies of condensed matter. This is achieved by repeated collision between neutrons and hydrogen nuclei in the hydrogenous moderators of water, liquid methane or liquid hydrogen around the target, which can determine the spectral distributions of neutrons and are chosen to suit different types of experiment.

The spallation source at ISIS results in a continuous distribution of neutron wavelengths. According to the de Broglie equation,

$$\lambda = \frac{h}{mv} \ , \qquad \text{(Equation 2.11),}$$

the neutron velocity is inversely proportional to its wavelength. Since the time that a neutron takes to travel a fixed path length can be measured by modern electronics, its velocity, and consequently its wavelength can be determined. This technique is referred to as the time-of-flight (TOF) method. In practice it is carried out by fixing the starting time of the neutron by pulsing the neutron source in short well-defined intervals and measuring its arriving time at the detector. The detectors are placed at constant angles on a Debye-Scherrer cone (Figure 2.15). Compared to the constant wavelength method, TOF does not require a monochromator to select specific wavelength which inevitably discards a large percent of the neutron flux; and it is also possible to collect data more quickly with TOF, although the peak shape may become more complicated due to the pulsed beam. The key equation of TOF can be yielded by combining the de Broglie equation with the Bragg equation:

$$\lambda = \frac{ht}{ml} = 2d\sin\theta \ , \qquad \text{(Equation 2.12),}$$

where t is the time-of-flight and l is the path length. It is readily seen that the d-spacing is proportional to t, so TOF diffraction patterns is usually displayed in the form where the ordinate axis goes from small to large d-spacing. Good wavelength resolution $\Delta\lambda/\lambda$, and hence high resolution for the diffraction peaks, is achieved for large values of d-spacing as we have the following relation:

$$\frac{\Delta\lambda}{\lambda} = \frac{\Delta t}{t} = \frac{\Delta t}{l} * \frac{h}{m\lambda} = \frac{\Delta t}{l} * \frac{h}{2md\sin\theta} \qquad \text{(Equation 2.13).}$$

The resolution of a TOF diffractometer, $\Delta d/d$, mainly depends on three factors: the angular uncertainty $\Delta\theta$, the timing uncertainty Δt, and the path length uncertainty Δl. The total uncertainty is a combination of the three factors:

$$\frac{\Delta d}{d} = [\Delta\theta^2\cot^2\theta + \left(\frac{\Delta t}{t}\right)^2 + \left(\frac{\Delta l}{l}\right)^2]^{1/2} \qquad \text{(Equation 2.14).}$$

The angular term comes from differentiating Bragg's equation and is a consequence of the divergence of neutron beam. The timing uncertainty arises from the moderation time of the neutrons, and the pathlength uncertainty is related to the thickness of the moderator. Resolution can thus be improved by increasing the time-of-flight, in other words increasing the path length of the neutrons.

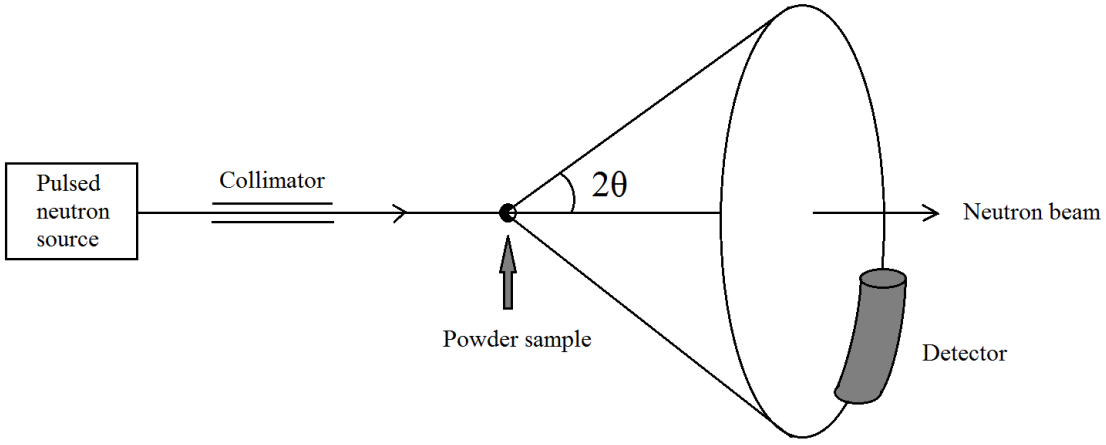

Figure 2.15 Principle of TOF technique in which a detector collects neutrons in a Debye-Scherrer cone at fixed scattering angle.

The TOF neutron diffraction experiments for this thesis were conducted on the GEneral Materials (GEM) diffractometer at ISIS (Figure 2.16). It has an incident flight path of 17.0 meters and the detectors cover an angle range from 1.1° to 169.3°. It is designed for both intense flux and high resolution, allowing quality data which are suitable for Rietveld analysis (see below) to be collected in relatively short period of time. During measurements powdered samples were mounted in vanadium cans, and standard cryostat was used to reach 5 K. Data were collected at both 5 K and 300 K from the detector banks 1, 2, 3, 4, 5, 6, although only data from bank 3 to bank 6 were used in Rietveld refinements as the *d*-spacing ranges of bank 1 and 2 are much higher than what we need.

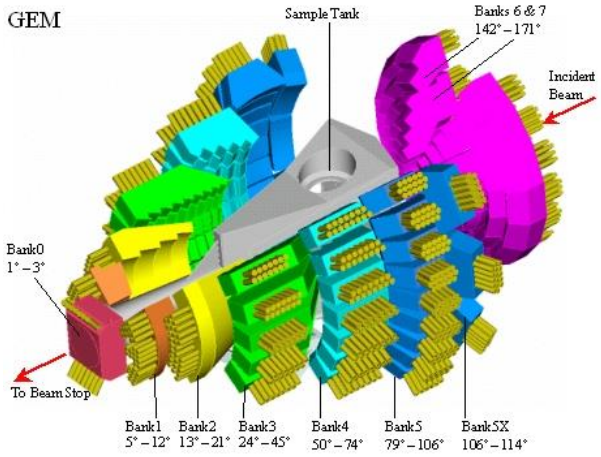

Figure 2.16 Diagram of the GEM time-of-flight diffractometer at ISIS[14].

2.3 Rietveld analysis

2.3.1 General principle of the Rietveld method

Crystal structures can be solved directly through the single-crystal diffraction technique, since data can be collected over four angular ranges as indicated in Figure 2.6. However, in powder diffraction method, data are collected over only one angular range and what we observe is the projection of peaks onto one axis. This results in overlapping of individual peaks which makes the measurement of separate peaks impossible, and direct structure determination thus becomes extremely difficult. Before the advent of the Rietveld method in the 1960s[15], structure refinement with powder diffraction method was limited to highly symmetric structures, although in fact many of those works have been proved to be wrong now with the development of modern instruments and techniques. To overcome this difficulty, the Rietveld method is based on the recognition that in the diffraction pattern, at every point there is information of the structure contained in the intensity, and a full profile analysis is applied in order to extract the maximum amount of information from the pattern instead of analysing separate groups of overlapping peaks. The general aim of this method is to achieve the best agreement between the observed diffraction pattern and the calculated pattern obtained from the proposed crystal structure together with instrumental factors.

The Rietveld method uses a least squares approach, meaning that it seeks to minimise the quantity S_y, which is the weighted sum of the squared difference between the observed intensity $y_{i,obs}$ and the calculated intensity $y_{i,calc}$ at each point in the diffraction pattern:

$$S_y = \sum_i w_i \, (y_{i,\mathrm{obs}} - y_{i,\mathrm{calc}})^2 \, , \qquad \text{(Equation 2.15),}$$

where w_i is the weighing term, and is equal to $1/y_{i,obs}$. This term has the effect that all the peaks in the pattern, no matter the intensity is relatively low or high, will be treated with equal significance as information contained in every point i is taken advantage of in the Rietveld analysis. In order to minimise S_y, we need to calculate a set of derivatives of the function $y_{i,calc}$ with respect to each variables v in the structure factor F_{hkl} shown in Equation 2.8. These derivatives have to satisfy the following relation:

$$\frac{\partial S_y}{\partial v_i} = 0 \quad . \qquad \text{(Equation 2.16).}$$

Thus a series of simultaneous equations is acquired, and the shift of the variables is solved by a matrix method. If we have a crystallographic model with parameters differing from those for the true minimum by an amount of Δv, then the value of a function $f(v+\Delta v)$ can be obtained through Taylor expansion, which allows the application of an iterative process. The newly calculated S_y using the new variables is then taken to the next cycle, and this procedure is usually repeated for several cycles until a convergence criterion is satisfied. Rietveld analysis is useful in refining many aspects including phase fractions, lattice parameters, atomic positions and occupancies, magnetic moments, and atomic displacement parameters of a material. However it is not for direct structure solution, which means the requirement for a converging refinement is that a proper starting model close to the true structure must be known. This is because when the value of Δv is too large, the higher terms in the Taylor expansion cannot be ignored, and the assumption made in the non-linear least-squares refinement becomes invalid. In this case, the global minimum of the function may not be found, and the refinement could diverge or fall into a local minimum which is not the correct solution that we are looking for (Figure 2.17).

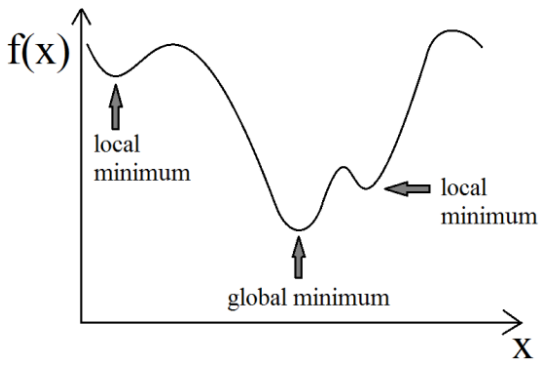

Figure 2.17 Global minimum and local minima of a non-linear function.

2.3.2 Computer program used for Rietveld refinement

As Rietveld analysis involves a great amount of calculation especially for complicated structures, it is not realistic to do it manually by hand. Fortunately a variety of computer programs have been developed to provide scientists with aid in this job. The program used in this thesis is the *G*eneral *S*tructure *A*nalysis *S*ystem (GSAS), which was first developed by A.C. Larson and R.B. Von Dreele in 1985[16]. It was originally designed for treating TOF neutron diffraction data, but has now been also expanded to analysing constant-wavelength neutron diffraction and X-ray diffraction patterns. It is possible to include a set of histograms (up to 99) and analyse them simultaneously, and multiple phases (up to 9) can be added to one refinement. When a refinement is finished, GSAS is able to display results including publishable powder pattern plots, bond lengths and angles, and CIF files of the result besides cell parameters and atomic coordinates.

2.3.3 Modelling of Background

In the Rietveld method the whole profile of the diffraction pattern is fitted, including those regions with no Bragg peaks from the crystalline sample. Consequently, a background contribution is required to account for other factors that might affect the pattern, such as air scattering, incoherent scattering, scattering from organic materials on the sample plate, etc. During this work the background function type 1: Chebyshev polynomial in GSAS is used to model the background intensity of diffraction patterns. The intensity I_b at a given point is described by the following equation:

$$I_b = \sum_{j=1}^{n} B_j \, T_{j-1} \qquad \text{(Equation 2.17)},$$

where the quantity B_j is the parameter being refined, and $T_{j\text{-}1}$ is angular or time-of-flight dependant. The number of background terms n is chosen according to the complexity of background, and from experience n is set to be 12 in this work so that the background can be nicely shaped with the least terms. However, for a better fit it is sometimes necessary to cut off part of the background, especially at the very low and high angles in the pattern for abnormal intensities resulting from instrumental factors, which would otherwise ruin the whole refinement. In the program there is also the option of manual background fitting where a background function is not needed, although this option was not used in the work described in this thesis.

2.3.4 Description of peak shape

It is the accurate description of peak profiles in Rietveld analysis that makes this method particularly powerful. Diffraction peak shapes vary with different samples as well as instrumental settings, and can be treated as a function of scattering angle. The methods for modelling peak shapes in powder diffraction patterns are slightly different for angle-dispersive and energy-dispersive data, but they are both based on empirical consideration.

For constant wavelength data, it is found that, in practice, peak shape is usually a mixture of a Gaussian profile shape and a Lorentzian profile shape (Figure 2.18). The pseudo-Voigt function works best to fit peak shapes as a linear combination of Gaussian (G) and Lorentzian (L) components, which occur in the ratio $\eta : (1 - \eta)$ with η being the pseudo-Voigt mixing parameter. The function for the Kth Bragg reflection in the diffraction pattern is given by:

$$V = \eta\, L_k + (1 - \eta)\, G_k \qquad \text{(Equation 2.18)},$$

where the mixing parameter η is given by:

$$\eta = 1.36603q - 0.47719q^2 + 0.116q^3 \qquad \text{(Equation 2.19)},$$

and q is a function of Γ, the full width at half-maximum (FWHM):

$$q = \frac{\Gamma_{L,K}}{\Gamma_K} \qquad \text{(Equation 2.20)}.$$

The Gaussian part and the Lorentzian part of the peak width are described by the following equations, respectively:

$$\Gamma_{G,K} = \sqrt{U\tan^2\theta + V\tan\theta + W + \frac{P}{\cos^2\theta}} \qquad \text{(Equation 2.21)},$$

$$\Gamma_{L,K} = \frac{X}{\cos\theta} + Y\tan\theta \qquad \text{(Equation 2.22)}.$$

The parameters *U, V, W, P,* X and *Y* are variable during a refinement process, and are denoted as GU, GV, GW, GP, LX, LY in GSAS. Besides these main quantities to be refined, there are also other terms which can be used to further improve peak shapes, such as the correction for peak asymmetry, sample misalignment and transparency, etc.

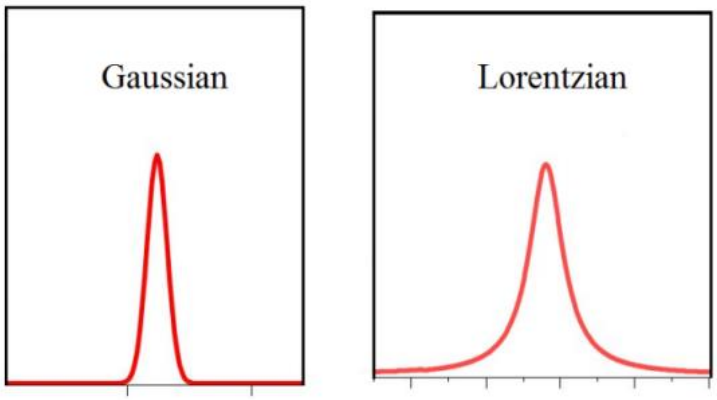

Figure 2.18 Gaussian profile shape and Lorentzian profile shape of a diffraction peak.

For time-of-flight data, there are three diffractometer constants which relate the time of flight to *d*-spacing via the following equation:

$$t = \mathrm{DIFC}d + \mathrm{DIFA}d^2 + \mathrm{ZERO} \qquad \text{(Equation 2.23),}$$

among which only the quantity DIFA should be refined for correction of peak shifts due to neutron absorption by the sample, while the other two are instrumental-specific. ZERO is for the correction of differences in the timing signals between the accelerator and the detector system, and DIFC links the theoretical time-of-flight position of a Bragg peak to its *d*-spacing according to the relation shown in Equation 2.24:

$$\mathrm{DIFC} = 505.56L\sin\theta \qquad \text{(Equation 2.24).}$$

The instrumental constant is always recommended to be refined in the later stages of the refinement process, as it is not expected to make significant changes to the quality of fit and should not deviate from its original value too much.

The peak shapes in TOF data are modelled with peak shape function 3 in GSAS, which applies a combination of the pseudo-Voigt function with exponential terms. The exponentials serve to describe the nature of the neutron beam produced at ISIS, as the protons striking the target material causes a rapid intensity increase, before a slow drop off in intensity resulting from the emergence of neutrons from the moderator. The rise and decay coefficients of the exponentials are given by the three parameters alp, bet-0 and bet-1, which are related to instrumental settings only and thus should be fixed during the refinement.

The pseudo-Voigt function for TOF is a linear combination of a Gaussian part (σ) and a Lorentzian part (γ) as well but with different forms, taking instrument design and detector geometry into consideration:

$$\sigma = \sqrt{\sigma_0^2 + \sigma_1^2 d^2 + \sigma_2^2 d^4} \qquad \text{(Equation 2.25)},$$

$$\gamma = \gamma_0 + \gamma_1 d + \gamma_2 d^2 \qquad \text{(Equation 2.26)}.$$

Among these parameters, only sig-0 and gam-0 should remain fixed while the other four can all be refined. Sig-1 and gam-1 link the peak width and *d*-spacing linearly, and sig-2 and gam-2 are for description of particle size and strain broadening.

2.3.5 Goodness of fit

The Rietveld method aims to minimise the difference between the observed and calculated diffraction patterns, however, this difference is rarely zero in reality. To judge the quality of a refinement, we usually refer to a series of goodness-of-fit parameters:

$$R_{\mathrm{p}} = 100 * \frac{\sum_i |y_{i,\mathrm{obs}} - y_{i,\mathrm{calc}}|}{\sum_i y_{i,\mathrm{obs}}} \qquad \text{(Equation 2.27)},$$

$$R_{\mathrm{wp}} = 100 * \sqrt{\frac{\sum_i w_i (y_{i,\mathrm{obs}} - y_{i,\mathrm{calc}})^2}{\sum_i w_i y_{i,\mathrm{obs}}^2}} \qquad \text{(Equation 2.28)},$$

$$\chi^2 = \frac{\sum_i w_i (y_{i,\mathrm{obs}} - y_{i,\mathrm{calc}})^2}{N-P} = \frac{R_{\mathrm{wp}}}{R_{\mathrm{e}}} \qquad \text{(Equation 2.29)},$$

where N is equal to the number of observables, P is the number of refined parameters, and R_{e} is the expected R_{wp}:

$$R_{\mathrm{e}} = \frac{N-P}{\sum_i w_i y_{i,\mathrm{obs}}^2} \qquad \text{(Equation 2.30)}.$$

In practice it is most common to quote the *R*-weighted profile, R_{wp}, to judge the fit quality, and a fit with R_{wp} less than 6% can usually be considered satisfactory. For two refinements with similar R_{wp} values, χ^2 can provide additional information for us to make a comparison. For example, it can be encouraging to get a smaller value of χ^2 by using more variables. However, sometimes two distinct structural models may lead to very similar agreement factors that do not allow us to decide which model is correct, and in that case we may resort to other techniques for further structural determination. Finally, besides studying the goodness-of-fit parameters, it is quick and useful to examine the fitted profiles directly by

eye. GSAS is able to display a difference curve for the observed and calculated profiles, which should be a relatively flat line for a good fit, and otherwise would show various features related to inaccurate cell parameters, bad peak shape and incorrect intensity when the fit quality is still to be improved.

2.4 SQUID magnetometry

2.4.1 General principle of SQUID and sample preparation

The magnetometry measurements for this thesis were carried out on two laboratory magnetometers: Quantum Design SQUID (Superconducting Quantum Inference Device) MPMS 5 and MPMS XL. Three types of measurement were made: the temperature dependence of the dc molar susceptibility, the field dependence of the magnetisation per formula unit, and the temperature and frequency dependence of the ac molar susceptibility.

A SQUID is the most sensitive instrument for detecting a sample's magnetic moment, as it is capable of resolving changes in magnetic field of 10^{-15} T (1T = 10^4 Oe)[17]. The device consists of a superconducting magnet ring separated in half by two Josephson junctions, which are used as insulating barriers (Figure 2.19). If a current I_0 is passed through the ring, the Josephson junctions are narrow enough to induce quantum mechanical tunnelling of the Cooper pairs in each half of the ring, leading to a measurable critical current I_C. When a magnetic flux is applied to the ring perpendicularly, a screening current I_S arises in the ring. This magnetic flux can be changed either by moving the sample through the ring (dc) or introducing an alternating magnetic field (ac). Thus, in one junction the current becomes $I_0/2+I_S$ and in another the current is $I_0/2–I_S$. A voltage ΔV appears across the ring if either $I_0/2+I_S$ or $I_0/2–I_S$ exceeds the value of I_C. This voltage is directly related to I_S quantitatively, and consequently is linked to the magnetic moment of the sample. The SQUID works by measuring the output voltage ΔV and hence the sample magnetic moment is known accurately. The output voltage is calibrated against a palladium standard reference and a set of detection coils is used to minimise any deviation from the true result, although the earth has a magnetic field of 0.5 Oe which might still have a minor effect on the sample in the chamber.

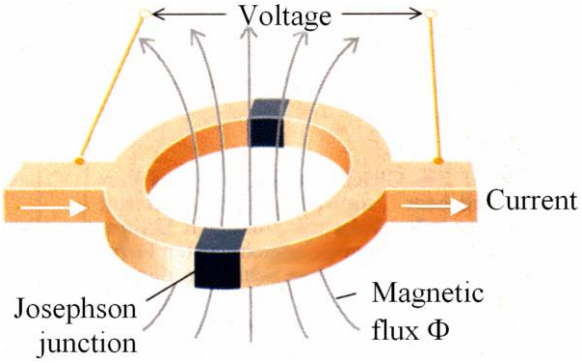

Figure 2.19 A superconducting ring separated in half by two Josephson junctions.

The samples measured in this thesis all take the form of powdered material. A portion of 30 to 40 mg of the sample was weighed accurately before being loaded into an empty gelatin capsule and sealed securely to restrict sample movement. The filled capsule was inserted into a plastic straw with four empty capsules at both sides to ensure a proper location of the sample inside the SQUID for a constant background. The straw was pieced with a needle to form small holes, so that free aerodynamic movement is allowed during the purging process. The straw was then sealed and attached to a long sample rod using diamagnetic tape, before being put into the air lock and purged with helium to remove the paramagnetic oxygen. The sample was centred in the chamber with a field of 100 Oe to adjust its position relative to the detection coils. The scan length for dc measurements was set to be 4 cm while for ac measurements it was changed to 6 cm. During dc measurements 4 repeated scans with scan length of 4 cm were performed to improve the signal to noise ratio, while the sample position was fixed for ac measurements. A curve simulating a magnetic dipole moving through the detection coils was fitted to the observed voltage vs. position signal by computer, and in this way the output voltage value was converted into the magnetic moment of the sample.

2.4.2 DC magnetisation measurements

For dc molar susceptibility measurements, samples were first cooled to base temperature in zero field (ZFC). An applied field was turned on, normally 100 Oe, and data were collected as the temperature was increased. The standard temperature range was set to be $5 \leq T\,(\mathrm{K}) \leq 300$ for MPMS 5 and $2 \leq T\,(\mathrm{K}) \leq 300$ for MPMS XL, although for some samples with higher ordering temperatures it was necessary to go up to 370 K. the sample was then cooled in the measuring field and the data collection was repeated. The field dependence of the magnetisation was measured as a function of field over the range $-50 \leq H\,(\mathrm{k\ Oe}) \leq 50$ at 300 K and 5 K after cooling in a field of 50 k Oe.

The output magnetic moment of the SQUID is in electromagnetic units (ergs G^{-1}), and we need to convert this moment into the sample's molar susceptibility. This is given by:

$$\chi_M = \frac{M}{H} * \frac{A_r}{m} \quad \text{(Equation 2.31),}$$

where M is the measured moment, A_r is the molar mass of the sample, m is the mass of the sample, and χ_M is reported in the units cm^3mol^{-1}. To calculate the magnetisation per formula unit in isothermal magnetisation measurements, the following conversion is applied:

$$\mu_{\text{f.u.}} = M * \frac{A_r}{m} * \frac{10^{-3}}{\mu_B * N_A} \quad \text{(Equation 2.32),}$$

where N_A is the Avogadro constant and the result is reported in the unit of μ_B.

2.4.3 AC magnetisation measurements

In contrast to dc measurements, an ac magnetisation measurement applies an alternating current to introduce an oscillating magnetic field, and therefore the output is not only temperature-dependant, but is also described as a function of the oscillating frequency. The ac current is given by a wave function:

$$i_{\text{ac}} = i_{\text{max}} \sin(\omega t) \quad \text{(Equation 2.33).}$$

The magnetic field consists of two components which are parallel to each other: one is the static magnetic field and the other is the oscillating component. At time t it is given by:

$$H_{\text{ac}} = H_0 + H_1 \sin(\omega t) \quad \text{(Equation 2.34),}$$

where the constant component H_0 can be either zero or nonzero, and H_1 is usually set to be a small field, typically below 5 Oe. The ac moment measured by the SQUID is given by:

$$M = \chi H_{\text{ac}}$$

where

$$\chi = \frac{dM}{dH} \quad \text{(Equations 2.35).}$$

At very low frequencies ac measurement is most similar to dc measurement as the magnetic field changes very slowly, and in this case the output moment would follow the $M(H)$ curve observed in a dc experiment. However, at high frequencies dynamic effects in the sample would cause deviation of the measured moment from the dc curve, as the detected magnetisation could lag behind the field. Therefore, the ac magnetisation measurement yields

two quantities: the magnitude of the susceptibility and the phase shift φ. An alternative description applies an in-phase or real component χ' together with an out-of-phase or imaginary component χ'', and they are related by:

$$\chi' = \chi\cos\varphi$$

$$\chi'' = \chi\sin\varphi$$

$$\chi = \sqrt{\chi'^2 + \chi''^2}$$

$$\varphi = \arctan(\frac{\chi''}{\chi'})$$ (Equations 2.36).

As the real component reflects magnetic dispersion in the sample while the imaginary component is indicative of magnetic absorption, an ac measurement is capable of showing the dynamic nature of the magnetic moment. One evident advantage of ac experiments is that it is very sensitive to the slope of *M*(*H*) curve rather than the absolute value, so that small magnetic shifts can be detected even when the absolute moment is large[18]. Because there is a phase shift of π/2 between the sine function and cosine function, two detection coils that are orthogonal to each other are used to collect signals of the real component and the imaginary component at the same time.

AC measurements for this thesis were carried out on SQUID MPMS XL. Data were collected using the temperature range $50 \leq T\,(\mathrm{K}) \leq 300$ or $50 \leq T\,(\mathrm{K}) \leq 320$ with an ac driving field of 3.5 Oe, and samples were cooled under a constant dc field of 3.0 Oe. Four frequencies: 1 Hz, 10 Hz, 100 Hz, and 1000 Hz were used in the experiment.

2.5 Transmission electron microscopy (TEM)

Electron microscopy is a powerful technique to visualise local structures of materials directly from various interactions between electrons and matter (Figure 2.20). It utilises a beam of accelerated electrons generated from a cathode filament typically made of tungsten, which is then scattered by the atomic potentials of the atoms in the specimen[1]. Similar to X-rays, there is a fall-off of scattering power with $\sin\theta/\lambda$, and the scattering factor increases with atomic number; however the scattering of electrons by matter is much stronger than X-rays and neutrons, so it is feasible to even analyse gaseous samples by diffraction of electrons.

Compared with light microscopy involving visible photons, electron microscopy uses much shorter wavelength of less than 1 Å, which is comparable to the size of an atom and thus able to provide atomic resolution under optimum conditions. A single column of atoms, which can be beautifully seen by electron microscopy, is thousands of times smaller than a resolvable object seen by light microscopy.

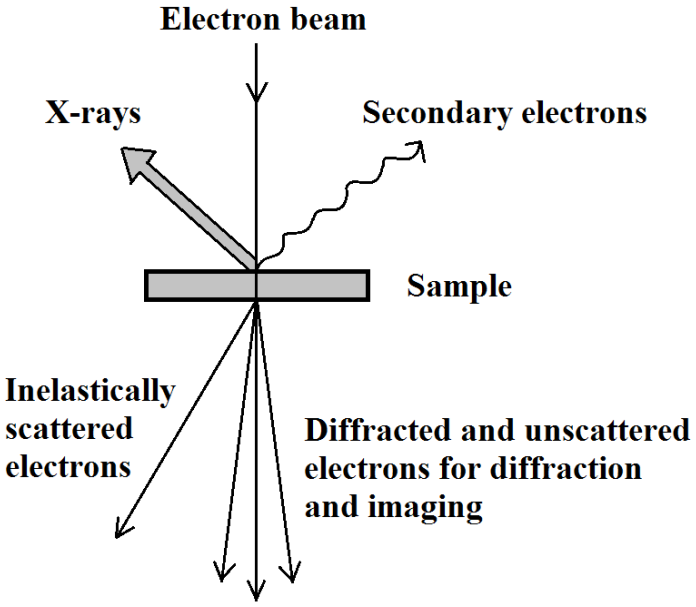

Figure 2.20 Phenomena resulting from interactions of the electron beam and the matter.

Transmission electron microscopy (TEM) is the original form of electron microscopy, where a high voltage electron beam is transmitted through an ultrathin section of the specimen (ideally less than 100 nm thick) or a suspension on a grid to illuminate it and create a diffraction pattern. The pattern is then transformed into an image with magnetic lenses, followed by being magnified and projected onto a viewing device. The diagram of a basic TEM setting is shown in Figure 2.21. The resolving power depends on the wavelength and the quality of the objective lens, which is judged by its spherical aberration coefficient C_S:

$$d_{\text{min.}} \propto C_S^{\frac{1}{3}} \lambda^{\frac{2}{3}} \qquad \text{(Equation 2.37).}$$

In modern electron microscopes the resolution is typically lowered to around 0.1 nm or even 50 pm. Images recorded at a set of focusing steps can be compared with calculated images based on proposed structural models, so a good starting model is preferred. The image is a projection of the structure along the beam direction, and will be dominated by heavier atoms.

In particular, the technique used in this thesis is called selected area electron diffraction (SAED), in which an area of interest of a sample is selected by inserting an aperture in the image plane, and the diffraction pattern will only contain reflections from that area.

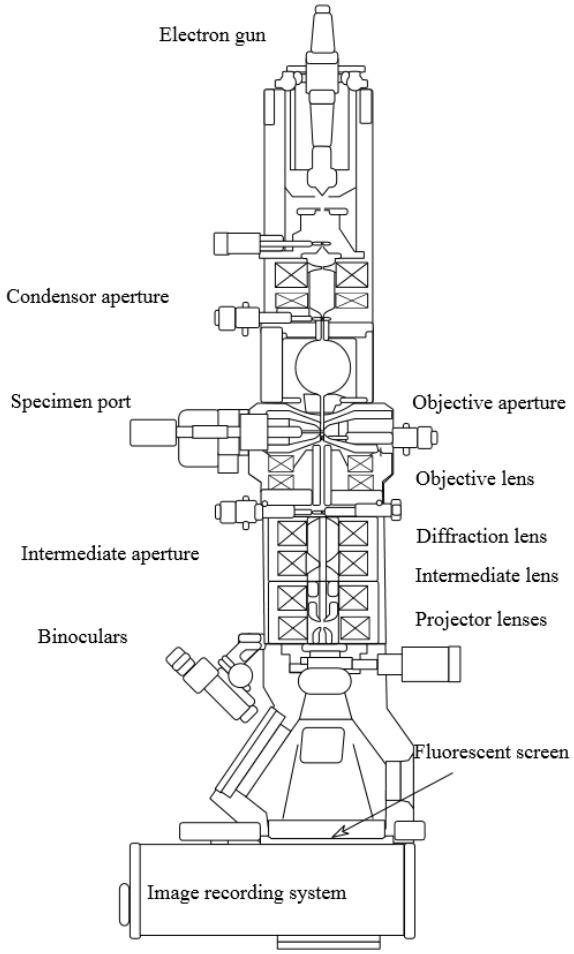

Figure 2.21 Diagram of the layout of components in a basic TEM[19].

In contrast to conventional TEM which uses a parallel beam of electrons, the scanning mode of TEM (STEM) was applied to the samples in this thesis. In STEM the electron beam is focused to a fine spot and scanned over the specimen. The spot diameter for our experiments is controlled to be no more than 100 pm. A very particular technique applied to our samples is high angle annular dark field (HAADF) imaging, where the images are only formed from inelastically scattered electrons. This type of scattering arises when electrons only interact with the nucleus and normally occurs at high angles; data can be collected by a ring detector with inner radius of 50 mrad and outer radius of 200 mrad. Unlike the bright-field mode, the detector lies outside of the path of the directly transmitted beam. One important feature of dark-field imaging is the high dependence of the contrast of atomic columns on atomic

numbers Z: the intensity of an atomic column is proportional to Z^2 in dark field while it is $Z^{1/3}$ in bright field, so this technique is only useful for imaging heavy elements. Since in this study we are more interested in the distribution of B-cations in perovskites rather than the position of the lighter oxygen atoms, dark-field mode is clearly the better choice which displays stronger contrast between distinct elements on the B sites.

Besides HAADF-STEM, another imaging technique appearing in the thesis is the energy dispersive X-ray scanning transmission electron microscopy spectroscopy (EDX-STEM). As the incident electron beam hits the electrons in the specimen, some electrons are excited to higher energy shells and the electrons in the outer shells can be ionized. The excited electrons will try to fall back to a more stable state, and this process leads to the generation of X-rays with a characteristic energy level directly related to the electronic configuration of the element present in the specimen. Silicon drift detectors equipped for aberration corrected electron microscopes are used for collecting these characteristic X-rays, and four detectors are mounted around the specimen symmetrically to improve the angle of collection. The advantage of using these detectors lies in the possibly to obtain STEM-EDX maps with atomic resolution by combining HAADF-STEM imaging.

All the TEM experiments for this study were conducted by Prof. Joke Hadermann, Dr. Robert Paria Sena [20] and Mylène Hendrickx at the University of Antwerp. Specimens for electron microscopy were prepared by dispersing crushed sample powder in ethanol and depositing a few drops of this solution on a copper grid covered with a holey carbon film. SAED patterns were acquired with a Phillips CM20 transmission electron microscope. HAADF-STEM images and atomic resolution EDX maps were obtained with an FEI Titan 80-300 cubed microscope equipped with a Super-X detector operated at 300 kV. Quantitative EDX measurements were also taken of 50 different crystallites on a JEOL 5590 scanning electron microscope.

2.6 Mössbauer spectroscopy

Mössbauer spectroscopy is a technique used to obtain information about solids by probing tiny changes in the energy levels of the nuclei in response to the environment. It is based on the theory of Mössbauer effect discovered in 1958[21]. There are three types of nuclear interaction that may be observed by this technique: isomer shift, quadrupole splitting and

magnetic hyperfine splitting, and in this thesis we mainly take advantage of Mössbauer spectroscopy in studying the magnetic properties of our compounds.

In quantum mechanics, a nucleus possesses a ground state and excited state just like an electron or an atom. It can be excited to a higher energy level and then make transitions back to lower levels, and during these processes it absorbs or emits photons. In contrast to X-rays which arise from electronic interactions, the photons generated from nuclear deexcitations are called γ-rays, which have much higher energies on the order of keV to MeV. During absorption or emission of γ-rays, a nucleus is required to recoil by conservation of momentum, and in this way energy is lost to recoil. In other words, when a nucleus at rest emits γ-rays, the energy of the γ-rays will be less than the energy of transition; similarly, for a nucleus to absorb γ-rays, the energy of the γ-rays must be greater than the natural transition energy. Consequently, for a free nucleus, the shift of energy is so great that the emission spectra do not overlap with the absorption spectra, and nuclear resonance cannot be observed. However, for a solid crystal, recoil-free emission and absorption of γ-rays becomes possible. As a lattice is much more massive than a nucleus and the nuclei are bound in place, the recoil momentum is absorbed by the entire lattice and the recoil kinetic energy is practically zero, unless the energy of the γ-rays is large enough to cause lattice vibration and resultant energy loss. In the case of a recoilless event, the emitted γ-rays have exactly the same energy as the transition, and the emission and absorption lines can now overlap, allowing another nucleus in the crystal to absorb that energy and being excited. This resonant absorption lies at the heart of Mössbauer spectroscopy, as we can use it to examine energy profiles of nuclear transitions in solids.

In practice, γ-rays of relatively low energies (10 to 200 keV) are used in Mössbauer spectroscopy for introducing recoilless nuclear resonance of high recoil-free fraction and ideal signal-to-noise ratio with short collection times. Excitation lifetimes of 0.1 ns to 1.0 μs are commonly chosen to achieve a peak line width, which is sharp enough for good resolution but not too sensitive to instrumental vibration and temperature. Long-lived precursors with stable ground states and high recoilless fractions are considered to be appropriate radiation sources, and the source atom emitting γ-rays must be the same isotope as the atom that absorbs the radiation in the sample. Typical radiation sources include ^{57}Fe, ^{83}Kr, ^{119}Sn, ^{149}Sm, ^{151}Eu, ^{161}Dy, ^{181}Ta. In a Mössbauer spectroscopy experiment, a solid sample is irradiated with a γ-ray beam, and the intensity of the transmitted beam is measured by a detector. If the emitting and absorbing atoms are in identical chemical environments, they will have equal

nuclear transition energies and resonant absorption will be observed. However, tiny energy shifts caused by slightly different environments will lead to large changes in absorbance, as spectral linewidths of γ-rays are extremely narrow. Consequently, it is necessary to change the energy of the radiation to bring the nuclei back to resonance, and this is achieved by the Doppler effect: a linear motor is used to accelerate the source through a range of velocities, and the energies of γ-rays are scanned. For instance, for ^{57}Fe source velocity range of ±11 mm/s is usually applied. The intensity of the γ-ray is plotted as a function of the velocity in the resulting spectrum. At velocities which correspond to resonant energies of the sample, a fraction of the radiation is absorbed, leading to a decrease in the measured intensity. The profile of the intensity across the spectrum is then able to provide information about the nuclei in different chemical environments in the sample.

In this thesis, ^{57}Fe Mössbauer spectroscopy was used to investigate the chemical environments of iron in perovskite samples. Spectra were collected from polycrystalline samples at 5 K and room temperature using a standard transmission spectrometer and a ^{57}Co**Rh** source. The Mössbauer spectrometer is a device formed by three main parts: a moving source generating the Doppler effect, a collimator filtering out non-parallel γ-rays and a detector (Figure 2.22). The source for ^{57}Fe consists of the radioactive parent ^{57}Co, which decays to an excited state of ^{57}Fe by electron capture after 270 days and in turn decays to a ground state, emitting the γ-ray of a characteristic energy (Figure 2.23). The experimental radiation energy is then 14.4 keV with a lifetime of 99.3 ns. The drive velocity of the spectrometer was calibrated using a 6μm thick α-Fe foil at 295 K, and all isomer shifts δ are quoted relative to the centre of the α-Fe calibration spectrum. Isomer shift is a measure describing the shift in resonance energy arising from the change of *s*-electron charge density. Therefore, different oxidation states and spin states can be determined from isomer shift as they affect the electronic environments that the nuclei experience. Besides the isomer shift, another important feature in the spectra is the quadrupole splitting, which originates from the interaction between nuclear energy levels and the surrounding electric field gradient and is indicative of site symmetry and the arrangement of ligands. All nuclei with a non-spherical charge distribution and spin quantum number $I > ½$ will show quadrupole splitting caused by an asymmetrical electric field. For ^{57}Fe, the ground-to-excited-state transitions appear as a pair of peaks known as a doublet. An energy diagram showing isomer shift and quadrupole splitting of ^{57}Fe is shown in Figure 2.24. Finally, the presence of magnetic field can split the energy levels further through the nuclear Zeeman effect (Figure 2.25). This is known as

magnetic hyperfine splitting, which gives six possible transitions following the selection rule of magnetic dipoles. In ^{57}Fe spectra, a typical sextet in the ratio 3:2:1:1:2:3 would be produced from powdered sample, and magnetic properties of the sample can be readily measured as the extent of splitting is proportional to the strength of internal magnetic field.

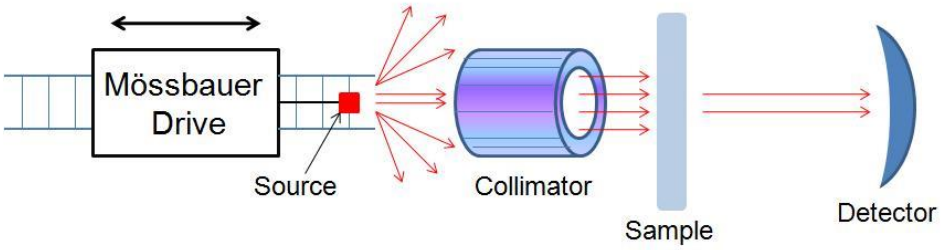

Figure 2.22 Diagram of the layout of a standard Mössbauer spectrometer[22].

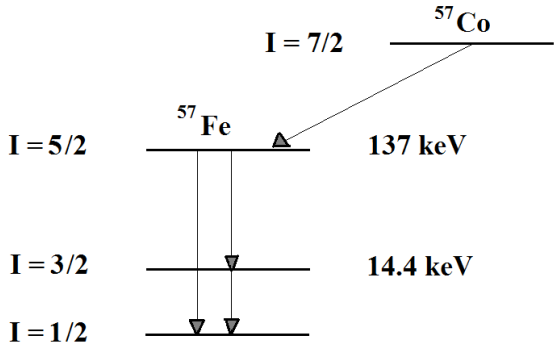

Figure 2.23 The decay process of ^{57}Co producing characteristic γ-rays.

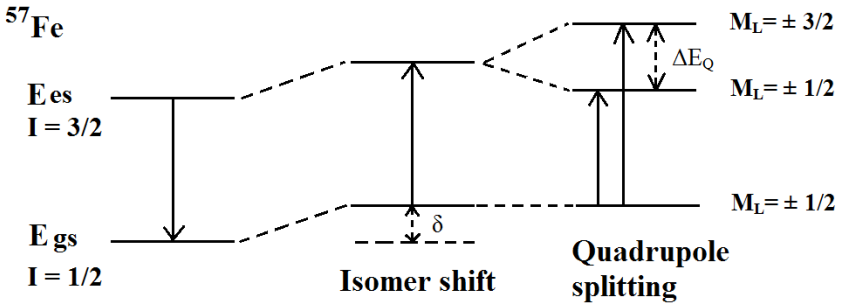

Figure 2.24 The energy levels of ^{57}Fe showing isomer shift and quadrupole splitting.

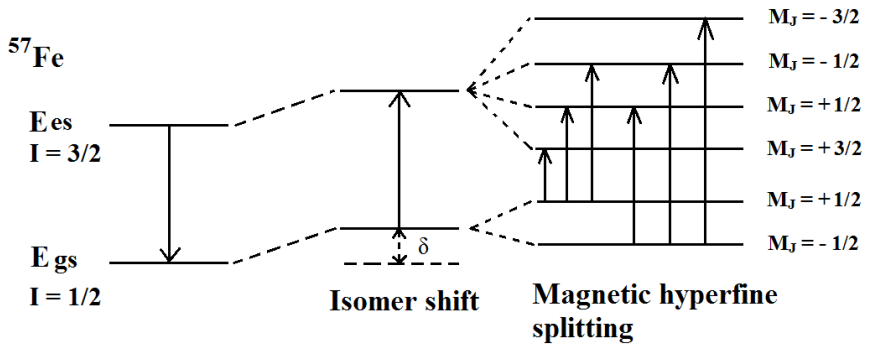

Figure 2.25 The energy levels of ^{57}Fe showing isomer shift and magnetic hyperfine splitting.

The ^{57}Fe Mössbauer spectroscopy experiments for this thesis were conducted by Prof. J. M. Cadogan at the Australian Defence Force Academy, Australia. All Mössbauer spectra were fitted using the NORMOS software [23]. For some samples due to the clear asymmetry of the lines associated with the magnetic component, spectra were also fitted with a distribution of magnetic hyperfine field, using the Le Caër – Dubois software [24].

References

[1] A.K. Cheetham, P. Day, Solid-State Chemistry: Techniques, Oxford University Press, 1987.

[2] M.M. Woolfson, X-ray Crystallography, Cambridge University Press, 1970.

[3] R. Lavinsky, http://www.iRocks.com.

[4] L. Klaus-Dieter, B. Arno, S. Andreas, C. Helmut, Textures and Microstructures 35 (2003) 219.

[5] C.M. Clark, B.L. Dutrow,
http://serc.carleton.edu/research_education/geochemsheets/techniques/SXD.html.

[6] P. Kuiper, http://en.wikipedia.org/wiki/Atomic_form_factor.

[7] J.K. Cockcroft, http://pd.chem.ucl.ac.uk/pdnn/inst1/optics1.htm.

[8] Diamond Light Source, http://www.diamond.ac.uk.

[9] G.E. Bacon, Neutron Diffraction, 3rd ed., Oxford University Press, 1975.

[10] http://en.wikipedia.org/wiki/Neutron.

[11] ILL, http://www.ill.eu.

[12] ILL, http://www.ill.fr/YellowBook/D2B.

[13] ANSTO, http://www.ansto.gov.au.

[14] ISIS, http://www.isis.stfc.ac.uk.

[15] H.M. Rietveld, Journal of Applied Crystallography 2 (1969) 65.

[16] A.C. Larson, R.B. von-Dreele, General Structure Analysis System (GSAS), Los Alamos National Laboratories, 1994.

[17] J. Clarke, Scientific American (1994) 36.

[18] D. Martien, http://www.qdusa.com/sitedocs/appNotes/ppms/1078-201.pdf.

[19] http://en.wikipedia.org/wiki/Transmission_electron_microscopy.

[20] R. Paria Sena, Structure characterisation of triple perovskites and related systems by transmission electron microscopy, Ph. D. thesis, University of Antwerp, 2017.

[21] R.S.o. Chemistry,
http://www.rsc.org/membership/networking/interestgroups/mossbauerspect/intropart1.asp.

[22] http://upload.wikimedia.org/wikipedia/commons/2/2f/Mossbauer_Spectrometer.jpg.

[23] R.A. Brand, NORMOS, http://www.wissel-instruments.de.

[24] G. Le Caër, J.M. Dubois, Journal of Physics E-Scientific Instruments 12 (1979) 1083.

Chapter 3: Structural and Magnetic Properties of $Sr_3Fe_2TeO_9$

3.1 Introduction

As discussed previously, partial cation substitution at either the A site, the B site or both, leading to the formulae $AA'BB'O_6$ and $A_2A'B_2B'O_9$, is one of the strategies that has been employed in order to induce desirable physical properties in perovskites. In this study we have focussed on the compound $Sr_3Fe_2TeO_9$ in which only the B site holds more than one species of cation. In two previous accounts [1, 2] this compound has been described as a tetragonal perovskite in which the Fe^{3+} and Te^{6+} cations are partially ordered over the six-coordinate B sites. More specifically, the octahedral sites are divided into two subsets that occur alternately in 3 dimensions throughout the structure in a checker-board pattern. The two subsets thus have the same multiplicity. Ivanov *et al* [2] concluded that one subset, or sublattice, is occupied by Fe^{3+} and Te^{6+} in a ratio of 0.72:0.28 and the Fe:Te ratio at the other site is thus 0.61:0.39, see Figure 3.1; the corresponding values reported by Augsberger *et al* [1] were 0.9:0.1 and 0.57:0.43.

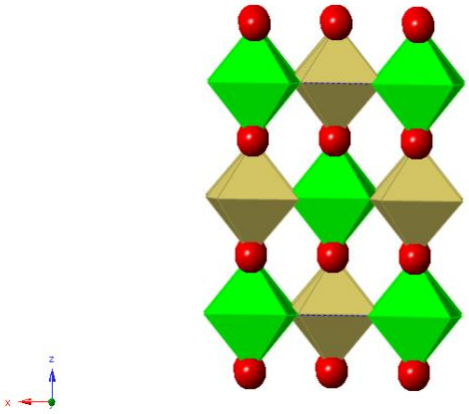

Figure 3.1 Polyhedral representation of the tetragonal structure proposed by Ivanov *et al* for $Sr_3Fe_2TeO_9$ in the space group *I*4/m. Red circles represent Sr^{2+}, green and khaki octahedra represent sites occupied by a partially ordered distribution of Fe^{3+} and Te^{6+}.

Neutron diffraction data collected by Ivanov *et al* suggested that the compound showed long-range magnetic ordering below ~260 K with the atomic moments on the two sublattices aligned antiparallel along [001]. The magnetic moments per Fe^{3+} cation on the two sites refined to values of ~1.6 and ~1.3 μ_B at 10 K. These values are very low for a high-spin d^5 cation. Furthermore, despite the mismatch in the moments on the two sites, no sharp increase

in the magnetisation was seen on cooling the sample below 260 K. However, hysteresis was apparent in the magnetic susceptibility below this temperature. A maximum was observed in the zero-field cooled (ZFC) susceptibility at ~90 K in a measuring field of 100 Oe and at ~60 K in a field of 30 kOe; the susceptibility was field dependent throughout the measured temperature range although, inconsistently, the magnetisation at 300 K was shown to be a linear function of field for $0 < H/kOe < 50$. The field-cooled susceptibility maintained a negative temperature gradient at all temperatures and in all fields. In order to interpret these data Ivanov *et al* suggested that ferrimagnetic ordering is present, at least over short length scales, below 260 K and that the susceptibility maximum observed at low temperature marks the formation of a re-entrant spin glass. In contrast, Augsburger *et al* reported the onset of ferromagnetism at ~717 K in their sample and they observed a remanent magnetisation 0.35 μ_B per Fe^{3+} cation at 5 K. They analysed their neutron diffraction data using a model in which nearest-neighbour Fe^{3+} cations were coupled antiferromagnetically and found an ordered moment of ~0.5 μ_B per Fe^{3+} cation at 300 K and 0.85 μ_B at 13 K, the latter lower even than the value reported by Ivanov *et al*. Both of these two studies used samples that were prepared in a solid-state reaction. Djerdi *et al* [3] have recently prepared a sample by a sol-gel route. It is reported to adopt the simple cubic perovskite structure with no cation ordering over the B sites and to be ferrimagnetic below 667 K. The temperature dependence of the magnetisation of the $Sr_3Fe_2TeO_9$ samples prepared by Ivanov *et al*, Augsburger *et al* and Djerdi *et al* are shown in Figure 3.2.

The suggestion by Ivanov *et al* that the length scale of the magnetic ordering might be important in determining the magnetic properties of $Sr_3Fe_2TeO_9$ is reminiscent of the behaviour of $La_3Ni_2SbO_9$, another $A_3B_2B'O_9$ perovskite, which has previously been described as a relaxor ferromagnet [4, 5]. The octahedral sites in this monoclinic compound are divided over two sublattices, as they are in $Sr_3Fe_2TeO_9$. Clearly, the net magnetisation is expected to be larger in a compound that contains a more strongly magnetic cation, and it is also likely that the transition temperature will increase above the value of 108 K seen in $La_3Ni_2SbO_9$. Bearing in mind the internal inconsistencies in the description given by Ivanov *et al,* the differences between the data collected by different authors and the potential of $Sr_3Fe_2TeO_9$ to show enhanced relaxor properties, we have undertaken our own investigation of this compound using a combination of X-ray and neutron diffraction, electron microscopy and Mössbauer spectroscopy. The results, which differ significantly from those reported previously, are described below.

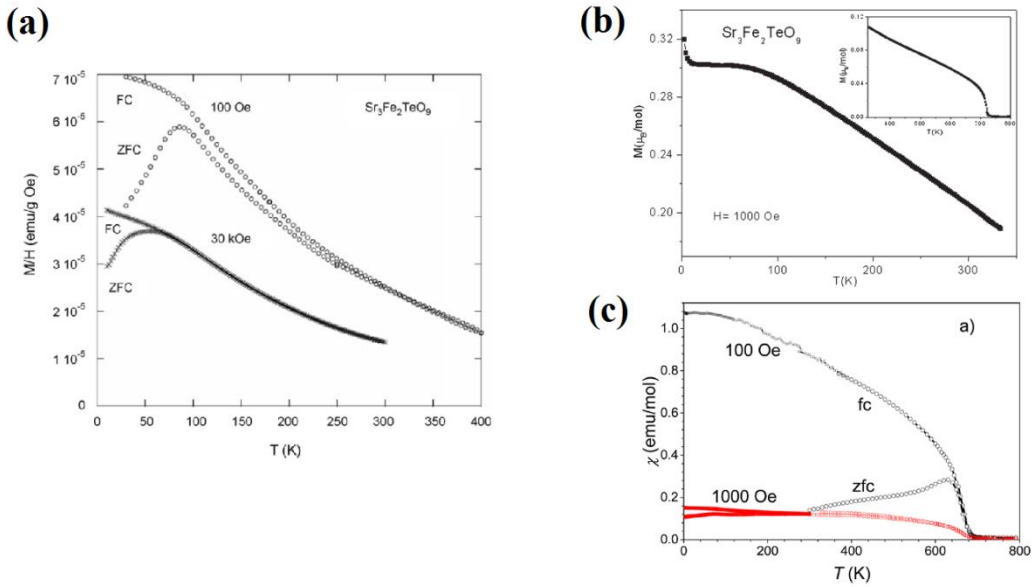

Figure 3.2 The temperature dependence of the magnetisation of the $Sr_3Fe_2TeO_9$ samples prepared by (a) Ivanov *et al* [2](b) Augsburger *et al* [1]and (c) Djerdi *et al* [3].

3.2 Experimental methods

A polycrystalline sample of $Sr_3Fe_2TeO_9$ was prepared using the standard ceramic method. $SrCO_3$, Fe_2O_3 and TeO_2 (purity >99.95%) were weighed out in the appropriate stoichiometric ratio and ground together in an agate mortar for 30 minutes to give a homogeneous mixture. The mixture was then loaded into an alumina crucible and fired at 700 °C for 24 h. It was then quenched to room temperature, reground and pressed into a pellet that was fired in air at 950 °C for 24 hours and subsequently annealed at 1200 °C for 48 hours after further grinding. Finally, the furnace was allowed to cool to 800 °C and then the sample was quenched to room temperature.

The black reaction product was initially characterised by X-ray powder diffraction (XRPD) using Cu $K\alpha_1$ radiation. The data, collected at room temperature, were analysed using the Rietveld method as implemented in the GSAS [6] program package. Neutron diffraction data were subsequently collected on the diffractometer Echidna at the Bragg Institute, ANSTO, Australia by Dr. Maxim Avdeev. The angular region $10 < 2\theta/° < 147.5$ was scanned in steps of 0.05° at temperatures of 300 and 3 K using neutron wavelengths of 1.6215(5) and 2.4395(5) Å. Data analysis was again performed using the Rietveld method [7]. The peak shape was modelled using the function devised by van Laar and Yelon [8] and the background was fitted using a twelve-term Chebyschev polynomial. The magnetic

susceptibility of $Sr_3Fe_2TeO_9$ was measured over the temperature range $2 < T/K < 300$ using a Quantum Design MPMS 5000 SQUID magnetometer. Data were collected on warming in a field of 100 Oe after cooling the sample both in the absence of an applied field (zero-field cooled, ZFC) and in the measuring field (field cooled, FC). The isothermal sample magnetisation was measured as a function of field over the range $-50 < H/kOe < 50$ at 300, 150 and 5 K. Transmission electron microscopy (TEM) experiments related to this chapter were carried out by Prof. Joke Hadermann and Dr. Robert Paria Sena at the University of Antwerp, and ^{57}Fe Mössbauer spectroscopy experiments were conducted by Prof. J. M. Cadogan at the Australian Defence Force Academy, as described in Chapter 2.

3.3 Results

Our preliminary consideration of the XRPD pattern of the product appeared to confirm that $Sr_3Fe_2TeO_9$ adopts a perovskite-like structure. The presence of weak Bragg peaks, most noticeably at angles $2\theta < 30°$, indicated a deviation away from the aristotype cubic perovskite structure, and, influenced by the earlier work of Ivanov *et al*, we initially indexed and analysed the pattern in the tetragonal space group *I*4/*m*, with the unit-cell parameters a = 5.5749(1), c = 7.8963(3) Å, that is $\sim\sqrt{2}a_p \times \sim 2a_p$. Although the fit between the observed and calculated diffraction patterns was good (R_{wpr} = 6.06 %, χ^2 = 1.47, see Figure 3.3) we noted that some weak reflections, for example at $2\theta = 18°$, could not be indexed in the tetragonal cell. These reflections were extremely weak and the fit was very good so we initially assumed that they derived from a minor impurity phase. The results of our electron microscopy study, described below, showed this to be a false assumption.

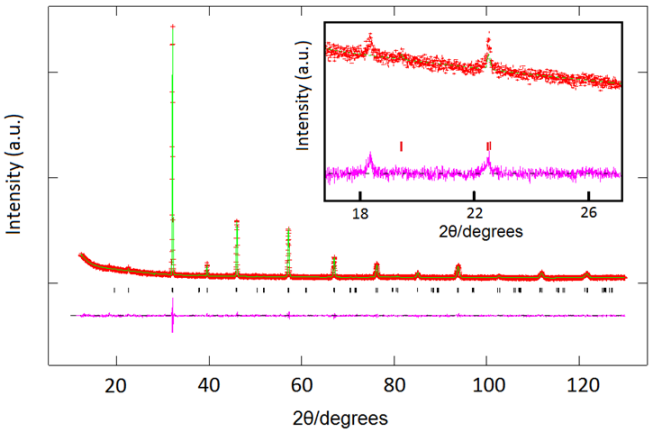

Figure 3.3 Observed (red crosses) and calculated (green line) X-ray powder diffraction patterns for $Sr_3Fe_2TeO_9$ sample indexed in *I*4/*m*; a difference curve (purple) is shown.

EDX analysis found a mean Fe:Te ratio of 2.3(3) across the crystallites studied. This value is consistent, within error, with the target composition. SAED patterns, including several tilt series, were taken from many different crystals. All the patterns could be indexed in the trigonal system, using the space group *P*-3*c*1 and the approximate unit cell parameters $a = b = 5.58$ Å, $c = 13.66$ Å. Figure 3.4 shows the SAED patterns from the main zone axes ([100]/[12-1], [12-1], [001], and [-110]) of $Sr_3Fe_2TeO_9$. The [100] and [12-1] SAED patterns overlap in the first frame as a consequence of twinning in nanodomains smaller than the smallest SAED aperture of the microscope. As a consequence, the [100] electron diffraction pattern could not be found separately. However, the [100] zone axis pattern can be seen in pure form as the Fourier transform of the [100] HAADF-STEM image in Figure 3.5. The reflection conditions *0kl: l=2n, 00l: l=2n* (4-index system: *h-h0l:l=2n, 000l:l=2n*) apparent in the electron diffraction patterns and Fourier transform confirm the assignment of the space group *P*-3*c*1. In the top left image in Figure 3.5, taken along [100], horizontal rows of uniformly bright dots alternate with rows in which pairs of weak dots are separated from each other by one bright dot. In HAADF-STEM images, the brightness of the dots increases rapidly with the average atomic number, *Z*, of a projected column. Sr, Fe and Te have the atomic numbers 38, 26 and 52, respectively. The weakest dots thus correspond to columns of Fe, and the brightest to columns of Te; the homogeneously bright rows are populated by Sr. This assignment is confirmed by the high resolution EDX maps shown in Figure 3.5. The contrast in the [001] image shown in Figure 3.6 and the inserted atomic resolution EDX map also show evidence of cation order. Here the structure is viewed down columns in which Sr atoms alternate with octahedral sites; the 2:1 sequence of weak and strong dots in the lines of atoms running down the page clearly shows the presence of 2:1 Fe:Te ordering. Figure 3.7 shows a [100] and a [001] view of a trigonal perovskite unit cell with this 2:1 ordering of Fe and Te over the octahedral sites. The observation of [100]/[12-1] twinning prompted the collection of more images, taken from more than one sample, in an attempt to assess the extent to which the microstructure is disrupted. These images showed that the [12-1] domains observed in what is essentially a [100] projection range in size from a few nanometers to ~50 nm in diameter, see Figure 3.8. Furthermore, although the trigonal phase dominates the images, we observed crystallites that contained both trigonal regions and regions showing a checkerboard-like alternation of cations over the six-coordinate sites, see Figure 3.9. The contrast variations in the latter regions match the variation of electron density in the tetragonal structural model described above. Therefore and for conciseness, in Figure 3.9 these areas are labelled as *I*4/*m*. Note that the electron diffraction patterns labelled as the

trigonal [12-1] zone in Figure 3.4 could also be the [100] zone of the *I*4/*m* phase as the two cannot be distinguished from their electron diffraction patterns alone. They can, however, be distinguished from their HAADF-STEM images.

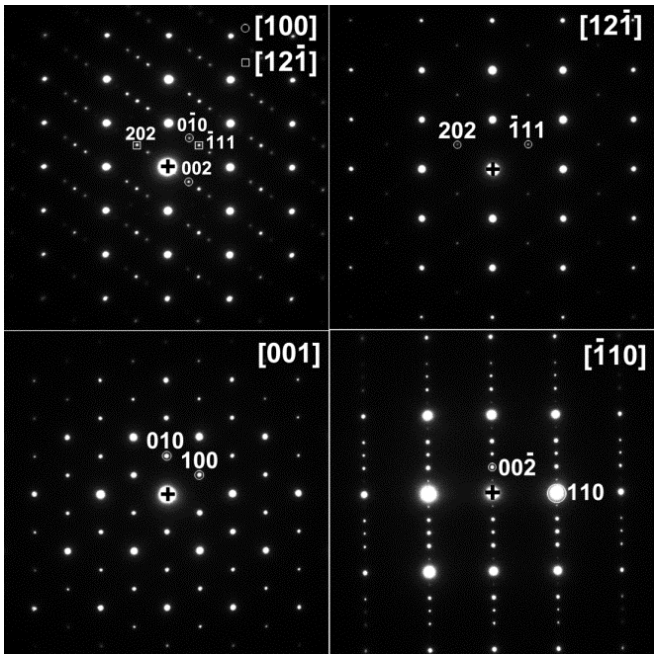

Figure 3.4 Representative SAED patterns of the main zones of $Sr_3Fe_2TeO_9$.

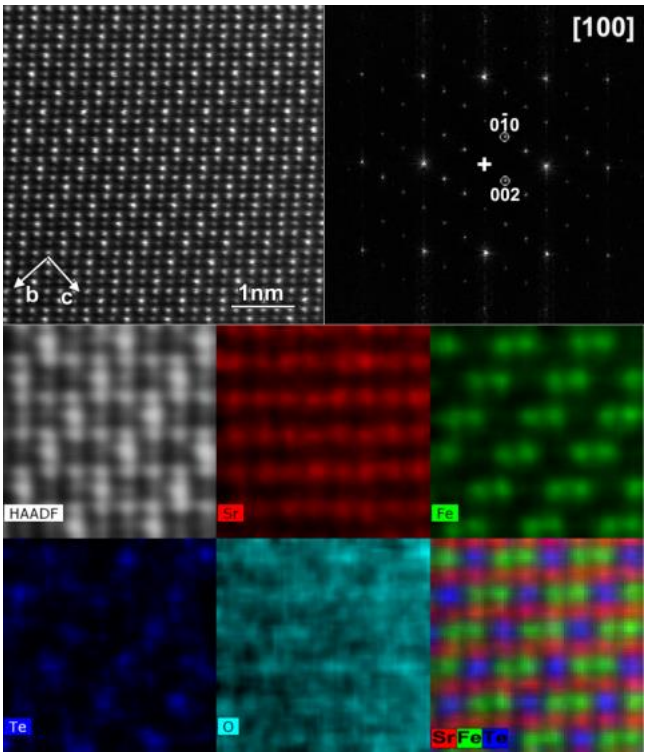

Figure 3.5 Top: HAADF-STEM image of $Sr_3Fe_2TeO_9$ taken along the zone axis [100] and a Fourier transform of a pure [100] area. Bottom: HAADF-STEM image and corresponding atomic resolution EDX map of a [100] oriented area, showing the positions of the columns of Sr, Fe, Te and O atoms.

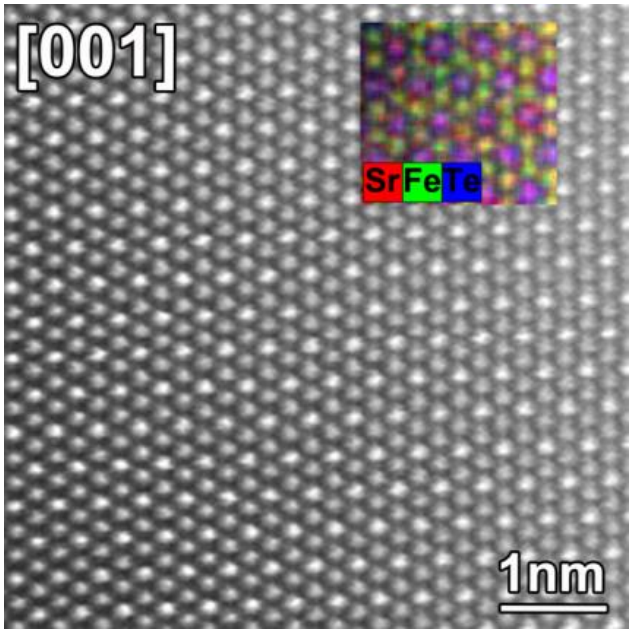

Figure 3.6 HAADF-STEM image of $Sr_3Fe_2TeO_9$ taken along the [001] zone axis. The inset is an atomic resolution EDX map showing the positions of the different cations along this projection. There is an overlap of A and B cations along this projection.

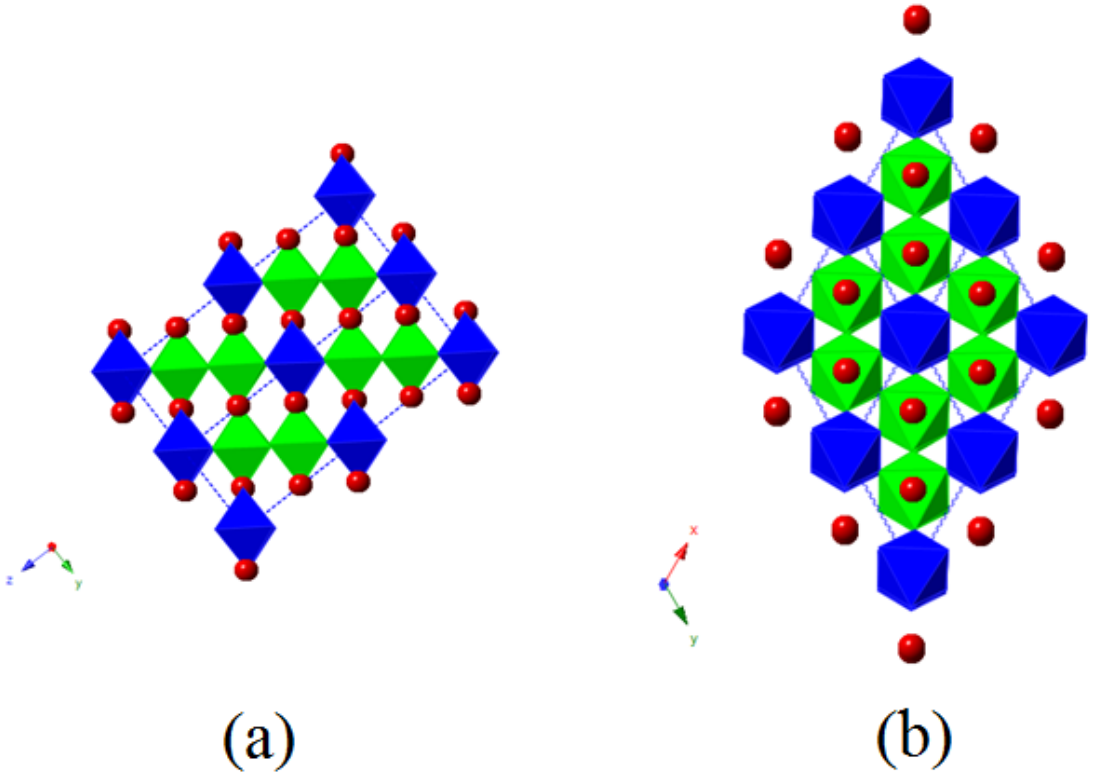

Figure 3.7 Polyhedral representation of the crystal structure of $Sr_3Fe_2TeO_9$ in the trigonal space group *P*-3*c*1 viewed along (a) [100] and (b) [001]; FeO_6 and TeO_6 octahedra are shown in green and blue, respectively. Red circles represent the Sr^{2+} cations.

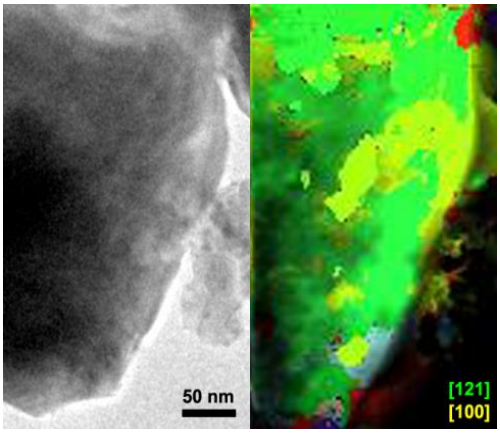

Figure 3.8 Low-magnification image of a crystallite of $Sr_3Fe_2TeO_9$. Electron diffraction patterns (not illustrated) show that yellow areas are being viewed along [100] and green areas along [121]. The crystallite is overlapping with others in the red region and the blue region shows only the basic perovskite reflections, probably because of the thinness of the crystal in this region.

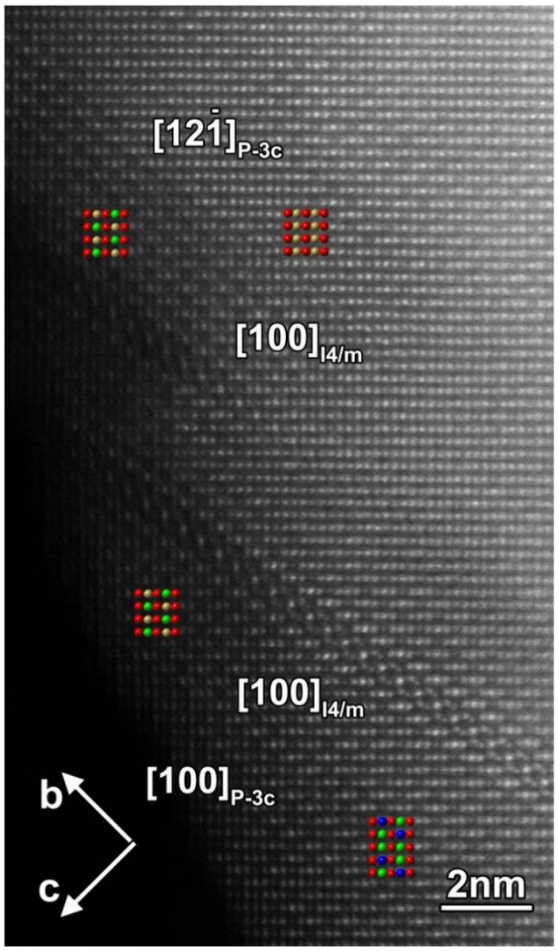

Figure 3.9 HAADF STEM image of $Sr_3Fe_2TeO_9$ showing the coexistence of areas with chessboard order (labelled *I*4/*m* [100]), *P*-3*c* [100] and *P*-3*c* [12-1]. The colour overlays clarify the order of the atoms in the surrounding areas; Sr, Fe and Te are red, green and blue respectively. Khaki represents columns with, in this projection, a mix of Fe and Te.

In the light of the microscopy data presented above, the XRPD data were reanalysed in space group *P*-3*c*1 using the structural model shown in Figure 3.7. The overall quality of the Rietveld fit achieved using this trigonal structure was essentially the same (R_{wpr} = 6.04 %, χ^2 = 1.46, see Figure 3.10) as that achieved in tetragonal symmetry, with different weak reflections, for example at 2θ = 19°, being unaccounted for. Consequently our final analysis treated the sample as a mixture of a trigonal phase and a tetragonal phase, the latter in space group *I*4/*m*. In the trigonal structure there are two independent oxygen sites (6*f* and 12*g*), two A sites (2*a* and 4*d*) that accommodate strontium atoms, and two independent B-sites (4*d* and 2*b*) for iron and tellurium, see Table 3.1. In our refinements we assumed that the iron and tellurium cations are completely ordered over the latter two sites and thus the cation arrangement in the trigonal phase can be expressed as $Sr[Fe^{3+}_{0.6667}]_{(4d)}[Te^{6+}_{0.3333}]_{(2b)}O_3$. In the tetragonal structure, however, there is only one position (4*d*) for strontium, and the two distinct B-sites (2*a* and 2*b*) have equal multiplicities. We assumed that one is fully occupied by iron and the other by a random distribution of iron (33%) and tellurium (67%) to give an overall 2:1 stoichiometry of iron and tellurium. In this case the cation arrangement can be described as $Sr[Fe^{3+}_{0.5}]_{(2a)}[Fe^{3+}_{0.1667}Te^{6+}_{0.3333}]_{(2b)}O_3$. This two-phase model, with the trigonal and tetragonal phases occurring in a ratio of 73.8(6):26.2(6), accounted for all the observed peaks. The agreement achieved between the observed and calculated diffraction patterns in this case (R_{wpr} = 5.93 %, χ^2 = 1.41) can be seen in Figure 3.11.

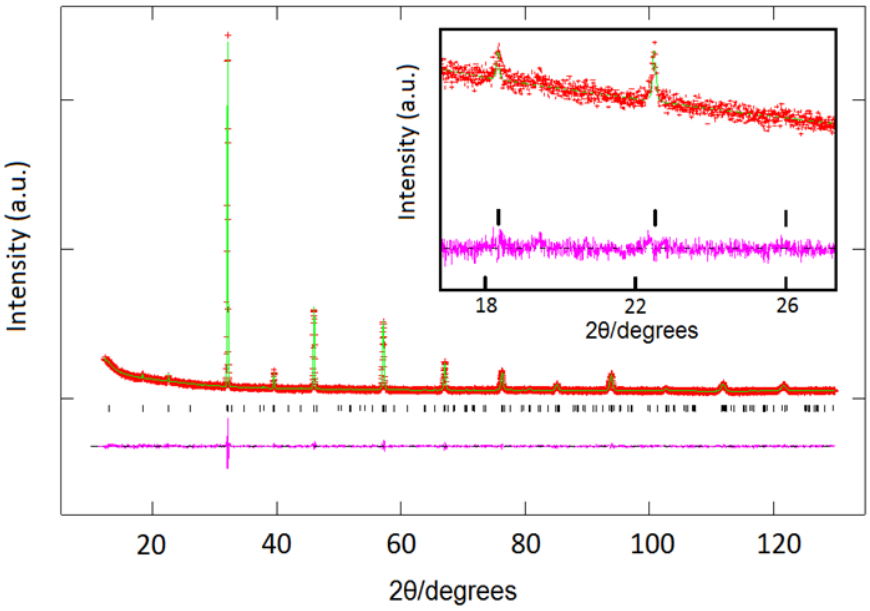

Figure 3.10 Observed (red crosses) and calculated (green line) X-ray powder diffraction patterns for $Sr_3Fe_2TeO_9$ sample indexed in *P*-3*c*1; a difference curve (purple) is shown.

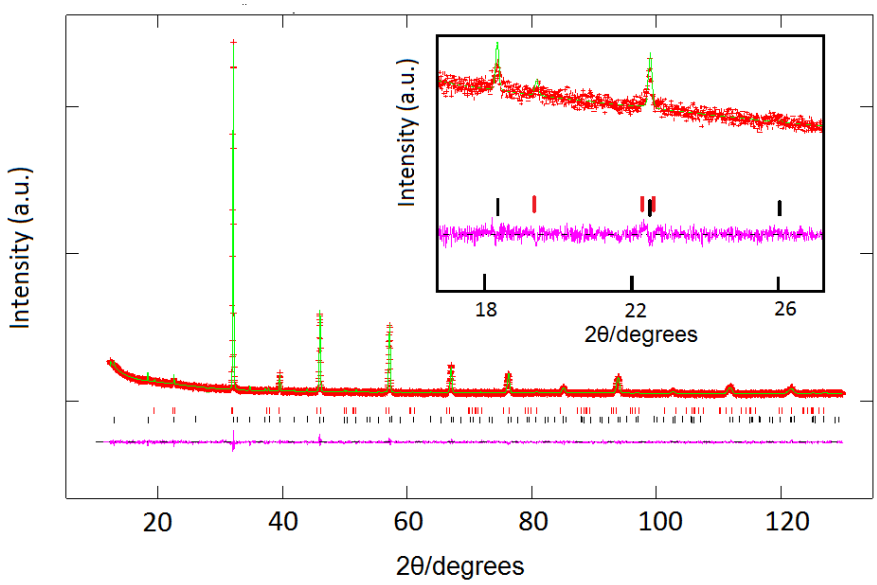

Figure 3.11 Observed (red crosses) and calculated (green line) X-ray powder diffraction patterns for $Sr_3Fe_2TeO_9$ sample; a difference curve (purple) is shown. Black (red) vertical bars represent the positions of Bragg reflection for the trigonal (tetragonal) phase.

Table 3.1 Atomic parameters of $Sr_3Fe_2TeO_9$, refined from neutron diffraction data collected at 300 K.

Atom	Site	*x*	*y*	*z*	U_{iso}	fractional occupancy
Phase 1						
Sr1	2*a*	0	0	0.25	0.005(1)	1.0
Sr2	4*d*	0.6667	0.3333	0.5834(6)	0.0088(6)	1.0
Fe	4*d*	0.6667	0.3333	0.3335(5)	0.0036(3)	1.0
Te	2*b*	0	0	0	0.0036(3)	1.0
O1	6*f*	0.521(1)	0	0.25	0.014(1)	1.0
O2	12*g*	0.1942(6)	0.3308(8)	0.5842(4)	0.0062(5)	1.0
Phase 2						
Sr	4*d*	0	0.5	0.25	0.026(1)	1.0
Fe1	2*a*	0	0	0	0.023(4)	1.0
Fe2	2*b*	0	0	0.5	0.003(3)	0.3333
Te	2*b*	0	0	0.5	0.003(3)	0.6667
O1	4*e*	0	0	0.242(6)	0.024(3)	1.0
O2	8*h*	0.285(3)	0.217(2)	0	0.021(1)	1.0

R_{wp} = 4.67 %, R_p = 3.56 %, χ^2= 4.568

Phase 1: space group *P* -3*c*1, a = 5.5761(3) Å, c = 13.654(1) Å, weight fraction=76 %

Phase 2: space group *I*4/*m*, a = 5.5886(5) Å, c = 7.9134(8) Å, weight fraction=24 %

^{57}Fe Mössbauer spectra collected from $Sr_3Fe_2TeO_9$ at room temperature are shown in Figure 3.12. The low-resolution spectrum, see Figure 3.12(a), clearly has a substantial magnetic component. From the shape of the lines in the magnetic sextet it is apparent that there is a distribution of magnetic hyperfine fields, rather than a single, well-defined field strength. This observation suggests that there might be slightly different nearest-neighbour environments around the iron sites. The higher-resolution, low velocity spectrum, see Figure 3.12(b), shows that the central part of the spectrum contains at least two paramagnetic doublets in addition to the two innermost lines of the hyperfine sextet. Quantitative analysis of this spectrum resulted in the parameters shown in Table 3.2. The tabulated spectral weights lead to the conclusion that ~41 % of the total absorption is in the hyperfine sextet. Our fit to the spectrum shown in Figure 3.12(a), obtained using the Le Caër – Dubois method, therefore included two quadrupole doublets and a hyperfine field distribution; the latter is shown in Figure 3.13. The average hyperfine magnetic field obtained from the distribution is 43.1 T with a standard deviation of 4.1 T and the average isomer shift of the magnetic component is + 0.41(3) mm s^{-1} relative to the centre of the α-Fe calibration spectrum. Although the degree of spectral overlap and the presence of a range of hyperfine fields make it difficult to obtain a unique description of the spectra, our analysis of the Mössbauer spectrum obtained on the extended velocity scale suggested that the magnetic component comprises ~36 % of the spectrum, slightly lower than the value obtained by analysis of the central absorption alone. The two doublets that account for the remaining ~64 % of the spectrum again have comparable spectral weights but significantly different quadrupole splittings, $|\Delta|$. In both analyses the isomer shifts of all components lie in the narrow range $0.27 \leq \delta/\text{mm s}^{-1} \leq 0.42$, suggesting that all the iron in $Sr_3Fe_2TeO_9$ is present as high-spin Fe^{3+}. The Mössbauer spectrum collected at 5 K is shown in Figure 3.14. The central, paramagnetic absorption is no longer present and the hyperfine field has increased to ~52 T on cooling, although the width of the lines shows that a range of field strengths is again present. In view of the complexity of the system it was not possible to identify a unique set of physically-meaningful fitting parameters and so we did not pursue a more detailed, quantitative analysis of the spectra.

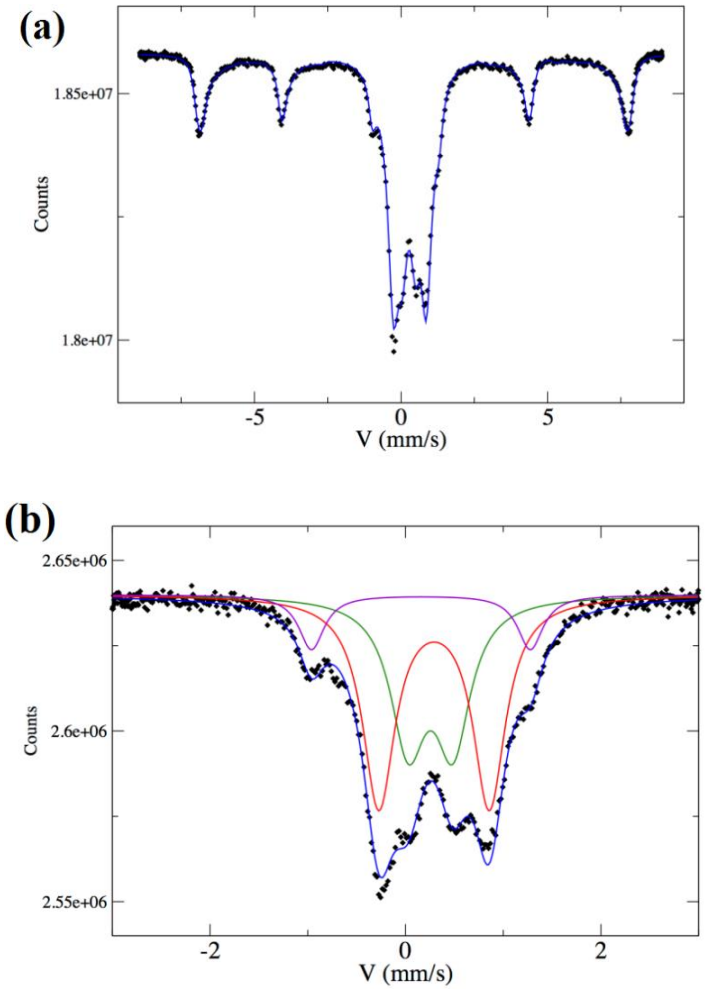

Figure 3.12 (a) ^{57}Fe Mössbauer spectrum of $Sr_3Fe_2TeO_9$ obtained at room temperature (295 K) on an extended velocity scale. (b) ^{57}Fe Mössbauer spectrum of $Sr_3Fe_2TeO_9$ obtained at room temperature (295 K) on a reduced velocity scale.

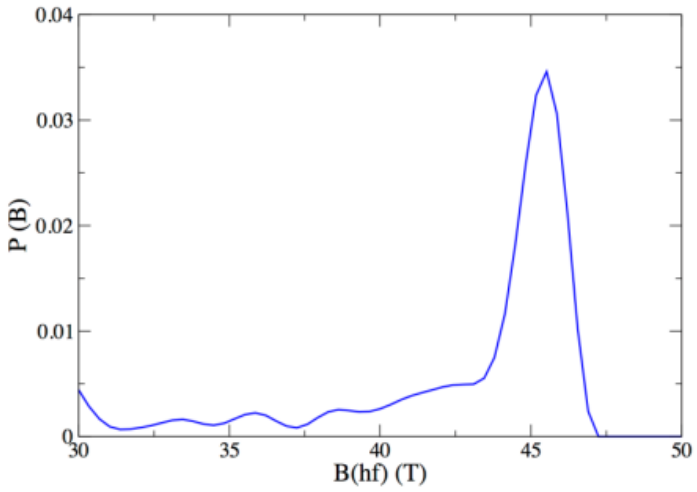

Figure 3.13 The distribution of hyperfine magnetic field obtained from the fit to the room temperature Mössbauer spectrum of $Sr_3Fe_2TeO_9$.

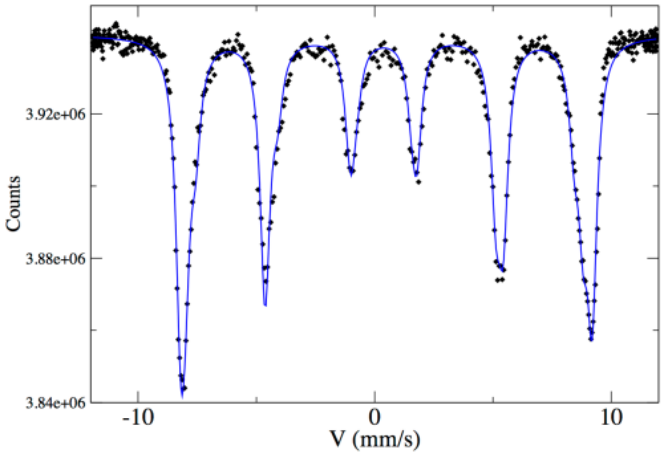

Figure 3.14 Mössbauer spectrum of $Sr_3Fe_2TeO_9$ recorded at 5 K.

Table 3.2 ^{57}Fe Mössbauer hyperfine parameters of $Sr_3Fe_2TeO_9$, obtained by fitting the spectrum shown in Figure 3.12(b). The errors are estimates.

Isomer shift (δ mm/s) ± 0.02 mm/s	Quadrupole splitting (|Δ| mm/s) ± 0.03 mm/s	% Area ± 1.5%
0.37	0.49	43.2
0.41	1.15	46.4
0.27	2.23	10.4 ('sextet' contribution)

The neutron diffraction data collected at 300 K using wavelengths of 1.6220 and 2.4395 Å were analysed simultaneously in the same two-phase model used in the final analysis of the XRPD data. Refinement of the atomic coordinates and atomic displacement parameters associated with this model did not give an entirely satisfactory account of the data. The discrepancies between the observed and calculated diffraction profiles were most noticeable at low angles and were therefore assumed to be magnetic in origin. Furthermore, Ivanov *et al.* reported a value of 260 K for the magnetic transition temperature in tetragonal $Sr_3Fe_2TeO_9$ and it is therefore reasonable to assume that the magnetic scattering observed at 300 K is associated with the trigonal phase. However, in order to complete the analysis and deduce a detailed model for the magnetic structure it was necessary to consider the Mössbauer spectra described above. We assumed the two doublets to be of equal intensity and assigned one to each of the trigonal and tetragonal phases. If the hyperfine field is associated with the trigonal

phase then, on the basis of the Le Caër – Dubois fit, (36 + 32) = 68 % of the sample is trigonal and 32 % is tetragonal. A calculation based on the data in Table 3.2 gives a ratio of 70.5:29.5. Both of these ratios are in reasonable agreement with the ratio of ~74:26 deduced from the XRPD data and so we assumed that our partition of the absorption between the two phases was correct. Hence we deduced that 53 - 58 % of the iron in the trigonal phase is magnetically ordered at room temperature. The antiferromagnetic structure shown in Figure 3.15 gives rise to additional intensity in the Bragg peaks that were mis-fitted when magnetic scattering was neglected in our initial analysis of the neutron data. Each Fe^{3+} cation is coupled antiferromagnetically to its neighbouring sites, whether they are nearest neighbours or next-nearest neighbours that are separated by a TeO_6 octahedron. When 53 % of the Fe^{3+} ions in the trigonal phase were assumed to contribute to the magnetic scattering, the ordered magnetic moment refined to 3.60(5) μ_B per ordered cation; the calculated value of the moment is inversely proportional to the percentage of the Fe^{3+} ions assumed to be ordered. A value of ~4.5 μ_B is expected in a defect-free, saturated antiferromagnet but the value of the hyperfine field is also lower than the value of ~55 T typically observed in that case and our model thus gives a reasonable and self-consistent account of the spectroscopic and diffraction data collected at room temperature. The inclusion of magnetic scattering in the Rietveld analysis resulted in agreement factors of R_{wpr} = 4.67 %, χ^2 = 4.57. The concentration ratio of the trigonal and tetragonal phases refined to be 76:24, in agreement with the ratio determined by X-ray diffraction. The final observed and calculated diffraction profiles (λ = 1.6215 Å and 2.4395 Å) are shown in Figure 3.16 and the refined structural parameters are listed in Table 3.1; the derived bond lengths and angles are listed in Table 3.3.

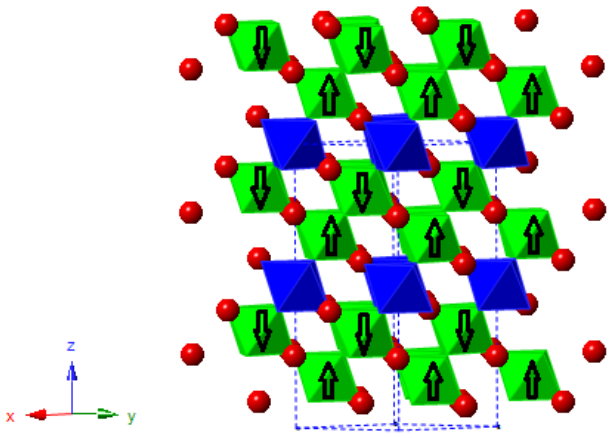

Figure 3.15 Magnetic structure of the trigonal phase of $Sr_3Fe_2TeO_9$. Green and blue octahedra represent Fe^{3+} and Te^{6+} sites, respectively, and red circles represent Sr^{2+} cations. Black arrows represent the ordered magnetic moments of the Fe^{3+} cations.

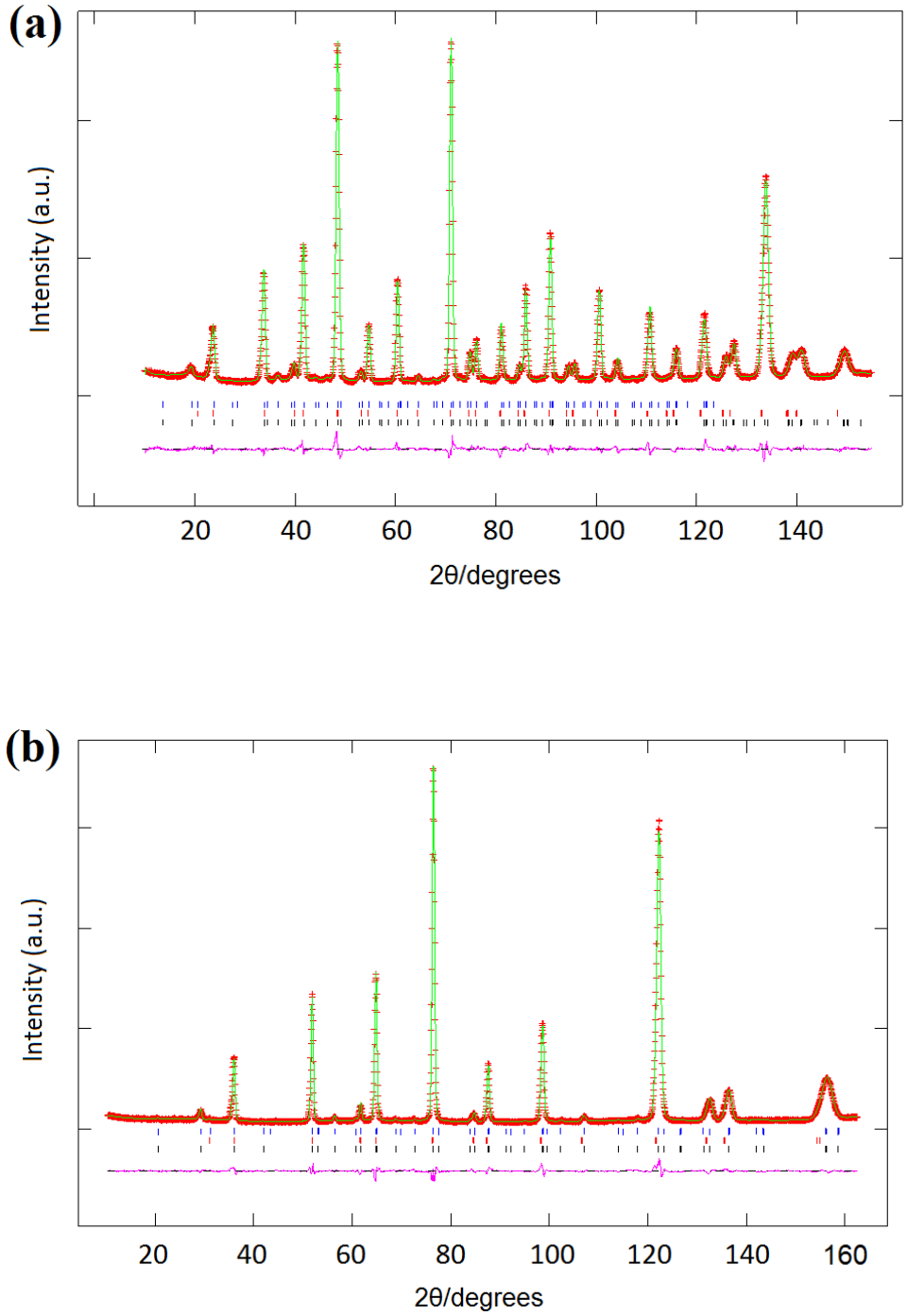

Figure 3.16 Observed (red crosses) and calculated (green line) neutron diffraction patterns for $Sr_3Fe_2TeO_9$ at 300 K using wavelengths of (a) 1.6215 Å and (b) 2.4395Å. A difference curve (purple) is shown. Black, red and blue vertical bars represent the positions of Bragg reflections for the trigonal, tetragonal and magnetic phases, respectively.

Table 3.3 Selected interatomic distances (Å) and bond angles (°) in $Sr_3Fe_2TeO_9$ at 300 K and 3 K.

	300 K	3 K
Trigonal phase, space group *P*-3*c*1		
Sr1 – O1	2.673(6) ×3	2.581(7) ×3
Sr1 – O1	2.903(6) ×3	2.982(7) ×3
Sr1 – O2	2.776(5) ×6	2.781(6) ×6
Sr2 – O1	2.790(7) ×3	2.798(8) ×3
Sr2 – O2	2.627(3) ×3	2.618(4) ×3
Sr2 – O2	2.949(3) ×3	2.945(4) ×3
Sr2 – O2	2.809(8) ×3	2.78(1) ×3
Fe – O1	1.976(4) ×3	1.974(4) ×3
Fe – O2	1.980(5) ×3	1.991(7) ×3
Te – O2	1.974(5) ×6	1.958(6) ×6
O1 – Fe – O1	90.1(2)	90.4(2)
O2 – Fe – O2	90.9(3)	90.3(4)
O1 – Fe – O2	178.6(3)	178.9(3)
	88.6(2)	88.9(2)
	90.4(2)	90.3(4)
Tetragonal phase, space group *I*4/*m*		
Sr – O1	2.795(1) ×4	2.7908(5) ×4
Sr – O2	2.991(4) ×4	2.988(3) ×4
Sr – O2	2.614(4) ×4	2.611(2) ×4
Fe1 – O1	1.92(5) ×2	2.02(3) ×2
Fe1 – O2	1.98(2) ×4	2.05(2) ×4
Fe2/Te – O1	2.04(5) ×2	1.94(3) ×2
Fe2/Te – O2	2.01(2) ×4	1.93(2) ×4

The observation of a hyperfine field of ~52 T at 5 K prompted us to assign a proportionately-enlarged magnetic moment to the ordered Fe^{3+} cations in the trigonal phase during the analysis of the neutron diffraction data collected at 3 K. The tetragonal phase was again assumed to be non-magnetic; the validity of this assumption is discussed below. When the moment was held fixed at 4.34 μ_B per ordered cation, the value calculated from the hyperfine field, the fraction of magnetic Fe^{3+} in the trigonal structure refined to be 55.6 %, a value that lies within the range deduced from the room-temperature Mössbauer spectra. The refined

structural parameters obtained at 3 K are listed in Table 3.4 and selected bond lengths are included in Table 3.3. The diffraction patterns are shown in Figure 3.17.

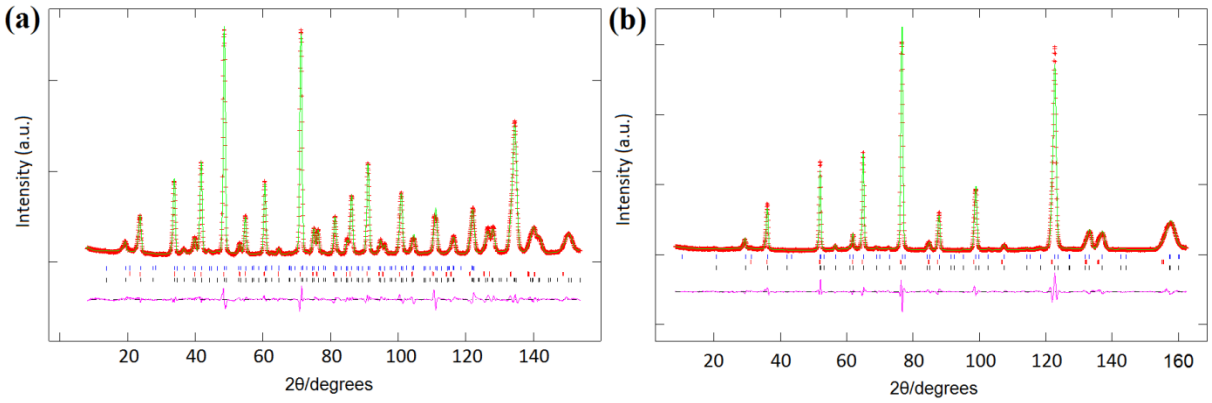

Figure 3.17 Observed (red crosses) and calculated (green line) neutron diffraction patterns for $Sr_3Fe_2TeO_9$ at 3 K using wavelengths of (a) 1.6215 Å and (b) 2.4395Å. A difference curve (purple) is shown. Black, red and blue vertical bars represent the positions of Bragg reflection positions for the trigonal, tetragonal and magnetic phases.

Table 3.4 Atomic parameters of $Sr_3Fe_2TeO_9$, refined from neutron diffraction data collected at 3 K.

Atom	Site	*x*	*y*	*z*	U_{iso}	fractional occupancy
Phase 1						
Sr1	2*a*	0	0	0.25	0.0003(14)	1.0
Sr2	4*d*	0.6667	0.3333	0.5824(7)	0.0041(7)	1.0
Fe	4*d*	0.6667	0.3333	0.3330(5)	0.0025(2)	1.0
Te	2*b*	0	0	0	0.0025(2)	1.0
O1	6*f*	0.536(1)	0	0.25	0.003(1)	1.0
O2	12*g*	0.1944(8)	0.330(1)	0.5830(5)	0.0058(7)	1.0
Phase 2						
Sr	4*d*	0	0.5	0.25	0.0156(8)	1.0
Fe1	2*a*	0	0	0	0.0037(6)	1.0
Fe2	2*b*	0	0	0.5	0.0037(6)	0.3333
Te	2*b*	0	0	0.5	0.0037(6)	0.6667
O1	4*e*	0	0	0.255(4)	0.0087(6)	1.0
O2	8*h*	0.291(2)	0.223(2)	0	0.0087(6)	1.0

R_{wp} = 6.23 %, R_p =4 .69 %, χ^2 = 8.033

Phase 1: space group *P* -3*c*1, a = 5.5626(3) Å, c = 13.622(1) Å, weight fraction=76 %

Phase 2: space group *I*4/*m*, a = 5.5810(4) Å, c = 7.9045(7) Å, weight fraction=24 %

The temperature dependence of the molar magnetic susceptibility of our sample is shown in Figure 3.18. The data collected under ZFC and FC conditions overlie at high temperatures but the ZFC susceptibility has a maximum at 80 K whereas the FC susceptibility has a negative temperature gradient throughout the measured temperature range. The field dependence of the molar magnetisation is shown in Figure 3.19. *M*(*H*) is linear at 300 K and no hysteresis is observed. At 150 K *M*(*H*) is no longer linear but hysteresis is only observed in the data collected at 5 K; the function is not symmetrical about the origin.

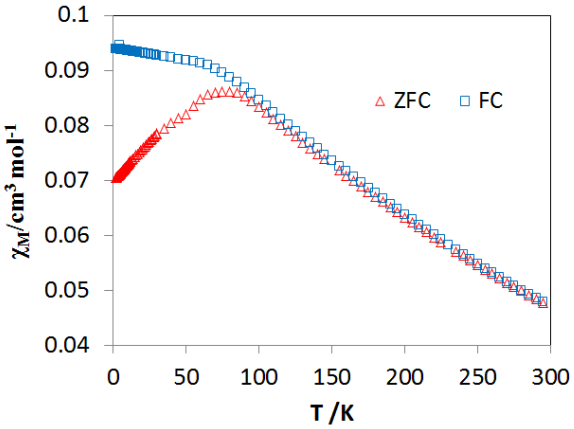

Figure 3.18 Temperature dependence of the molar magnetic susceptibility of $Sr_3Fe_2TeO_9$.

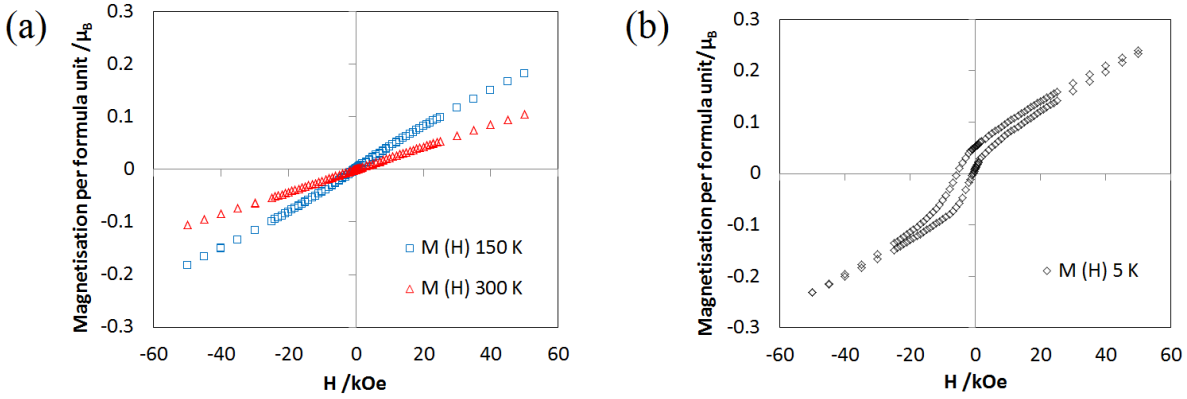

Figure 3.19 Field dependence of the molar magnetisation of $Sr_3Fe_2TeO_9$ at (a) 300 and 150 K and (b) 5 K.

3.4 Discussion

It is clear that our sample of $Sr_3Fe_2TeO_9$ differs from those prepared by Djerdi *et al*, Ivanov *et al* and Augsburger *et al*, and that their samples are different from each other. This is most clearly shown by a comparison of the temperature dependence of the magnetic susceptibility

measured in each case and, in the case of Augsburger *et al*, by a comparison of the X-ray diffraction patterns. The most obvious differences between our synthesis and those performed by Ivanov *et al* and Augsburger *et al* lie in the use of telluric acid, rather than TeO_2, by Augsburger *et al* and of SrO, rather than $SrCO_3$, by Ivanov *et al*. Furthermore, both of these groups used an annealing temperature of only 950 °C. Our choice of 1200 °C was made when heating the reactants at 950 °C failed to produce a perovskite-like phase. The sol-gel protocol used by Djerdi *et al* ended with an anneal at 1300 °C. Their cubic sample differs most markedly from our own in terms of both crystal structure and physical properties. For example, although magnetic order is present in our sample at 300 K, there is no evidence of a spontaneous magnetisation at that temperature.

Our initial attempts to analyse our X-ray diffraction pattern were influenced by our awareness of the earlier studies of this compound and our apparent success in accounting for the data using a monophasic model in tetragonal symmetry will make us more cautious in the future. The results of our electron-microscopy study demonstrated that our approach was flawed and they also revealed the full complexity of the system. The electron diffraction patterns indicated that the sample has trigonal symmetry and the HAADF-STEM images and EDX maps reveal the presence of the 2:1 Fe:Te ordering pattern. This type of cation ordering over the B sites of a perovskite is relatively unusual, with many $A_3B_2B'O_9$ compositions, for example $La_3Ni_2SbO_9$ adopting the 1:1 ordering pattern, even though the trigonal pattern might be considered a better match for their stoichiometry. Although there are some exceptions, for example $Ba_3Bi_2TeO_9$ [9], the latter pattern is most commonly observed in $A^{2+}{}_3B^{5+}{}_2B'^{2+}O_9$ compounds [10, 11]. Like $Sr_3Fe_2TeO_9$, these compounds have only divalent cations on the A site and two types of cation with a charge difference of +3 on the octahedral sites. $Sr_3CaRu_2O_9$ and the high-pressure forms of $Ba_3CaRu_2O_9$ and $Ba_3CaIr_2O_9$ are the only such compounds wherein the majority six-coordinate cation is paramagnetic [12-14]. The high-pressure phase of $Ba_3NaRu_2O_9$ has a different charge distribution over the octahedral sites but also adopts the 2:1 ordered structure [15]. We note that $Ba_3Fe_2TeO_9$ is a 6*H* hexagonal perovskite [1, 3] because, in the absence of the large Bi^{3+} cation, the cation size ratio r_A/r_B is too large to stabilize a pseudo-cubic perovskite structure.

Our microscopy study revealed that defects are present in the structure of $Sr_3Fe_2TeO_9$. More specifically, the electron diffraction patterns indicated that twinning was present on the nanoscale in some of the crystallites studied and the HAADF-STEM images showed that, in addition to the dominant 2:1 cation ordering, some crystallites had regions where 1:1 ordering

was present. This ordering is consistent with the tetragonal structure proposed by Ivanov *et al*, but also with the monoclinic structure of $La_3Ni_2SbO_9$[4]. Our data do not allow us to distinguish unambiguously between the two symmetries so, in the light of the previous studies of this compound, we assumed these regions to be tetragonal. We were able to optimize the fit to our XRPD pattern when we included a trigonal phase and a minority tetragonal phase, thus demonstrating that some of the 1:1 ordered regions are large enough to give rise to Bragg peaks. Given that our mixed trigonal/tetragonal sample was prepared at a higher temperature than the tetragonal sample described by Ivanov *et al*, we carried out further syntheses with week-long anneals at 950 and 1200 °C in an attempt to prepare monophasic tetragonal and trigonal samples, respectively. The resulting XRPD patterns always showed the presence of both phases, with a trigonal: tetragonal ratio that varied between 70: 30 and 80: 20.

The agreement between the observed and calculated neutron diffraction profiles shown in Figure 3.16 is good. The Fe – O and Te – O bond lengths determined by neutron diffraction are essentially equal in the trigonal phase at 300 K but the Te – O bond is shorter, as expected [16] at 5 K. The difference in bond lengths around the two, six-coordinate sites is apparently more marked in the minority tetragonal phase, although these distances are less precisely determined. In addition to the quality of the fit, two additional pieces of evidence show that the magnetic hyperfine splitting observed in the Mössbauer spectra collected at room temperature is associated with the trigonal phase. Firstly, the fraction of the total absorption contained in the sextet is too large to derive from the iron in the minority tetragonal phase and, secondly, neutron diffraction data collected at room temperature by Ivanov *et al* showed no evidence of magnetic ordering. We put more weight on their data than those of Augsburger *et al* because the latter draw attention to the presence of one impurity, albeit diamagnetic, in their sample and we believe that the near-coincidence of the magnetic ordering temperatures of their $Ba_3Fe_2TeO_9$ and $Sr_3Fe_2TeO_9$ samples suggests that the same magnetic impurity might be present in both. With this assignment, the phase fractions derived from the diffraction and spectroscopic data are essentially self-consistent. It appears that some, but not all, of the Fe^{3+} cations in the trigonal phase are antiferromagnetically ordered at room temperature. We attribute the range of observed hyperfine fields and the incomplete ordering to the presence of the defects described above. The spectrum collected at 5 K shows an increased magnetisation but when the atomic moment measured by neutron diffraction was fixed to be consistent with the internal hyperfine field there was no evidence to suggest

that significantly more spins join the antiferromagnetic phase on cooling below room temperature. The absence of a paramagnetic component in the spectrum collected at 5 K demonstrates that all the spins in the sample are either ordered or frozen in a spin glass at that temperature. Unlike Ivanov *et al* we see no evidence for a magnetic transition in the tetragonal phase at 260 K, and hysteresis is clearly present in $\chi(T)$ below 80 K. We therefore suggest that all the spins that are disordered at room temperature undergo a transition to a spin-glass state on cooling below 80 K. If the tetragonal regions in our sample were to adopt a long-range ordered structure with atomic moments as small as those reported by Ivanov *et al*, then the combination of the low phase-fraction and the weak moments would prevent it from being detected in the neutron diffraction data collected at 3 K. However, there is no evidence in the low-temperature Mössbauer spectrum for a component with a weak internal hyperfine field and there is no evidence in the neutron data for a second magnetic component with a strong moment. The participation of the tetragonal regions in the spin-glass transition is thus consistent with all the available data. The magnetic structure shown in Figure 3.15 satisfies what must be the very strong superexchange interactions between Fe^{3+} cations in neighbouring, corner-sharing octahedra. We cannot offer a detailed discussion of the magnitudes of the ordered magnetic moments because of the correlations between the fraction of the total iron in the ordered phase and the magnitude of the moment. We believe this to be the first observation of long-range magnetic ordering in a trigonal 2:1 cation-ordered perovskite.

The behaviour of $M(H)$ shown in Figure 3.19 is consistent with our model. The absence of hysteresis at 300 K confirms that the magnetic Bragg scattering observed in the neutron diffraction pattern comes from a phase that is antiferromagnetic, rather than ferrimagnetic or ferromagnetic. The non-linearity of the function at 150 K suggests that significant, intercation interactions are present, as is to be expected at this temperature in an oxide rich in Fe^{3+} cations, and the shifted hysteresis loop recorded at 5 K is typical of a spin glass. The observation of this type of behaviour in pseudo-cubic perovskites with a partially ordered distribution of equal numbers of two cation species has been seen previously and attributed to the competition between nearest – neighbour and next – nearest – neighbour interactions [17, 18]. In the case of the minority phase in $Sr_3Fe_2TeO_9$, the small domain size is also likely to be a factor.

3.5 Conclusions

$Sr_3Fe_2TeO_9$ is a complex material. The structure and properties are clearly sensitive to the synthesis conditions. We have shown for the first time that the compound, when synthesized at 1200 °C, adopts a trigonal perovskite-like structure with the Fe^{3+} and Te^{6+} cations ordering in a 2:1 sequence that is compatible with both the chemical composition and the multiplicities of the crystallographically distinct six-coordinate sites in the trigonal space group. This is not the case in many other $A_3B_2B'O_9$ compounds, including the relaxor ferromagnet $La_3Ni_2SbO_9$. The difference in the cation ordering pattern is the most likely reason that the magnetic behaviour of the two compounds differs so markedly, with the trigonal phase of $Sr_3Fe_2TeO_9$ being antiferromagnetic at room temperature. However, the trigonal structure is disrupted by both nano-twinning and regions where the cations order in a 1:1 sequence. These disruptions prevent full antiferromagnetic ordering throughout the sample and the unordered spins form a spin-glass phase that coexists with the antiferromagnetic phase below 80 K.

This work described in this chapter has been published as: Y. Tang, E. C. Hunter, P. D. Battle, R. Paria Sena, J. Hadermann, M. Avdeev, J. M. Cadogan, Journal of Solid State Chemistry 242 (2016) 86.

References

[1] M.S. Augsburger, M.C. Viola, J.C. Pedregosa, R.E. Carbonio, J.A. Alonso, J. Mater. Chem. 16 (2006) 4235.

[2] S.A. Ivanov, P. Nordblad, S.G. Eriksson, R. Tellgren, H. Rundlof, Mater. Res. Bull. 42 (2007) 776.

[3] I. Djerdj, J. Popović, S. Mal, T. Weller, M. Nuskol, Z. Jagličić, Ž. Skoko, D. Pajić, C. Suchomski, P. Voepel, R. Marschall, B. Kozlevčar, B.M. Smarsly, Crystal Growth & Design (2016) 2535.

[4] P.D. Battle, S.I. Evers, E.C. Hunter, M. Westwood, Inorg. Chem. 52 (2013) 6648.

[5] P.D. Battle, M. Avdeev, J. Hadermann, J. Solid State Chem. 220 (2014) 163.

[6] A.C. Larson, R.B. von Dreele, General Structural Analysis System (GSAS), Los Alamos National Laboratories, 1990.

[7] H.M. Rietveld, Journal of Applied Crystallography 2 (1969) 65.

[8] B. vanLaar, W.B. Yelon, J. Appl. Cryst. 17 (1984) 47.

[9] J.H. Park, P.M. Woodward, International Journal of Inorganic Materials 2 (2000) 153.

[10] P.K. Davies, H. Wu, A.Y. Borisevich, I.E. Molodetsky, L. Farber, Annual Review of Materials Research (2008) 369.

[11] U. Treiber, S. Kemmlersack, Journal of Solid State Chemistry 43 (1982) 51.

[12] J.T. Rijssenbeek, S. Malo, V. Caignaert, K.R. Poeppelmeier, Journal of the American Chemical Society 124 (2002) 2090.

[13] J.T. Rijssenbeek, T. Saito, S. Malo, A.T. Masaki, M. Takano, K.R. Poeppelmeier, Journal of the American Chemical Society 127 (2005) 675.

[14] J.G. Zhao, L.X. Yang, Y. Yu, F.Y. Li, R.C. Yu, C.Q. Jin, Journal of Solid State Chemistry 182 (2009) 327.

[15] A.M. Arevalo-Lopez, M.S. Senn, L. Skedd, J.P. Attfield, Zeitschrift Fur Anorganische Und Allgemeine Chemie 640 (2014) 1164.

[16] R.D. Shannon, Acta Crystallographica A 32 (1976) 519.

[17] P.D. Battle, T.C. Gibb, A.J. Herod, S.-H. Kim, P.H. Munns, Journal of Materials Chemistry 5 (1995) 865.

[18] P.D. Battle, T.C. Gibb, A.J. Herold, J.P. Hodges, Journal of Materials Chemistry 5 (1995) 75.

Chapter 4: Structural and Magnetic Properties of $Ba_3Fe_2TeO_9$ and $Sr_xBa_{3-x}Fe_2TeO_9$

4.1 Introduction

As described in Chapter 1, the structure of a cubic perovskite ABO_3 can be considered to consist of pseudo-close-packed AO_3 layers stacked in a cubic-close-packed (ccp) sequence, with *B* cations occupying six-coordinate interstitial sites between the layers; the layers lie perpendicular to the [111] axis of the cubic unit cell. As the size of the cation *A* increases relative to that of the cation *B*, the stacking sequence of the layers changes from ccp to hexagonal-close-packed (hcp), with the layers now lying perpendicular to the [001] axis of a hexagonal unit cell. $BaMnO_3$ and $BaNiO_3$ exemplify the hcp structure [1, 2]. One significant consequence of the change in stacking sequence is that the connectivity between BO_6 octahedra switches from vertex-sharing to face-sharing, thus introducing short contacts between *B* cations. Many compounds exhibit mixed stacking sequences due to the incomplete switch from ccp stacking to hcp stacking, with the so-called 6*H* structure, based on the six-layer *cchcch* sequence being particularly common, see Figure 1.6 in Chapter 1. This structure contains B_2O_9 dimers, formed by face sharing BO_6 octahedra, which are linked together by single, vertex-sharing BO_6 octahedra sites. The six-coordinate sites in many perovskites, both pseudo-cubic and hexagonal, are occupied by more than one species of cation, leading to the use of formulae of the form $A_2BB'O_6$ and $A_3B_2B'O_9$ in cases where the distribution of cations is non-random and a particular cation species has a preference for one of the crystallographically-distinct sites. This cation ordering can have a marked effect on the physical properties of the compound.

The variation of cation radius down Group 2 of the Periodic Table is such that it is common for a strontium-containing perovskite to be pseudo-cubic and for the barium-containing analogue to have a mixed or hexagonal stacking sequence [3, 4]. The two compounds are often reported together in the literature, with attention being focussed on the structural change and the resulting differences in physical properties. $Sr_3Fe_2TeO_9$ and $Ba_3Fe_2TeO_9$ constitute one such pair of compounds [5, 6]. They have also been studied independently and our own investigation into $Sr_3Fe_2TeO_9$ was described in Chapter 3[7]. That study revealed a hitherto undetected complexity in the structural chemistry, including the occurrence of unusual 2:1 cation ordering in the pseudo-cubic structure. The earliest study [8] of $Ba_3Fe_2TeO_9$ identified

a 6*H* structure with Fe^{3+} in the vertex sharing octahedra and a disordered distribution of Fe^{3+} and Te^{6+} in the dimers. The compound was found to show weak ferromagnetism below 220 K. Gagulin *et al.* [9] carried out a neutron diffraction study of $Ba_3Fe_2TeO_9$ at room temperature and concluded that it is a Seignette-magnet, the name given to multiferroic materials when they were last the focus of research interest. Augsburger *et al.* [6] found evidence for cation disorder in their sample, which they found to be magnetic below 711 K. In contrast, the sample prepared by Djerdj *et al.* [10] was described as paramagnetic above 100 K and showed a susceptibility maximum at 20 K.

There is clearly disagreement over the magnetic properties of $Ba_3Fe_2TeO_9$. We have therefore undertaken a study in which low-temperature neutron diffraction and Mössbauer spectroscopy have been used for the first time to resolve some of the controversial issues. We have also used high-resolution electron microscopy to look more closely at the distribution of the cations occupying the dimers within the 6*H* structure. Moreover, to examine the structural switch from the pseudo-cubic $Sr_3Fe_2TeO_9$ to the hexagonal $Ba_3Fe_2TeO_9$, we have synthesised the perovskites with compositions $Sr_xBa_{3-x}Fe_2TeO_9$ (x=2.5, 2.25, 2, 1.5, 1.25, 1) and studied the crystal structures with X-ray diffraction. The results are described below.

4.2 Experimental methods

A polycrystalline sample of $Ba_3Fe_2TeO_9$ was prepared using the standard ceramic method. $BaCO_3$, Fe_2O_3 and TeO_2 (purity >99.95%) were weighed out in the appropriate stoichiometric ratio and ground together in an agate mortar for 30 minutes to give a homogeneous mixture. The mixture was then loaded into an alumina crucible and fired at 700 °C for 24 h. It was then quenched to room temperature, reground and pressed into a pellet that was fired in air at 950 °C for 24 hours and subsequently annealed at 1200 °C for 48 hours after further grinding. Finally, the furnace was allowed to cool to 800 °C and then the sample was quenched to room temperature. The series $Sr_xBa_{3-x}Fe_2TeO_9$ (x=2.5, 2.25, 2, 1.5, 1.25, 1) was synthesised under the same conditions using the appropriate ratio of starting materials.

The brown $Ba_3Fe_2TeO_9$ reaction product was initially characterised by X-ray powder diffraction (XRPD) using Cu $K\alpha_1$ radiation. The data, collected at room temperature on a Panalytical X'Pert diffractometer, were analysed using the Rietveld method as implemented in the GSAS [11] program package. X-ray diffraction patterns of the brown-grey reaction

products $Sr_xBa_{3-x}Fe_2TeO_9$ (x=2.5, 2.25, 2, 1.5, 1.25, 1) were collected in the same way. Neutron diffraction data of $Ba_3Fe_2TeO_9$ were subsequently collected on the diffractometer Echidna at the Bragg Institute, ANSTO, Australia. The angular region $10 < 2\theta/° < 162.5$ was scanned in steps of 0.05° at temperatures of 300, 250, 200, 150, 100, 50 and 3 K using neutron wavelengths of 1.6215(5) or 2.4395(5) Å as appropriate. Data analysis was again performed using the Rietveld method [12]. The peak shape was modelled using the function devised by van Laar and Yelon [13] and the background was fitted using a twelve-term Chebyschev polynomial. The magnetic susceptibility of $Ba_3Fe_2TeO_9$ was measured over the temperature range $2 < T/K < 300$ using a Quantum Design MPMS 5000 SQUID magnetometer. Data were collected on warming in fields of 100 and 1000 Oe after cooling the sample both in the absence of an applied field (zero-field cooled, ZFC) and in the measuring field (field cooled, FC). The isothermal sample magnetisation was measured as a function of field over the range $-50 < H/kOe < 50$ at 5 K after cooling in a field of 50 kOe. Transmission electron microscopy (TEM) experiments related to this chapter were carried out by Prof. Joke Hadermann and Dr. Robert Paria Sena at the University of Antwerp. Calculated images were produced using QSTEM 2.2 [14]. ^{57}Fe Mössbauer spectra of finely ground $Ba_3Fe_2TeO_9$ were acquired at 295 K, 200 K, 100 K and 13 K by Prof. J. M. Cadogan at the Australian Defence Force Academy, as described in the Chapter 2.

4.3 Results

The XRPD pattern of the reaction product suggested that the synthesis had produced a phase-pure 6*H* hexagonal perovskite. Influenced by the earlier work of Augsburger *et al.* [6], we first indexed and analysed the pattern in the hexagonal space group $P6_3/mmc$. Reasonably good agreement between the observed and calculated diffraction patterns was achieved with R_{wpr}=5.40 %, χ^2=1.85, see Figure 4.1. The unit-cell parameters were refined to values of a = 5.76882(2) Å, c = 14.19859(6) Å. This structural model (Figure 4.2a) contains two independent A sites, 2*b* (0, 0, ¼) and 4*f* (⅓, ⅔, *z*) which accommodate Ba^{2+} cations and two B sites, 2*a* (0, 0, 0) and 4*f* (⅓, ⅔, *z*), for Fe^{3+} and Te^{6+} cations. The 2*a* B sites lie at the centre of the vertex-sharing octahedra and the 4*f* B sites lie within the M_2O_9 dimers. The shared face of the dimers is formed by three O1 ions on 6*h* (*x*, 2*x*, ¼) sites and the O2 ions on 12*k* (*x*, 2*x*, *z*) sites connect the dimers to the vertex-sharing octahedra. Refinements of the distribution of Fe and Te over the crystallographically-distinct B sites showed that the 2*a* (0,0,0) sites are

largely occupied by Fe and that Fe/Te are randomly distributed over the 4*f* (⅓, ⅔, *z*) sites. The cation distribution can be represented by the formula $Ba_3(Fe_{0.92}Te_{0.08})_{2a}(Fe_{0.53}Te_{0.47})_{4f}O_9$.

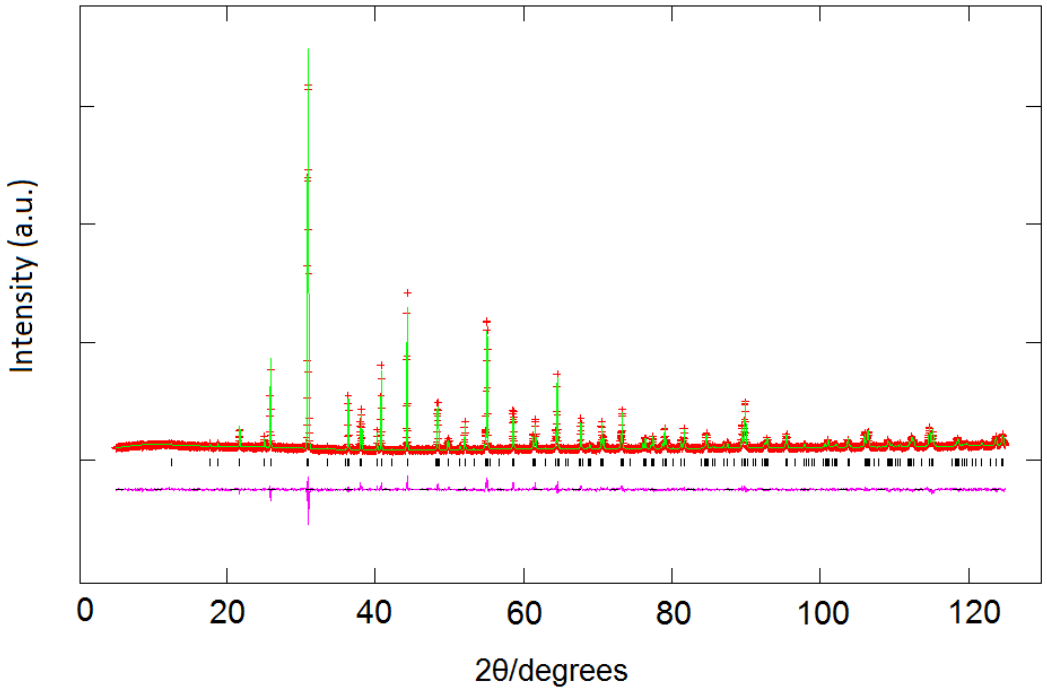

Figure 4.1 Observed (red), calculated (green) XRPD patterns of $Ba_3Fe_2TeO_9$ at room temperature. A difference curve (purple) is shown and reflection positions are marked.

Structure refinements were also carried out in the non-centrosymmetric space group $P6_3mc$, in which the two cation sites within the M_2O_9 dimers are inequivalent. The reflection conditions of this group are the same as those of $P6_3/mmc$ and the agreement factors resulting from the analyses in the former, R_{wpr}=5.53 %, χ^2=1.94, were only slightly worse than those achieved in centrosymmetric $P6_3/mmc$. The essential difference between the two models is that in $P6_3/mmc$ the sites in the dimer are occupied in a disordered manner whereas in $P6_3mc$ the cations adopt an ordered, or partially ordered, distribution over these sites, see Figure 4.2. The correct space group was determined by considering the [100] HAADF-STEM image recorded in the electron microscope. The calculated images for both models are compared to the experimental image in Figure 4.3(a). In this figure the brightest dots are the projected Ba columns, the weaker ones the columns containing Fe and Te, see Figure 4.3(b). The difference between the two calculated images lies in the columns of B cations occupying the sites within the dimers. One such pair, along with a neighbouring Ba column, is encircled on the experimental image, on each of the calculated images and in Figure 4.3(b). In $P6_3/mmc$

these two sites are equivalent because of the mirror plane perpendicular to the *c*-axis, whereas in $P6_3mc$ they are independent positions (2*b* of $P6_3mc$). Analysis of the X-ray diffraction data in $P6_3mc$ results in these 2*b* positions taking on different Fe:Te ratios which can be seen in the calculated image as a systematic brightness difference between the two columns; this would also be apparent in experimental images taken from thicker areas of the crystal. In $P6_3/mmc$, the two columns have the same brightness in the calculated image and would be expected to do so in the thicker areas of the experimental image; only in very thin areas will the random occupation of the 4*f* site by either Te or Fe give a difference in brightness between the two columns. In the experimental image shown in Figure 4.3(a) the columns in the thick regions away from the edge of the crystallite have equal brightness and thus match the image calculated for $P6_3/mmc$. The difference in the Fe:Te ratio on the crystallographically distinct 2*a* and 4*f* B positions of $P6_3/mmc$ is also clear in the HAADF-STEM images. The brightness of the dots in this type of image increases with the average atomic number along the column of atoms that the dot represents. The white dots representing columns of Fe and Te in Figure 4.3(a) come in groups of three and the middle one is always the darkest. One such group is identified by the rectangle drawn in Figure 4.3(b). It can be seen that the outer two dots correspond to the 4*f* columns and the darker middle dot corresponds to the 2*a* column. The 2*a* column is thus Fe-rich, in agreement with the cation distribution determined by X-ray diffraction.

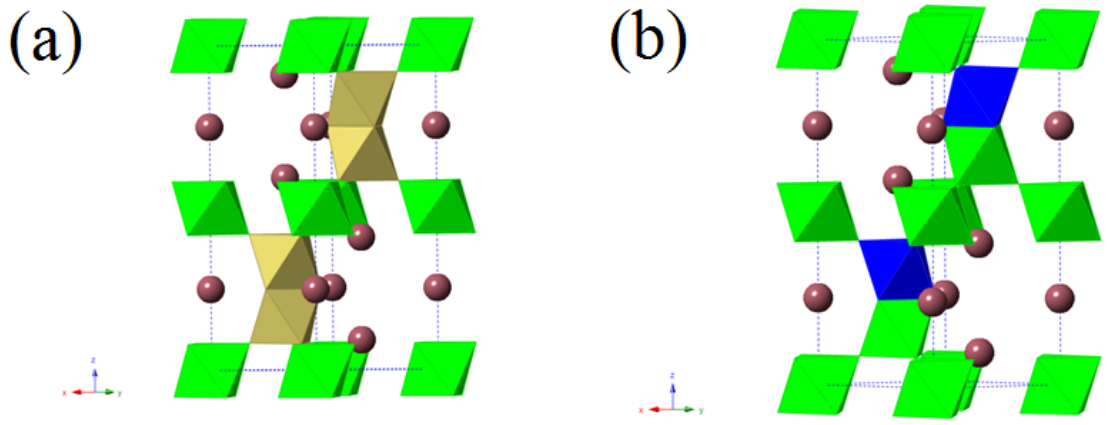

Figure 4.2 (a) $P6_3/mmc$ and (b) $P6_3mc$ structure of $Ba_3Fe_2TeO_9$. Green octahedra are occupied largely by Fe, khaki octahedra are occupied by a disordered arrangement of Fe and Te and blue octahedra are occupied largely by Te. Mauve circles represent Ba atoms.

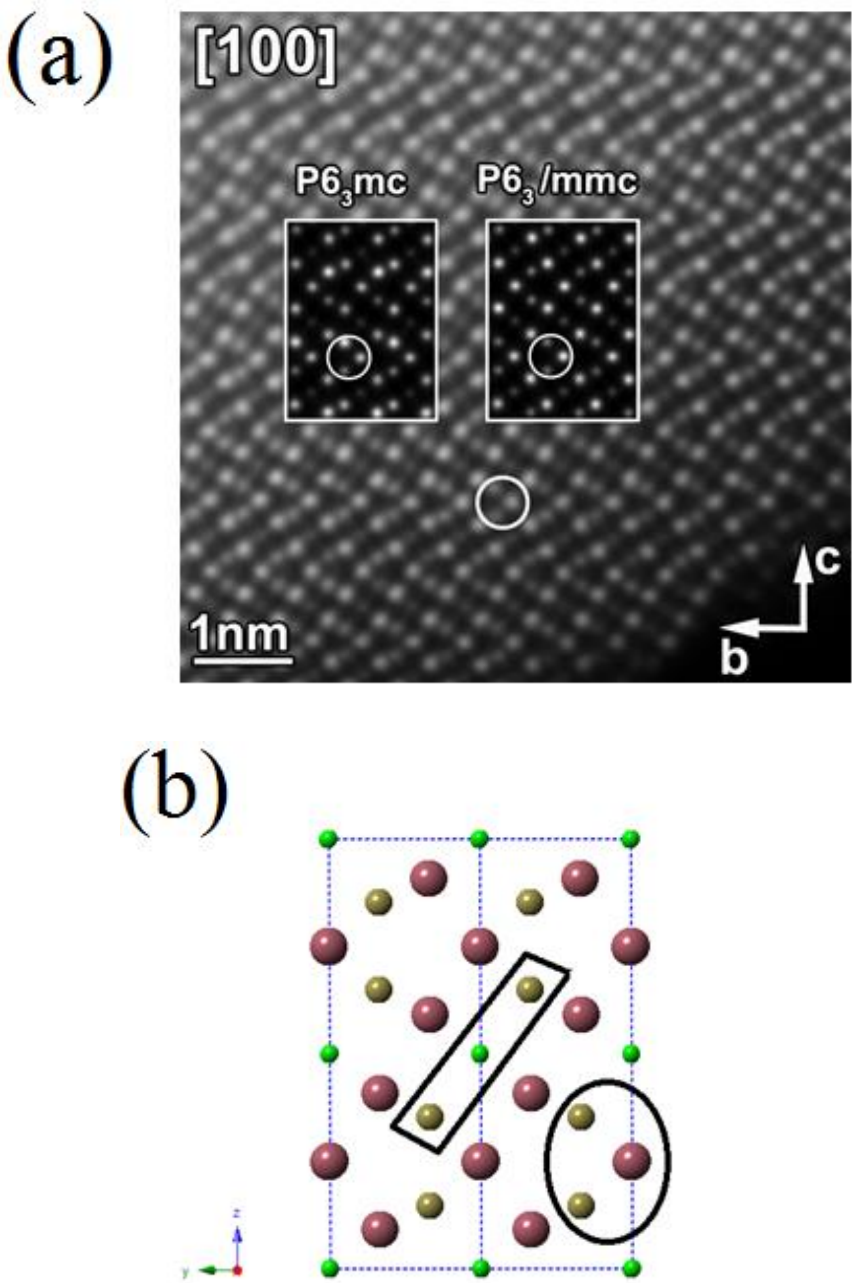

Figure 4.3 (a) Aberration-corrected high angle annular dark field scanning transmission electron microscopy (HAADF-STEM) image of $Ba_3Fe_2TeO_9$ along the [100] zone axis and calculated HAADF-STEM images (b)The cation arrangement within the structure in space group $P6_3/mmc$, viewed along [100]. Green, khaki and mauve circles represent Fe (2*a* site), disordered Te/Fe (4*f* site) and Ba, respectively.

In the light of the electron-microscopy results, the neutron diffraction data collected at 300 K were analysed in the space group $P6_3/mmc$. The refined atomic parameters and the agreement factors are listed in Table 4.1 and the most significant bond lengths and bond angles are presented in Table 4.2. The cation distribution over the sites within the dimers is refined to be

$Ba_3(Fe_{0.93}Te_{0.07})_{2a}(Fe_{0.53}Te_{0.47})_{4f}O_9$, which is in good agreement with that determined by XRPD. The resulting agreement between the observed and calculated profiles can be seen in Figure 4.4; this fit was obtained without assigning ordered magnetic moments to any of the cations.

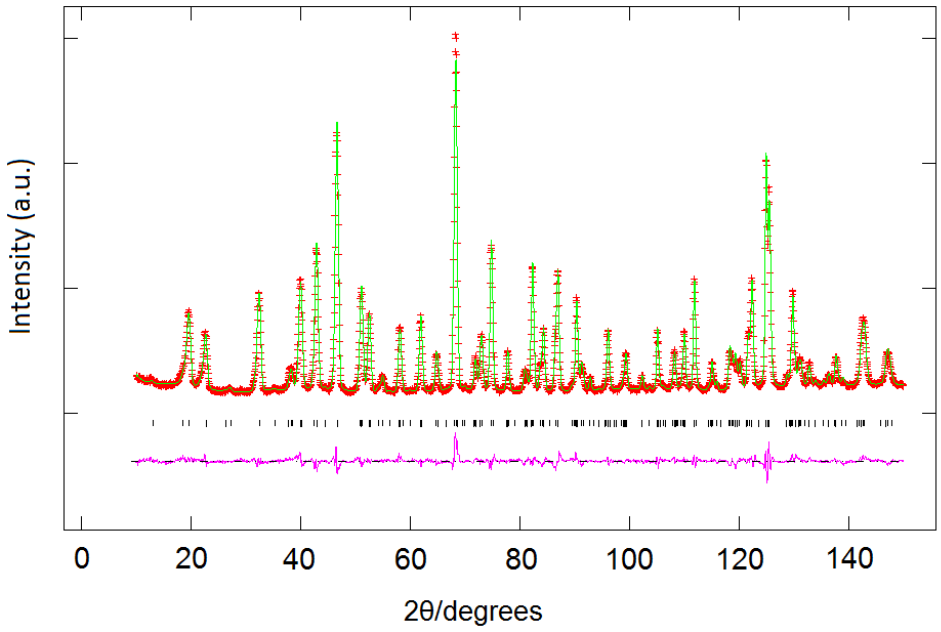

Figure 4.4 Observed (red), calculated (green) neutron diffraction patterns of $Ba_3Fe_2TeO_9$ at room temperature (λ=1.6215 Å). A difference curve (purple) is shown and reflection positions are marked.

Table 4.1 Atomic parameters of $Ba_3Fe_2TeO_9$, refined from neutron diffraction data collected at 300 K.

Atom	Site	*x*	*y*	*z*	U_{iso}	fractional occupancy
Ba1	2*b*	0	0	0.25	0.0050(5)	1.0
Ba2	4*f*	⅓	⅔	0.0919(1)	0.0062(4)	1.0
Fe1	2*a*	0	0	0	0.0065(5)	0.933(16)
Fe2	4*f*	⅓	⅔	0.85236(9)	0.0088(4)	0.529(8)
Te1	2*a*	0	0	0	0.0065(5)	0.067(16)
Te2	4*f*	⅓	⅔	0.85236(9)	0.0088(4)	0.471(8)
O1	6*h*	0.5153(2)	0.0306(3)	0.25	0.0111(4)	1.0
O2	12*k*	0.8314(2)	0.6628(3)	0.08198(7)	0.0093(2)	1.0

Space group $P6_3/mmc$, a = 5.76622(6) Å, c = 14.1966(2) Å

R_{wp} = 4.62 %, R_p = 3.69 %, χ^2= 3.754

Table 4.2 Selected interatomic distances (Å) and bond angles (°) in $Ba_3Fe_2TeO_9$ at 300 K and 3K.

	300 K	3 K
Ba1 – O1	2.88715(9) ×6	2.88095(7) ×6
Ba1 – O2	2.920(1) ×6	2.9126(9) ×6
Ba2 – O1	2.888(2) ×3	2.876(1) ×3
Ba2 – O2	2.8866(1) ×6	2.88071(7) ×6
	2.967(2) ×3	2.966(1) ×3
Fe1/Te1 – O2	2.047(1) ×6	2.046(1) ×6
Fe2/Te2 – O1	2.097(2) ×3	2.093(1) ×3
Fe2/Te2 – O2	1.891(2) ×3	1.885(1) ×3
O1 – Fe2/Te2 – O1	77.27(6)	77.49(5)
O2 – Fe1/Te1 – O2	89.13(5)	89.19(4)
	90.87(5)	90.81(4)
O2 – Fe2/Te2 – O2	97.78(6)	97.74(4)
O1 – Fe2/Te2 – O2	165.67(7)	165.85(6)
	91.61(3)	91.54(3)

The temperature dependence of the molar magnetic susceptibility of our sample of $Ba_3Fe_2TeO_9$ measured in 100 G is shown in Figure 4.5(a). The ZFC and FC susceptibilities are essentially equal above 250 K and the difference between them is small, ~5 x 10^{-4} cm^3 $mole^{-1}$, in the temperature range 90 < T/K < 250. They differ more obviously below ~90 K as they increase rapidly to a maximum at 18 K. A Curie-Weiss fit to the temperature region 250 <*T*/K < 300 gives $\theta = -167$ K, and $\mu_{eff} = 6.74\ \mu_B$ per Fe^{3+}. The limited temperature range in which reversible paramagnetic behaviour was observed limits the significance of these values and they are reported only for completeness. Figure 4.5(a) also shows the ZFC susceptibility measured in 1000 Oe. There is clearly a difference between these data and those measured in 100 Oe. The field dependence of the magnetisation at 300 K, see Figure 4.6(a), shows a weak remanent magnetisation, M_r ~5 x 10^{-4} μ_B per formula unit. Figure 4.5(b) shows the susceptibility after subtraction of this component, that is when we assume that the sample is contaminated by a magnetically-saturated impurity. The susceptibility clearly remains field-dependent at low temperature, but the effect is less marked close to room temperature. The field dependence of the molar magnetisation at 5 K is shown in Figure 4.6(b); *M*(*H*) is

nonlinear and a weak hysteresis is observed in low fields. The coercive field and remanent magnetisation are ~ 0.1 kOe and ~ 0.005 μ_B per formula unit, respectively.

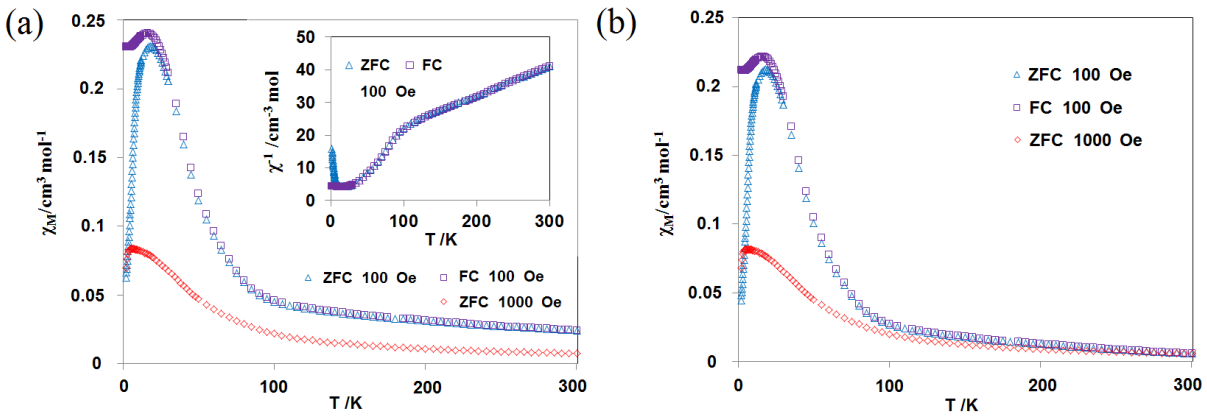

Figure 4.5 Temperature and field dependence of the molar magnetic susceptibility of $Ba_3Fe_2TeO_9$ (a) as measured (b) after correction for a magnetic impurity.

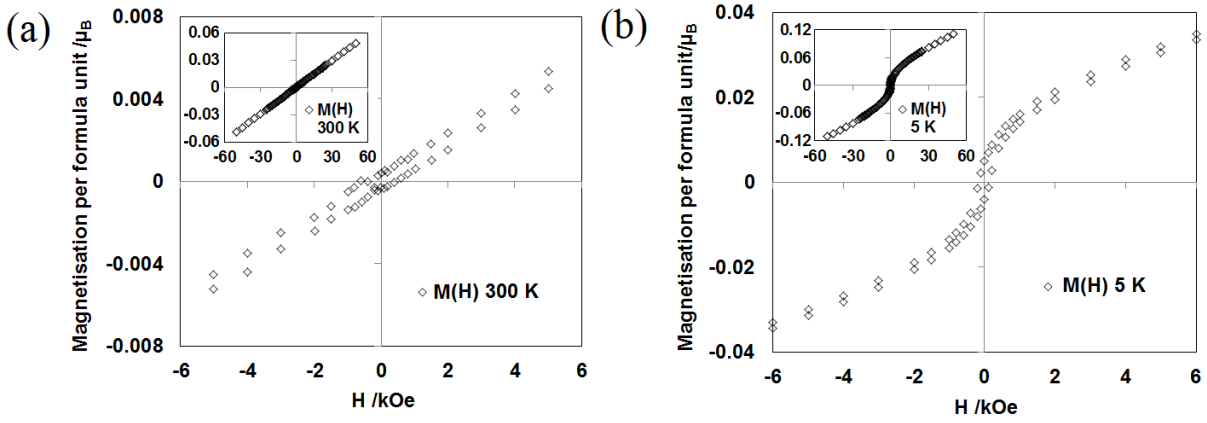

Figure 4.6 Field dependence of the magnetisation of $Ba_3Fe_2TeO_9$ at (a) 300 K, (b) 5 K.

The behaviour of $\chi(T)$, even after correction for the presence of an impurity, shows that $Ba_3Fe_2TeO_9$ does not undergo a simple transition from a paramagnetic phase to an antiferromagnetic phase at 18 K, the temperature of the susceptibility maximum. The Mössbauer spectra collected between room temperature and 13 K further illustrate the complexity of the system, see Figures 4.7 and 4.8. No sextet indicative of the presence of a magnetically-saturated phase could be detected in the spectrum obtained over a wide velocity scale at room temperature, see Figure 4.7(a). In Figure 4.7(b) we show a second spectrum

collected on a narrower velocity scale, also at room temperature. It is clear that at least three quadrupole-split doublets are required to fit this higher-resolution spectrum using a paramagnetic model and in Table 4.3 we give the fitted Mössbauer parameters for these doublets. Their isomer shifts all lie in a narrow range from 0.37 to 0.45 mm/s, indicating trivalent iron. The need to use at least three components when there are only two crystallographically-distinct iron sites might reflect the presence of occupational disorder on both of the six-coordinate sites; this will introduce many different local environments for the Fe^{3+} cations. An alternative explanation is that at 300 K the sample is close to a magnetic transition and that the peak broadening is associated with that transition. Figure 4.7(c) shows the fit to a model based on two quadrupole doublets and a weakly-split sextet, the separation of the outer lines corresponding to an internal hyperfine field of only around 52 kG. We note here that this latter fit is purely *ad hoc* and serves to illustrate that we cannot rule out the presence of a weakly magnetic Fe component at room temperature. The relative subspectral areas of these three components (2 doublets and 1 sextet) at room temperature are 50(2) %, 35(3) % and 15(1) %, respectively. The relative merits of the different interpretations of these data are discussed further below. The Mössbauer spectrum observed at 200 K, see Figure 4.8, is best accounted for using a doublet and a sextet. The relative area of the sextet has increased compared to that shown in Figure 4.7(c) (47 % *cf* 15 %), the overall magnetic splitting has increased to H_{int} = 302 (9) kG but the individual lines are rather broad, consistent with the effects of electronic relaxation. The isomer shift and the quadrupole splitting of the lines in the doublet change little on cooling to 200 K (apart from the effect of the second-order Doppler shift on the isomer shift). After further cooling to 100 K the doublet is absent from the spectrum, which consists of six broad lines that clearly do not have a 3:2:1:1:2:3 intensity ratio. At least four overlapping sextets are needed to model the observed spectrum. The separation of the two outer maxima leads to a value of 410(2) kG for the mean hyperfine field. The 13 K spectrum shows clearly that none of the Fe^{3+} cations in $Ba_3Fe_2TeO_9$ are paramagnetic at that temperature. Furthermore, all Fe^{3+} cations experience essentially the same hyperfine magnetic field. A single-sextet fit to the 13 K spectrum yields a hyperfine magnetic field of 478(2) kG with an isomer shift of 0.514(5) mm/s, significantly larger than the weighted isomer shift of 0.398(7) mm/s measured at 295 K, reflecting the second-order Doppler shift.

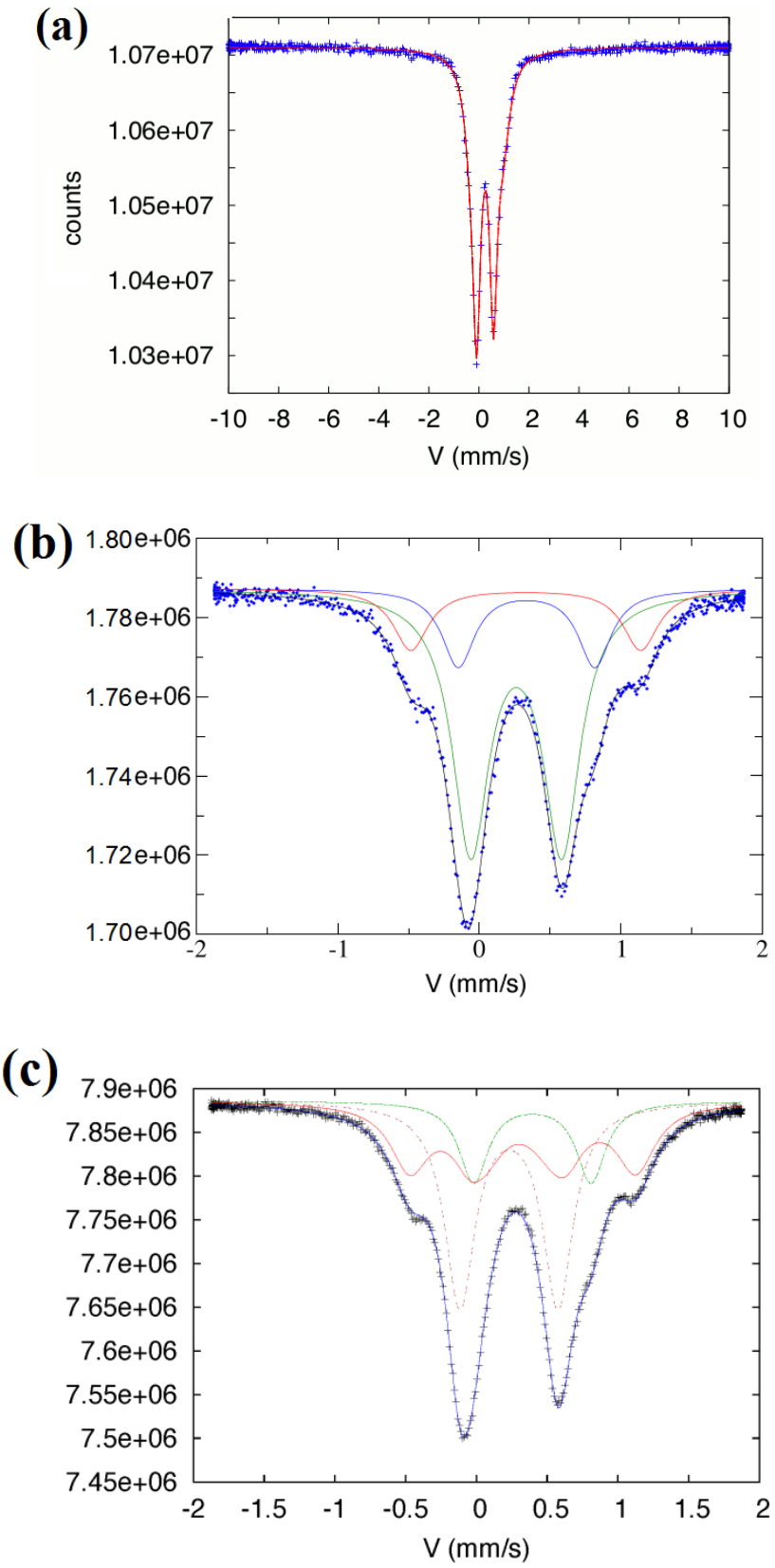

Figure 4.7 ^{57}Fe Mössbauer spectra of $Ba_3Fe_2TeO_9$ acquired at room temperature (a) on an extended velocity scale; (b) on a narrower velocity scale and fitted to three doublets; (c) on a narrow velocity scale and fitted to two doublets and a sextet.

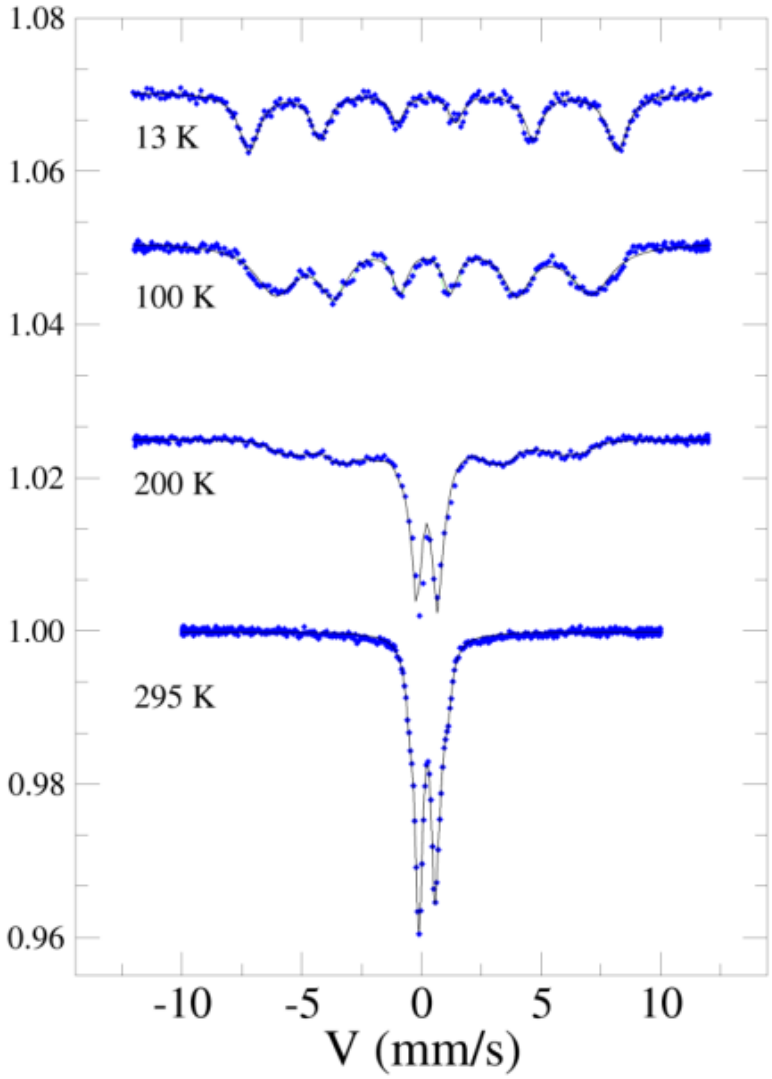

Figure 4.8 ^{57}Fe Mössbauer spectra of $Ba_3Fe_2TeO_9$ acquired at 295, 200, 100 and 13 K.

Table 4.3 Mössbauer parameters of $Ba_3Fe_2TeO_9$, determined by fitting the higher-resolution spectrum obtained at 295 K (shown in Figure 4.7b).

Spectral Component	δ (mm/s)	|Δ| (mm/s)	HWHM (mm/s)	Area (%)
Doublet 1	0.375(4)	0.643(3)	0.31(2)	66.7(5)
Doublet 2	0.447(4)	0.965(7)	0.28(2)	18.0(4)
Doublet 3	0.442(4)	1.625(8)	0.30(2)	15.3(3)

δ is the isomer shift relative to α-Fe; |Δ| is the magnitude of the quadrupole splitting; HWHM is the line half-width at half maximum intensity; Area is the relative subspectral contribution to the total spectrum.

The neutron diffraction data patterns collected at 3K using wavelengths of 1.6215 Å and 2.4395 Å were analysed simultaneously using the structural model described above. Refinement of the atomic coordinates and atomic displacement did not give an entirely satisfactory account of these data. The discrepancies between the observed and calculated diffraction profiles were most noticeable at low angles and were therefore assumed to be magnetic in origin. The Bragg scattering associated with the antiferromagnetic structure illustrated in Figure 4.9 accounted for the intensity mismatch, see Figure 4.10. In this structure the magnetic moment of each Fe^{3+} cation is coupled in an antiparallel manner to those on the nearest-neighbour sites. The direction along which the spin vectors align could not be determined unambiguously from the neutron data alone. However, the Mössbauer spectrum collected at 13 K, see Figure 4.8, allowed this issue to be resolved. Analyses of the neutron data in which the atomic moments on the 2*a* and 4*f* sites were allowed to vary independently resulted in similar values (3.40(4) and 3.40(6) μ_B per Fe^{3+} cation, respectively) at the two sites only when the spins were aligned along [001], fully consistent with our Mössbauer result. Table 4.4 lists the refined atomic parameters and agreement factors at 3 K, and selected bond lengths are included in Table 4.2.

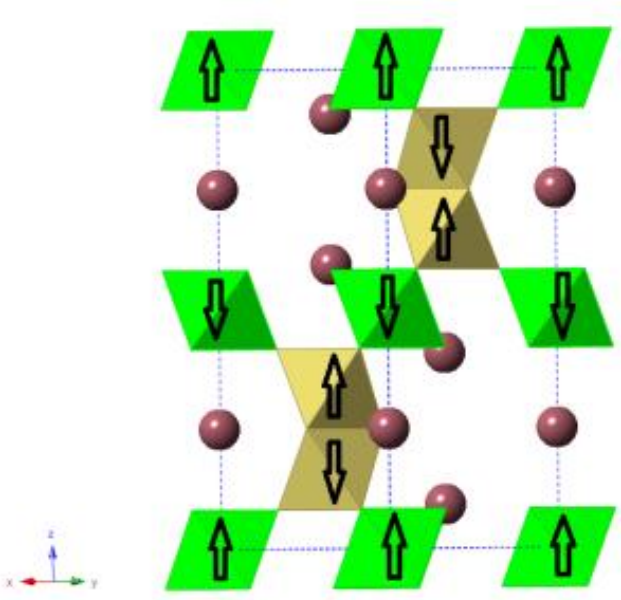

Figure 4.9 Magnetic structure of $Ba_3Fe_2TeO_9$; arrows indicate the direction of ordered spins within each octahedron. Green octahedra are occupied largely by Fe and khaki octahedra are occupied by a disordered arrangement of Fe and Te. Mauve circles represent Ba atoms.

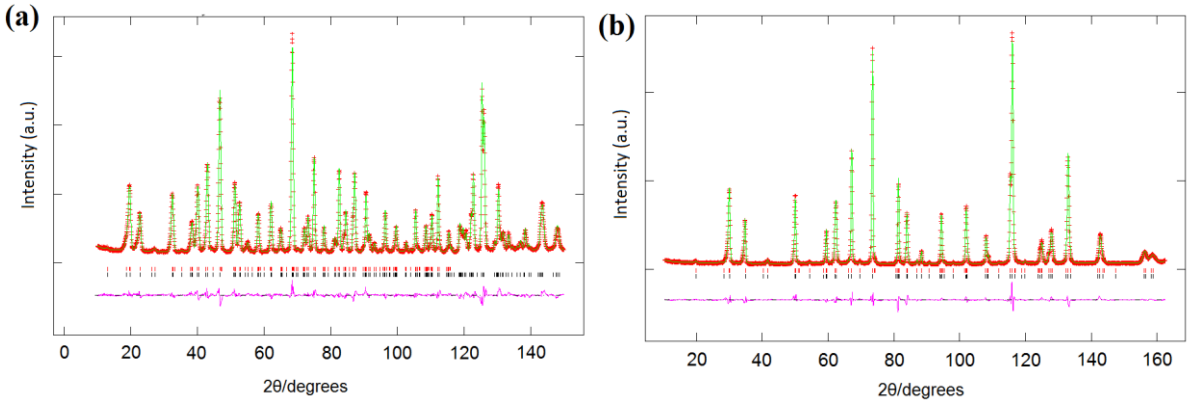

Figure 4.10 Observed (red), calculated (green) neutron diffraction patterns of $Ba_3Fe_2TeO_9$ at 3 K using wavelengths of (a) 1.6215 Å and (b) 2.4395Å. A difference curve (purple) is shown and reflection positions are marked.

Table 4.4 Atomic parameters of $Ba_3Fe_2TeO_9$, refined from neutron diffraction data collected at 3 K.

Atom	Site	*x*	*y*	*z*	U_{iso}	fractional occupancy
Ba1	2*b*	0	0	0.25	0.0001(5)	1.0
Ba2	4*f*	⅓	⅔	0.09222(9)	0.0006(4)	1.0
Fe1	2*a*	0	0	0	0.0013(3)	0.933
Fe2	4*f*	⅓	⅔	0.85213(7)	0.0065(3)	0.529
Te1	2*a*	0	0	0	0.0013(3)	0.067
Te2	4*f*	⅓	⅔	0.85213(7)	0.0065(3)	0.471
O1	6*h*	0.5149(1)	0.0298(3)	0.25	0.0074(3)	1.0
O2	12*k*	0.8312(1)	0.6623(2)	0.08220(5)	0.0053(2)	1.0

Space group $P6_3/mmc$, a = 5.75427(4) Å, c = 14.1675(1) Å

R_{wp} = 5.30 %, R_p = 4.12 %, χ^2= 4.884

The neutron diffraction patterns collected at all temperatures 3 < *T*/K < 300 were analysed satisfactorily using the model described above although the magnitudes of the two moments were no longer equal; that on the sites within the dimers was greater than that on the corner-sharing sites, see Figure 4.11. The values of the ordered magnetic moments, $\langle M_i \rangle$, shown in Figure 4.11 were derived with the assumption that all the cations take part in the long-range ordering. Our data do not allow us to distinguish between this model and one in which a fraction p_i of the cations on site i are ordered with a moment of $\langle M_i \rangle / p_i$. Figure 4.12 shows the fitted neutron diffraction pattern of our $Ba_3Fe_2TeO_9$ sample collected at 50 K using the wavelength 2.4395(5) Å, and other neutron diffraction patterns collected using this

wavelength over the temperature range $100 \leq T/K \leq 250$ are presented in the Appendix as Figure A4.1.

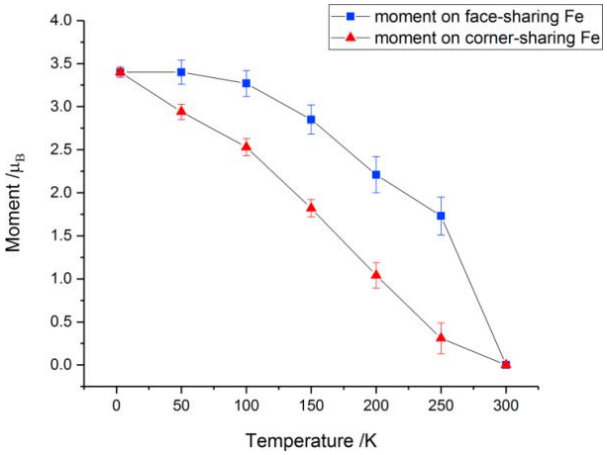

Figure 4.11 Temperature dependence of the ordered magnetic moment on the 2*a* and 4*f* sites in $Ba_3Fe_2TeO_9$.

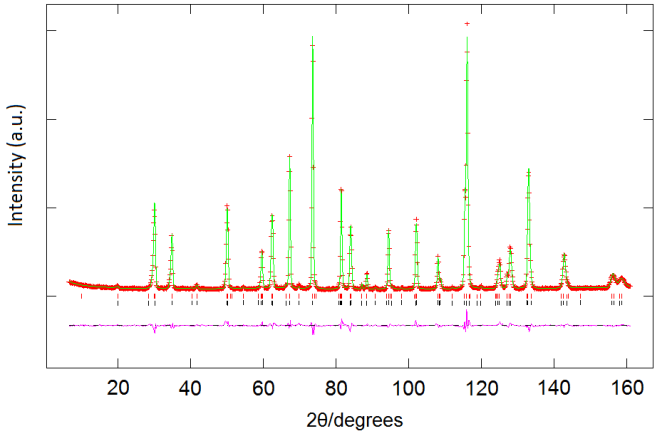

Figure 4.12 Observed (red), calculated (green) neutron diffraction patterns of $Ba_3Fe_2TeO_9$ at 50 K (λ = 2.4395 Å). A difference curve (purple) is shown and reflection positions are marked.

The XRPD patterns of the six reaction products $Sr_xBa_{3-x}Fe_2TeO_9$ (*x*=2.5, 2.25, 2, 1.5, 1.25, 1) shown in Figure 4.13 suggest that they exist in different perovskite-like crystal structures. $Sr_{2.5}Ba_{0.5}Fe_2TeO_9$ has a purely pseudo-cubic crystal structure but as the value of *x* decreases from 2.5 to 1, a hexagonal phase begins to form and grow in the material, which results in mixtures of a pseudo-cubic phase and a hexagonal phase for $Sr_{2.25}Ba_{0.75}Fe_2TeO_9$, $Sr_2BaFe_2TeO_9$, $Sr_{1.5}Ba_{1.5}Fe_2TeO_9$ and $Sr_{1.25}Ba_{1.75}Fe_2TeO_9$, until $SrBa_2Fe_2TeO_9$ finally becomes purely hexagonal. Shift of peak positions is observed, which indicates variation in cell parameters and hence variation in compositions. As it is impossible to identify the accurate compositions of different phases, reliable quantitative analysis cannot be applied to

the mixtures. An impurity peak at ~29° is observed for all the six products, which might arises from the minor presence of strontium-barium tellurate.

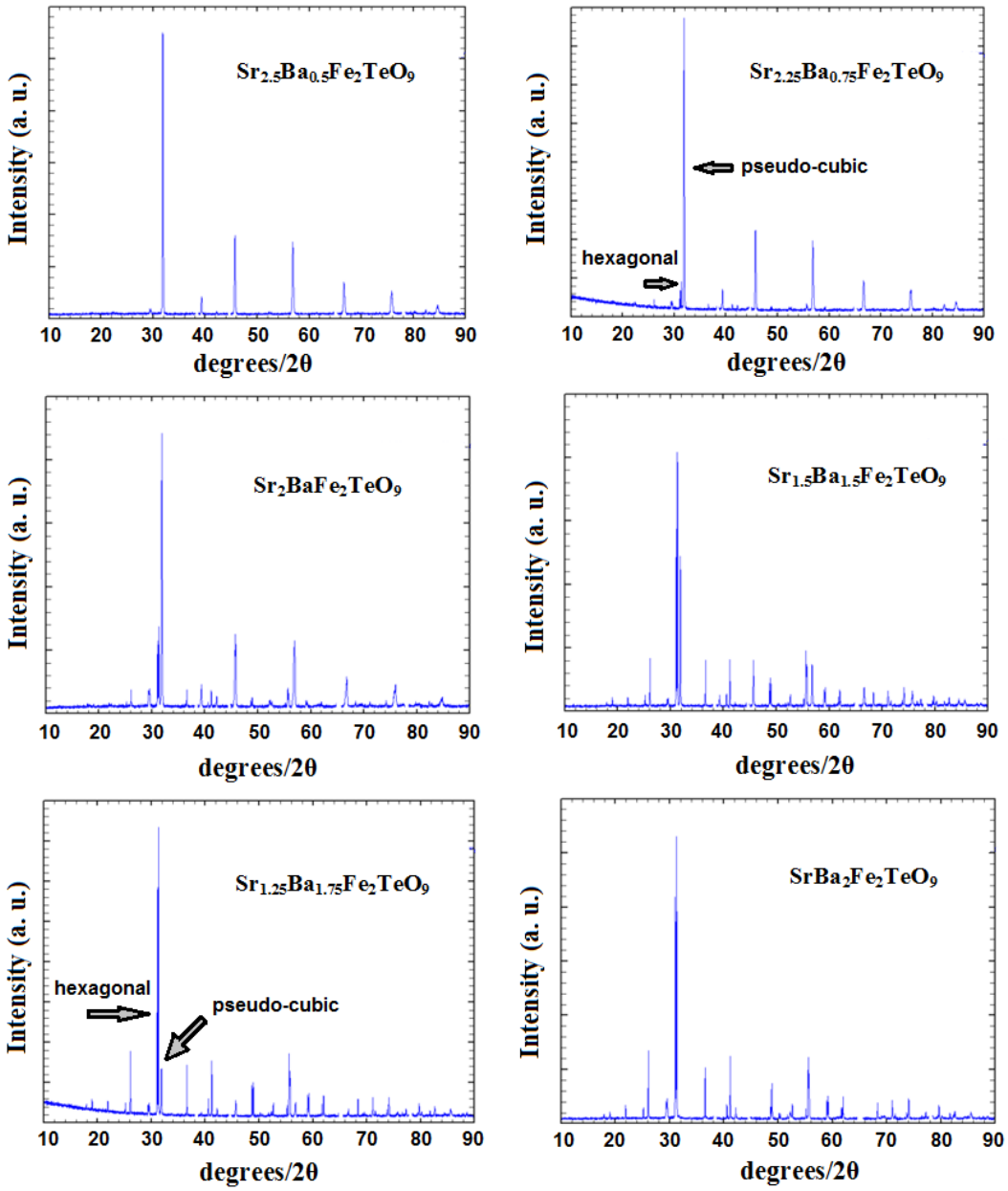

Figure 4.13 XRPD patterns of $Sr_xBa_{3-x}Fe_2TeO_9$ (x=2.5, 2.25, 2, 1.5, 1.25, 1). For $Sr_{2.25}Ba_{0.75}Fe_2TeO_9$ and $Sr_{1.25}Ba_{1.75}Fe_2TeO_9$ selected peaks from pseudo-cubic phase and hexagonal phase are marked with arrows, indicating the formation of solid solutions.

4.4 Discussion

The hexagonal crystal structure of our $Ba_3Fe_2TeO_9$ sample agrees with the structure proposed in the literature. However, the magnetic properties of our sample differ significantly from

those of the samples prepared by Augsburger *et al.* [6] and Djerdj *et al.*[10]. The former appears to undergo a single ferromagnetic transition at 711 K, an unusually high transition temperature for a 6*H* perovskite. The most noticeable difference between our synthesis of $Ba_3Fe_2TeO_9$ and that performed by Augsburger *et al.* is that we used TeO_2 as the source of tellurium, while they used telluric acid as a starting material. Furthermore, Augsburger *et al.* used an annealing temperature of only 950 °C, lower than our choice of 1200 °C; no perovskite-like phase formed during our initial 24 hour heating at 950 °C. The sol-gel protocol used recently by Djerdj *et al.* ended with an anneal at 1250 °C and also resulted in an XRD pattern characteristic of a 6*H* perovskite. However, the magnetic behaviour of their sample also differs from that of our own. They observed the transition at ~20 K reported above but the ZFC and FC susceptibilities they measured in 100 G are markedly different below ~80 K. They did not detect the transition at 711 K reported by Augsburger *et al.* but the susceptibility of their sample was nevertheless field-dependent at room temperature. It is clear that variations in the synthesis method can have significant consequences for the properties of the final product. In the following paragraphs we present what we believe is a self-consistent account of the behaviour of our sample.

We shall discuss the data collected at room temperature and below the temperature of the susceptibility maximum and then consider the more complex behaviour observed at intermediate temperatures. The shift from a pseudo-cubic perovskite in the case of $Sr_3Fe_2TeO_9$ to a 6*H* structure in the case of $Ba_3Fe_2TeO_9$ reflects the well-established dependence of the structure type on the radius ratio r_A/r_B. The fact that the series $Sr_xBa_{3-x}Fe_2TeO_9$ (x=2.5, 2.25, 2, 1.5, 1.25, 1) proceeds from a pseudo-cubic structure through a mixed phase region to a hexagonal structure is consistent with this. $Ba_3Fe_2WO_9$ is also a 6*H* perovskite [15], whereas $Ba_3Bi_2TeO_9$ [16] has the same trigonal structure as our $Sr_3Fe_2TeO_9$ sample and $Sr_3Fe_2WO_9$ is a tetragonal, pseudo-cubic perovskite [17]. Despite the discrepancies in the magnetic properties discussed above, the structural parameters derived from our room-temperature neutron diffraction study are, with the exception of the Fe:Te distribution over the 2*a* and 4*f* sites, in excellent agreement with those determined by Augsburger *et al*. Table 4.1 shows an Fe:Te ratio of 0.933 : 0.067 on the 2*a* site, significantly larger than that reported in the earlier work. The mean bond length around the 4*f* site, 1.994 Å, is shorter than that around the 2*a* site, consistent with a lower concentration of the larger Fe^{3+} cations on the former site. At room temperature there is no evidence of magnetic Bragg scattering in the neutron data.

All the bond lengths listed in Table 4.2 are shorter at 3 K than at 300 K, as is to be expected. There is, however, no significant structural change on cooling. The additional Bragg scattering present in the neutron diffraction data collected at 3 K identified the presence of long-range magnetic ordering, and the antiferromagnetic structure shown in Figure 4.9 is consistent with the observed intensity distribution. The magnitude of the mean ordered moment determined by neutron diffraction, 3.40 μ_B per cation, is lower than that determined in many antiferromagnetic compounds of Fe^{3+} [18-21], suggesting that not all the Fe^{3+} cations take part in the long-range magnetic ordering. The absence of a central resonance in the Mössbauer spectrum recorded at 13 K suggests that any decoupled spins freeze in a glassy state rather than remaining paramagnetic. The presence of only one sextet in this spectrum, albeit with some evidence of peak broadening, shows that the glassy spins experience essentially the same internal hyperfine field as those that are coupled to the magnetically-ordered backbone. The magnitude of the field is somewhat low for a compound of Fe^{3+}, but not anomalously so. This model is consistent with our magnetometry data, wherein the field dependence of $\chi(T)$ and the hysteresis observed below the temperature of the susceptibility maximum are both characteristic not of generic antiferromagnetic behaviour but rather of spin glasses. The cations that are decoupled from the magnetic ordering are likely to be those in octahedra that are linked to a disproportionately high fraction of TeO_6 octahedra, and thus are part of relatively few Fe – O – Fe superexchange pathways. The magnetic ordering shown in Figure 4.9 propagates through the three-dimensional structure without frustration despite the fact that 33 % of the octahedra are occupied by diamagnetic cations.

The NPD data and Mössbauer spectra collected between room temperature and 13 K reveal additional complexity in the electronic properties of $Ba_3Fe_2TeO_9$. The diffraction data reveal that the two crystallographic sites containing Fe^{3+} are both involved in long-range magnetic ordering in this temperature range. However, the magnetisations of the sublattices saturate at different rates. As explained above, the correlation between the fraction of ordered spins and their moment prevents an unambiguous determination of the ordered fraction from the neutron data. The Mössbauer spectrum observed at 200 K shows that at this temperature around 47(5) % of the Fe^{3+} spins are static on a timescale of 10^{-7} s while the remainder relax more rapidly. Any spin that is static on the Mössbauer timescale will be static on the shorter timescale associated with magnetic neutron diffraction. However, we cannot know whether they are involved in long-range magnetic ordering or whether they are in a glass-like state. Those in the former group are responsible for the magnetic Bragg scattering observed in the

NPD patterns. At 100 K all the spins are static on the Mössbauer timescale but a wide range of internal hyperfine fields appears to be present. Again it seems likely that some of these static spins are part of the magnetically-ordered network detected by neutron diffraction whereas the remainder are in regions showing only short-range magnetic order. We expect the latter to occur where there is a relative excess of Te^{6+}, for example in the vicinity of Te_2O_9 dimers, and the former in regions where –Fe – O – Fe –O – superexchange interactions can most readily percolate through the structure, for example in the vicinity of Fe_2O_9 dimers.

It is clear from these data that the onset of magnetic ordering in $Ba_3Fe_2TeO_9$ occurs at a temperature higher than that suggested by both our susceptibility data and those collected by Djerdj *et al.*; neither the susceptibility maximum at 18 K nor the change in gradient of $\chi^{-1}(T)$ at ~90 K correspond to the ordering temperature. It seems likely that the hysteresis observed below 90 K indicates the presence of blocked spin-clusters [22-24] and that the spins that do not participate in the long-range ordering form a spin-glass below 18 K. There are no features at higher temperatures in $\chi(T)$ that indicate an alternative transition temperature. We tentatively propose that it lies very close to 300 K. This is consistent with the interpretation of the Mössbauer spectrum acquired at room temperature in terms of a quadrupole doublet from each of the distinct octahedral sites and a developing sextet, rather than in terms of three doublets of uncertain parentage.

The above account of $Ba_3Fe_2TeO_9$ bears some similarity to that of $Ba_3Fe_2WO_9$ given previously [15], although there are also differences. The 2*a* sites in that 6*H* perovskite were found to be occupied only by Fe^{3+}; the cation disorder seen in $Ba_3Fe_2TeO_9$ is absent in the tungsten analogue. The available neutron diffraction patterns showed that $Ba_3Fe_2WO_9$ is paramagnetic at room temperature and antiferromagnetic at 200 K although the temperature gradient of the sample magnetisation was constant and negative for $100 < T/K < 400$, implying that not all the spins participate in the long-range ordering. Furthermore, the magnetic moments at the Fe1 and Fe2/W2 sites were found to be low and different, 3.24 and 3.93 μ_B respectively, throughout the temperature range $10 < T/K < 200$. The neutron data on $Ba_3Fe_2WO_9$ are consistent with an earlier Mössbauer study that reported a Néel temperature of 223 K [9], close to the temperature at which the hysteresis in the susceptibility of $Ba_3Fe_2TeO_9$ becomes clear.

In order to account for the field-dependence of $\chi(T)$ at temperatures close to 300 K we have assumed that our sample contains a magnetic impurity, the concentration of which is too low

to be detected by XRPD, NPD or Mössbauer spectroscopy. $BaFe_{12}O_{19}$ has a Curie temperature of 723 K and a saturation magnetisation of ~40 emu g^{-1} [25, 26]. An impurity level of 1 part in 10^4, undetectable using the above techniques, would therefore be enough to account for the room-temperature magnetisation of our sample. We note that the Curie temperature of the ferrite is close to the ferromagnetic transition temperature reported by Augsburger *et al.* for $Ba_3Fe_2TeO_9$.

4.5 Conclusions

$Ba_3Fe_2TeO_9$ is a 6*H* perovskite in which the cation sites in the face-sharing octahedra are occupied randomly by Fe^{3+} and Te^{6+} in a ratio that is close to, but different from, 1:1. The sites in the vertex-sharing octahedra are occupied predominantly by Fe^{3+} although some Te^{6+} is also present. At a temperature close to 300 K the atomic moments begin to order in an antiferromagnetic manner. A backbone of ordered spins forms within the structure and on further cooling more spins join the backbone. Spins in locally iron-rich regions order before those in regions where the superexchange pathways are prevented from percolating by a local excess of Te^{6+}. The spins that are unable to take part in the long-range magnetic order form clusters that freeze to form a spin glass at 18 K. In the series $Sr_xBa_{3-x}Fe_2TeO_9$ (x=2.5, 2.25, 2, 1.5, 1.25, 1), as x decreases the crystal structure switches from purely pseudo-cubic to purely hexagonal via a biphasic region, illustrating the effect of the radius ratio r_A/r_B on crystal structures of such double perovskites.

The work described in this chapter has been published as: Y. Tang, R. Paria Sena, M. Avdeev, P. D. Battle, J. M. Cadogan, J. Hadermann, E. C. Hunter, Journal of Solid State Chemistry 253 (2017) 347.

References

[1] E.J. Cussen, P.D. Battle, Chem. Mater. 12 (2000) 831.

[2] H. Krischner, K. Torkar, B.O. Kolbesen, Journal of Solid State Chemistry 3 (1971) 349.

[3] P.D. Battle, T.C. Gibb, A.J. Herod, S.-H. Kim, P.H. Munns, Journal of Materials Chemistry 5 (1995) 865.

[4] P.C. Donohue, L. Katz, R. Ward, Inorganic Chemistry 5 (1966) 335.

[5] S.A. Ivanov, P. Nordblad, S.G. Eriksson, R. Tellgren, H. Rundlof, Mater. Res. Bull. 42 (2007) 776.

[6] M.S. Augsburger, M.C. Viola, J.C. Pedregosa, R.E. Carbonio, J.A. Alonso, J. Mater. Chem. 16 (2006) 4235.

[7] Y.W. Tang, E.C. Hunter, P.D. Battle, R. Paria Sena, J. Hadermann, M. Avdeev, J.M. Cadogan, Journal of Solid State Chemistry 242 (2016) 86.

[8] D. Harari, J.C. Bernier, P. Poix, Journal of Solid State Chemistry 5 (1972) 382.

[9] V.V. Gagulin, N.V. Fadeeva, A.G. Belous, A.V. Titov, K.P. Mitrofanov, M.V. Plotnikova, S.P. Soloviev, Y.N. Venevtsev, Phys. Status Solidi A-Appl. Res. 48 (1978) 183.

[10] I. Djerdj, J. Popović, S. Mal, T. Weller, M. Nuskol, Z. Jagličić, Ž. Skoko, D. Pajić, C. Suchomski, P. Voepel, R. Marschall, B. Kozlevčar, B.M. Smarsly, Crystal Growth & Design (2016) 2535.

[11] A.C. Larson, R.B. von Dreele, General Structural Analysis System (GSAS), Los Alamos National Laboratories, 1990, 86.

[12] H.M. Rietveld, Journal of Applied Crystallography 2 (1969) 65.

[13] B. vanLaar, W.B. Yelon, J. Appl. Cryst. 17 (1984) 47.

[14] C. Koch, Determination of core structure periodicity and point defect density along dislocations (Ph. D. thesis), Arizona State University, 2002.

[15] S.A. Ivanov, S.G. Eriksson, J. Erikssen, R. Tellgren, H. Rundlof, Materials Research Bulletin 39 (2004) 615.

[16] J.H. Park, P.M. Woodward, International Journal of Inorganic Materials 2 (2000) 153.

[17] S.A. Ivanov, S.G. Eriksson, R. Tellgren, H. Rundlof, Materials Research Bulletin 36 (2001) 2585.

[18] P.D. Battle, G.R. Blake, T.C. Gibb, J.F. Vente, Journal of Solid State Chemistry 145 (1999) 541.

[19] G.J. Long, G. Longworth, P. Battle, A.K. Cheetham, R.V. Thundathil, D. Beveridge, Inorganic Chemistry 18 (1979) 624.

[20] P.D. Battle, T.C. Gibb, P. Lightfoot, J. Solid State Chem. 84 (1990) 237.

[21] W.C. Koehler, E.O. Wollan, Journal of Physics and Chemistry of Solids 2 (1957) 100.

[22] D. Fiorani, S. Viticoli, J.L. Dormann, J.L. Tholence, A.P. Murani, Phys. Rev. B 30 (1984) 2776.

[23] S.H. Kim, P.D. Battle, J. Magnetism Magnetic Mater. 123 (1993) 273.

[24] A. Labarta, R. Rodriguez, L. Balcells, J. Tejada, X. Obradors, F.J. Berry, Phys. Rev. B 44 (1991) 691.

[25] K. Haneda, H. Kojima, Journal of Applied Physics 44 (1973) 3760.

[26] J.J. Went, G.W. Rathenau, E.W. Gorter, G.W. Vanoosterhout, Physical Review 86 (1952) 424.

Chapter 5: Structural and Magnetic Properties of the Perovskites: $A_2LaFe_2SbO_9$ (A=Ba, Sr, Ca) and $CaLa_2Fe_2SnO_9$

5.1 Introduction

The study of the perovskites described in Chapter 3 and 4 was originally undertaken to investigate whether the relaxor behaviour shown by $La_3Ni_2SbO_9$[1, 2] could be reproduced when the magnetic cation was Fe^{3+} rather than Ni^{2+}. It is difficult in solid-state chemistry to change only one factor at a time. On this occasion, in order to maintain charge neutrality, it was necessary either to introduce cation disorder on the A site or to change the diamagnetic d^{10} cation on the six-coordinate sites. The latter approach was adopted in the research described in the two preceding chapters. In this chapter we report the properties of Fe^{3+}-based compositions in which A-site disorder is allowed. Most of the compositions described below contain Sb^{5+}, as did the original Ni^{2+}-based compound, and a 2:1 ratio of divalent and trivalent cations on the A site. The study has been extended to include a compound containing Sn^{4+} and, consequently, a 1:2 ratio of divalent and trivalent cations on the A site.

As a d^{10} cation in the *p*-block similar to Sb^{5+} and Te^{6+}, Sn^{4+} can also lead to cation ordering in perovskites. For instance, La_2CuSnO_6 has an unusual layered ordering pattern of the B sites, as described in Chapter 1[3]. In another study, La_2MgSnO_6 was reported to have extensive but incomplete 1:1 ordering of the Mg^{2+} and Sn^{4+} cations in three dimensions[4]. It seems that a charge difference of two on the B-cations is likely to induce complete or partial ordering. When the charge difference decreases to one, B-site ordering in such perovskites begins to vanish. For example, $SrLaFeSnO_6$ is reported to adopt a disordered orthorhombic crystal structure involving antiferromagnetism with some degree of spin frustration due to the formation of clusters[5]. The three perovskites in the series ALaMnSnO$_6$ (A=Ba, Sr, Ca) are all reported to have disordered B sites, although the strontium- and barium- containing compounds are ferromagnets while the calcium analogue shows spin-glass behaviour[6, 7]. In a continuation of our work on the perovskites containing both Fe^{3+} and d^{10} *p*-block-cations, we have now investigated the compositions $A_2LaFe_2SbO_9$ (A=Ca, Sr, Ba) and $CaLa_2Fe_2SnO_9$. In this chapter we report the structural and magnetic properties of these compounds as determined using a combination of magnetometry, X-ray diffraction and neutron diffraction.

5.2 Experimental methods

Polycrystalline samples of $A_2LaFe_2SbO_9$ (*A*=Ba, Sr, Ca) were prepared using the standard ceramic method. ACO_3 (*A*=Ba, Sr, Ca), La_2O_3, Fe_2O_3, and Sb_2O_5 (purity >99.95%) were weighed out in the appropriate stoichiometric ratio and ground together in an agate mortar for 30 minutes to give a homogeneous mixture. La_2O_3 was heated at 800 °C for 24 hours prior to use to ensure it was completely dry. The mixture was then loaded into an alumina crucible and fired at 800 °C for 24 h. It was then quenched to room temperature, reground and pressed into a pellet which was fired in air at 1150 °C for 48 hours and subsequently annealed at 1150 °C for another 48 hours after further grinding. Finally, the furnace was allowed to cool to 800 °C and then the sample was quenched to room temperature. A polycrystalline sample of $CaLa_2Fe_2SnO_9$ was prepared with the same method using starting materials $CaCO_3$, La_2O_3, Fe_2O_3, and SnO_2 (purity >99.95%) with a firing and subsequent annealing temperature of 1250 °C.

The dark brown compounds $A_2LaFe_2SbO_9$ (*A*=Ba, Sr, Ca) and dark green $CaLa_2Fe_2SnO_9$ were initially characterised by X-ray powder diffraction (XRPD) using Cu $K\alpha_1$ radiation. The data, collected at room temperature on a Panalytical X'Pert diffractometer, were analysed using the Rietveld method as implemented in the GSAS[8] program package. Neutron diffraction patterns were collected from some of the products on the constant-wavelength powder diffractometers D1b and D2b at ILL, Grenoble, France. Data were collected at temperatures of 300 and 5 K using wavelengths of 2.52 Å and 1.594 Å on D1b and D2b, respectively. The data from the former have a relatively high signal:noise ratio and are principally used in the study of magnetic ordering whereas D2b produces high-resolution data suitable for use in the refinement of crystal structures. Neutron diffraction data were subsequently collected for $CaLa_2Fe_2SnO_9$ on the diffractometer Echidna at the Bragg Institute, ANSTO, Australia by Dr. Maxim Avdeev. The angular region $10 < 2\theta/° < 147.5$ was scanned in steps of 0.05° at room temperature using neutron wavelength of 1.6215(5) Å, and at 3.5 K using neutron wavelengths of 1.6215(5) and 2.4395(5) Å. In all cases data analysis was performed using the Rietveld method[9]. The peak shape was modelled using the function devised by van Laar and Yelon[10] and the background was fitted using a twelve-term Chebyschev polynomial. Data were collected from the other reaction products at 5 K and 300 K on the GEM time-of-flight diffractometer at the ISIS spallation source. The data collected on detector banks at scattering angles, 2θ, of 34.96°, 63.62°, 91.30° and

154.40° were refined simultaneously. The molar magnetic susceptibilities of these compounds were measured over the temperature range 2 < *T*/K < 300 or 2 < *T*/K < 370 using a Quantum Design MPMS 5000 SQUID magnetometer. Data were collected on warming in a field of 100 Oe after cooling the samples both in the absence of an applied field (zero-field cooled, ZFC) and in the measuring field (field cooled, FC). The isothermal sample magnetisation of each sample was measured as a function of field over the range –50 < H/kOe < 50 at 300 and 5 K after cooling in a field of 50 kOe.

5.3 Results

The XRPD patterns of the reaction products $A_2LaFe_2SbO_9$ (*A*=Ba, Sr, Ca) suggested that the syntheses had produced phase-pure pseudo-cubic perovskites. However, the three compounds apparently deviate from the ideal primitive cubic symmetry in different ways. The XRPD pattern of $Ca_2LaFe_2SbO_9$ shown in Figure 5.1 was indexed using the monoclinic space group $P2_1/n$ with $a \sim\sqrt{2}a_p$, $b \sim\sim\sqrt{2}a_p$ and $c \sim 2a_p$, where a_p is the unit cell parameter of a primitive cubic perovskite. In this space group the structural model, see Figure 5.2, involves a 4*e* site that accommodates a disordered distribution of Ca and La, three further 4*e* sites that accommodate oxide anions and two independent B sites, *2d* (½, 0, 0) and *2c* (0, ½, 0) which accommodate the two cation species Fe^{3+} and Sb^{5+}. Refinements of the distribution of Fe and Sb over the crystallographically-distinct B sites suggested that the 2*d* sites are largely occupied by Fe and that the Sb and the remaining Fe atoms are randomly distributed over the 2*c* sites.

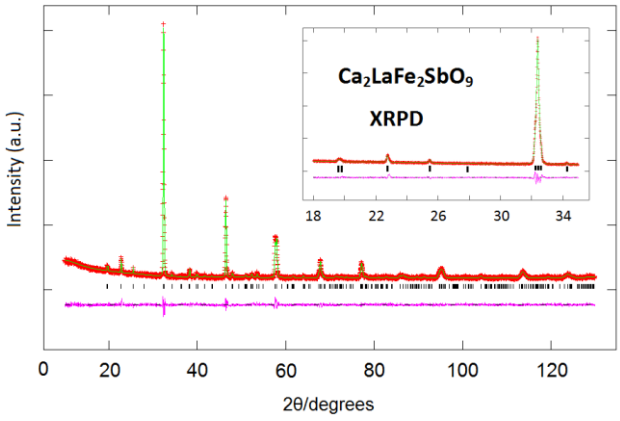

Figure 5.1 Observed (red), calculated (green) X-ray powder diffraction patterns of $Ca_2LaFe_2SbO_9$ at room temperature. A difference curve (purple) is shown and reflection positions are marked. The low angle region is magnified in the inset.

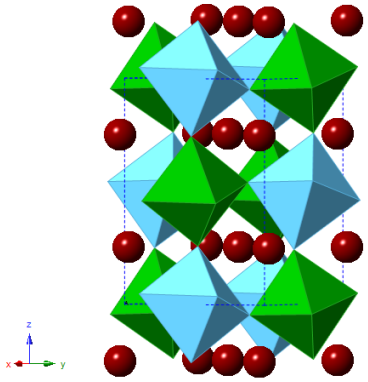

Figure 5.2 Crystal structure of $Ca_2LaFe_2SbO_9$. Green octahedra are largely occupied by Fe, and blue octahedra are occupied by approximately equal amounts of Fe and Sb. Red circles represent the Ca and La atoms at the A site.

The peak distribution in the XRPD pattern of $Sr_2LaFe_2SbO_9$ could only be accounted for in a unit cell with $a \sim\sqrt{2}a_p$, $b \sim\sim\sqrt{2}a_p$ and $c \sim 2a_p$ if the symmetry was reduced to triclinic and the absence of many reflections suggested that this cell was *I* centred. However the neutron diffraction data, which will be discussed below, showed this to be a false conclusion. The pattern of the barium analogue, $Ba_2LaFe_2SbO_9$, was initially thought to adopt the ideal perovskite structure in space group *Pm*-3*m*; every peak observed in the XRPD pattern is allowed in this space group and the intensities are consistent with a disordered arrangement of cations over the six-coordinate sites. However, as we shall show below, neutron diffraction again indicated that the true symmetry is lower than that deduced from the X-ray data.

The XRPD pattern of the reaction product $CaLa_2Fe_2SnO_9$ shown in Figure 5.3 suggested that the synthesis had produced a phase-pure, pseudo-cubic perovskite. The pattern can be indexed using the monoclinic space group $P2_1/n$, as shown in Figure 5.2, and refinements of the distribution of Fe and Sn over the crystallographically-distinct B sites suggested that the 2*d* sites and 2*c* sites have different concentrations of Fe and Sn, but the difference is small compared with $Ca_2LaFe_2SbO_9$. In $CaLa_2Fe_2SnO_9$, Fe atoms slightly preferred occupying the 2*d* sites while Sn atoms had a preference for the 2*c* sites, which resulted in a less well-developed 1:1 B-site ordering pattern with the cation distribution $CaLa_2(Fe_{1.09}Sn_{0.41})_{2d}(Fe_{0.91}Sn_{0.59})_{2c}O_9$.

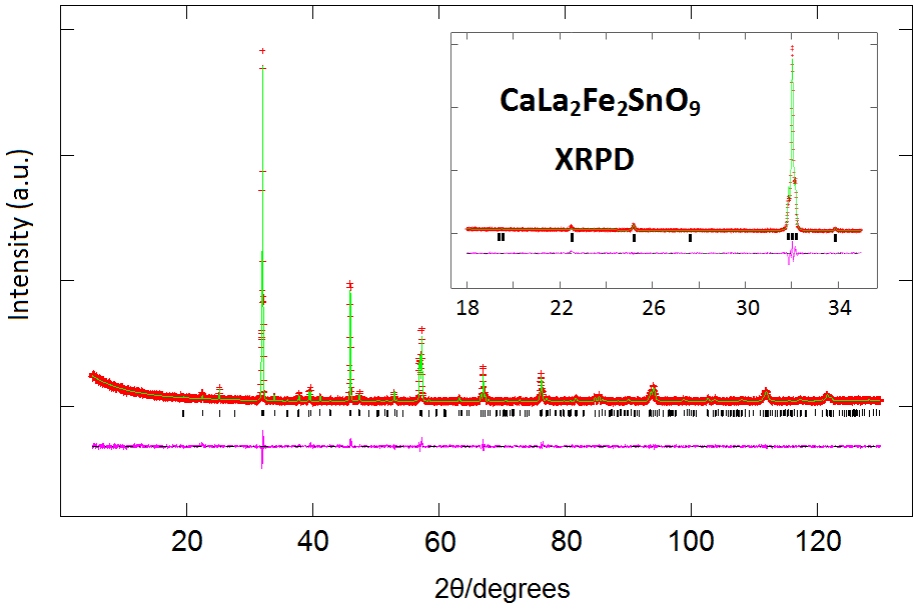

Figure 5.3 Observed (red), calculated (green) X-ray powder diffraction patterns of $CaLa_2Fe_2SnO_9$ at room temperature. A difference curve (purple) is shown and reflection positions are marked. The low angle region is magnified in the inset.

The temperature dependence of the dc molar magnetic susceptibilities of $A_2LaFe_2SbO_9$ (*A*=Ba, Sr, Ca) is shown in Figure 5.4, along with the field dependence of the magnetisation measured at 300 and 5 K. The susceptibility data collected on the three compositions are qualitatively similar and all three compounds show a maximum in the ZFC susceptibility at ~50 K. However, the ZFC and FC susceptibilities are not equal at 300 K, and this, together with the non-linearity of the *M*(*H*) curves collected at 300 K and the presence of a small remanent magnetisation shows that none of the three compounds is a simple paramagnet at this temperature. Differences are apparent in the three *M*(*H*) curves recorded at 5 K. Those collected for $Ca_2LaFe_2SbO_9$ and $Sr_2LaFe_2SbO_9$ are symmetric, with the strontium compound displaying a broader hysteresis loop and approaching a lower saturation value than the calcium analogue. In the case of the barium analogue, *M*(*H*) is asymmetric and the saturation value is the lowest of the three. The coercive field and remanent magnetisation per formula unit of each compound at 5 K are listed in Table 5.1; H_c increases and M_r decreases as the radius of the alkaline-earth cation increases.

Table 5.1 Coercive field, H_c, and remanent magnetisation per formula unit, M_r, of $A_2LaFe_2SbO_9$ (*A*=Ca, Sr, Ba) at 5 K.

Compound	H_c (kOe)	M_r (μ_B)
$Ca_2LaFe_2SbO_9$	0.60	0.18
$Sr_2LaFe_2SbO_9$	2.0	0.074
$Ba_2LaFe_2SbO_9$	3.0	0.058

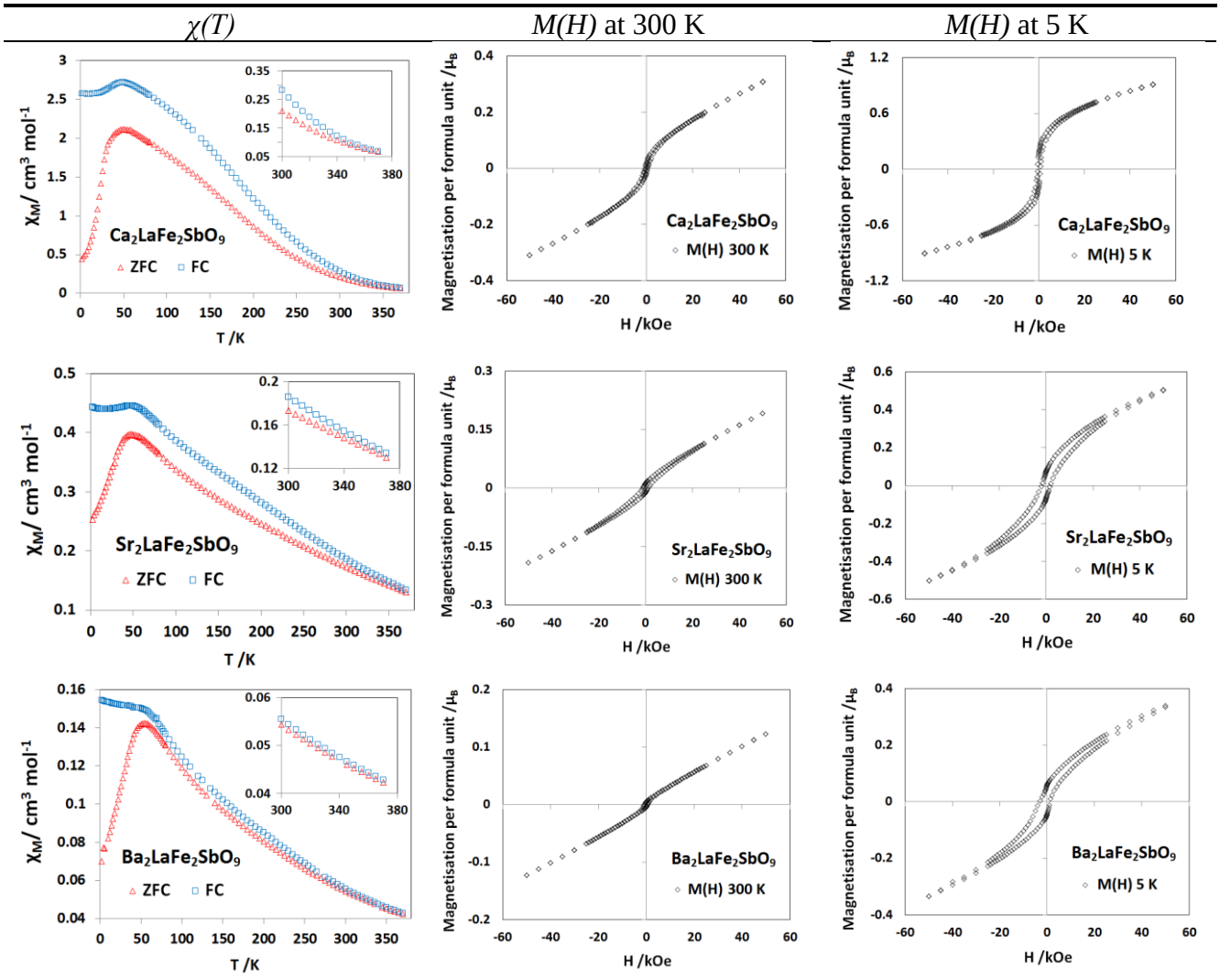

Figure 5.4 The temperature dependence of the dc molar magnetic susceptibilities and the field dependence of the magnetisation per formula unit of $A_2LaFe_2SbO_9$ at 300 K and 5 K (*A*=Ca, Sr, Ba).

The temperature dependence of the dc molar magnetic susceptibility of $CaLa_2Fe_2SnO_9$ is shown in Figure 5.5, along with the field dependence of the magnetisation measured at 300 and 5 K. The ZFC and FC susceptibilities are close to each other, but not equal at 300 K. Hysteresis loops are apparent in the *M*(*H*) curves collected at both 300 K and 5 K with the presence of an obvious remanent magnetisation, indicating that this compound is not paramagnetic at and below room temperature. The *M*(*H*) curves recorded at 300 K and 5 K are qualitatively similar, with the main change on cooling being the increase in saturated moment. The *M*(*H*) curves display broad hysteresis loops both at room temperature and 5 K, indicating "hard" magnetic character for this compound. The coercive field and remanent magnetisation per formula unit at 5 K are 9.1 kOe and 0.040 μ_B, respectively.

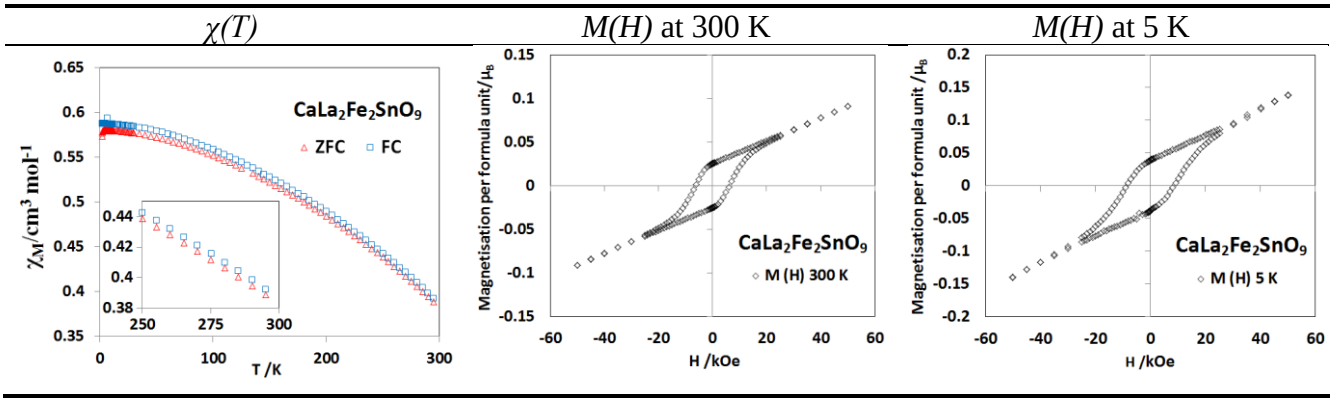

Figure 5.5 The temperature dependence of the dc molar magnetic susceptibilities and the field dependence of the magnetisation per formula unit of $CaLa_2Fe_2SnO_9$ at 300 K and 5 K.

The time-of-flight neutron diffraction patterns collected from $Ca_2LaFe_2SbO_9$ at 300 K were analysed using the structural model derived from the XRPD data as a starting point. The magnetic data described above suggest that magnetic Bragg scattering might be present in these patterns and many of the reflections that might be expected to have a magnetic contribution are also sensitive to the degree of cation ordering over the two distinct six-coordinate sites in space group $P2_1/n$. In order to decouple these effects a combined refinement based on both the neutron pattern and the XRPD pattern was performed. The

distribution of Fe and Sb across the 2*d* and 2*c* sites was allowed to vary, and the resulting cation distribution can be represented by the formula $Ca_2La(Fe_{1.25}Sb_{0.25})_{2d}(Fe_{0.75}Sb_{0.75})_{2c}O_9$. The neutron pattern did indeed contain additional intensity in the 101 and 011 reflections and in order to account for this intensity it was necessary to include a G-type magnetic structure, see Figure 5.6, in which the magnetic moment of Fe^{3+} on each B site is coupled in an antiparallel manner to those of the six nearest-neighbour sites. The refined structural parameters at 300 K are listed in Table 5.2. The fit to the patterns collected at the four detector banks can be seen in Figure 5.7. When we assumed that the Fe^{3+} cations on both sites have the same moment and that the moments on all the Fe^{3+} cations are ordered, then the moment per Fe^{3+} cation was refined to be 1.87(2) μ_B. Given that Sb^{5+} cation is diamagnetic and the occupancies of Fe on the 2*d* and 2*c* sites are 83.6(4) % and 49.7(4) % respectively, the mean moments per cation on the 2*d* and 2*c* sites were calculated to be 1.56(2) and 0.93(2) μ_B. Analysis of the neutron data thus leads to a description of $Ca_2LaFe_2SbO_9$ as a ferrimagnet at 300 K with a net moment of 0.95(4) μ_B per formula unit.

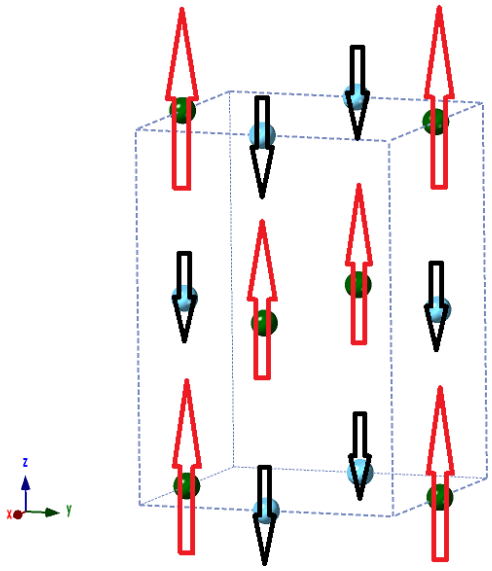

Figure 5.6 The G-type magnetic structure adopted by $Ca_2LaFe_2SbO_9$. Arrows indicate the direction of ordered spins at the B sites. Every magnetic ion in the cell is coupled in an antiferromagnetic manner to its six nearest neighbours.

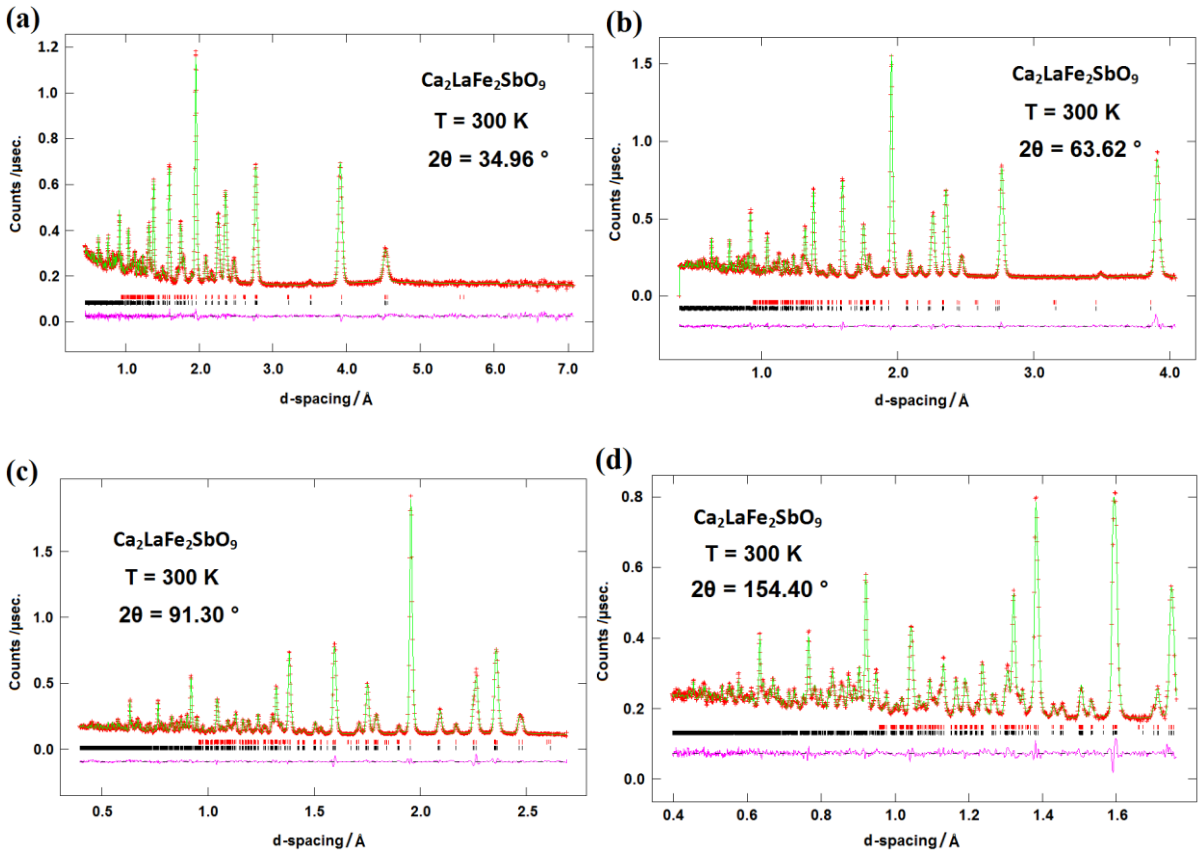

Figure 5.7 Observed (red), calculated (green) TOF neutron diffraction patterns of $Ca_2LaFe_2SbO_9$ at 300 K collected at four banks. A difference curve (purple) is shown and reflection positions are marked. Black bars represent structural reflections and red bars represent magnetic reflections.

Table 5.2 Structural parameters of $Ca_2LaFe_2SbO_9$ at 300 K.

Atom	Site	*x*	*y*	*z*	U_{iso}	fractional occupancy
Ca	4*e*	0.4897(3)	0.5330(1)	0.2507(4)	0.0122(2)	0.6667
La	4*e*	0.4897(3)	0.5330(1)	0.2507(4)	0.0122(2)	0.3333
Fe1	2*d*	0.5	0	0	0.0056(6)	0.836(4)
Fe2	2*c*	0	0.5	0	0.0028(6)	0.497(4)
Sb1	2*d*	0.5	0	0	0.0056(6)	0.164(4)
Sb2	2*c*	0	0.5	0	0.0028(6)	0.503(4)
O1	4*e*	0.2897(7)	0.2894(8)	0.0352(3)	0.0066(6)	1.0
O2	4*e*	0.2092(7)	0.7899(8)	0.0471(3)	0.0102(8)	1.0
O3	4*e*	0.5778(2)	0.9804(2)	0.2496(9)	0.0091(3)	1.0

Space group $P2_1/n$, a = 5.4967(1) Å, b = 5.5466(1), c = 7.8079(2) Å, β = 89.944(5)°

R_{wp} = 3.72 %, χ^2= 1.636

Analysis of the neutron patterns collected from $Ca_2LaFe_2SbO_9$ at 5 K was carried out using the structural model described above with the cation distribution over the B sites fixed to be the same as that determined from the room temperature data. The observed magnetic scattering was consistent with the G-type structure described above, with the principal change on cooling being an increase in the intensity of the magnetic scattering at higher d-spacings. The structural parameters derived from analysis of the data collected at 5 K are listed in Table 5.3, with the bond lengths and angles at both 300 K and 5 K in Table 5.4. The fits to the data collected on the four detector banks are shown in Figure 5.8. With the same assumptions as at 300 K, the mean ordered moment on the 2*d* site at 5 K increased to a value of 2.55(2) μ_B per cation and that on the 2*c* site to 1.52(2) μ_B, leading to a calculated net magnetisation of 1.55(4) μ_B per formula unit at the lower temperature.

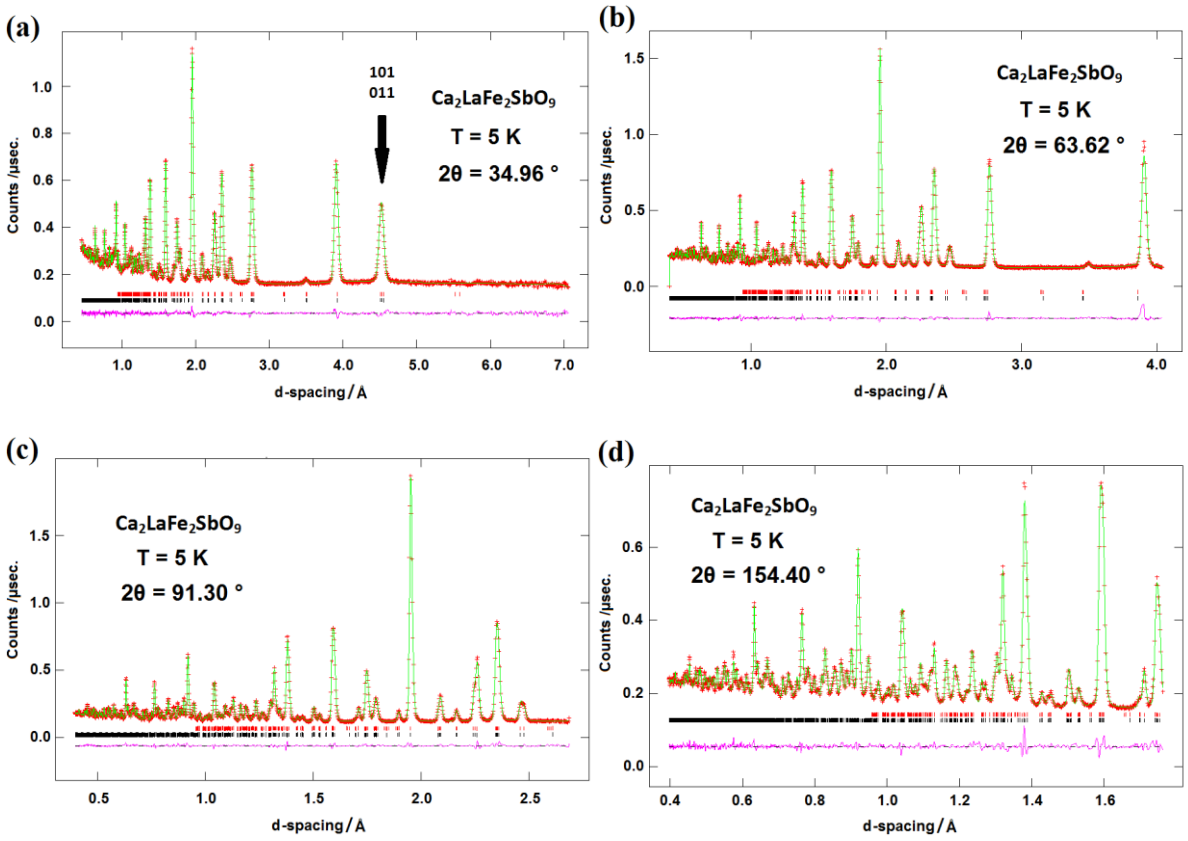

Figure 5.8 Observed (red), calculated (green) time-of-flight neutron diffraction patterns of $Ca_2LaFe_2SbO_9$ at 5 K collected at four banks. A difference curve (purple) is shown and reflection positions are marked. Black bars represent structural reflections and red bars represent magnetic reflections. An arrow indicates the peak with the strongest magnetic contribution.

Table 5.3 Structural parameters of $Ca_2LaFe_2SbO_9$ at 5 K.

Atom	Site	*x*	*y*	*z*	U_{iso}	fractional occupancy
Ca	4*e*	0.4908(3)	0.5371(1)	0.2512(8)	0.0080(2)	0.6667
La	4*e*	0.4908(3)	0.5371(1)	0.2512(8)	0.0080(2)	0.3333
Fe1	2*d*	0.5	0	0	0.0036(7)	0.836
Fe2	2*c*	0	0.5	0	0.0025(7)	0.497
Sb1	2*d*	0.5	0	0	0.0036(7)	0.164
Sb2	2*c*	0	0.5	0	0.0025(7)	0.503
O1	4*e*	0.2885(6)	0.2912(8)	0.0387(3)	0.0050(5)	1.0
O2	4*e*	0.2069(6)	0.7887(8)	0.0441(4)	0.0072(6)	1.0
O3	4*e*	0.5805(2)	0.9790(2)	0.2492(5)	0.0065(2)	1.0

Space group $P2_1/n$, a = 5.4902(4) Å, b = 5.5449(4), c = 7.7959(6) Å, β = 89.839(3)°

R_{wp} = 2.26 %, χ^2= 2.483

Table 5.4 Selected bond lengths (Å) and bond angles (degrees) in $Ca_2LaFe_2SbO_9$ at 300 and 5 K.

	300 K	5 K		300 K	5 K
Ca/La – O_1	2.423(3)	2.418(5)	O_1 – Fe_1/Sb_1 – O_2	88.9(2)	88.9(2)
Ca/La – O_1	2.678(4)	2.647(5)	O_1 – Fe_1/Sb_1 – O_3	88.05(9)	88.26(8)
Ca/La – O_1	2.724(4)	2.732(6)	O_2 – Fe_1/Sb_1 – O_3	87.8(1)	88.8(1)
Ca/La – O_2	2.634(4)	2.645(5)	O_1 – Fe_2/Sb_2 – O_2	89.2(2)	89.3(2)
Ca/La – O_2	2.346(3)	2.369(5)	O_1 – Fe_2/Sb_2 – O_3	89.8(1)	89.5(1)
Ca/La – O_2	2.789(4)	2.751(6)	O_2 – Fe_2/Sb_2 – O_3	89.2(1)	89.84(9)
Ca/La – O_3	2.528(1)	2.450(1)	Fe_1/Sb_1 – O_1 – Fe_2/Sb_2	156.1(2)	154.9(2)
Ca/La – O_3	2.395(2)	2.375(2)	Fe_1/Sb_1 – O_2 – Fe_2/Sb_2	152.2(2)	153.0(2)
Fe_1/Sb_1 – O_1	1.997(5) * 2	2.011(4) * 2	Fe_1/Sb_1 – O_3 – Fe_2/Sb_2	154.51(7)	153.59(7)
Fe_1/Sb_1 – O_2	2.012(4) * 2	2.019(4) * 2			
Fe_1/Sb_1– O_3	1.998(7) * 2	1.997(4) * 2			
Fe_2/Sb_2 – O_1	1.994(4) * 2	1.986(4) * 2			
Fe_2/Sb_2 – O_2	2.011(5) * 2	1.993(4) * 2			
Fe_2/Sb_2 – O_3	2.004(7) * 2	2.007(4) * 2			

Time-of-flight neutron diffraction patterns collected from $Sr_2LaFe_2SbO_9$ at 300 K were analysed using the same strategy. The triclinic space group *I* -1, which could account for the XRPD pattern, could not account for the NPD pattern because the weak peaks observed at d-spacings of ~2.1 Å and ~2.5 Å, see Figures 5.9(a), are forbidden for a body-centred structure. Hence the primitive triclinic space group *P* -1 was chosen to analyse the diffraction patterns and a combined refinement using NPD and XRPD data was carried out. In contrast to the monoclinic model described above, this triclinic model consists of four distinct B sites: 1*d* (½, 0, 0), 1*g* (0, ½, ½), 1*c* (0, ½, 0) and 1*f* (½, 0, ½). In order to stabilize the refinements, the cation occupancies at the 1*d* and 1*g* sites were fixed to be the same; as were those at the 1*c* and 1*f* sites. This assumption imposes a body-centred arrangement on the six-coordinate cations which is consistent with the absence of $h + k + l = 2n + 1$ reflections in the XRPD pattern. The refined cation distribution across the four B sites can then be written as $Sr_2La(Fe_{0.41}Sb_{0.34})_{1d}(Fe_{0.41}Sb_{0.34})_{1g}(Fe_{0.59}Sb_{0.16})_{1c}(Fe_{0.59}Sb_{0.16})_{1d}O_9$, which suggests partial B-site ordering. The additional intensity observed at higher d-spacings in the neutron pattern at 300 K could again be accounted for by a G-type magnetic model shown in Figure 5.6. Good agreement between the calculated and observed patterns was also achieved with the *P* -1 model when the XRPD data were re-analysed. The fits to the neutron and X-ray diffraction patterns are shown in Figure 5.9 and 5.10, respectively. The primitive triclinic crystal structure proposed for $Sr_2LaFe_2SbO_9$ is shown in Figure 5.11. The neutron data collected at 5 K showed an increase in the intensity of the magnetic scattering but could be fitted using the same triclinic structural model. The structural parameters at 300 K are listed in Table 5.5 and those at 5 K in Table 5.6. The most significant bond lengths and bond angles are presented in Table 5.7. The fits to the data collected at 5 K on the four detector banks are shown in Figure 5.12.

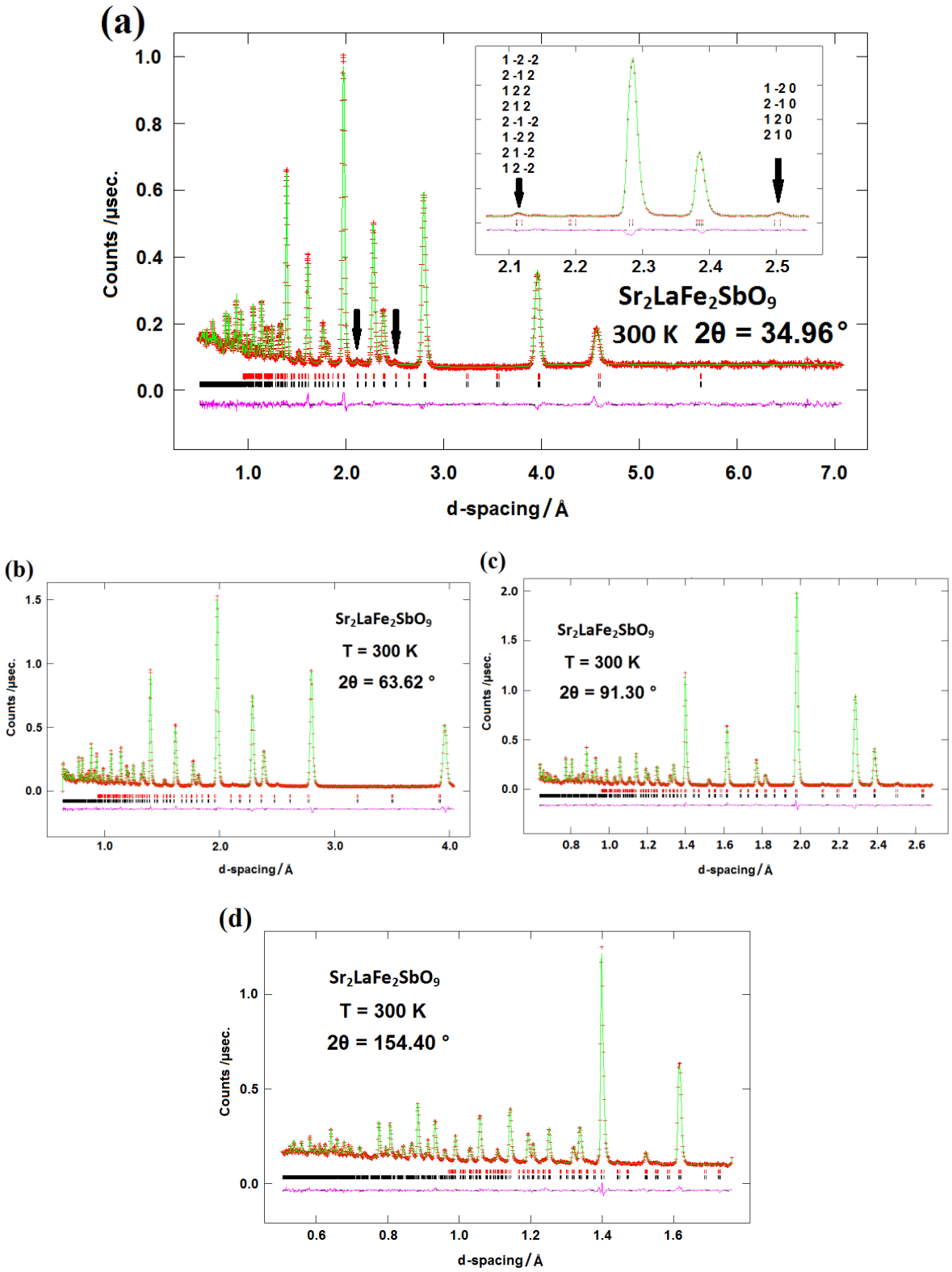

Figure 5.9 Observed (red), calculated (green) time-of-flight neutron diffraction patterns of $Sr_2LaFe_2SbO_9$ at 300 K collected at four banks. A difference curve (purple) is shown and reflection positions are marked. Black bars represent structural reflections and red bars represent magnetic reflections. Arrows indicate peaks that are forbidden in an *I*-centred cell.

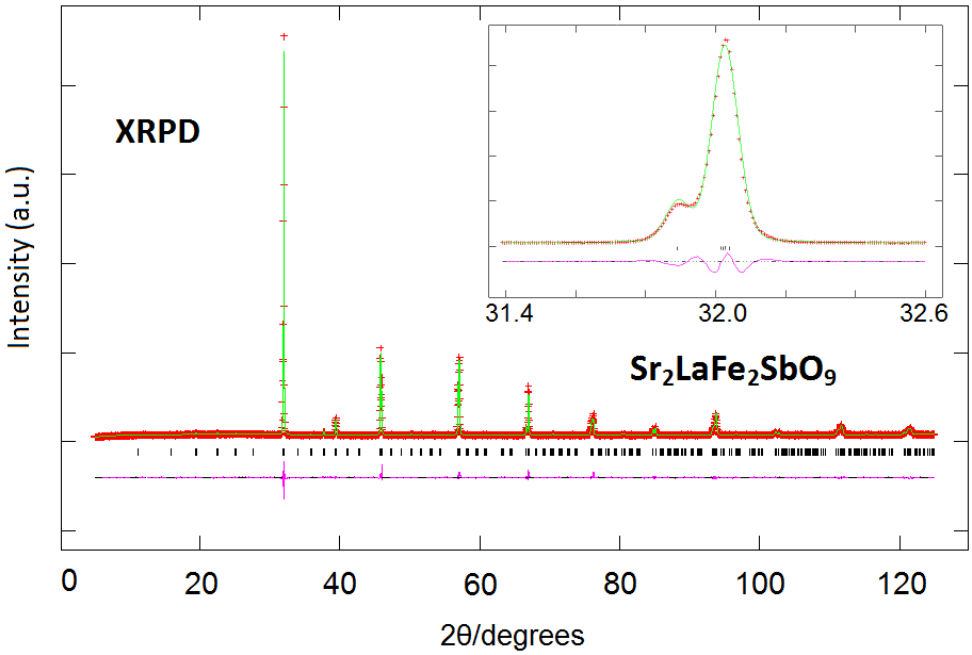

Figure 5.10 Observed (red), calculated (green) X-ray powder diffraction patterns of $Sr_2LaFe_2SbO_9$ at room temperature. A difference curve (purple) is shown and reflection positions are marked. The inset shows the splitting of the strongest peak.

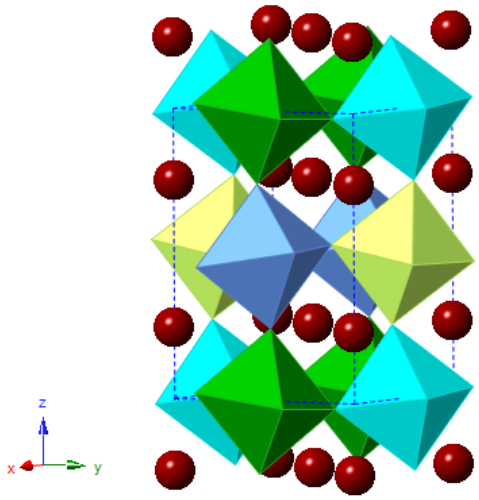

Figure 5.11 *P* -1 structure adopted by $Sr_2LaFe_2SbO_9$. Four distinct B sites are represented by octahedra in four different colours in the cell. Red circles represent the Sr and La atoms at the A site.

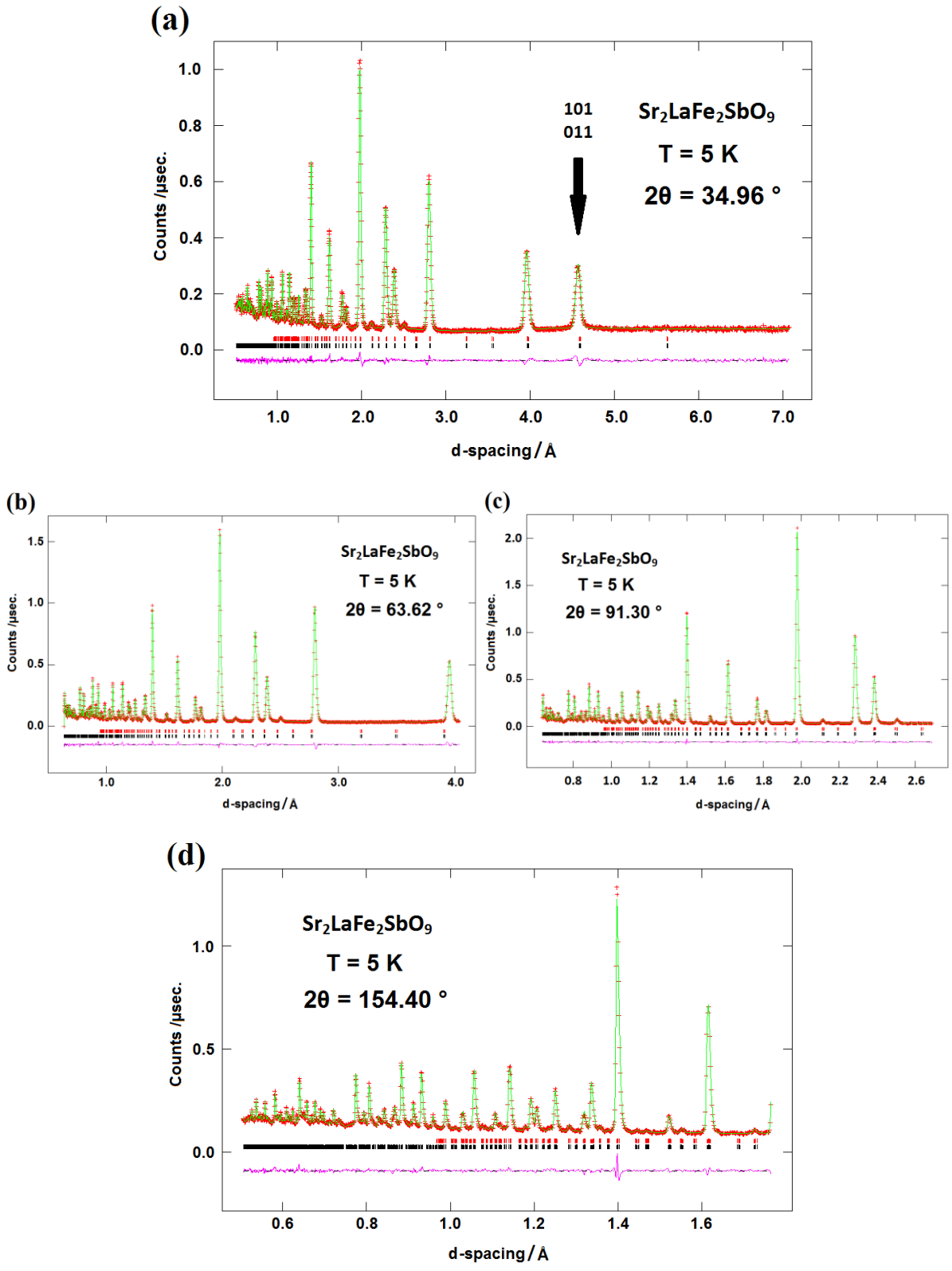

Figure 5.12 Observed (red), calculated (green) time-of-flight neutron diffraction patterns of $Sr_2LaFe_2SbO_9$ at 5 K collected at four banks. A difference curve (purple) is shown and reflection positions are marked. Black bars represent structural reflections and red bars represent magnetic reflections. An arrow indicates the peak with the strongest magnetic contribution.

Table 5.5 Structural parameters of $Sr_2LaFe_2SbO_9$ at 300 K.

Atom	Site	*x*	*y*	*z*	U_{iso}	fractional occupancy
Sr1	2*i*	0.006(1)	0.003(1)	0.2489(7)	0.009(1)	0.6667
Sr2	2*i*	0.503(1)	0.503(1)	0.2481(7)	0.009(1)	0.6667
La1	2*i*	0.006(1)	0.003(1)	0.2489(7)	0.009(1)	0.3333
La2	2*i*	0.503(1)	0.503(1)	0.2481(7)	0.009(1)	0.3333
Fe1	1*c*	0	0.5	0	0.00156(9)	0.788(4)
Fe2	1*f*	0.5	0	0.5	0.00156(9)	0.788(4)
Fe3	1*d*	0.5	0	0	0.00156(9)	0.545(4)
Fe4	1*g*	0	0.5	0.5	0.00156(9)	0.545(4)
Sb1	1*c*	0	0.5	0	0.00156(9)	0.212(4)
Sb2	1*f*	0.5	0	0.5	0.00156(9)	0.212(4)
Sb3	1*d*	0.5	0	0	0.00156(9)	0.455(4)
Sb4	1*g*	0	0.5	0.5	0.00156(9)	0.455(4)
O1	2*i*	0.248(1)	0.250(1)	0.0349(7)	0.0065(1)	1.0
O2	2*i*	0.261(2)	0.741(1)	0.9859(8)	0.0065(1)	1.0
O3	2*i*	0.281(2)	0.279(2)	0.4677(7)	0.0065(1)	1.0
O4	2*i*	0.216(1)	0.786(1)	0.5256(8)	0.0065(1)	1.0
O5	2*i*	0.517(2)	0.948(1)	0.250(1)	0.0065(1)	1.0
O6	2*i*	0.980(2)	0.526(1)	0.250(1)	0.0065(1)	1.0

Space group *P* -1, a = 5.5880(4) Å, b = 5.5879(4), c = 7.91055(8) Å, α = 90.188(8)°, β = 90.189(8)°, γ = 89.792(1)°

R_{wp} = 4.24 %, χ^2= 2.161

Table 5.6 Structural parameters of $Sr_2LaFe_2SbO_9$ at 5 K.

Atom	Site	*x*	*y*	*z*	U_{iso}	fractional occupancy
Sr1	2*i*	0.014(2)	0.005(1)	0.2493(9)	0.0032(9)	0.6667
Sr2	2*i*	0.511(2)	0.494(1)	0.252(1)	0.0070(9)	0.6667
La1	2*i*	0.014(2)	0.005(1)	0.2493(9)	0.0032(9)	0.3333
La2	2*i*	0.511(2)	0.494(1)	0.252(1)	0.0070(9)	0.3333
Fe1	1*c*	0	0.5	0	0.0006(1)	0.788
Fe2	1*f*	0.5	0	0.5	0.0006(1)	0.788
Fe3	1*d*	0.5	0	0	0.0006(1)	0.545
Fe4	1*g*	0	0.5	0.5	0.0006(1)	0.545
Sb1	1*c*	0	0.5	0	0.0006(1)	0.212
Sb2	1*f*	0.5	0	0.5	0.0006(1)	0.212
Sb3	1*d*	0.5	0	0	0.0006(1)	0.455
Sb4	1*g*	0	0.5	0.5	0.0006(1)	0.455
O1	2*i*	0.265(1)	0.268(1)	0.0277(8)	0.0034(1)	1.0
O2	2*i*	0.257(1)	0.751(1)	0.9804(9)	0.0034(1)	1.0
O3	2*i*	0.279(2)	0.280(1)	0.4662(8)	0.0034(1)	1.0
O4	2*i*	0.219(1)	0.785(1)	0.522(1)	0.0034(1)	1.0
O5	2*i*	0.506(1)	0.950(1)	0.250(1)	0.0034(1)	1.0
O6	2*i*	0.9822(9)	0.5631(9)	0.250(1)	0.0034(1)	1.0

Space group *P* -1, a = 5.582(2) Å, b = 5.591(2), c = 7.902(2) Å, α = 90.184(3)°, β = 90.147(3)°, γ = 89.813(2)°

R_{wp} = 3.70 %, χ^2= 2.902

Table 5.7 Selected bond lengths (Å) and bond angles (degrees) in $Sr_2LaFe_2SbO_9$ at 300 and 5 K.

	300 K	5 K		300 K	5 K
$Sr_1/La_1 – O_1$	2.574(5)	2.688(5)	$O_1 – Fe_1/Sb_1 – O_2$	88.5(3)	86.2(3)
$Sr_1/La_1 – O_1$	3.004(9)	3.085(9)	$O_1 – Fe_1/Sb_1 – O_6$	87.2(3)	87.5(3)
$Sr_1/La_1 – O_2$	2.914(6)	2.890(7)	$O_2 – Fe_1/Sb_1 – O_6$	87.1(3)	89.6(2)
$Sr_1/La_1 – O_2$	2.776(9)	2.73(1)	$O_3 – Fe_2/Sb_2 – O_4$	89.5(3)	90.0(3)
$Sr_1/La_1 – O_3$	2.77(1)	2.73(1)	$O_3 – Fe_2/Sb_2 – O_5$	89.1(3)	89.2(3)
$Sr_1/La_1 – O_3$	3.185(5)	3.214(6)	$O_4 – Fe_2/Sb_2 – O_5$	86.8(4)	89.1(3)
$Sr_1/La_1 – O_4$	2.761(9)	2.73(1)	$O_1 – Fe_3/Sb_3 – O_2$	87.6(3)	85.0(3)
$Sr_1/La_1 – O_4$	2.467(6)	2.518(8)	$O_1 – Fe_3/Sb_3 – O_5$	89.9(3)	89.5(3)
$Sr_1/La_1 – O_5$	2.75(1)	2.857(9)	$O_2 – Fe_3/Sb_3 – O_5$	88.6(3)	89.1(3)
$Sr_1/La_1 – O_5$	2.872(9)	2.76(1)	$O_3 – Fe_4/Sb_4 – O_4$	88.1(3)	88.7(3)
$Sr_1/La_1 – O_6$	2.672(6)	2.475(8)	$O_3 – Fe_4/Sb_4 – O_6$	87.7(3)	89.2(3)
$Sr_1/La_1 – O_6$	2.923(7)	3.127(8)	$O_4 – Fe_4/Sb_4 – O_6$	86.0(3)	88.3(3)
$Sr_2/La_2 – O_1$	2.619(9)	2.57(1)	$Fe_1/Sb_1 – O_1 – Fe_3/Sb_3$	164.1(3)	165.3(4)
$Sr_2/La_2 – O_1$	2.989(5)	2.872(6)	$Fe_1/Sb_1 – O_2 – Fe_3/Sb_3$	172.1(3)	170.9(4)
$Sr_2/La_2 – O_2$	2.81(1)	2.94(1)	$Fe_2/Sb_2 – O_3 – Fe_4/Sb_4$	160.0(2)	159.6(3)
$Sr_2/La_2 – O_2$	2.647(6)	2.626(7)	$Fe_2/Sb_2 – O_4 – Fe_4/Sb_4$	160.2(3)	162.1(3)
$Sr_2/La_2 – O_3$	2.482(5)	2.454(7)	$Fe_2/Sb_2 – O_5 – Fe_3/Sb_3$	162.3(3)	163.7(3)
$Sr_2/La_2 – O_3$	2.83(1)	2.81(1)	$Fe_1/Sb_1 – O_6 – Fe_4/Sb_4$	169.5(4)	159.0(3)
$Sr_2/La_2 – O_4$	3.145(6)	3.136(8)			
$Sr_2/La_2 – O_4$	2.88(1)	2.81(1)			
$Sr_2/La_2 – O_5$	3.102(6)	3.045(8)			
$Sr_2/La_2 – O_5$	2.489(6)	2.546(8)			
$Sr_2/La_2 – O_6$	2.92(1)	2.98(1)			
$Sr_2/La_2 – O_6$	2.67(1)	2.66(1)			
$Fe_1/Sb_1 – O_1$	1.99(1) * 2	1.977(9) * 2			
$Fe_1/Sb_1 – O_2$	1.991(9) * 2	2.017(7) * 2			
$Fe_1/Sb_1 – O_6$	1.986(9) * 2	2.008(8) * 2			
$Fe_2/Sb_2 – O_3$	2.00(1) * 2	2.01(1) * 2			
$Fe_2/Sb_2 – O_4$	2.002(9) * 2	1.985(9) * 2			
$Fe_2/Sb_2 – O_5$	1.999(9) * 2	1.998(9) * 2			
$Fe_3/Sb_3 – O_1$	2.00(1) * 2	1.999(9) * 2			
$Fe_3/Sb_3 – O_2$	1.977(9) * 2	1.952(8) * 2			
$Fe_3/Sb_3 – O_5$	2.004(9) * 2	1.994(8) * 2			
$Fe_4/Sb_4 – O_3$	2.01(1) * 2	2.00(1) * 2			
$Fe_4/Sb_4 – O_4$	2.016(9) * 2	2.021(9) * 2			
$Fe_4/Sb_4 – O_6$	1.986(9) * 2	2.011(8) * 2			

Constant-wavelength neutron diffraction patterns of $Ba_2LaFe_2SbO_9$ were collected on both D2b and D1b. It was clear from a preliminary inspection of the data that the primitive cubic space group assigned on the basis of the XRPD pattern was incorrect and preliminary analyses of the neutron data suggested orthorhombic *Pbnm*, with $a \sim\sqrt{2}a_p$, $b \sim\sim\sqrt{2}a_p$ and $c \sim 2a_p$, as a possible alternative; attempts to fit the data using an *I*-centred cell of the same volume gave higher agreement factors. The X-ray data were therefore reanalysed in *Pbnm* in order to determine accurate values for the unit cell parameters. The resulting values were then held constant during the final analysis of the neutron data collected on D2b at 300 K, thus allowing the wavelength of the neutron beam to be refined. The structural parameters determined in this way were then used to model the nuclear scattering present in the data collected at 300 K using D1b. Only the ordered magnetic moment in a G-type structure and the instrumental parameters were varied during the analysis of these data. This procedure was then repeated in order to analyse the data collected at 5 K, although in this case the refined neutron wavelength was held constant and the unit cell parameters were refined. In this orthorhombic structural model all the six-coordinate cations occupy just one crystallographic site and hence the type of cation ordering described above cannot occur in this compound, see Figure 5.13. The observed and calculated neutron and X-ray diffraction patterns for $Ba_2LaFe_2SbO_9$ at 300 K are shown in Figure 5.14 and the fits to the neutron patterns at 5 K are shown in Figure 5.15. The structural parameters at 300 K are listed in Table 5.8 and those at 5 K in Table 5.9. Selected bond lengths and bond angles at both temperatures are listed in Table 5.10. The refined magnetic parameters of all the compositions in the series are presented in Table 5.11.

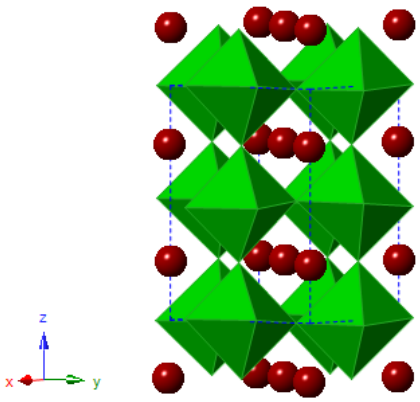

Figure 5.13 Crystal structure of $Ba_2LaFe_2SbO_9$. Disordered B sites are represented by octahedra of the same colour. Red circles represent the Ba and La atoms at the A site.

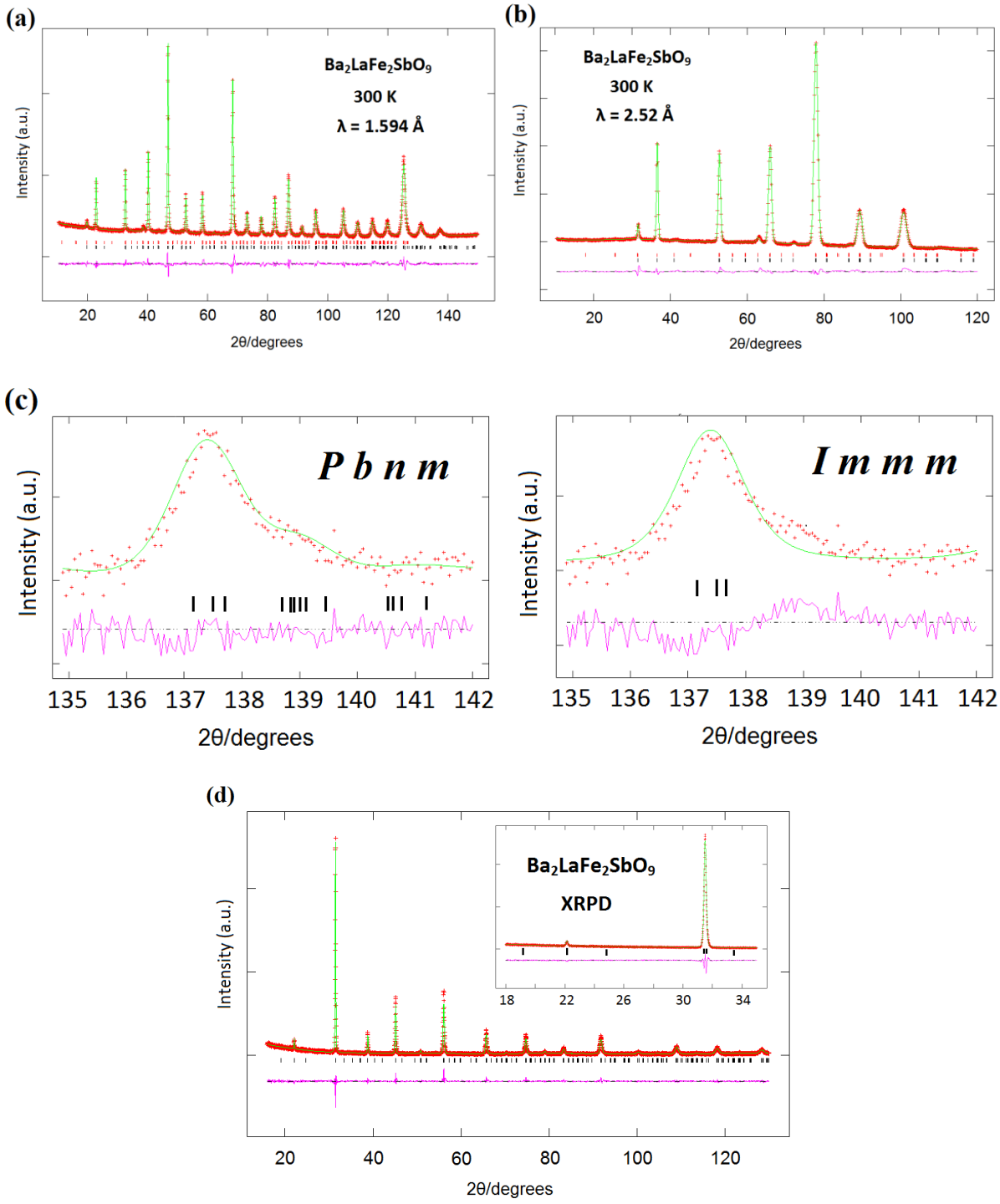

Figure 5.14 Observed (red), calculated (green) neutron diffraction patterns of $Ba_2LaFe_2SbO_9$ at 300 K collected using wavelength of (a) 1.594 Å and (b) 2.52 Å. A difference curve (purple) is shown and reflection positions are marked. Black bars represent structural reflections and red bars represent magnetic reflections. (c) Both the fits to the asymmetric peaks using *Pbnm* and *Immm* structure models in the 2θ region from 135 to 142 degrees. (d) Observed (red), calculated (green) X-ray powder diffraction patterns of $Ba_2LaFe_2SbO_9$ at room temperature. A difference curve (purple) is shown and reflection positions are marked. Inset shows the peaks at lower angles.

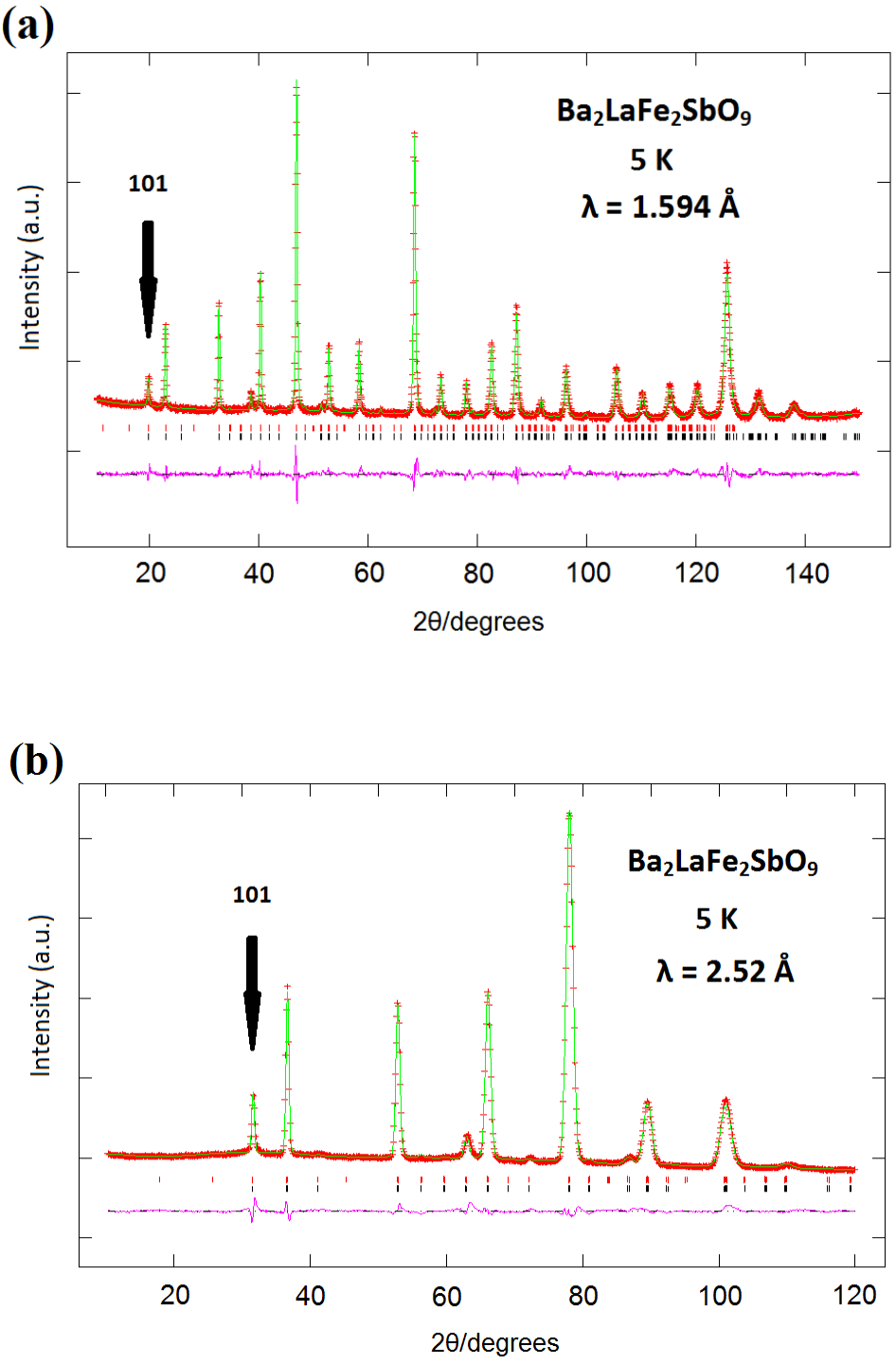

Figure 5.15 Observed (red), calculated (green) neutron diffraction patterns of $Ba_2LaFe_2SbO_9$ at 5 K collected using wavelength of (a) 1.594 Å and (b) 2.52 Å. A difference curve (purple) is shown and reflection positions are marked. Black bars represent structural reflections and red bars represent magnetic reflections. An arrow indicates the peak with the strongest magnetic contribution.

Table 5.8 Structural parameters of $Ba_2LaFe_2SbO_9$ at 300 K.

Atom	Site	*x*	*y*	*z*	U_{iso}	fractional occupancy
Ba	4*c*	0.9985(9)	0.0058(1)	0.25	0.0080(3)	0.6667
La	4*c*	0.9985(9)	0.0058(1)	0.25	0.0080(3)	0.3333
Fe	4*a*	0	0.5	0	0.0034(3)	0.6667
Sb	4*a*	0	0.5	0	0.0034(3)	0.3333
O1	4*c*	0.018(1)	0.526(1)	0.25	0.0090(4)	1.0
O2	8*d*	0.743(2)	0.255(2)	0.989(5)	0.0090(4)	1.0

Space group *Pbnm*, *a* = 5.6672(5) Å, *b* = 5.6801(3), *c* = 8.0382(5) Å

R_{wp} = 3.81 %, χ^2= 5.022

Table 5.9 Structural parameters of $Ba_2LaFe_2SbO_9$ at 5 K.

Atom	Site	*x*	*y*	*z*	U_{iso}	fractional occupancy
Ba	4*c*	0.998(3)	0.0055(9)	0.25	0.0040(3)	0.6667
La	4*c*	0.998(3)	0.0055(9)	0.25	0.0040(3)	0.3333
Fe	4*a*	0	0.5	0	0.0010(3)	0.6667
Sb	4*a*	0	0.5	0	0.0010(3)	0.3333
O1	4*c*	0.023(1)	0.525(1)	0.25	0.0056(4)	1.0
O2	8*d*	0.743(2)	0.256(2)	0.000(2)	0.0056(4)	1.0

Space group *Pbnm*, *a* = 5.6560(7) Å, *b* = 5.6704(4), *c* = 8.0241(7) Å

R_{wp} = 4.44 %, χ^2= 4.492

Table 5.10 Selected bond lengths (Å) and bond angles (degrees) in $Ba_2LaFe_2SbO_9$ at 300 and 5 K.

	300 K	5 K
Ba/La – O_1	2.73(1)	2.73(1)
Ba/La – O_1	2.95(1)	2.95(1)
Ba/La – O_1	2.93(3)	2.95(2)
Ba/La – O_1	2.74(3)	2.71(2)
Ba/La – O_2	2.85(1) * 2	2.849(9) * 2
Ba/La – O_2	2.82(1) * 2	2.810(9) * 2
Ba/La – O_2	2.79(1) * 2	2.789(9) * 2
Ba/La – O_2	2.90(1) * 2	2.891(9) * 2
Fe/Sb – O_1	2.0174(7) * 2	2.0152(7) * 2
Fe/Sb – O_2	2.01(1) * 2	2.01(1) * 2
Fe/Sb – O_2	2.00(1) * 2	2.00(1) * 2
O_1 – Fe/Sb – O_2	89.0(6)	89.5(5)
O_1 – Fe/Sb – O_2	85.0(6)	84.6(5)
O_2 – Fe/Sb – O_2	89.86(2)	89.85(2)
Fe/Sb – O_1 – Fe/Sb	169.9(4)	169.1(4)
Fe/Sb – O_2 – Fe/Sb	177.2(4)	177.2(4)

Table 5.11 Refined magnetic moment per cation and calculated net magnetisation per formula unit at 300 and 5 K in $A_2LaFe_2SbO_9$ (*A*=Ca, Sr, Ba), and at 300 and 3.5 K in $CaLa_2Fe_2SnO_9$.

Compound	Site / moment (μ_B)				Net magnetisation (μ_B)	
	300 K		3.5/5 K		300 K	3.5/5 K
$CaLa_2Fe_2SnO_9$	2*d*/2.38(7)	2*c*/1.93(7)	2*d*/3.08(2)	2*c*/2.50(2)	0.7(1)	0.87(4)
$Ca_2LaFe_2SbO_9$	2*d*/1.56(2)	2*c*/0.93(2)	2*d*/2.55(2)	2*c*/1.52(2)	0.95(4)	1.55(4)
$Sr_2LaFe_2SbO_9$	1*c*,1*f*/1.46(2)	1*d*,1*g*/1.01(2)	1*c*,1*f*/2.19(2)	1*d*,1*g*/1.51(2)	0.68(4)	1.02(4)
$Ba_2LaFe_2SbO_9$	4*a*/1.07(3)		4*a*/1.69(2)		0	0

Constant-wavelength neutron diffraction patterns collected from $CaLa_2Fe_2SnO_9$ on Echidna at 300 K were analysed using the structural model derived from the XRPD data as a starting point. As in the above cases, a combined refinement based on both the neutron pattern and the XRPD pattern was performed. The distribution of Fe and Sn across the 2*d* and 2*c* sites was allowed to vary, and the resulting cation distribution can be represented by the formula $CaLa_2(Fe_{1.10}Sn_{0.60})_{2d}(Fe_{0.90}Sn_{0.40})_{2c}O_9$. It was clear that the neutron pattern contained significant additional intensity in the 101 and 011 reflections and in order to account for this intensity a G-type magnetic structure was included in the refinement. The fitted neutron profiles at 300 K are shown in Figure 5.16, and the refined structural parameters at 300 K are listed in Table 5.12. When we assumed that the Fe^{3+} cations on both sites have the same moment and that the moments on all the Fe^{3+} cations are ordered, then the moment per Fe^{3+} cation was refined to be 3.21(3) μ_B. Given that the concentrations of magnetic ions over the two B sites are different, analysis of the neutron data thus leads to a description of $CaLa_2Fe_2SnO_9$ as a ferrimagnet at 300 K with a net moment of 0.7(1) μ_B per formula unit, see Table 5.11.

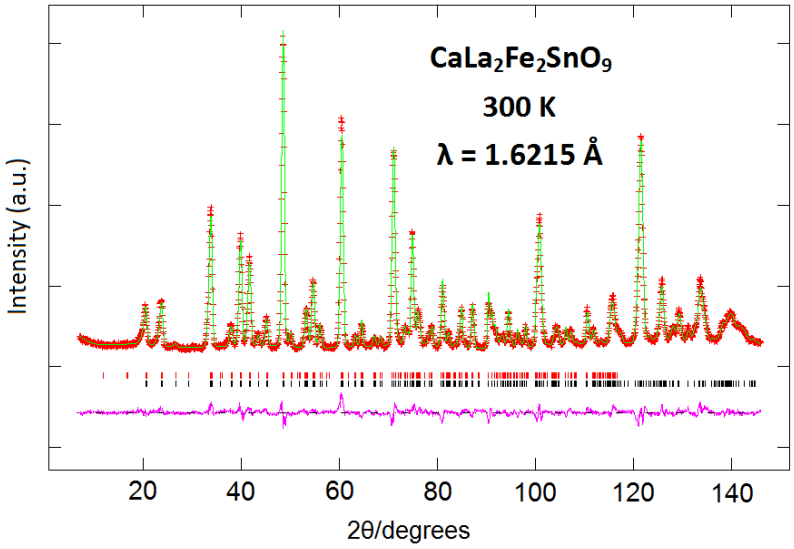

Figure 5.16 Observed (red), calculated (green) neutron diffraction patterns of $CaLaFe_2SnO_9$ at 300 K collected using wavelength of 1.6215 Å. A difference curve (purple) is shown and reflection positions are marked. Black bars represent structural reflections and red bars represent magnetic reflections.

Table 5.12 Structural parameters of $CaLa_2Fe_2SnO_9$ at 300 K.

Atom	Site	*x*	*y*	*z*	U_{iso}	fractional occupancy
Ca	4*e*	0.4943(4)	0.5352(2)	0.2471(8)	0.0105(2)	0.3333
La	4*e*	0.4943(4)	0.5352(2)	0.2471(8)	0.0105(2)	0.6667
Fe1	2*d*	0.5	0	0	0.0022(2)	0.74(2)
Fe2	2*c*	0	0.5	0	0.0022(2)	0.60(2)
Sn1	2*d*	0.5	0	0	0.0022(2)	0.26(2)
Sn2	2*c*	0	0.5	0	0.0022(2)	0.40(2)
O1	4*e*	0.282(1)	0.285(1)	0.0448(9)	0.0084(2)	1.0
O2	4*e*	0.206(1)	0.793(1)	0.0399(9)	0.0084(2)	1.0
O3	4*e*	0.5770(4)	0.9796(3)	0.250(3)	0.0084(2)	1.0

Space group $P2_1/n$, a = 5.56019(8) Å, b = 5.60803(8), c = 7.8916(1) Å, β = 90.00(1)°

R_{wp} = 5.98 %, χ^2= 1.725

The neutron patterns collected from $CaLa_2Fe_2SnO_9$ at 3.5 K with both wavelengths 1.6215 and 2.4395 Å were analysed simultaneously. They can be indexed using the same $P2_1/n$ model with the cation distribution being held constant as in the room-temperature data, and the moment on the magnetic ions was allowed to vary. The principal change on cooling was an increase in the intensity of the magnetic scattering at higher d-spacings. The atomic

displacement parameters (*U*iso) for the B-cations were fixed to be zero. The moment of Fe^{3+} cations at the 2*d* and 2*c* sites was then refined to 4.16(2) μ_B per Fe^{3+} cation, which leads to a net moment of 0.87(4) μ_B per formula unit, as shown in Table 5.12. The observed and calculated neutron patterns for $CaLa_2Fe_2SnO_9$ at 3.5 K are shown in Figure 5.17, and the refined structural parameters at 3.5 K are listed in Table 5.13. Selected bond lengths and bond angles at 300 K and 3.5 K are listed in Table 5.14.

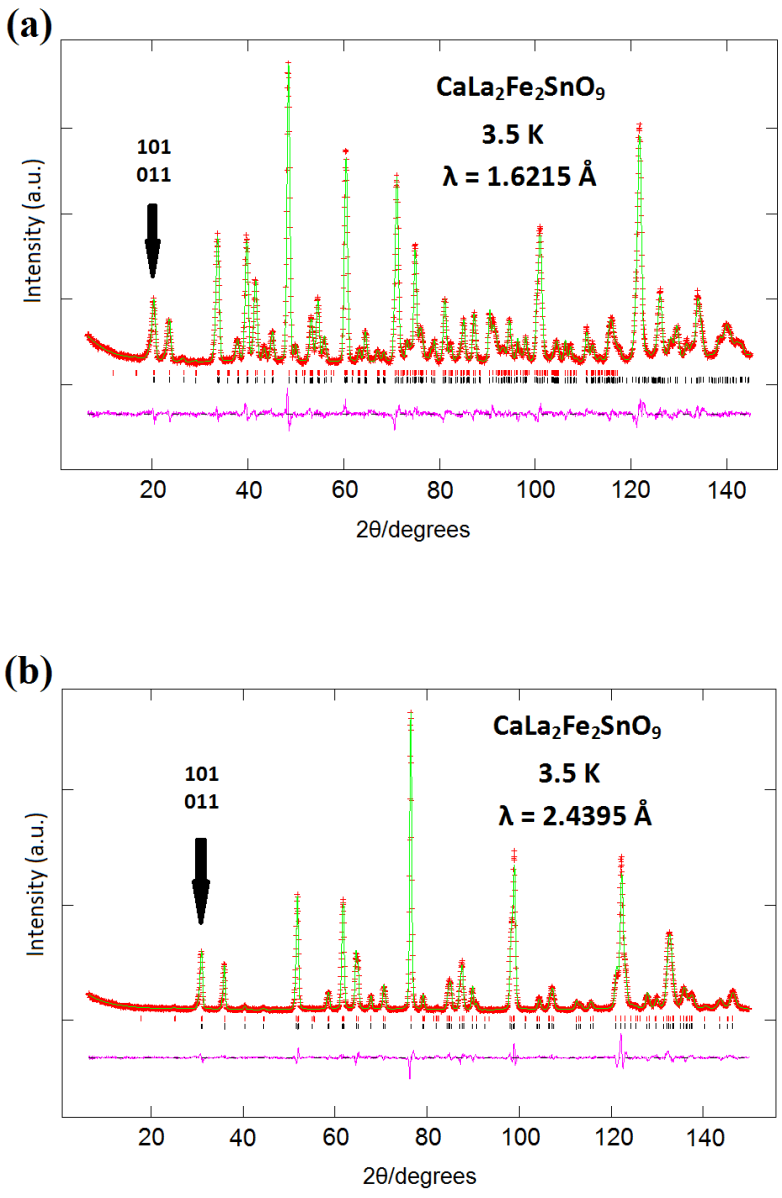

Figure 5.17 Observed (red), calculated (green) neutron diffraction patterns of $CaLaFe_2SnO_9$ at 3.5 K collected using wavelength of (a) 1.6215 Å and (b) 2.4395 Å. A difference curve (purple) is shown and reflection positions are marked. Black bars represent structural reflections and red bars represent magnetic reflections. An arrow indicates the peak with the strongest magnetic contribution.

Table 5.13 Structural parameters of $CaLa_2Fe_2SnO_9$ at 3.5 K.

Atom	Site	*x*	*y*	*z*	U_{iso}	fractional occupancy
Ca	4*e*	0.4930(5)	0.5375(2)	0.245(1)	0.0051(4)	0.3333
La	4*e*	0.4930(5)	0.5375(2)	0.245(1)	0.0051(4)	0.6667
Fe1	2*d*	0.5	0	0	0	0.74
Fe2	2*c*	0	0.5	0	0	0.60
Sn1	2*d*	0.5	0	0	0	0.26
Sn2	2*c*	0	0.5	0	0	0.40
O1	4*e*	0.289(2)	0.282(1)	0.045(1)	0.0041(3)	1.0
O2	4*e*	0.211(2)	0.797(1)	0.041(1)	0.0041(3)	1.0
O3	4*e*	0.5786(5)	0.9779(3)	0.253(2)	0.0041(3)	1.0

Space group $P2_1/n$, a = 5.5521(1) Å, b = 5.6048(1), c = 7.8790(2) Å, β = 90.00(2)°

R_{wp} = 5.84 %, χ^2= 3.140

Table 5.14 Selected bond lengths (Å) and bond angles (degrees) in $CaLa_2Fe_2SnO_9$ at 300 and 3.5 K.

	300 K	3.5 K		300 K	3.5 K
Ca/La – O_1	2.432(9)	2.41(1)	O_1 – Fe_1/Sn_1 – O_2	86.7(3)	87.1(5)
Ca/La – O_1	2.649(8)	2.66(1)	O_1 – Fe_1/Sn_1 – O_3	89.9(3)	90.0(3)
Ca/La – O_1	2.806(9)	2.78(1)	O_2 – Fe_1/Sn_1 – O_3	89.2(2)	88.9(2)
Ca/La – O_2	2.706(7)	2.68(1)	O_1 – Fe_2/Sn_2 – O_2	89.0(3)	89.4(5)
Ca/La – O_2	2.432(9)	2.44(1)	O_1 – Fe_2/Sn_2 – O_3	87.7(2)	88.0(2)
Ca/La – O_2	2.768(9)	2.78(1)	O_2 – Fe_2/Sn_2 – O_3	89.2(2)	88.7(3)
Ca/La – O_3	2.534(2)	2.515(2)	Fe_1/Sn_1 – O_1 – Fe_2/Sn_2	154.8(4)	154.3(5)
Ca/La – O_3	2.405(3)	2.402(4)	Fe_1/Sn_1 – O_2 – Fe_2/Sn_2	153.5(4)	153.2(5)
Fe_1/Sn_1 – O_1	2.037(7) * 2	2.002(8) * 2	Fe_1/Sn_1 – O_3 – Fe_2/Sn_2	154.7(1)	154.1(1)
Fe_1/Sn_1 – O_2	2.027(7) * 2	1.99(1) * 2			
Fe_1/Sn_1– O_3	2.02(2) * 2	2.04(2) * 2			
Fe_2/Sn_2 – O_1	2.009(7) * 2	2.04(1) * 2			
Fe_2/Sn_2 – O_2	2.029(8) * 2	2.062(8) * 2			
Fe_2/Sn_2 – O_3	2.03(2) * 2	2.00(2) * 2			

5.4 Discussion

Our diffraction data demonstrate that our three samples: $A_2LaFe_2SbO_9$ (*A*=Ba, Sr, Ca) have different crystal structures. The calcium compound has a monoclinic unit cell with 1:1 B-site ordering, and this crystal structure is also observed in double perovskites that our group has studied previously, such as $SrLa_2Ni_2TeO_9$[11] and $CaLa_2Ni_2WO_9$[12]. As expected, on cooling the volume of the cell decreases, however the average Fe-O bond length at the 2*d* site slightly increases, leading to a more significant difference in size between the octahetra on the two B sites. At 5 K the 2*d* octahedra are bigger than the 2*c* octahedra, which can be explained by the cation distribution, as the 2*d* site is largely occupied by Fe^{3+} cations rather than Sb^{5+} cations. This difference is less obvious at 300 K. We note that the mean Ca/La-O bond length at 300 K in $Ca_2LaFe_2SbO_9$ is 2.565 Å, which is close to, but smaller than the mean Ca/La-O bond length of 2.579 Å observed in $CaLa_2Ni_2WO_9$ and 2.582 Å in the $P2_1/n$ double perovskite $LaCaMnNbO_6$[13].

The primitive triclinic space group *P* -1 has been assigned to $Sr_2LaFe_2SbO_9$ on the basis of the neutron diffraction data. This relatively low symmetry is not very common in perovskites, with only a few examples, such as $BiNiO_3$[14] and Sr_2ZnWO_6[15], having been reported. Although there are two distinct A sites, no A-cation ordering is observed, as A-site ordering is rare in stoichiometric perovskites[16]. There is partial B-site ordering in the structure, however the difference in cation distribution among the B sites is even less than that seen in the calcium analogue, and the octahedra on different sites have approximately the same average Fe-O bond length both at room temperature and 5 K. Some Sr/La-O bond lengths increase on cooling, indicating a slight change in the coordination around the A sites. The mean Sr/La-O bond length of 2.802 Å in this compound is larger than the mean Sr/La-O bond length of 2.704 Å in triclinic body-centred $Sr_2LaCr_2SbO_9$ at 300 K[17], although the error on the former value is considerable, see Table 5.7. While the triclinic distortion of the unit cell can be seen in the X-ray diffraction, it is neutron diffraction that shows the structure to be primitive. These facts suggest that, despite the displacement of oxygen atoms, the B-cations arrange themselves in a body-centred cell, and this is an occasion when, X-ray diffraction is not able to identify the true crystal structure.

Unlike the calcium and strontium analogues, $Ba_2LaFe_2SbO_9$ has a disordered distribution of cations over the B-site in a primitive orthorhombic unit cell, and there is no noticeable

structural change on cooling. This compound has the longest mean *A*/La-O bond length of 2.839 Å at room temperature among the three analogues, as expected. The difference in size and charge between Fe^{3+} and Sb^{5+} is not sufficiently large to ensure an ordered structure. These two cations have been found to take a disordered distribution in other perovskites. For example, the formation of disordered Ca_2FeSbO_6 in space group *Pbnm* has been reported[18]. Many barium-containing perovskites for example, $BaPrO_3$[19] and Ba_2PrIrO_6[20], have *Pbnm* symmetry, if the *A* and *B* cation size mismatch is not large enough to lead to a hexagonal crystal structure as it is in the case of $Ba_3Fe_2TeO_9$, see Chapter 4. As the radius of the alkaline earth atom decreases in the series $A_2LaFe_2SbO_9$ (*A*=Ca, Sr, Ba), the symmetry is lowered, and the degree of B-site ordering increases. According to the Goldschmidt tolerance factor that describes the cation size mismatch in perovskites[21],

$$t = \frac{r_A + r_O}{\sqrt{2}(r_B + r_O)},$$

the ideal cubic structure is only achieved when t =1. In $Ca_2LaFe_2SbO_9$ and $Sr_2LaFe_2SbO_9$, as the A-cations are relatively small, and the structures compensate for the size mismatch by distorting to relieve the strain. However, the distortion patterns in the calcium and strontium analogues are different. In the calcium compound, the tilting of BO_6 octahedra leads to the reduction of the coordination number of the A-cations from twelve to eight, see Table 5.4. However in the strontium compound, although a triclinic distortion of the unit cell occurs, the tilting of BO_6 octahedra is not so significant as in the calcium analogue, as is shown by the higher coordination number of A-cations, see Table 5.7. Interestingly, it has been noted that even with similar tolerance factors, compounds with *A*=Ba tend to have higher symmetry than those with *A*=Sr, and this has been assumed to be related to the flexibility of the Ba-O bond lengths which helps to stabilise the cubic structure[22]. Also, it can be readily seen that the degree of B-site ordering in the three compounds increases as the radius of the alkaline earth atom at the A site decreases. A similar trend was reported in a study of the partially ordered double perovskites Sr_2FeSbO_6 and Ca_2FeSbO_6[23]. This effect is believed to result from the fact that the B-cations will be closer together with smaller A-cations, and the electrostatic repulsion will thus be higher, leading to an increased Madelung energy of ordering[24].

Neutron diffraction has shown that the three antimony-containing samples have a G-type magnetic structure both at room temperature and 5 K. Every Fe^{3+} is coupled in an antiparallel

manner with its nearest neighbours, interacting through a superexchange mechanism. In the calcium and strontium compounds, as iron is distributed over the crystallographically-distinct B-sites in different concentrations, the two compounds can be described as ferrimagnets. Ferrimagnetism resulting from cation ordering is also observed in other iron-containing ordered perovskites such as $Sr_3Fe_2MoO_6$[25] and $Sr_3Fe_2WO_9$[26]. The room-temperature neutron-diffraction data and the hysteresis observed in the susceptibility throughout the measured temperature range show that the ordering temperatures of our samples are higher than 370 K; due to technical limitations we were unable to determine the exact ordering temperatures of our compounds. The ordering temperatures of the members of this series are thus higher than those of $Sr_2LaCr_2SbO_9$ and $Sr_3Fe_2MoO_6$, but this is not surprising as $Sr_3Fe_2WO_9$ is reported to have an ordering temperature of 373 K. The refined moments on the Fe^{3+} cations are below the spin-only value, see Table 5.11, suggesting that not all the Fe^{3+} cations take part in the long-range magnetic ordering. This can be explained by the partial cation ordering pattern, which could result in some antimony-rich regions that disrupt the network of Fe-O-Fe interactions. The refined moment of the Fe^{3+} cations in the calcium compound, which possesses the highest degree of B-site ordering and the lowest chance of the presence of Sb-O-Sb nearest-neighbour environments, is larger than that in the strontium compound, although still lower than what would have been predicted in a fully-ordered antiferromagnet. However, in contrast to the relaxor ferromagnet $La_3Ni_2SbO_9$, this variation of local composition is not dominant in determining the magnetic properties of this series, since neutron diffraction still detects magnetic Bragg peaks and overall long-range order must therefore persist over relatively large distances in the sample. In the $M(H)$ plots shown in Figure 5.4, we can see the net magnetisation of $Ca_2LaFe_2SbO_9$ is greater than $Sr_2LaFe_2SbO_9$, which results from the higher degree of cation ordering as discussed above. However, the observed net magnetisation per formula unit for both compounds is lower than the calculated value based on the simple ferrimagnetic model. One possible reason is that the full magnetisation of the polycrystalline sample is not observed in the measured field range. Another explanation is that the presence of the diamagnetic Sb^{5+} reduces the effectiveness and dominance of the nearest-neighbour (NN) antiferromagnetic Fe – O – Fe interaction and results in the competition between the NN and next-nearest-neighbour (NNN) 90° interactions along the Fe – O – O – Fe pathway, which has been observed in other antimony-containing perovskites[5, 17].

$Ba_2LaFe_2SbO_9$ behaves differently from the calcium and strontium analogues not only in crystal structure, but also in magnetic properties. Although a G-type magnetic structure was assigned to this cation-disordered compound and the magnetisation should thus be zero, in practice hysteresis is observed both at room temperature and at 5 K, indicating it is not a simple antiferromagnet. The presence of weak ferromagnetism is not rare in *Pbnm* perovskites[27-29] owing to the Dzyaloshinsky-Moriya interaction, which has the effect of canting spins so that a ferromagnetic component is introduced[30, 31]. However due to higher degree of disorder at the B site, the average ordered component of the magnetic moment per Fe^{3+} cation is even lower than that in the calcium and strontium analogues, and the difference between ZFC and FC is less marked in the dc molar susceptibility.

It can be seen that the ZFC and FC susceptibilities of all three compounds do not completely coincide above 50 K as they would in a simple Curie-Weiss paramagnet or antiferromagnet. Furthermore, in each case the FC susceptibility becomes almost constant below ~50 K, at which temperature the ZFC susceptibility reaches a maximum. In order to explain all our data within a single model, we propose that strong Fe-O-Fe superexchange interactions are present in these compounds above 370 K; we note that the perovskite $LaFeO_3$ has a magnetic ordering temperature of 750 K[32]. The cation disorder, and the resulting competition between different exchange pathways, prevents a conventional transition to a magnetically-ordered phase but at 300 K a backbone of magnetically-ordered spins, large enough to be detected by neutron diffraction, exists within the structure. As the sample is cooled further, more spins join the backbone and the average ordered moment detected by neutron diffraction increases. At ~50 K, the remaining paramagnetic spins, presumably relatively isolated in antimony-rich regions, undergo spin-glass freezing. In a previous study of partially ordered double perovskite Sr_2FeSbO_6, similar susceptibility behaviour was observed with a maximum in ZFC at ~40 K[33], and it was proposed that the coexistence of magnetic backbone of ordered spins and clusters of frustrated spins led to the relatively low moment of 3.06 μ_B per Fe^{3+} cation observed by neutron diffraction at 1.5 K[34]. Spin frustration was also observed in completely-ordered Ca_2FeSbO_6 as a result of the competition between NN and NNN interactions, while in the 6*H* perovskite Ba_2FeSbO_6 weak ferromagnetism or magnetic clusters with an uncompensated magnetic moment were believed to be present[35].

The monoclinic structure of $CaLa_2Fe_2SnO_9$ was confirmed by XRPD and neutron diffraction. The cation distribution observed in ordered $CaLa_2Fe_2SnO_9$ shows a lower degree of B-site

ordering than $Ca_2LaFe_2SbO_9$ and $Sr_2LaFe_2SbO_9$, which can be accounted for by the smaller difference in charge between Fe^{3+} and Sn^{4+} given that the difference in size between these two cations is approximately the same as that between Fe^{3+} and Sb^{5+}. The B-site ordering pattern for $CaLa_2Fe_2SnO_9$ is consistent with the fact that in this compound the octahedra on the 2*c* sites, which are occupied by more tin, are larger than the octahedra on the 2*d* sites at 3.5 K, see Table 5.14. This difference in size between the octahedra on the 2*d* and 2*c* sites is less obvious at room temperature. As discussed above, for a perovskite containing Sn^{4+} to form an ordered structure, the presence of a divalent cation on the B site is usually necessary to introduce sufficient charge difference, so the partial B-site ordering observed in $CaLa_2Fe_2SnO_9$ is rather unusual.

The magnetic properties of $CaLa_2Fe_2SnO_9$ differ significantly from those of the antimony-containing series as seen in Figure 5.5. This compound show relatively broad hysteresis loops both at room temperature and 5 K in the *M*(*H*) plots, suggesting it is not paramagnetic or purely antiferromagnetic over the measured temperature range. In contrast to the antimony-containing series, the saturated magnetisation of the tin-containing compound does not drop significantly with increasing temperature. The presence of long-range magnetic ordering is clearly demonstrated by the presence of magnetic Bragg scattering in the neutron diffraction patterns collected at both 300 and 3.5 K for $CaLa_2Fe_2SnO_9$. The magnetic model used to explain the magnetic scattering is essentially the antiferromagnetic G-type magnetic structure involving nearest-neighbour interactions as was assigned to the antimony-containing series. The difference in magnetic moment between the 2*d* and 2*c* sites results in a net ferrimagnetism, and the model is thus qualitatively consistent with the magnetometry data. The ordered moment of 4.16 μ_B on Fe^{3+} determined by neutron diffraction at low temperature is lower than, but not far away from the spin-only value of 5 μ_B, and would be expected to lead to a larger net magnetisation than was observed in *M*(*H*) at 5 K. As explained for the antimony-containing series, the competition between different types of magnetic interaction in the crystal would lead to the decrease of observed magnetisation. In addition, the standard deviation on the occupancies of Fe^{3+} cations over the B sites, see Table 5.12, could also potentially lead to relatively large error on the expected magnetisation, so that the experimental value deviates from our calculation. There is little difference between ZFC and FC throughout the temperature range. As the moment on Fe^{3+} in $CaLa_2Fe_2SnO_9$ at room temperature is significantly higher than that in the antimony-containing series, we deduce that

the growth of magnetic clusters in $CaLa_2Fe_2SnO_9$ is nearly complete at 300 K, with a well-defined long-range magnetic backbone having been established.

5.5 Conclusions

In this study four perovskites: $A_2LaFe_2SbO_9$ (*A*=Ba, Sr, Ca) and $CaLa_2Fe_2SnO_9$ have been prepared using standard solid-state reactions. X-ray and neutron diffraction data show that they adopt different crystal structures. In $A_2LaFe_2SbO_9$ (*A*=Ba, Sr, Ca), the calcium and strontium analogues show different levels of cation ordering, although the former adopts a monoclinic $P2_1/n$ structure and the latter adopts a triclinic $P\,\bar{1}$ structure, reflecting different types of crystal distortion. The barium analogue is shown by neutron diffraction to adopt a primitive orthorhombic structure *Pbnm* with disordered B sites. Magnetometry data together with neutron diffraction data have shown that these perovskites are not simple paramagnets at room temperature, and they all adopt a G-type magnetic structure, which leads to long-range ferrimagnetic or weak ferromagnetic behaviour. These three compounds all contain a minor spin-glass-like phase below 50 K, which is most clearly indicated by the asymmetric *M*(*H*) loop in the case of the barium analogue. Neutron diffraction data collected from $CaLa_2Fe_2SnO_9$ showed it to have a monoclinic $P2_1/n$ structure with cation ordering. In this case the B-site ordering is less complete than in the antimony-containing series, which is consistent with the smaller difference in charge between Fe^{3+} and Sn^{4+}. Magnetometry data together with neutron diffraction data suggest that $CaLa_2Fe_2SnO_9$ is a ferrimagnet with a Curie temperature above room temperature, and the moment on the Fe^{3+} cations in this compound drops relatively slowly as the sample is warmed up from 5 K to room temperature.

References

[1] P.D. Battle, S.I. Evers, E.C. Hunter, M. Westwood, Inorg. Chem. 52 (2013) 6648.

[2] P.D. Battle, M. Avdeev, J. Hadermann, J. Solid State Chem. 220 (2014) 163.

[3] M.T. Anderson, K.R. Poeppelmeier, Chemistry of Materials 3 (1991) 476.

[4] G. Santosh Babu, V. Subramanian, V.R.K. Murthy, Journal of the European Ceramic Society 27 (2007) 2973.

[5] M.P. Attfield, P.D. Battle, S.K. Bollen, T.C. Gibb, R.J. Whitehead, Journal of Solid State Chemistry 100 (1992) 37.

[6] A.M. Abakumov, M.D. Rossell, S.A. Seryakov, M.G. Rozova, M.M. Markina, G. van Tendeloo, E.V. Antipov, Journal of Materials Chemistry 15 (2005) 4899.

[7] T. Yang, T. Perkisas, J. Hadermann, M. Croft, A. Ignatov, G. van Tendeloo, M. Greenblatt, Journal of Materials Chemistry 21 (2011) 199.

[8] A.C. Larson, R.B. von Dreele, General Structural Analysis System (GSAS), Los Alamos National Laboratories, 1990.

[9] H.M. Rietveld, Journal of Applied Crystallography 2 (1969) 65.

[10] B. vanLaar, W.B. Yelon, J. Appl. Cryst. 17 (1984) 47.

[11] R. Paria Sena, J. Hadermann, C.-M. Chin, E.C. Hunter, P.D. Battle, Journal of Solid State Chemistry 243 (2016) 304.

[12] C.-M. Chin, R. Paria Sena, E.C. Hunter, J. Hadermann, P.D. Battle, Journal of Solid State Chemistry 251 (2017) 224.

[13] J.G. Bos, J.P. Attfield, Zeitschrift fuer Anorganische und Allgemeine Chemie 630 (2004) 2248.

[14] S. Ishiwata, M. Azuma, M. Takano, E. Nishibori, M. Takata, M. Sakata, k. Kato, Journal of Materials Chemistry 12 (2002) 3733.

[15] N. Li, B. Manoun, L. Tang, F. Ke, F. Liu, H. Dong, P. Lazor, W. Yang, Inorganic Chemistry 55 (2016) 6770.

[16] P.K. Davies, H. Wu, A.Y. Borisevich, I.E. Molodetsky, L. Farber, Annual Review of Materials Research 38 (2008) 369.

[17] E.C. Hunter, P.D. Battle, R. Paria Sena, J. Hadermann, Journal of Solid State Chemistry 248 (2017) 96.

[18] M. Retuerto, M.J. Martinez Lopez, M. Garcia Hernandez, A. Munoz, M.T. Fernandez Diaz, J.A. Alonso, Materials Research Bulletin 45 (2010) 1449.

[19] A.J. Jacobson, B.C. Tofield, B.E.F. Fender, Acta Crystallographica B 28 (1972) 956.

[20] E.M. Ramos, I. Alvarez, R. Saez-Puche, M.L. Veiga, C. Pico, Journal of Alloys and Compounds 225 (1995) 212.

[21] V.M. Goldschmidt, Naturwissenschaften 14 (1926) 477.

[22] P.W. Barnes, M.W. Lufaso, P.M. Woodward, Acta Crystallographica Section B: Structural Science 62 (2006) 384.

[23] A. Faik, J.M. Igartua, E. Iturbe-Zabalo, G.J. Cuello, Journal of Molecular Structure 963 (2010) 145.

[24] S. Vasala, M. Karppinen, Progress in Solid State Chemistry 43 (2015) 1.

[25] M.C. Viola, J.A. Alonso, J.C. Pedregosa, R.E. Carbonio, Eur. J. Inorg. Chem. (2005) 1559.

[26] S.A. Ivanov, S.-G. Eriksson, R. Tellgren, H. Rundlof, Materials Research Bulletin 36 (2001) 2585.

[27] S. Chanda, S. Saha, A. Dutta, B. Irfan, R. Chatterjee, T.P. Sinha, Journal of Alloys and Compounds 649 (2015) 1260.

[28] J. Blasco, J. Garcia, Journal of Physics and Chemistry of Solids 55 (1994) 843.

[29] A. Ghosh, M.G. Masud, K. Dey, B.K. Chaudhuri, Journal of Physics and Chemistry of Solids 75 (2014) 374.

[30] I. Dzyaloshinski, Journal of Physics and Chemistry of Solids 4 (1958) 241.

[31] T. Moriya, Physical Review 120 (1960) 91.

[32] W.C. Koehler, E.O. Wollan, Journal of Physics and Chemistry of Solids 2 (1957) 100.

[33] P.D. Battle, T.C. Gibb, A.J. Herod, J.P. Hodges, Journal of Materials Chemistry 5 (1995) 75.

[34] E.J. Cussen, J.F. Vente, P.D. Battle, T. Gibb, Journal of Materials Chemistry 7 (1997) 459.

[35] S.-O. Lee, T.Y. Cho, S.H. Byeon, Bulletin of the Korean Chemical Society 18 (1997) 91.

Chapter 6: Structural and Magnetic Properties of $SrLa_2FeCoSbO_9$

6.1 Introduction

As has been explained in Chapter 1, our group has previously described a perovskite, $La_3Ni_2SbO_9$, that behaves as a relaxor ferromagnet[1, 2] below 110 K. This compound adopts a monoclinic structure in which two crystallographically-distinct B sites occur in a 1:1 ratio. The imbalance in the concentration of Ni^{2+} cations on the two sites leads to the observed ferrimagnetic behaviour, although local variations in the composition cause the formation of small magnetic domains and, consequently, relaxor behaviour. $La_3Co_2SbO_9$ shows the same cation ordering pattern as $La_3Ni_2SbO_9$ but the sharp increase in magnetisation observed in the latter at 108 K is not observed in the former [3]. Franco *et al* postulated that frustration prevents the development of long-range ferromagnetism and their neutron diffraction data, collected at 2 K, contained a magnetic Bragg peak which they took to be indicative of an unidentified antiferromagnetically-ordered structure. They have also studied [4] the system $La_3Ni_{2-y}Co_ySbO_9$ wherein they found a similarly-ordered distribution of cations but no evidence for long-range magnetic ordering. The temperature dependence of the magnetisation of $La_3Ni_2SbO_9$ and $La_3Co_2SbO_9$ is shown in Figure 6.1. These compounds illustrate the effect of different cation choices on the physical properties of a material.

In general, magnetic transition temperatures are expected to be highest in the members of an isostructural series that contain the most strongly magnetic cations. In an attempt to prepare a relaxor ferromagnet with an enhanced transition temperature we have therefore synthesized Fe^{3+}-containing analogues of $La_3Ni_2SbO_9$, for example $Sr_3Fe_2TeO_9$. We have also prepared compositions in which only 33 % of the B sites are occupied by Fe^{3+}, for example $A La_2FeCoSbO_9$ and $A La_2FeNiSbO_9$ (*A*= Ba, Sr, Ca). In this chapter we describe the synthesis and characterisation of one such compound that shows particularly interesting behaviour; the more complex and varied properties of the other members of the series will be described in a later chapter. More specifically, we describe below how a combination of X-ray and neutron diffraction, magnetometry, electron microscopy and Mössbauer spectroscopy has revealed a novel cation-ordering pattern and consequential ferrimagnetism in $SrLa_2FeCoSbO_9$.

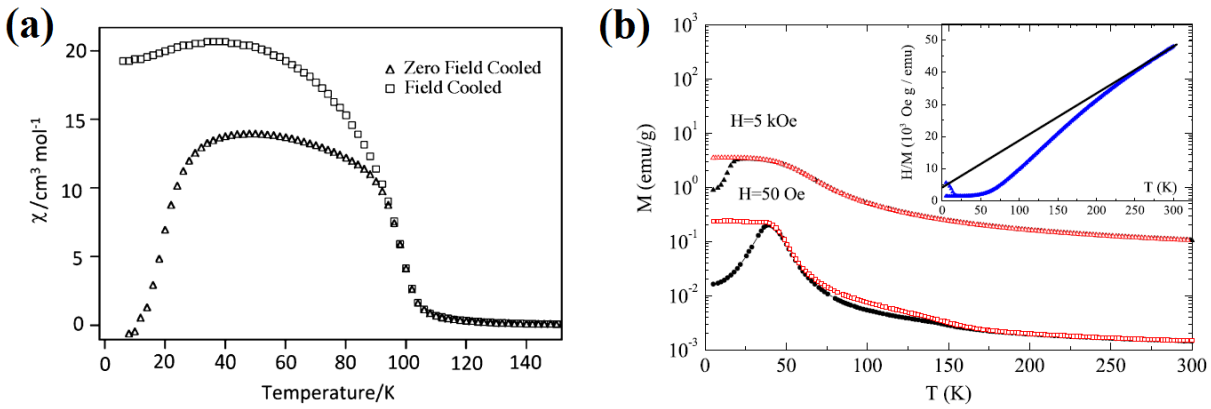

Figure 6.1 The temperature dependence of the magnetisation of (a) $La_3Ni_2SbO_9$[1] and (b) $La_3Co_2SbO_9$[3].

6.2 Experimental methods

A polycrystalline sample of $SrLa_2FeCoSbO_9$ was prepared using the standard ceramic method. $SrCO_3$, La_2O_3, Fe_2O_3, Co_3O_4 and Sb_2O_5 (purity >99.95%) were weighed out in the appropriate stoichiometric ratio and ground together in an agate mortar for 30 minutes to give a homogeneous mixture. La_2O_3 was heated at 800 °C for 24 hours prior to use to ensure it was completely dry. The mixture was then loaded into an alumina crucible and fired at 800 °C for 24 h. It was then quenched to room temperature, reground and pressed into a pellet which was fired in air at 1300 °C for 48 hours and subsequently annealed at 1300 °C for another 48 hours after further grinding. Finally, the furnace was allowed to cool to 800 °C and then the sample was quenched to room temperature.

The brown-black reaction product was initially characterised by X-ray powder diffraction (XRPD) using Cu $K\alpha_1$ radiation. The data, collected at room temperature on a Panalytical X'Pert diffractometer, were analysed using the Rietveld method as implemented in the GSAS[5] program package. Neutron diffraction patterns were collected from the reaction product at 5K and 300K on the GEM time-of-flight diffractometer at the ISIS spallation source. The data collected on detector banks at scattering angles, 2θ, of 34.96°, 63.62°, 91.30° and 154.40° were refined simultaneously.

The dc molar magnetic susceptibility of the product was measured over the temperature range $2 < T/K < 370$ using a Quantum Design MPMS 5000 SQUID magnetometer. Data were collected on warming in a field of 100 Oe after cooling the sample both in the absence of an

applied field (zero-field cooled, ZFC) and in the measuring field (field cooled, FC). The isothermal magnetisation was measured as a function of field over the range –50 < H/kOe < 50 at 300 and 5 K after cooling in a field of 50 kOe. The ac susceptibility of $SrLa_2FeCoSbO_9$ was measured over the temperature range 50 < *T*/K < 300 in a field of amplitude 3.5 Oe oscillating at frequencies of 1, 10, 100 and 1000 Hz.

Transmission electron microscopy (TEM) experiments related to this chapter were carried out by Prof. Joke Hadermann and Mylène Hendrickx at the University of Antwerp, and ^{57}Fe Mössbauer spectroscopy experiments at room temperature were conducted by Prof. J. M. Cadogan at the Australian Defence Force Academy, as described in Chapter 2.

6.3 Results

The XRPD pattern of the reaction product $SrLa_2FeCoSbO_9$ suggested that the synthesis had produced a phase-pure pseudo-cubic perovskite. The XRD pattern was indexed and analysed in the primitive monoclinic space group $P2_1/n$ with $a \sim\sqrt{2}a_p$, $b \sim\sim\sqrt{2}a_p$ and $c \sim 2a_p$, where a_p is the unit cell parameter of a primitive cubic perovskite. The fit to the observed pattern is shown in Figure 6.2. In this space group the structural model involves a 4*f* site that accommodates a disordered distribution of Sr and La, three further 4*f* sites that accommodate oxide anions and two independent B sites, *2d* (½, 0, 0) and *2c* (0, ½, 0) which accommodate the three cation species Fe^{3+}, Co^{2+} and Sb^{5+}. The X-ray scattering lengths of iron and cobalt are very similar and it was impossible to distinguish between these two elements using our X-ray data. In this analysis they were therefore treated as if they were identical. Refinements of the distribution of a representative transition metal and antimony over the crystallographically-distinct B sites showed that in each case the 2*d* (½,0,0) sites are largely occupied by transition metals, while nearly all the antimony atoms are on the *2c* (0, ½, 0) sites; the fit to the data shown in Figure 6.2 is based on the refined cation distribution $SrLa_2(Fe/Co_{1.42}Sb_{0.08})_{2d}(Fe/Co_{0.58}Sb_{0.92})_{2c}O_9$. Although they did not establish the distribution of iron and cobalt, our XRPD data thus enabled us to establish the space group symmetry of $SrLa_2FeCoSbO_9$ and that essentially all the antimony is located on a single six-coordinate site.

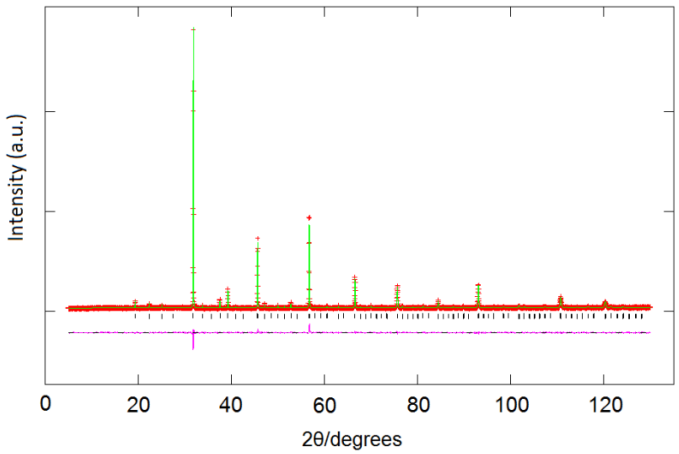

Figure 6.2 Observed (red crosses) and calculated (green line) X-ray powder diffraction patterns for $SrLa_2FeCoSbO_9$ sample indexed in $P2_1/n$; a difference curve (purple) is shown.

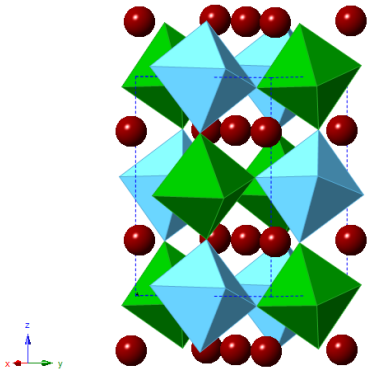

Figure 6.3 $P2_1/n$ structure adopted by $SrLa_2FeCoSbO_9$. Green octahedra are occupied by Fe and Co; blue octahedra by Fe and Sb. Red circles represent the Sr and La atoms at the A site.

The time-of-flight neutron diffraction patterns collected from $SrLa_2FeCoSbO_9$ at 300 K were analysed using the structural model derived from the XRPD data as a starting point. After some preliminary refinements, the antimony occupancy of the *2d* site of $SrLa_2FeCoSbO_9$ was fixed to zero. We were then able to allow the distribution of cobalt and iron atoms over the 2*c* and 2*d* sites to vary, provided that the overall composition was held constant. The occupancy of cobalt on the *2c* site refined to zero, and the iron atoms were found to be equally distributed over the two sites, see Figure 6.3. The formula of this compound is thus best written as $SrLa_2(Fe_{0.5}Co)_{2d}(Fe_{0.5}Sb)_{2c}O_9$. The fit to the pattern collected at $2\theta = 34.96°$ can be seen in Figure 6.4(a) and Figure 6.4(d) shows the fit to the data collected at $2\theta = 154.40°$; the latter have a higher resolution but cover a more limited range of *d*-spacing. Patterns collected

at 2θ = 63.62° and 2θ = 91.30° with intermediate resolution and *d*-spacing range are shown in Figure 6.4(b) and Figure 6.4(c), respectively. There was no evidence of long-range magnetic ordering in this compound at 300 K. The refined structural parameters are listed in Table 6.1 and the most important bond lengths and angles are presented in Table 6.2.

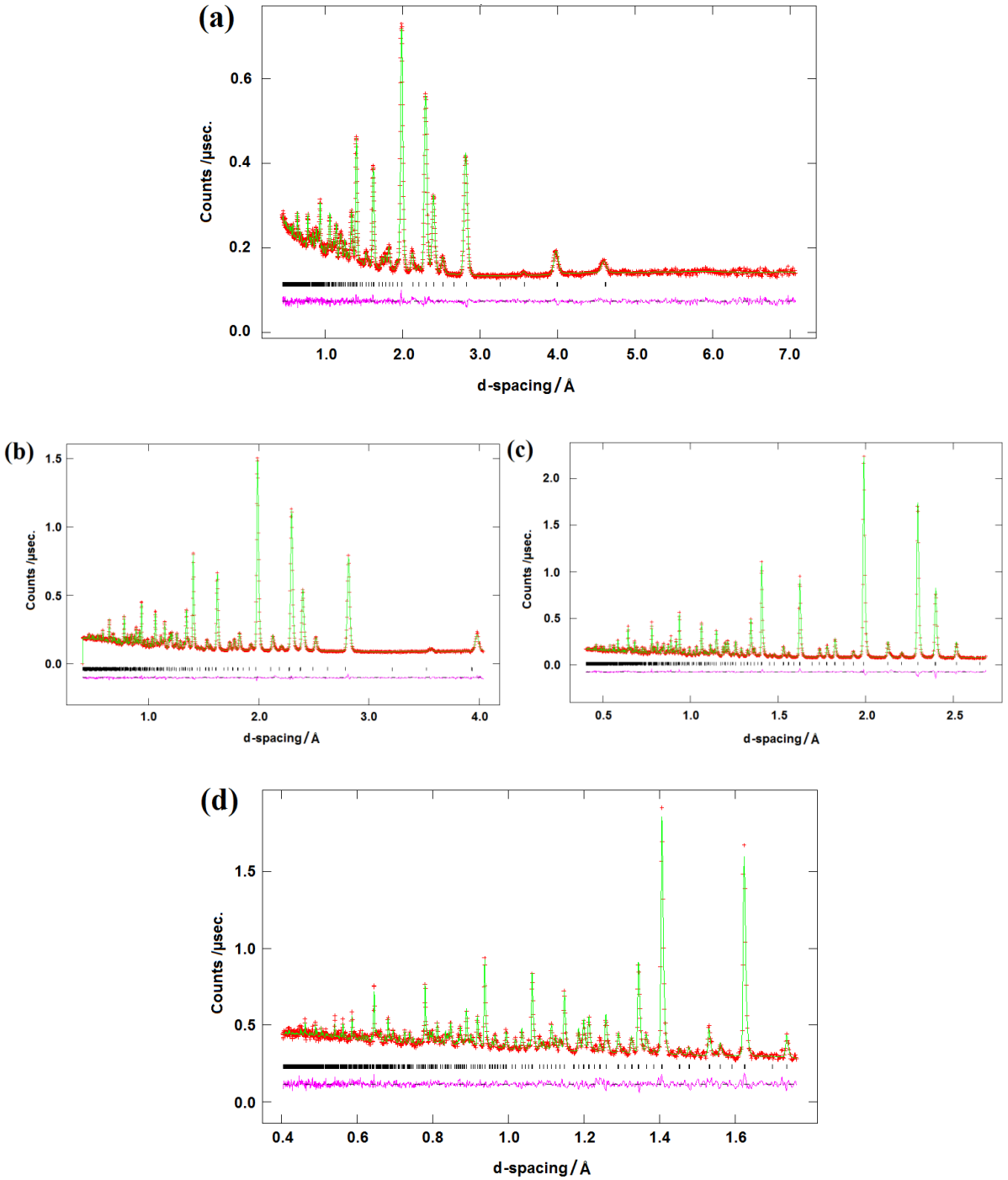

Figure 6.4 Observed (red) and calculated (green) time-of-flight neutron diffraction patterns of $SrLa_2FeCoSbO_9$ at room temperature collected at (a) 2θ = 34.96°, (b) 2θ = 63.62°, (c) 2θ = 91.30° and (d) 2θ = 154.40°. A difference curve (purple) is shown and reflection positions are marked.

Table 6.1 Refined structural parameters for $SrLa_2FeCoSbO_9$ at 300 and 5 K; space group $P2_1/n$.

T (K)			300	5
a (Å)			5.6218(6)	5.6091(4)
b (Å)			5.6221(6)	5.6148(4)
c (Å)			7.9440(8)	7.9279(6)
β (°)			90.050(7)	89.999(9)
R_{wpr}			2.34%	2.63%
χ^2			1.51	1.82
A/La	4*e*	Occupancy	0.3333/0.6667	0.3333/0.6667
		x	0.4932(4)	0.4930(3)
		y	0.5262(2)	0.5294(1)
		z	0.2510(9)	0.2504(8)
		*U*iso (Å^2)	0.0123(2)	0.0080(1)
Fe_1/Co	2*d*	Occupancy	0.3333/0.6667	0.3333/0.6667
		*U*iso (Å^2)	0.0038(7)	0.0023(5)
Fe_2/Sb	2*c*	Occupancy	0.3333/0.6667	0.3333/0.6667
		*U*iso (Å^2)	0.0051(6)	0.0026(4)
O_1	4*e*	*x*	0.2764(7)	0.2757(7)
		y	0.2827(9)	0.2836(9)
		z	0.0316(4)	0.0340(4)
		*U*iso (Å^2)	0.0129(8)	0.0081(7)
O_2	4*e*	*x*	0.2143(7)	0.2116(6)
		y	0.7821(8)	0.7831(9)
		z	0.0405(4)	0.0403(4)
		*U*iso (Å^2)	0.0091(7)	0.0064(6)
O_3	4*e*	*x*	0.5723(3)	0.5726(3)
		y	0.9879(3)	0.9866(2)
		z	0.2531(9)	0.254(1)
		*U*iso (Å^2)	0.0101(3)	0.0070(2)

Table 6.2 Selected bond lengths (Å) and bond angles (degrees) in $SrLa_2FeCoSbO_9$ at 300 and 5 K.

	300 K	5 K
A/La – O_1	2.530(6)	2.516(6)
A/La – O_1	2.713(6)	2.689(6)
A/La – O_1	2.806(6)	2.805(6)
A/La – O_2	2.705(6)	2.701(6)
A/La – O_2	2.448(6)	2.446(6)
A/La – O_2	2.826(6)	2.810(7)
A/La – O_3	2.632(2)	2.606(1)
A/La – O_3	2.453(3)	2.449(2)
Fe_1/Co – O_1	2.042(5) * 2	2.047(5) * 2
Fe_1/Co – O_2	2.046(4) * 2	2.050(4) * 2
Fe_1/Co – O_3	2.052(7) * 2	2.052(8) * 2
Fe_2/Sb – O_1	1.992(5) * 2	1.985(5) * 2
Fe_2/Sb – O_2	2.018(4) * 2	2.010(4) * 2
Fe_2/Sb – O_3	2.004(7) * 2	1.998(8) * 2
O_1 – Fe_1/Co – O_2	87.9(3) * 2	87.5(2) * 2
O_1 – Fe_1/Co – O_3	88.5(1) * 2	88.8(1) * 2
O_2 – Fe_1/Co – O_3	88.9(1) * 2	90.0(1) * 2
O_1 – Fe_2/Sb – O_2	89.8(3) * 2	89.9(2) * 2
O_1 – Fe_2/Sb – O_3	89.2(1) * 2	89.8(1) * 2
O_2 – Fe_2/Sb – O_3	89.6(1) * 2	89.7(1) * 2
Fe_1/Co – O_1 – Fe_2/Sb	160.4(2)	159.5(2)
Fe_1/Co – O_2 – Fe_2/Sb	156.1(2)	155.7(2)
Fe_1/Co – O_3 – Fe_2/Sb	156.6(1)	156.38(9)

This structural model is consistent with the results from our electron microscopy study. Low magnification EDX confirmed the homogeneous distribution over the crystallites of both the A cations (Sr, La) and the B cations (Fe, Co, Sb) with an averaged composition of $Sr_{0.37(2)}La_{0.63(2)}Fe_{0.30(2)}Co_{0.32(2)}Sb_{0.32(2)}$, see Figure 6.5. The different SAED patterns (representative patterns are shown in Figure 6.6) agree with the monoclinic space group $P2_1/n$. The high resolution HAADF-STEM images (Figure 6.7) show the expected order at

the positions of the B-cations. In such images, the intensity of the atom columns is proportional to the atomic number of the elements: $I \sim Z^2$.The continuous rows of bright dots along the *a or b*-axis correspond to the (La, Sr) atom columns. Parallel to these, there are rows with alternation of brighter and darker dots: these correspond to the alternating (Sb, Fe) and (Co, Fe) atom columns respectively. In addition, when viewed along zone axis [100], the A site columns are slightly shifted along *b* in alternating sense, in agreement with the $P2_1/n$ model. Atomic-resolution EDX (Figure 6.8) shows the ordering between Sb and Co over the *2d* and *2c* positions of this $P2_1/n$ model, while Fe is present on both sites.

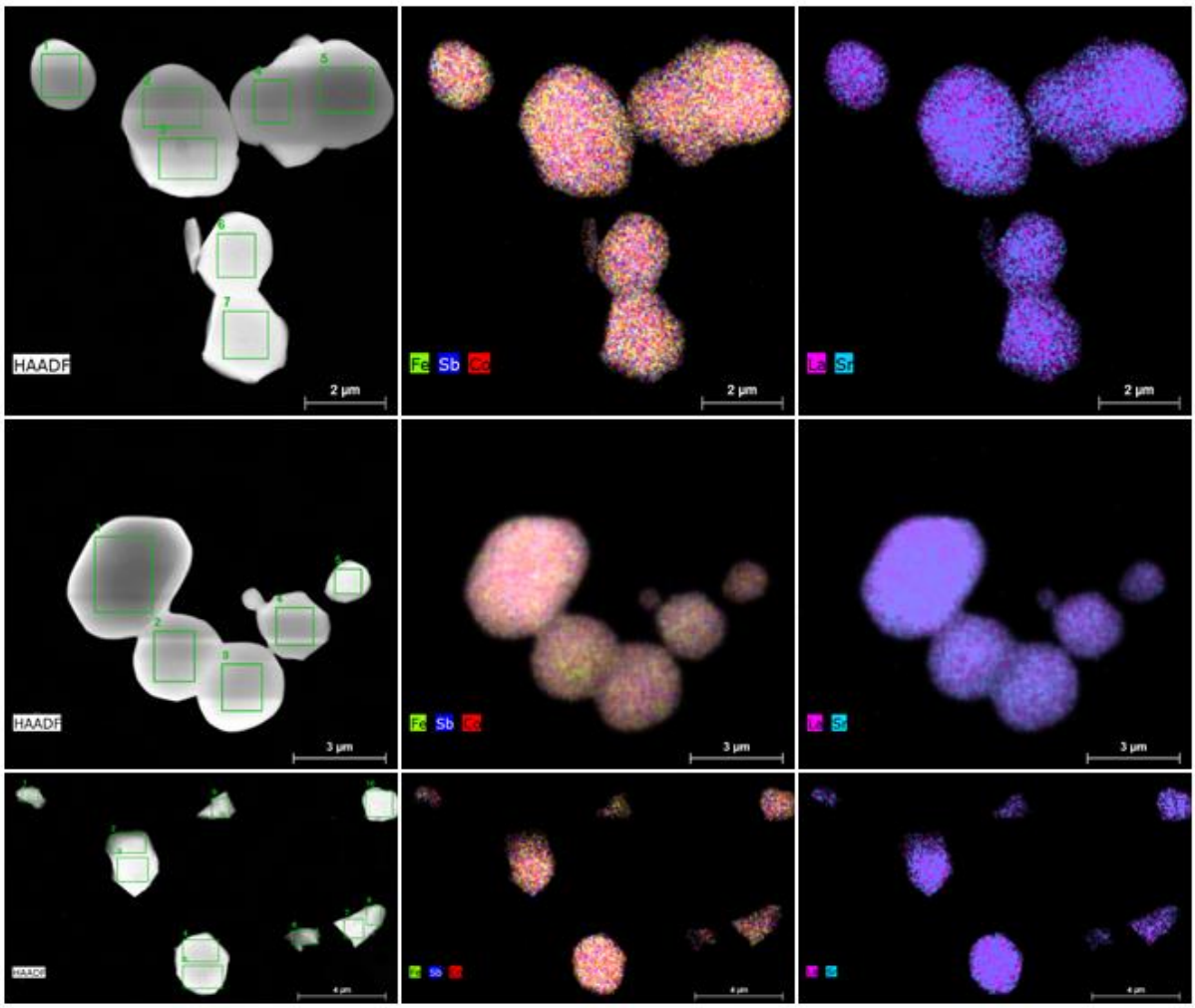

Figure 6.5 HAADF-STEM images together with mixed element maps (Fe,Co,Sb) and (Sr,La). The regions marked in the HAADF-STEM images are for quantitative composition analysis. The relevant data are tabulated in the Appendix as Table A6.1 and Table A6.2. This sample appears to have a homogeneous distribution of elements.

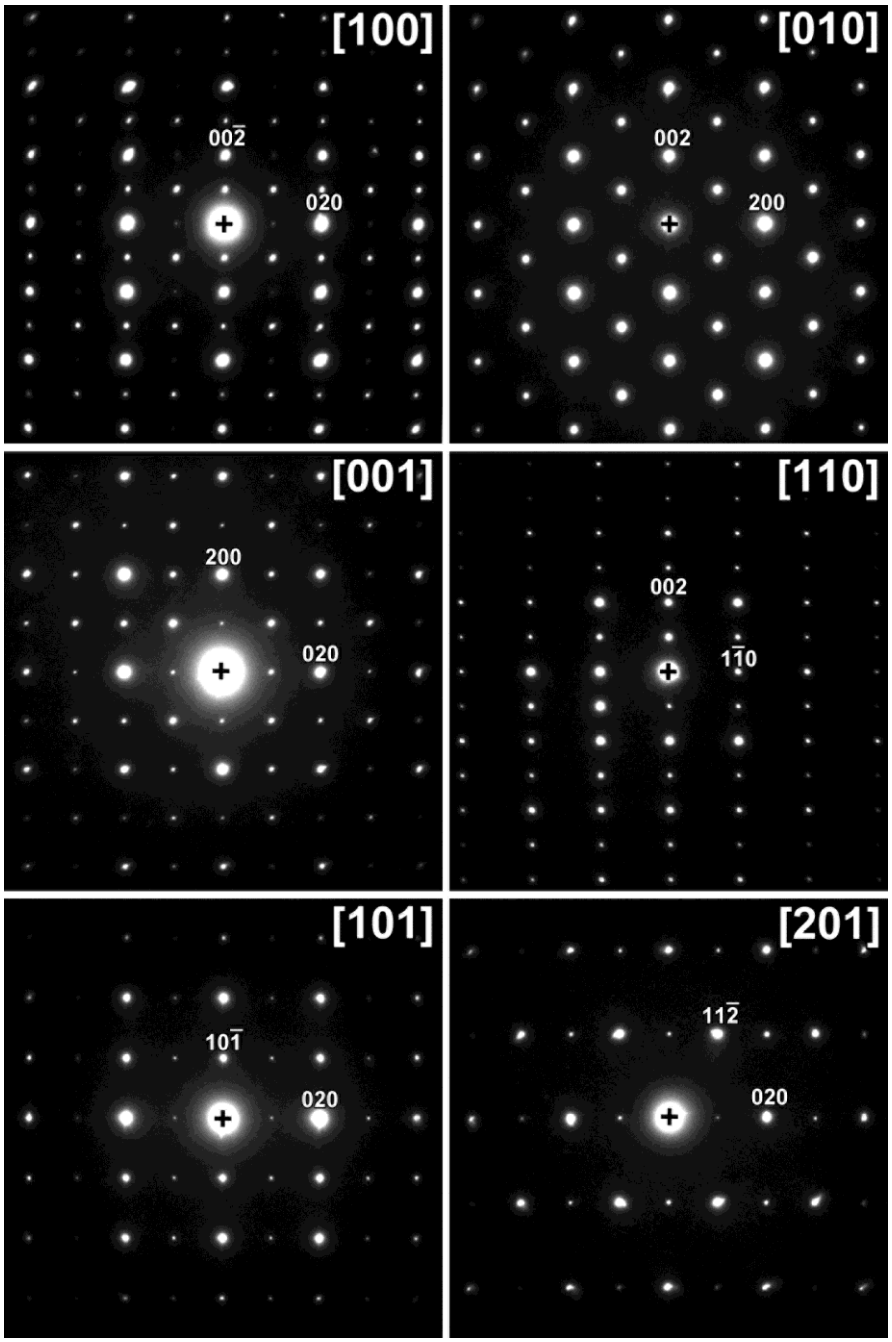

Figure 6.6 SAED patterns of the $SrLa_2FeCoSbO_9$ sample along the zone axes [100], [010], [001], [110], [101] and [201].

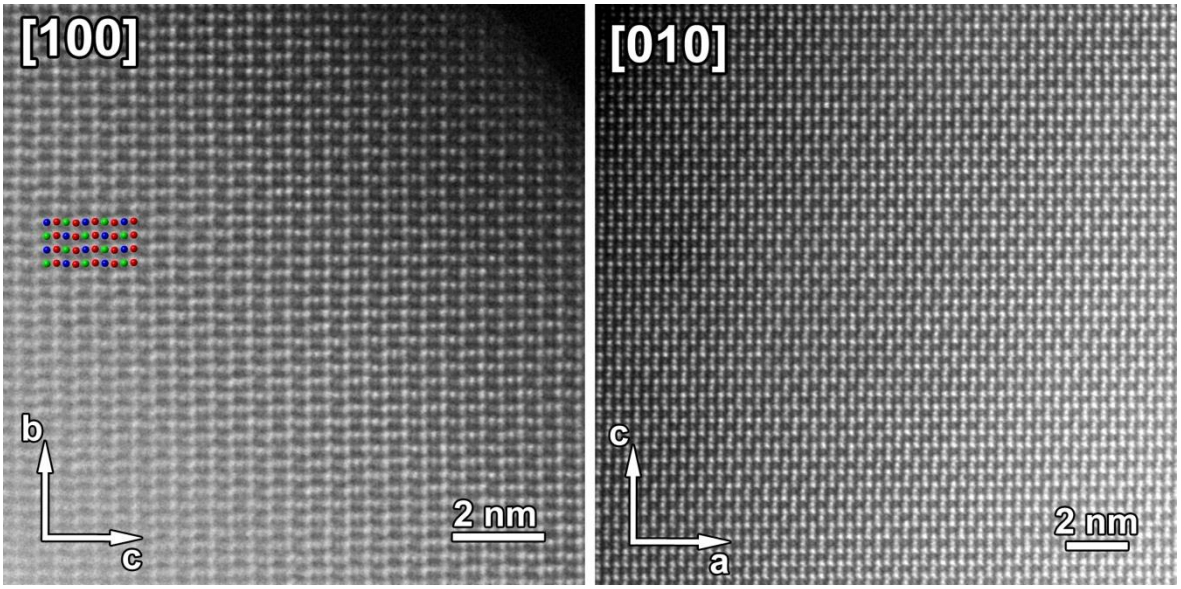

Figure 6.7 High resolution HAADF-STEM images taken along the [100], [010], [110] and [201] zone axes, where red dots represent atomic columns primarily occupied by La and Sr, blue by Fe and Sb, and green by Fe and Co, respectively.

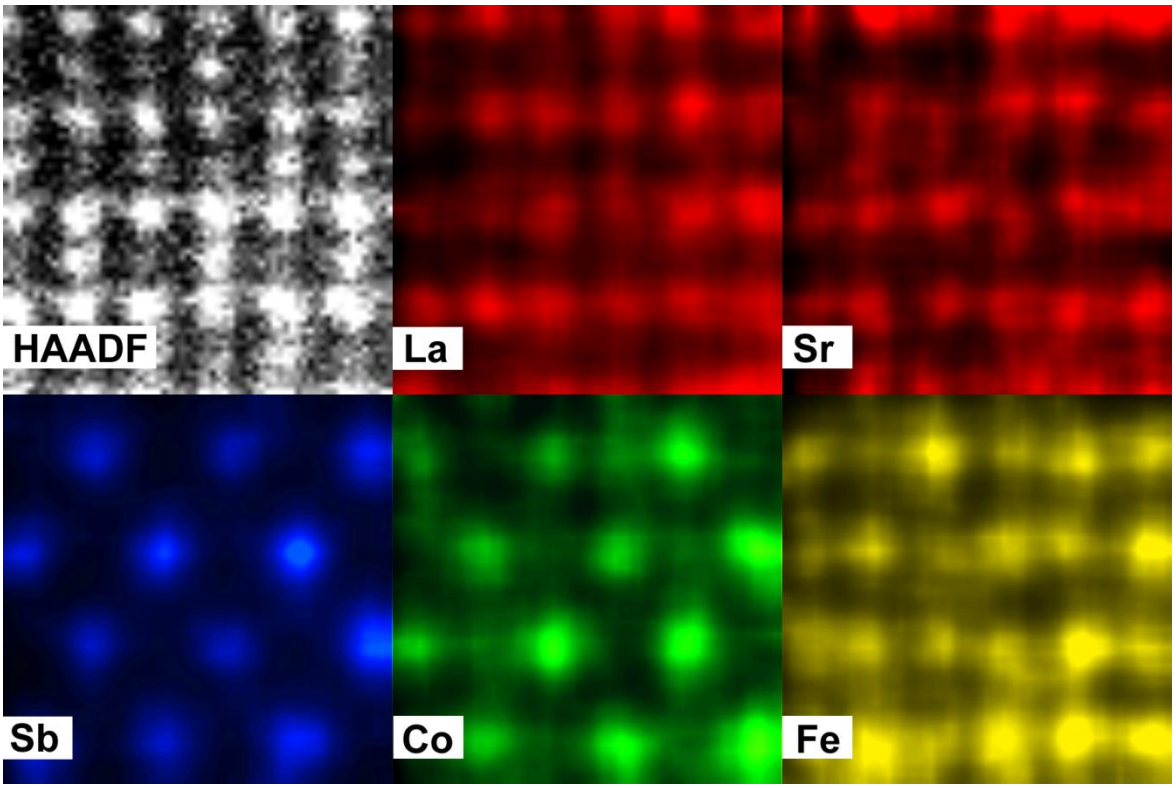

Figure 6.8 Top left: high resolution HAADF-STEM image of the $SrLa_2FeCoSbO_9$ sample along [010]. There is a clear alternation in the occupation of the B site columns, corresponding to different occupancies for sites 2*d* and 2*c*.

In Figure 6.9 we show the room temperature Mössbauer spectrum of $SrLa_2FeCoSbO_9$ acquired over a large velocity range of around ±11.5 mm/s. This spectrum confirms the absence of an ordered magnetic moment on the Fe at 295 K. In Figure 6.10 we show the room temperature Mössbauer spectrum of $SrLa_2FeCoSbO_9$ acquired over a narrower velocity range of around ± 4.8 mm/s. To be consistent with the EDX and diffraction data described above, this spectrum was fitted with two doublets, although the local environments of the Fe atoms on the 2*c* and 2*d* sites in the $SrLa_2FeCoSbO_9$ structure are clearly very similar. The diffraction data show that the Fe cations occupy the two crystallographic sites with equal Fe occupancies. Hence, a basic modelling of the room temperature Mössbauer spectrum is based on two quadrupole-split doublets with equal spectral areas. In this situation it is impossible to obtain a unique, unambiguous fit to the spectrum due to the fact that there are three possible line-pairings of the four equal-area lines that make up the two doublets. A spectral fit in which the relative areas of the two doublets were unconstrained resulted in an area ratio of 44(5):56(5) %. Modelling the spectrum with the area ratio constrained to be 50:50%, consistent with the model used in the analysis of the neutron diffraction data, yields the hyperfine parameters listed in Table 6.3 for each of the three possible line-pairings; the fit to the spectrum is shown in Figure 6.10. Despite the ambiguity in the Mössbauer fitting, one can state that in all cases the refined values of the isomer shifts (IS) and quadrupole splittings (QS) are characteristic of Fe^{3+} and that the spectrum showed no evidence of magnetic hyperfine splitting.

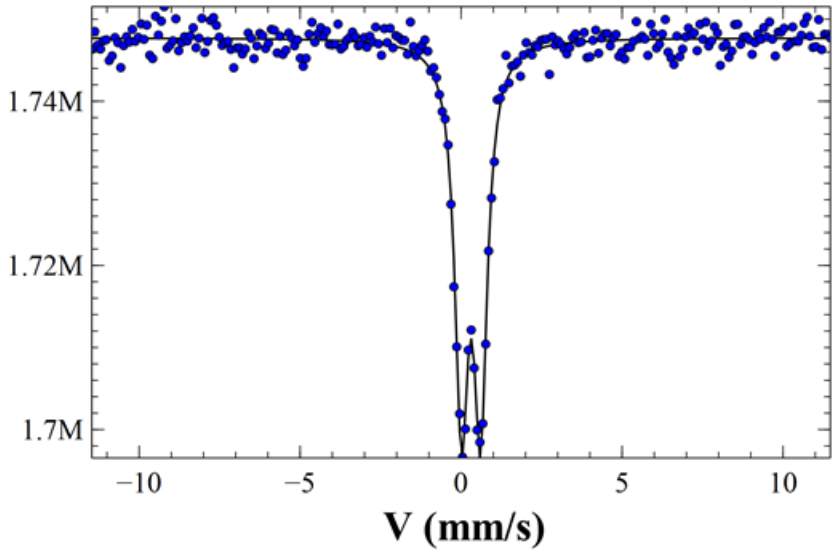

Figure 6.9 Room temperature ^{57}Fe Mössbauer spectrum of $SrLa_2FeCoSbO_9$ acquired over a velocity range of around ± 11.5 mm/s.

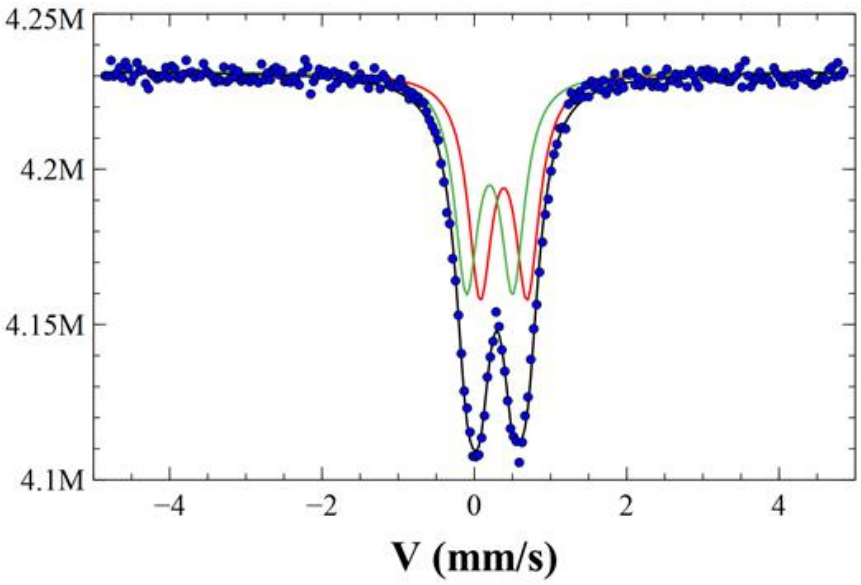

Figure 6.10 Room temperature ^{57}Fe Mössbauer spectrum of $SrLa_2FeCoSbO_9$ acquired over a velocity range of around ± 4.8 mm/s; this spectrum was fitted with two quadrupole-split doublets of equal area and one possible line-pairing combination (1:3 & 2:4 in Table 6.3) is shown.

Table 6.3 Mössbauer hyperfine parameters, Isomer Shift (IS) relative to α-Fe, and Quadrupole Splitting (QS), obtained from fits to the narrower-velocity-range room temperature spectrum of $SrLa_2FeCoSbO_9$ for the three possible line-pairing combinations discussed in the text. (The line numbering, 1 to 4, is in order of increasingly positive velocity).

Line Pairings	QS (mm/s)	IS (mm/s)
1:2 & 3:4	0.182 (6) & 0.191 (4)	+0.096 (2) & +0.710 (2)
1:3 & 2:4	0.609 (4) & 0.619 (4)	+0.310 (3) & +0.496 (3)
1:4 & 2:3	0.801 (4) & 0.428 (4)	+0.404 (3) & +0.400 (3)

The temperature dependence of the dc molar magnetic susceptibility of $SrLa_2FeCoSbO_9$ is shown in Figure 6.11, along with the field dependence of the magnetisation as measured at 300 K and 5 K. The ZFC and FC susceptibilities both suggest that a magnetic phase transition occurs at ~200 K, although the two curves do not overlie below ~350 K. The non-linearity of $M(H)$ at 300 K provides further evidence that this compound is not a simple paramagnet at room temperature. No remanent magnetisation could be detected at 300 K but at 5 K $M(H)$

shows a remanent magnetisation of ~1 μ_B and a coercive field of 6.1 kOe; the magnetisation is unsaturated in a field of 50 kOe. The ac susceptibility of $SrLa_2FeCoSbO_9$, see Figure 6.12, is complex and frequency-dependent. However, the temperature of the maximum in the real part, 215 K, is frequency-independent, suggesting that below this temperature the material is a ferro- or ferrimagnet rather than a spin glass. Below we describe the results of the experiments that we have performed in an attempt to understand the magnetic behaviour of this compound.

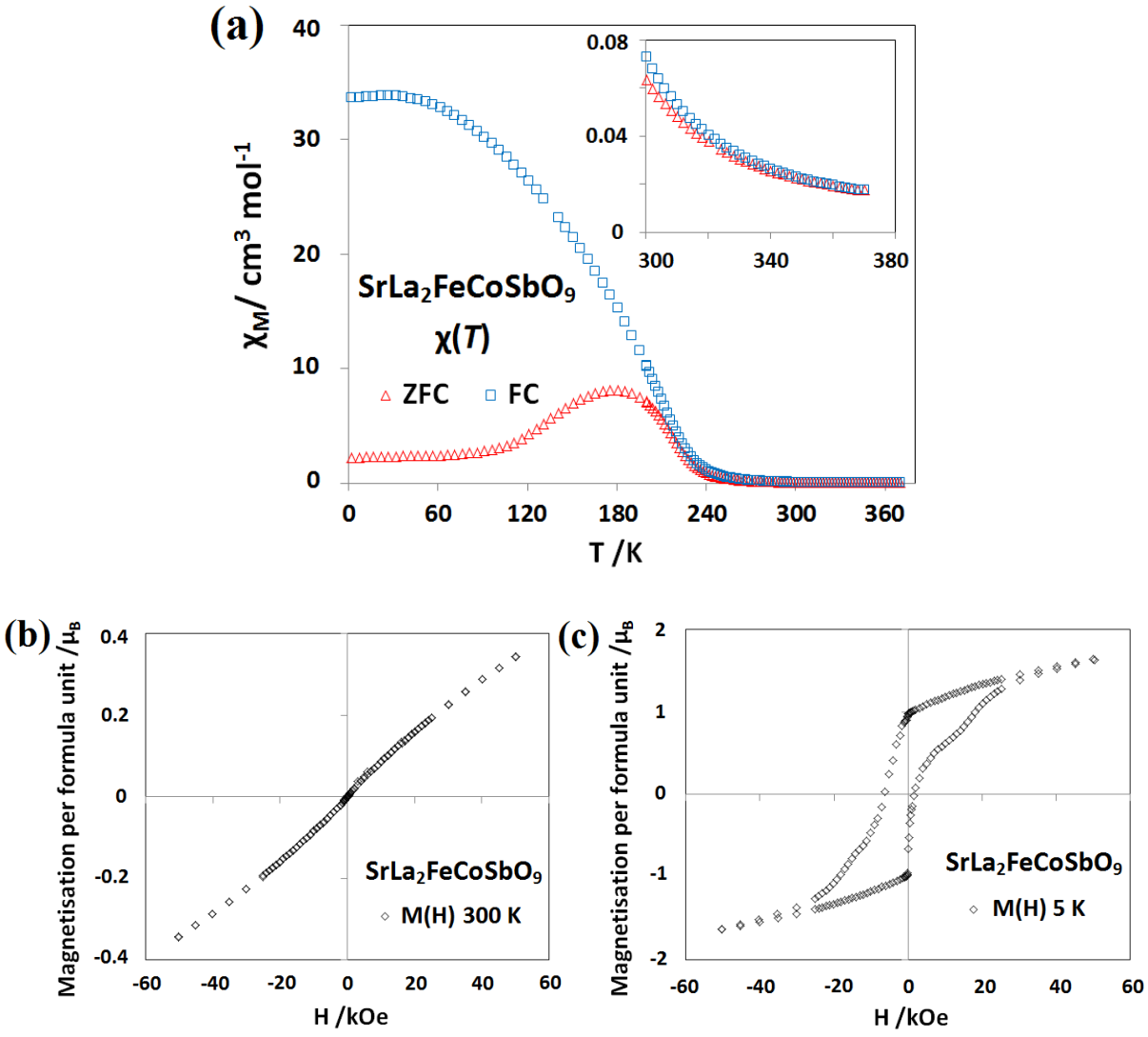

Figure 6.11 (a) Temperature dependence of the dc molar magnetic susceptibilities and the field dependence of the magnetisation per formula unit at (b) 300 K and (c) 5 K of $SrLa_2FeCoSbO_9$.

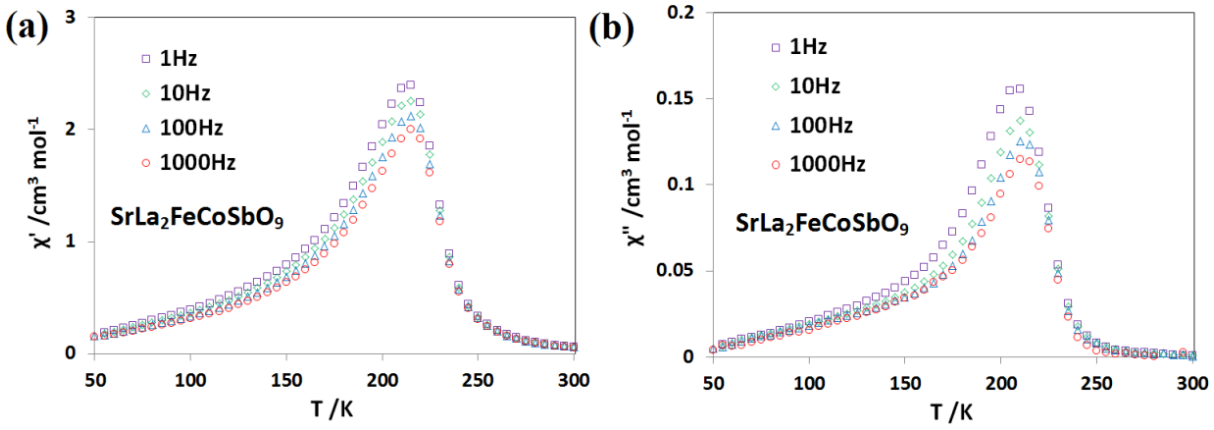

Figure 6.12 Temperature dependence of (a) the real part and (b) the imaginary part of the ac susceptibility of $SrLa_2FeCoSbO_9$.

Analysis of the neutron patterns collected from $SrLa_2FeCoSbO_9$ at 5 K was carried out using the structural model described above with the cation distribution over the B sites fixed to be the same as that determined from the room temperature data. However, in order to model an increase in intensity of the 101 and 011 reflections it was necessary to allow for the presence of magnetic Bragg scattering. The extra intensity could be accounted for by the magnetic structure shown in Figure 6.13 where the mean magnetic moment on each B site is coupled in an antiparallel manner to those of the six nearest-neighbour sites. This spin arrangement is similar to that found in G-type antiferromagnets but in the present case the ordered moments on the two crystallographically-distinct sites are allowed to differ, thus leading to ferrimagnetism rather than antiferromagnetism. The refined structural parameters and bond lengths are listed in Tables 6.1 and 6.2, respectively. The fitted diffraction profiles collected at the four detector banks are shown in Figure 6.14. The mean moments on the Fe/Co-containing 2*d* sites and the Fe/Sb-containing 2*c* sites refined to values of 2.45(3) and 0.87(2) μ_B per cation, respectively. Given that Sb^{5+} is diamagnetic, the latter value corresponds to a moment of 2.61(7) μ_B per magnetic cation. Analysis of the neutron data thus leads to a description of $SrLa_2FeCoSbO_9$ as a ferrimagnet at 5 K with a net moment of 2.37(6) μ_B per formula unit.

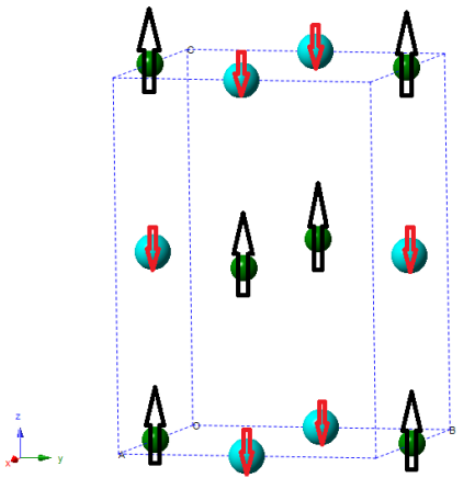

Figure 6.13 Magnetic structure adopted by $SrLa_2FeCoSbO_9$; arrows indicate the direction of ordered spins at the B sites. Green spheres represent the 2*d* sites and blue spheres represent the 2*c* sites.

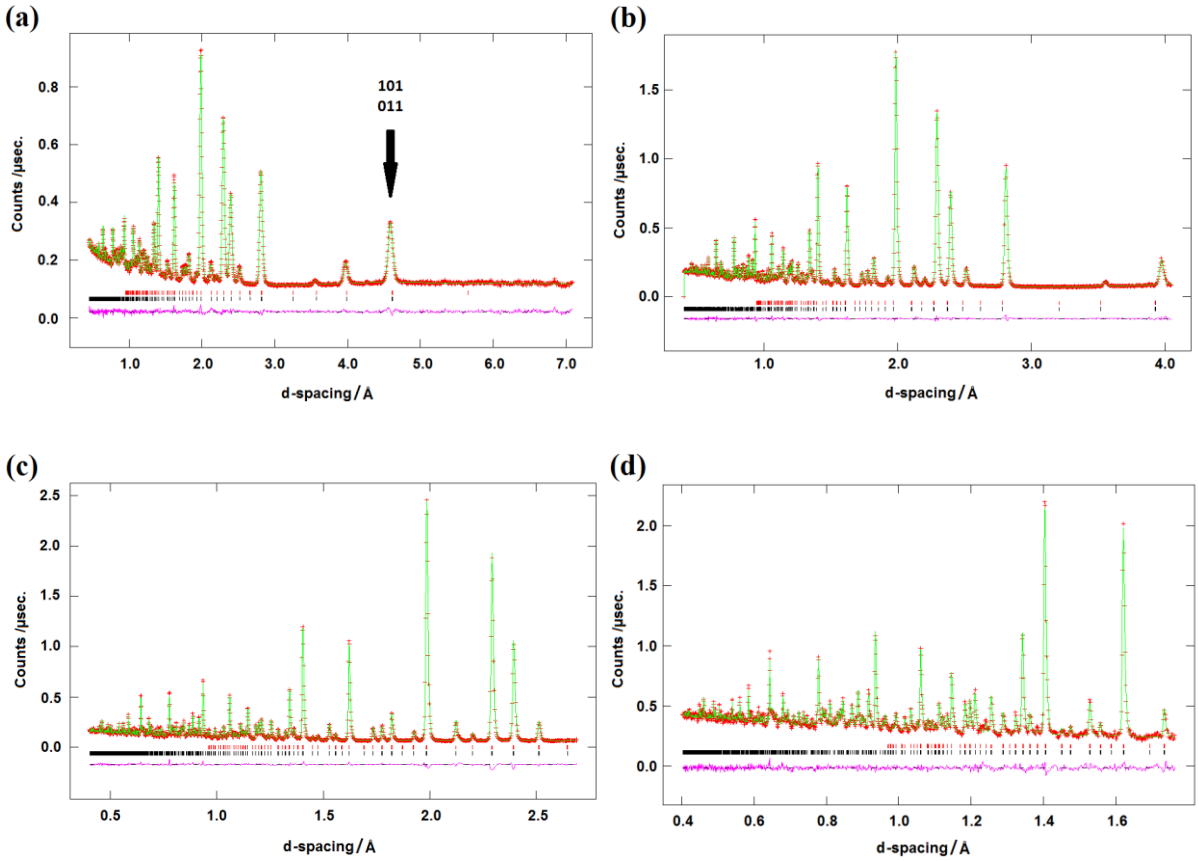

Figure 6.14 Observed (red) and calculated (green) time-of-flight neutron diffraction patterns of $SrLa_2FeCoSbO_9$ at 5 K collected at (a) 2θ = 34.96°, (b) 2θ = 63.62°, (c) 2θ = 91.30° and (d) 2θ = 154.40°. A difference curve (purple) is shown and reflection positions are marked. An arrow indicates the peak with the strongest magnetic contribution.

6.4 Discussion

$SrLa_2FeCoSbO_9$ adopts a crystal structure in which two distinct six-coordinate sites with the same multiplicity must accommodate three species of cations, Fe^{3+}, Co^{2+} and Sb^{5+}, that are present in a 1:1:1 ratio. Our diffraction and microscopy data show that the trio of cations are distributed in a way which, we believe, has not been seen in any other perovskite-related compound; one site is occupied by Co^{2+} and Fe^{3+} in a 2:1 ratio and the other by Sb^{5+} and Fe^{3+} in the same ratio. As was discussed above, cations that are similar in size and charge are able to occupy a single site in a disordered manner, whereas when significant differences exist the cations must occupy distinct sites in order to satisfy their bonding requirements. Fe^{3+} is sufficiently similar to Sb^{5+} and Co^{2+} to share a site with either of them [6, 7]. The difference in both size and charge between Sb^{5+} and Co^{2+} is larger, although they do share a site in $La_3Co_2SbO_9$. However, the presence of an equal concentration of Fe^{3+}, intermediate in both size and charge, eliminates the need for them to do so in $SrLa_2FeCoSbO_9$. The Fe/Co – O bond lengths around the 2*d* sites are, as expected, significantly longer than the Fe/Sb – O bond lengths around the 2*c* sites. We note that the mean *M* – O bond lengths around the six-coordinate cation sites in Sb_2O_5, Fe_2O_3, and CoO are 1.992, 2.029 and 2.129 Å, respectively [8-10]. The mean Sr/La – O bond length in $SrLa_2FeCoSbO_9$ is 2.639 Å, slightly larger than the mean La – O distance of 2.616 Å found in $La_3Co_2SbO_9$ [3].

The magnetic frustration introduced by the cation ordering pattern found in $La_3Co_2SbO_9$ has been blamed for the absence of well-defined long-range magnetic order in that compound and also in $La_3Ni_{2-y}Co_yO_9$ [3, 4]. In the case of $La_3Ni_2SbO_9$ we have argued that small ferrimagnetic microdomains exist below 108 K, but that they are too small to be detected in a zero-field neutron diffraction experiment [1, 2]. In the case of $SrLa_2FeCoSbO_9$, 50 % of the divalent transition-metal cations have been replaced by Fe^{3+} in a way that eliminates the former from the antimony-containing site. The magnetometry data shown in Figures 6.11 and 6.12 suggest that this results in a transition to a ferrimagnetic state at 215 K; the presence of long-range magnetic ordering is clearly demonstrated by the presence of magnetic Bragg scattering in the neutron diffraction patterns collected at 5 K, see Figure 6.14. The magnetic model used to account for the magnetic scattering is essentially an antiferromagnetic G-type magnetic structure [11], albeit with different ordered moments on the 2*c* and 2*d* sites, see Figure 6.13. This difference results in a net ferrimagnetism, and the model is thus qualitatively consistent with the magnetometry data. A G-type structure occurs when antiferromagnetic superexchange between nearest-neighbour (NN) cations is the dominant

magnetic interaction. If we assume that this is the only significant interaction operating in $SrLa_2FeCoSbO_9$ then we would expect to see a mean ordered moment of $M_{Fe}/3$ on the 2*c* site and an antiparallel moment of $(M_{Fe} + 2M_{Co})/3$ on the 2*d* site, resulting in a net magnetisation of M_{Co} per formula unit. Here M_{Fe} and M_{Co} are the magnetic moments of Fe^{3+} and Co^{2+} which would be expected to take values of ~5 and ~3 μ_B, respectively. The ordered moments determined by neutron diffraction and the magnetisation measured in 50 kOe are all lower than the values predicted by this simplistic model. We suggest that the presence of diamagnetic Sb^{5+} on 66 % of the 2*c* sites reduces the effectiveness and dominance of the NN coupling. Although there will be antiferromagnetic Fe – O – Fe and Co – O – Fe interactions between NN sites, it is likely that there will also be significant next-nearest-neighbour (NNN) 90 ° interactions along Fe – O – O – Fe or Fe – O – O – Co pathways. This type of interaction dominates in the 1:1 cation-ordered perovskite $SrLaNiSbO_6$ [12], where it results in the adoption of an Type I antiferromagnetic structure. We thus attribute the low values of the mean ordered moments on the six-coordinate sites to spin disorder that is itself a consequence of the presence of a disordered distribution of Sb^{5+} over 66 % of the 2*c* sites. The magnetic transition temperature of $SrLa_2FeCoSbO_9$ is higher than those of the other triple perovskites described above, which might in part be attributable to the large magnetic moment associated with Fe^{3+}. It might also be significant that the NN superexchange pathways are closer to linearity in $SrLa_2FeCoSbO_9$ than they are in $La_3Co_2SbO_9$. Close inspection of the temperature dependence of the magnetic susceptibility and the $M(H)$ data shows that our sample is not truly paramagnetic at 300 K. Superexchange interactions between NN Fe^{3+} cations in pseudo-cubic perovskites are known to be very strong [13, 14] and we suggest that the hysteresis seen in $\chi(T)$ above the Curie temperature is caused by short-range spin ordering involving some of these cations. It is also noticeable that the hysteresis loop of $SrLa_2FeCoSbO_9$ at 5 K displays an unusual asymmetric shape, which has also been observed in $La_3Co_2SbO_9$ and $La_3Ni_{2-y}Co_ySbO_9$. Although no explanation has been given yet, this feature might be in some way related to the presence of Co^{2+} in these perovskites. These issues will not be resolved until further experimental work has been undertaken.

6.5 Conclusions

The six-coordinate cations in $SrLa_2FeCoSbO_9$ order, we believe, in a previously-unreported manner. Consequently, and unlike $La_3Ni_2SbO_9$, $La_3Co_2SbO_9$ and $La_3Ni_{2-y}Co_ySbO_9$, this compound shows clear evidence of long-range magnetic order when studied by neutron

diffraction at low temperatures. The observed cation distribution, with diamagnetic Sb^{5+} partially occupying only one of the six-coordinate sites, results in ferrimagnetism below the Curie temperature of 215 K. This ordering temperature is considerably higher than the temperature of the magnetic transitions observed in the other three compounds, perhaps as a result of the involvement of the strongly-magnetic Fe^{3+} cations.

This work described in this chapter has been published as: Y. Tang, E. C. Hunter, P. D. Battle, M. Hendrickx, J. Hadermann, J. M. Cadogan, Inorganic Chemistry 57 (2018) 7438.

References

[1] P.D. Battle, S.I. Evers, E.C. Hunter, M. Westwood, Inorg. Chem. 52 (2013) 6648.

[2] P.D. Battle, M. Avdeev, J. Hadermann, J. Solid State Chem. 220 (2014) 163.

[3] D.G. Franco, V.C. Fuertes, M.C. Blanco, M.T. Fernandez-Diaz, R.D. Sanchez, R.E. Carbonio, J. Solid State Chem. 194 (2012) 385.

[4] D.G. Franco, R.E. Carbonio, G. Nieva, J. Solid State Chem. 207 (2013) 69.

[5] A.C. Larson, R.B. von Dreele, General Structural Analysis System (GSAS), Los Alamos National Laboratories, 1990.

[6] P.D. Battle, T.C. Gibb, A.J. Herod, S.-H. Kim, P.H. Munns, Journal of Materials Chemistry 5 (1995) 865.

[7] P.D. Thang, G. Rijnders, D.H.A. Blank, Journal of Magnetism and Magnetic Materials 295 (2005) 251.

[8] M. Jansen, Angew. Chem.-Int. Edit. Engl. 17 (1978) 137.

[9] E.N. Maslen, V.A. Streltsov, N.R. Streltsova, N. Ishizawa, Acta Crystallographica Section B-Structural Science 50 (1994) 435.

[10] N.C. Tombs, H.P. Rooksby, Nature 165 (1950) 442.

[11] E.O. Wollan, W.C. Koehler, Physical Review 100 (1955) 545.

[12] M.P. Attfield, P.D. Battle, S.K. Bollen, T.C. Gibb, R.J. Whitehead, Journal of Solid State Chemistry 100 (1992) 37.

[13] S.A. Ivanov, S.G. Eriksson, R. Tellgren, H. Rundlof, Materials Research Bulletin 36 (2001) 2585.

[14] W.C. Koehler, E.O. Wollan, J. Phys. Chem. Solids 2 (1957) 100.

Chapter 7: Structural and Magnetic Properties of $CaLa_2FeCoSbO_9$ and $ALa_2FeNiSbO_9$ (*A* = Ba, Sr, Ca)

7.1 Introduction

As described in Chapter 6, we have synthesised $SrLa_2FeCoSbO_9$, a double perovskite which exhibits a novel cation-ordering pattern that has not previously been reported in the literature. This compound adopts a monoclinic crystal structure and a G-type magnetic structure, and the complete 1:1 ordering of the cobalt and antimony cations, together with the random distribution of iron cations over the two crystallographically distinct B sites, leads to strong ferrimagnetism and a relatively high Curie temperature. The synthesis of perovskites containing more than one magnetic species on the B site has been attempted previously[1, 2], but without the presence of a pentavalent or hexavalent cation, ordering on the B site is usually absent. For example, it has been reported that the perovskite-type system $LaFe_xNi_{1-x}O_3$ ($0 \leq x \leq 1$) crystallizes in a rhombohedral or orthorhombic space group, with iron and nickel being completely disordered over the B site[3]. In another study, which involved simultaneous substitution of the alkaline earth element on the A site, the system of $La_{0.5}Ba_{0.5}Co_{1-x}Fe_xO_{3-\delta}$ ($0 \leq x \leq 1$ and $0.05 \leq \delta \leq 0.07$) was reported to adopt cubic symmetry without ordering of the iron and cobalt cations on the B site[4]. Our previous work on $Sr_3Fe_2TeO_9$ revealed relatively unusual 2:1 ordering of Fe^{3+} and Te^{6+} over the B sites, and the antiferromagnetic nature of this compound largely stems from this ordering pattern[5]. These facts emphasize how B-site ordering results from the charge and size differences between ions and how the ordering then leads to particular physical properties. In this chapter we have focused on the calcium analogue of $SrLa_2FeCoSbO_9$, $CaLa_2FeCoSbO_9$, and the nickel-containing series: $ALa_2FeNiSbO_9$ (*A*=Ba, Sr, Ca), which might potentially show similar B-site ordering pattern to that in $SrLa_2FeCoSbO_9$ and consequently ferrimagnetic behaviour. We have undertaken our investigation of these compounds using a combination of X-ray and neutron diffraction, electron microscopy and Mössbauer spectroscopy. The results of this study, which reveal the differences both in crystal structure and magnetic properties between these four compounds and $SrLa_2FeCoSbO_9$, are described in this chapter.

7.2 Experimental methods

Polycrystalline sample of $CaLa_2FeCoSbO_9$ was prepared using the standard ceramic method. $CaCO_3$, La_2O_3, Fe_2O_3, Co_3O_4 and Sb_2O_5 (purity >99.95%) were weighed out in the appropriate stoichiometric ratio and ground together in an agate mortar for 30 minutes to give a homogeneous mixture. La_2O_3 was heated at 800 °C for 24 hours prior to use to ensure it was completely dry. The mixture was then loaded into an alumina crucible and fired at 800 °C for 24 h. It was then quenched to room temperature, reground and pressed into a pellet which was fired in air at 1300 °C for 48 hours and subsequently annealed at 1300 °C for another 48 hours after further grinding. Finally, the furnace was allowed to cool to 800 °C and then the sample was quenched to room temperature. Polycrystalline samples of $ALa_2FeNiSbO_9$ (*A*=Ba, Sr, Ca) were prepared under the same conditions with starting materials of ACO_3(*A*=Ba, Sr, Ca), La_2O_3, Fe_2O_3, NiO and Sb_2O_5 (purity >99.95%) in the appropriate stoichiometric ratio.

The brown-black reaction products were initially characterised by X-ray powder diffraction (XRPD) using Cu $K\alpha_1$ radiation. The data, collected at room temperature on a Panalytical X'Pert diffractometer, were analysed using the Rietveld method as implemented in the GSAS[6] program package. Neutron diffraction patterns were collected from some of the products on the constant-wavelength powder diffractometers D1b and D2b at ILL, Grenoble, France. Data were collected at temperatures of 300 and 5 K using wavelengths of 2.52 Å and 1.594 Å for D1b and D2b at ILL, respectively. The data from the former have a relatively high signal:noise ratio and are principally used in the study of magnetic ordering whereas D2b produces high-resolution data suitable for use in the refinement of crystal structures. In both cases data analysis was performed using the Rietveld method[7]. The peak shape was modelled using the function devised by van Laar and Yelon[8] and the background was fitted using a twelve-term Chebyschev polynomial. Data were collected from the other reaction products at 5K and 300K on the GEM time-of-flight diffractometer at the ISIS spallation source. The data collected on detector banks at scattering angles, 2θ, of 34.96°, 63.62°, 91.30° and 154.40° were refined simultaneously.

The molar magnetic susceptibilities of these compounds were measured over the temperature range $2 < T/K < 370$ using a Quantum Design MPMS 5000 SQUID magnetometer. Data were collected on warming in a field of 100 Oe after cooling the samples both in the absence of an

applied field (zero-field cooled, ZFC) and in the measuring field (field cooled, FC). The isothermal sample magnetisation of each sample was measured as a function of field over the range –50 < H/kOe < 50 at 300 and 5 K after cooling in a field of 50 kOe.

Transmission electron microscopy (TEM) studies were carried out on all four compounds in this chapter by Prof. Joke Hadermann and Mylène Hendrickx at the University of Antwerp, and ^{57}Fe Mössbauer spectroscopy experiments were conducted on the sample $CaLa_2FeCoSbO_9$ by Prof. J. M. Cadogan at the Australian Defence Force Academy, as described in Chapter 2.

7.3 Results

The XRPD patterns of the reaction products $CaLa_2FeCoSbO_9$ and $ALa_2FeNiSbO_9$ (*A*=Ba, Sr, Ca) suggested that the syntheses had produced pseudo-cubic perovskites. The temperature dependence of the dc molar magnetic susceptibilities of these four compounds is shown in Figure 7.1, along with the field dependence of the magnetisation as measured at 300 K and 5 K. In the case of $CaLa_2FeCoSbO_9$, the ZFC and FC susceptibilities differ below a temperature which is in excess of 300 K. The non-linearity of the $M(H)$ curve and the presence of a small but clear remanent magnetisation provides evidence that this compound is not a simple paramagnet at 300 K. The curve collected at 5 K is asymmetric with an unusual shape similar to that of $SrLa_2FeCoSbO_9$ (see Chapter 6) and shows a remanent magnetisation of ~1 μ_B, see Table 7.1; the magnetisation is unsaturated in a field of 40 kOe. The data collected on the three nickel-containing compounds are similar to each other but different from those collected on the cobalt analogues. The $\chi(T)$ curves of all three compositions show a small difference between the ZFC and FC susceptibilities at 300 K and a remanent magnetisation is seen in each case. The remanent magnetisation at 5 K is smaller than that observed in the cobalt containing compositions, the $M(H)$ loops are much narrower and the curves appear to be approaching lower saturation values. Below we describe the results of the X-ray and neutron diffraction studies that we have performed in an attempt to understand the magnetic behaviour of these compounds, although electron microscopy studies, which will also be discussed later, have revealed that these techniques do not give a complete description of these compounds.

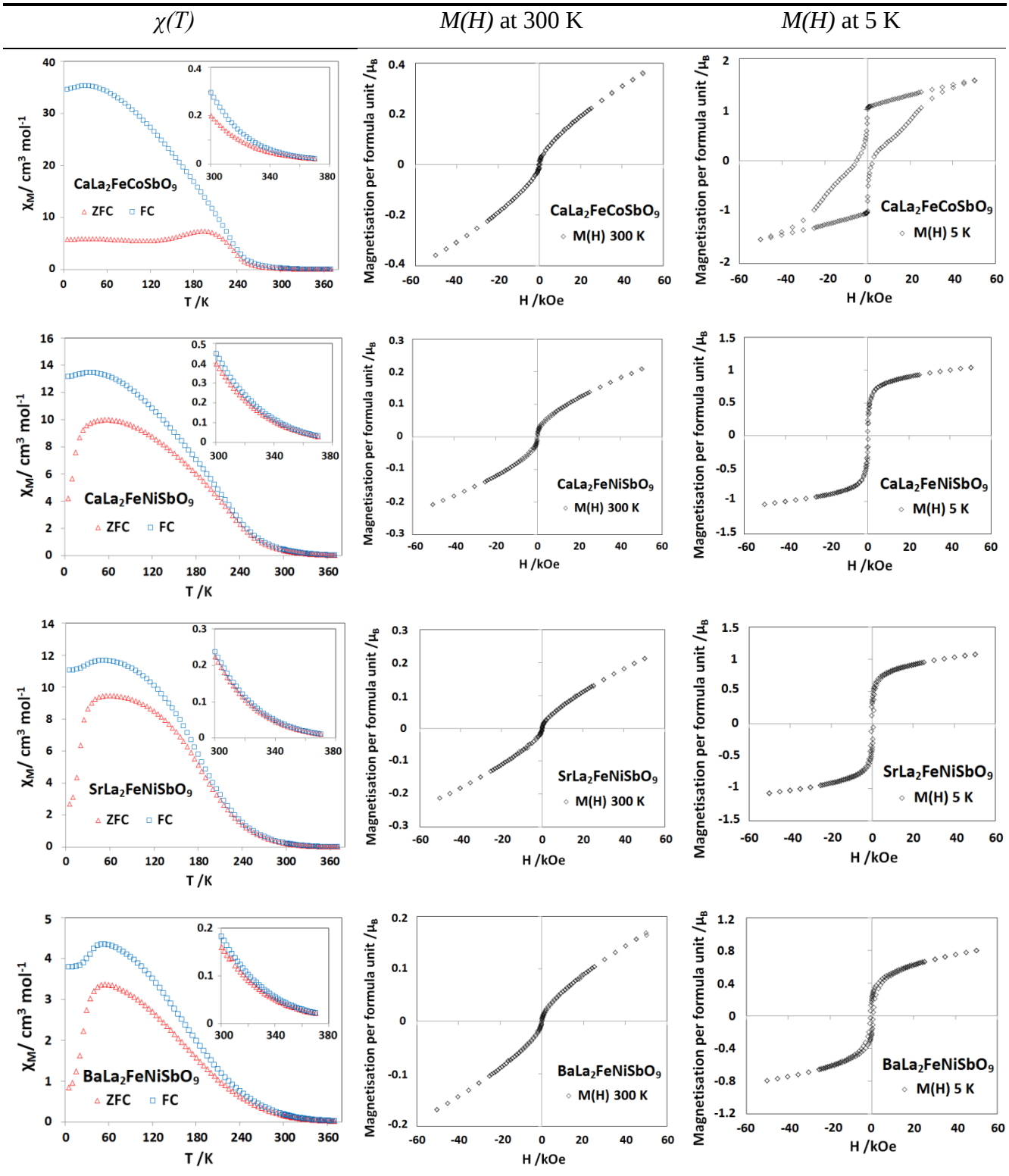

Figure 7.1 The temperature dependence of the dc molar magnetic susceptibilities and the field dependence of the magnetisation per formula unit at 5 K of $CaLa_2FeCoSbO_9$ and $ALa_2FeNiSbO_9$ (*A*=Ca, Sr, Ba).

Table 7.1 Coercive fields and remanent magnetisation per formula unit, H_c (kOe) and M_r (μ_B) at 5 K of $CaLa_2FeCoSbO_9$ and $ALa_2FeNiSbO_9$ (*A*=Ca, Sr, Ba)

Compound	H_c (kOe)	M_r (μ_B)
$CaLa_2FeCoSbO_9$	5.0	1.0
$BaLa_2FeNiSbO_9$	7.0	0.21
$SrLa_2FeNiSbO_9$	4.5	0.35
$CaLa_2FeNiSbO_9$	2.3	0.24

The XRD pattern of each compound was indexed and analysed in the primitive monoclinic space group $P2_1/n$ with $a \sim\sqrt{2}a_p$, $b \sim\sim\sqrt{2}a_p$ and $c \sim 2a_p$, where a_p is the unit cell parameter of a primitive cubic perovskite. The data are shown in Figure 7.2 from which it can be seen that $CaLa_2FeCoSbO_9$ shows the largest monoclinic strain. In this space group the structural model, see Figure 7.3, involves a 4*f* site that accommodates a disordered distribution of *A* and La, three further 4*f* sites that accommodate oxide anions and two independent B sites, *2d* (½, 0, 0) and *2c* (0, ½, 0) which accommodate the three cation species Fe^{3+}, Co^{2+}/Ni^{2+} and Sb^{5+}. The X-ray scattering lengths of iron, cobalt and nickel are very similar and it was impossible to distinguish between them using our X-ray data. As in Chapter 6, they were therefore treated as if they were identical in this analysis. Refinements of the distribution of a representative transition-metal and antimony over the crystallographically-distinct B sites showed that in each case the 2*d* (½,0,0) sites are largely occupied by transition metals, while nearly all the antimony atoms are on the *2c* (0, ½, 0) sites. For example, the fit to the data shown in Figure 7.2(a) is based on the refined cation distribution $CaLa_2(Fe/Co_{1.47}Sb_{0.03})_{2d}(Fe/Co_{0.53}Sb_{0.97})_{2c}O_9$. Although they did not establish the distribution of iron and cobalt or iron and nickel, our XRPD data thus enabled us to establish the space group symmetry of these compounds and that essentially all the antimony is located on a single six-coordinate site in each of the four compositions.

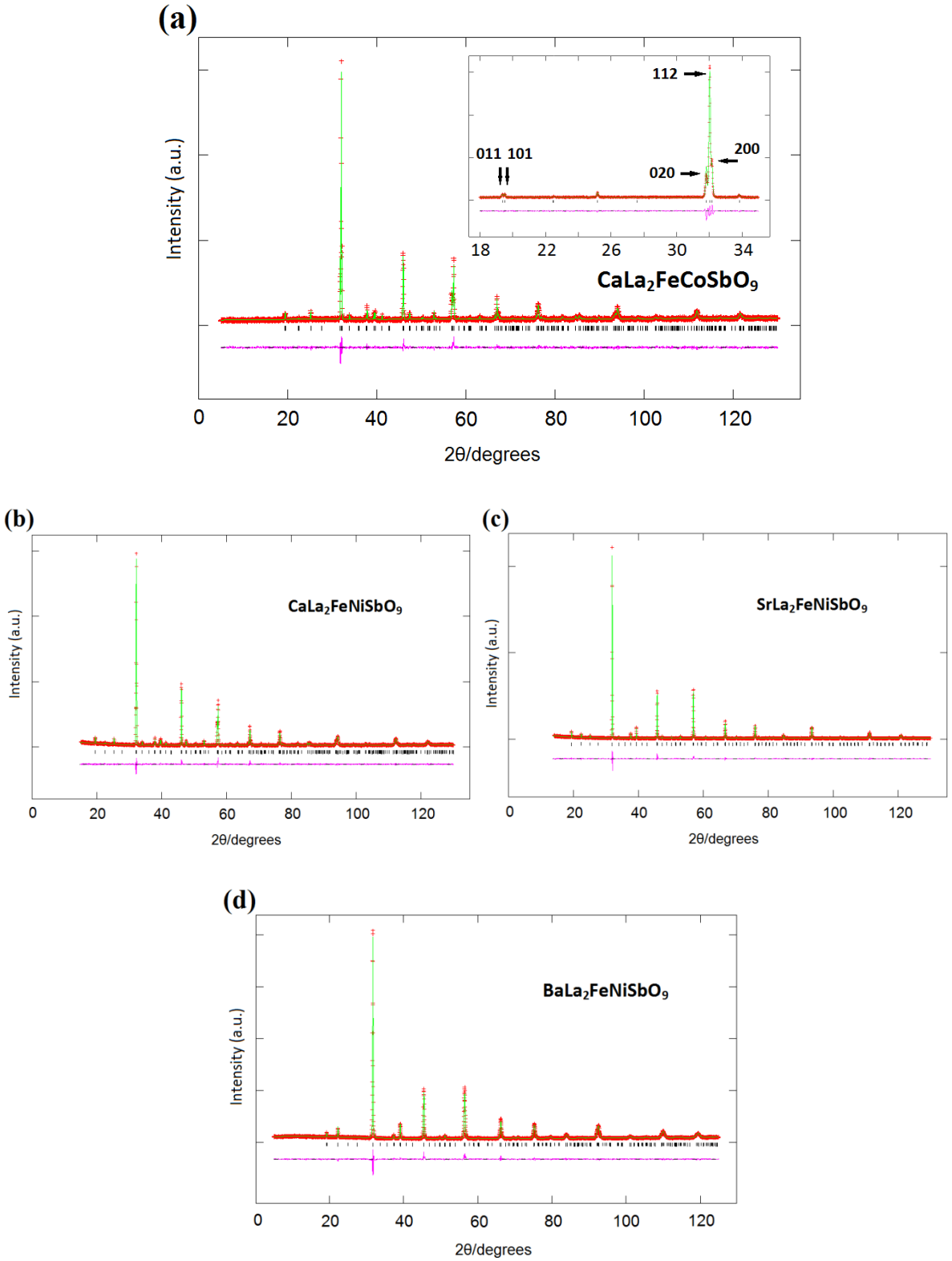

Figure 7.2 Observed (red), calculated (green) X-ray powder diffraction patterns of (a) $CaLa_2FeCoSbO_9$, (b) $CaLa_2FeNiSbO_9$, (c) $SrLa_2FeNiSbO_9$ and (d) $BaLa_2FeNiSbO_9$ at room temperature. A difference curve (purple) is shown and reflection positions are marked. Inset shows the splitting of peaks at lower angles.

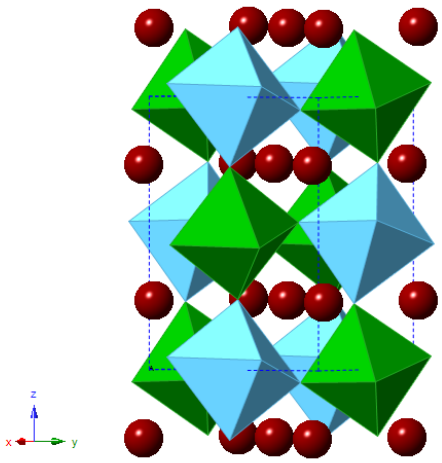

Figure 7.3 $P2_1/n$ structure adopted by $CaLa_2FeCoSbO_9$ and $ALa_2FeNiSbO_9$ (*A*=Ca, Sr, Ba). Green octahedra and blue octahedra are occupied by different distribution of cations. Red circles represent the alkaline earth and La atoms at the A site.

Although the XRPD patterns presented above suggest the formation of pure perovskite-like phases, our TEM data show that these samples are actually inhomogeneous. The Fe/Co/Sb mixed-element map of $CaLa_2FeCoSbO_9$ shown in Figure 7.4 shows some regions with an inhomogeneous distribution of the transition metals. In addition, the regions that have an excess of Fe also have an increased La content. This implies that the A-cations, La and Ca, are also inhomogeneously distributed, see Table 7.2. It appears that there are entire particles with an excess of Fe and La, not only small domains within larger particles. Similar element-distribution maps were acquired from the sample of $CaLa_2FeNiSbO_9$. Figure 7.5 clearly shows an inhomogeneous distribution for both the A-cations (La, Ca) and the B-cations (Fe, Ni, Sb). The variations between the minimum and maximum content are significant, especially for the B-cations, see Table 7.3. Three main phases or compositions were observed. The first consists of the expected composition with equal concentration of the B cations and a 1:2 ratio for the A-cations Ca:La; the second phase is Fe-poor, with increased concentrations of Ni and Sb and a decreased Ca content; the third phase is Fe-rich, in which case the concentrations of Ni and Sb decrease (Ni < Sb) and the La content slightly increases. The relevant data are tabulated in the Appendix as Table A7.1.

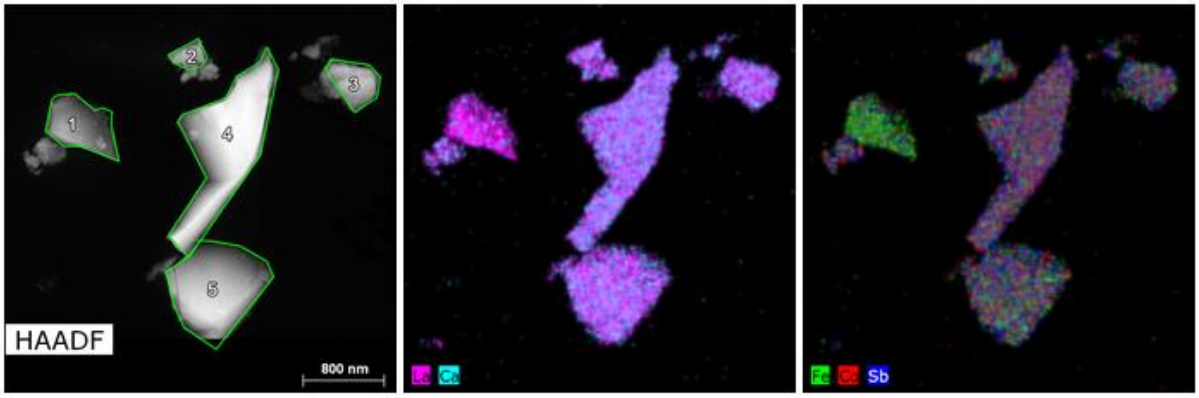

Figure 7.4 HAADF-STEM image of particles in the sample of $CaLa_2FeCoSbO_9$ with mixed (La/Ca, Fe/Co/Sb) element maps. The composition of the regions marked in the HAADF-STEM image is presented in Table 7.2.

Table 7.2 Element content of $CaLa_2FeCoSbO_9$ from the crystals marked in Figure 7.4. Values are given in atomic %; the ideal values across a row would be 16.6, 33.3, 16.6, 16.6 and 16.6.

crystal	Ca	La	Fe	Co	Sb
1	8.18	45.57	28.46	9.64	8.16
2	18.00	35.90	15.77	14.76	15.57
3	18.76	34.72	13.75	16.52	16.24
4	20.50	32.51	11.82	16.81	18.36
5	18.58	34.78	14.81	15.50	16.33

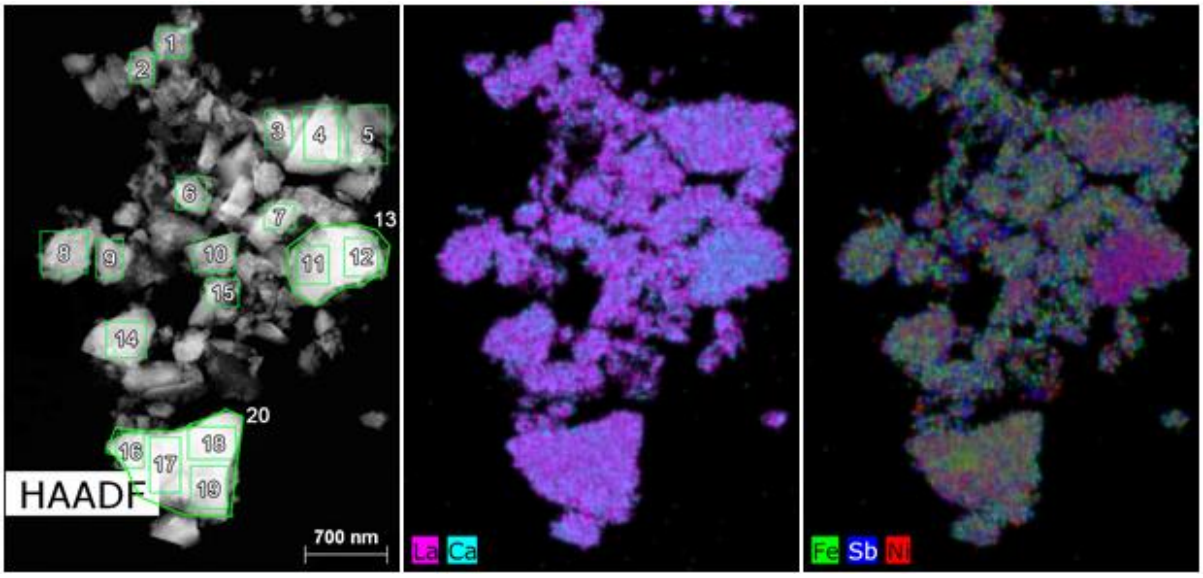

Figure 7.5 HAADF-STEM image of particles in the sample of $CaLa_2FeNiSbO_9$ with mixed (La/Ca, Fe/Ni/Sb) element maps. Both the two mixed element maps show regions with different compositions.

Table 7.3 Element content of $CaLa_2FeNiSbO_9$ from the regions being investigated. Values are given in atomic %.

	Ca	La	Fe	Ni	Sb
average	18.32	34.61	14.96	15.17	16.94
standard deviation	2.29	2.49	4.36	2.43	2.35
min	12.89	27.39	4.51	7.84	10.74
max	24.88	42.71	27.92	21.56	23.28

$SrLa_2FeNiSbO_9$ and $BaLa_2FeNiSbO_9$ were selected to be studied with techniques having higher resolution. SAED patterns taken from different zone axes ([100], [010], [001], [110] and [201]) of the $SrLa_2FeNiSbO_9$ sample shown in Figure 7.6 can be indexed with the $P2_1/n$ model. Figure 7.7 shows the HAADF-STEM image along the [100] orientation where ordering of the B-cations is clearly visible. The continuous rows of bright dots along the *a*-axis correspond to the non-ordered A sites occupied by La and Sr. The rows with alternation of darker and brighter dots along the *a*-axis correspond to the alternating (Ni,Fe) and (Sb,Fe) atom columns, respectively. In addition, the A site columns are slightly shifted along *b* in alternating sense, which confirms the symmetry described by $P2_1/n$. Figure 7.8 shows averaged atomic resolution EDX maps from two independent EDX measurements obtained along the [010] orientation of $SrLa_2FeNiSbO_9$. The A-cations, La and Sr, are indicated in red in the EDX map and do not show ordering. The B-cations are indicated by three different colours: Fe, Ni and Sb mapped in yellow, blue and green, respectively. Ordering of Ni and Sb over neighbouring sites is observed, while Fe is on both B sites. This crystallite thus shows ordering similar to that seen in $SrLa_2FeCoSbO_9$. Inhomogeneity was identified in this sample by overview EDX maps, see Figure 7.9, although it is less pronounced than in the calcium analogue. The average element content was acquired from studying different crystals of the sample, and again a deviation from the ideal composition was observed, which is a direct consequence of the inhomogeneity, see Table 7.4 and Table A7.2.

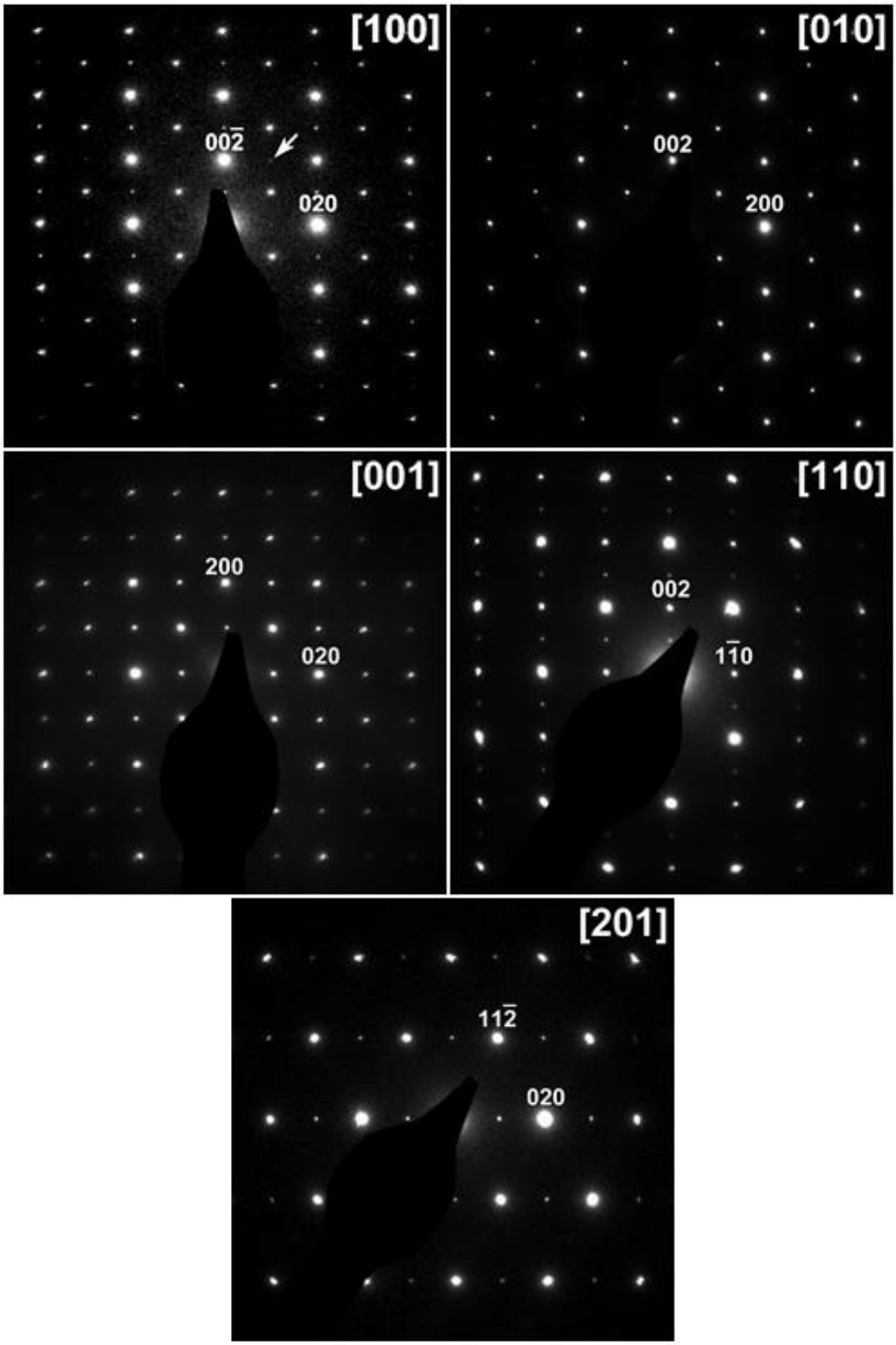

Figure 7.6 SAED patterns of the $SrLa_2FeNiSbO_9$ sample along the zone axes [100], [010], [001], [110] and [201].

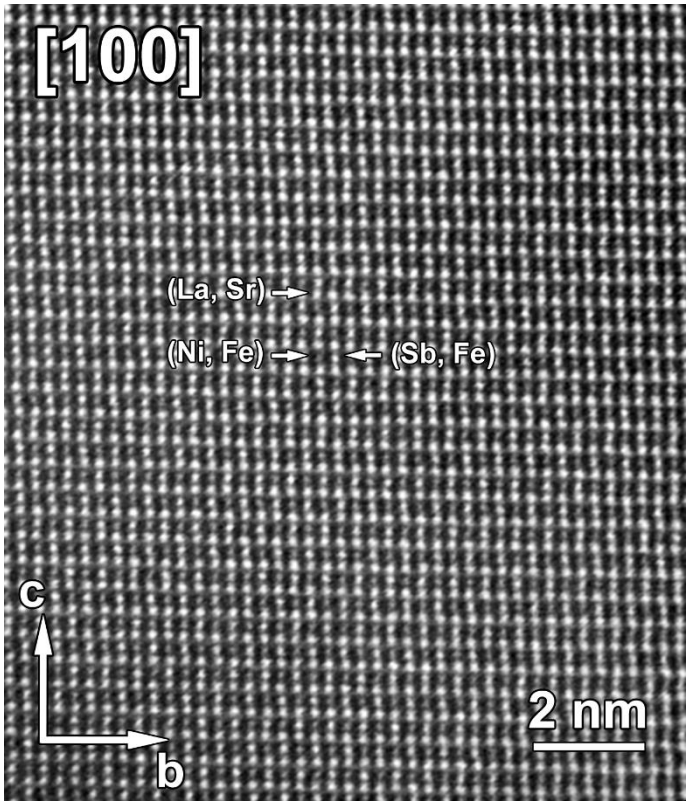

Figure 7.7 High resolution HAADF-STEM image of $SrLa_2FeNiSbO_9$ along the [100] zones axis, where the continuous rows of bright dots along the a-axis are occupied by both La and Sr. The rows with alternation of darker and brighter dots along the a-axis correspond to (Ni,Fe) and (Sb,Fe) atom columns, respectively.

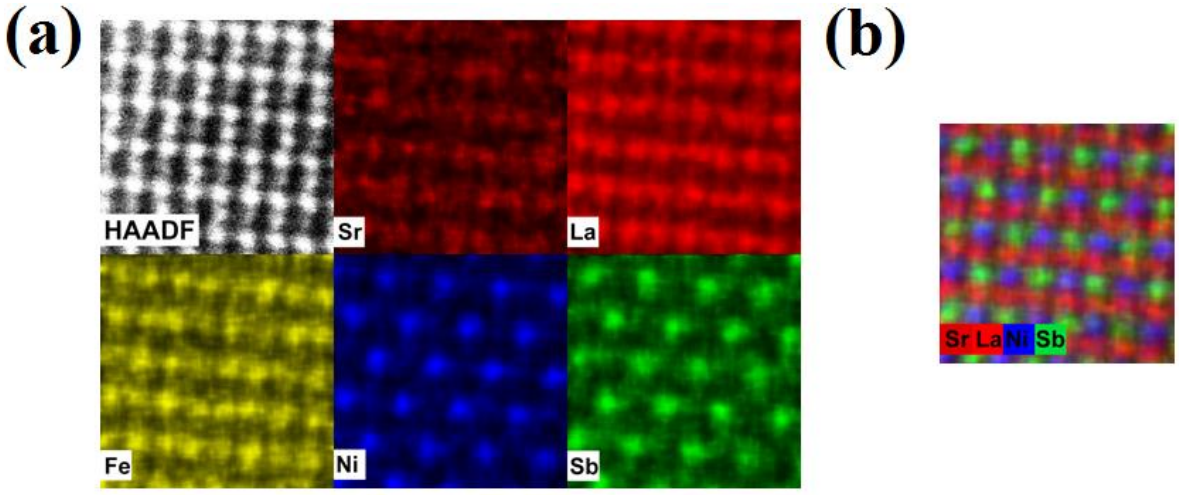

Figure 7.8 (a) Top left: high resolution HAADF-STEM image of the $SrLa_2FeNiSbO_9$ sample along [010]. Ni and Sb atoms are ordered in a 1:1 ratio, while Fe is present at both B sites. (b) High resolution EDX map in which the individual element maps of Sr, La, Ni and Sb are combined. 1:1 ordering between Ni and Sb over the B sites is clearly seen.

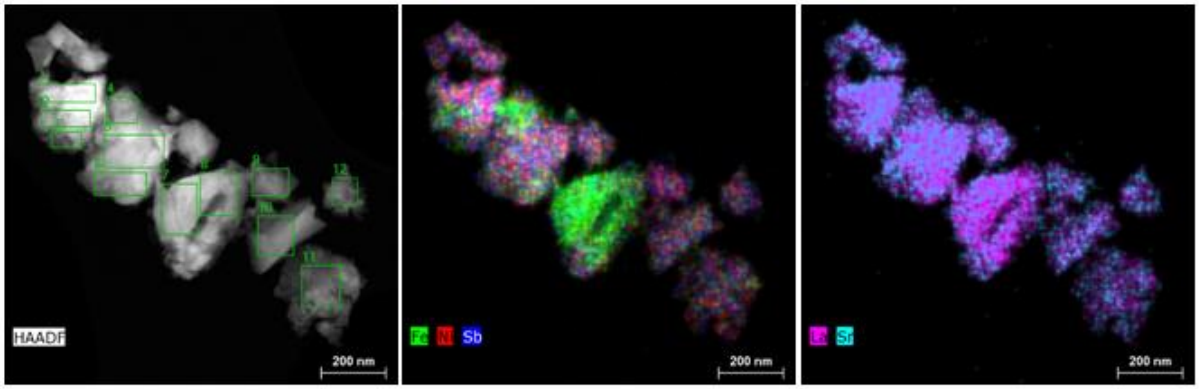

Figure 7.9 HAADF-STEM image of $SrLa_2FeNiSbO_9$ together with mixed element maps (Fe,Ni,Sb) and (Sr,La). The marked regions in the HAADF-STEM image were used in composition analysis.

Table 7.4 Element content of the sample $SrLa_2FeNiSbO_9$ derived from the regions studied by TEM. Values are present in atomic %.

	Sr	La	Fe	Ni	Sb
average	15.1	35.6	17.1	15.4	16.8
standard deviation	2.5	3.9	7.1	3.8	3.4

The inhomogeneity observed in these perovskites is most significant in $BaLa_2FeNiSbO_9$. The electron diffraction patterns, see Figure 7.10 and 7.11, clearly suggest that our sample consists of two ordered phases with symmetries *I*2/*m* or *I*4/*m* and $P2_1/n$. Figure 7.12 shows the HAADF-STEM image along the [100] orientation of the $P2_1/n$ phase, where the order at the positions of the B-cations is clearly visible. The continuous rows of bright dots along the *b*-axis represent atom columns occupied by La and Ba. The rows with alternating dark and bright dots along the *b*-axis correspond to the (Ni, Fe) and (Sb, Fe) atom columns, respectively. Figure 7.13 shows an averaged atomic-resolution EDX map from five independent measurements obtained along the [010] orientation for either the $P2_1/n$ or *I*2/*m* (*I*4/*m*) phase. As in the strontium analogue, it is clear that the A-cations are disordered, while the B-cations are ordered in a 1:1 ratio, with Fe present on both B sites. The EDX map also shows a slight preference of Fe for the Sb positions. EDX maps with lower resolution were taken in order to understand the presence of the two different phases, potentially with

different compositions. Figure 7.14 exemplifies the EDX maps of different particles, where an inhomogeneous distribution is seen for both the B-cations and A-cations. There are regions with an equal distribution of the B-cations (Fe, Ni and Sb), while some other regions contain either more or less Fe. When the concentration of Fe is high, the concentration of La again increases (La/Ba > 2). Furthermore, the average composition of the independent particles can deviate from the expected composition, see Table 7.5 and Table A7.3.

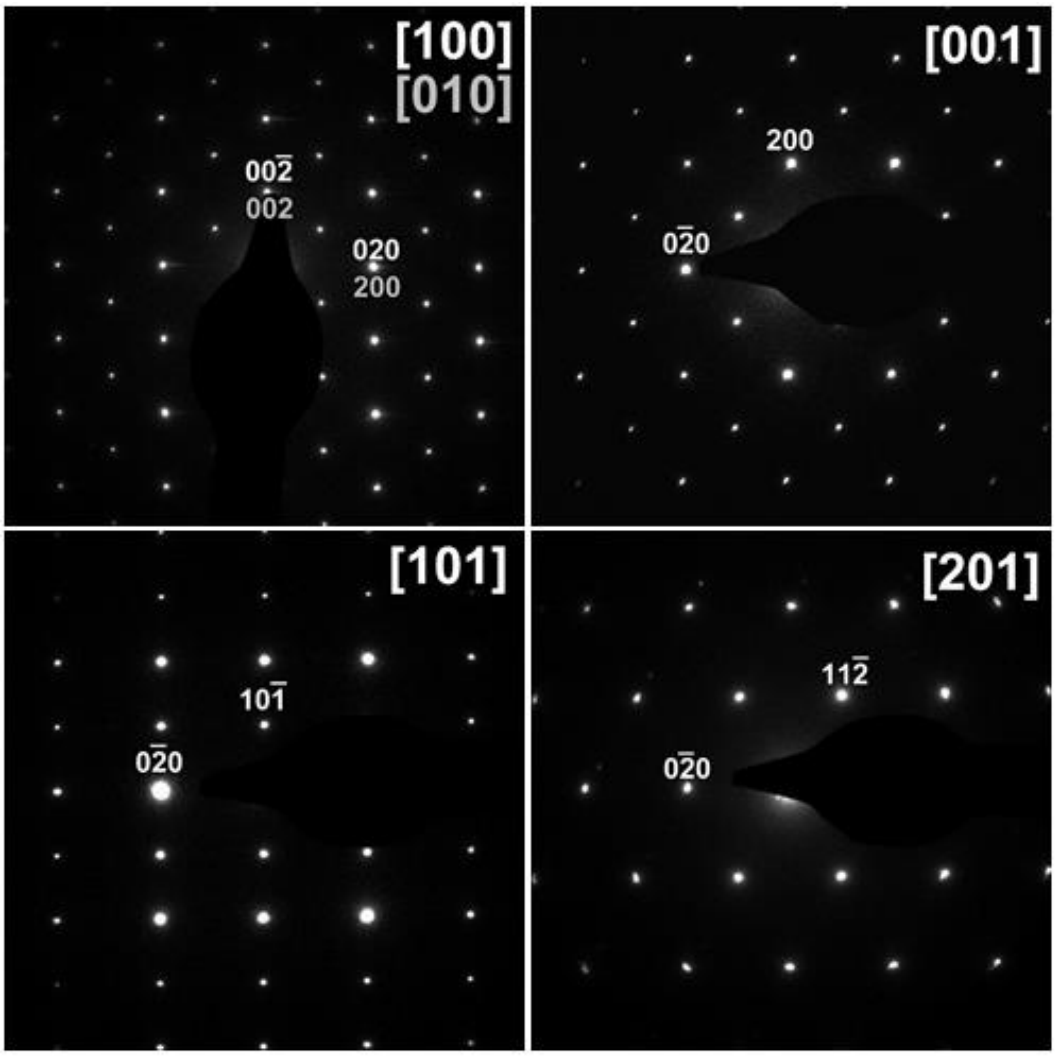

Figure 7.10 SAED patterns of the $BaLa_2FeNiSbO_9$ sample along the zone axes [100], [010], [001], [101] and [201] corresponding to space group *I*2/*m* or *I*4/*m*.

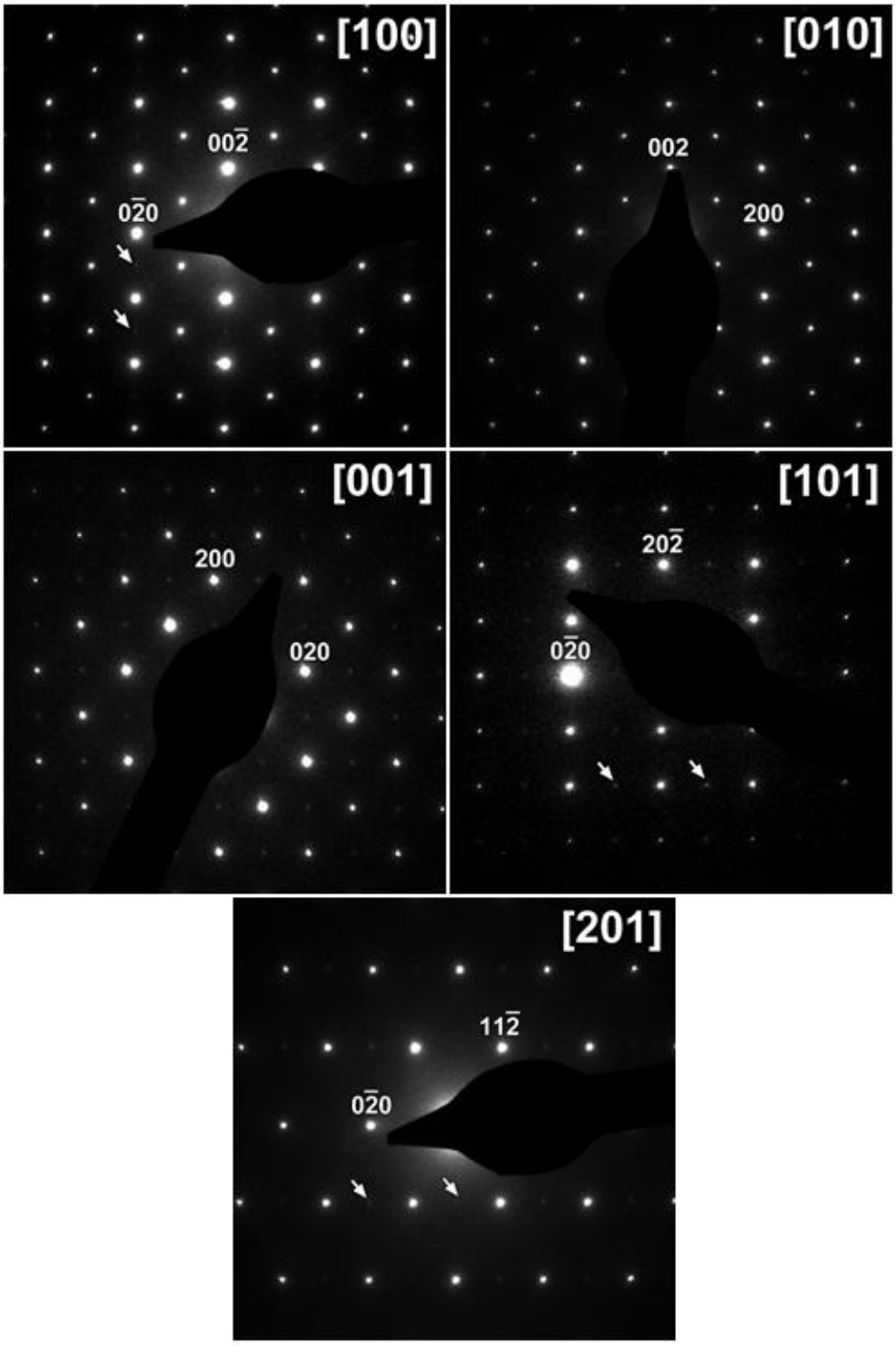

Figure 7.11 SAED patterns of the $BaLa_2FeNiSbO_9$ sample along the zone axes [100], [010], [001], [101] and [201] corresponding to space group $P2_1/n$.

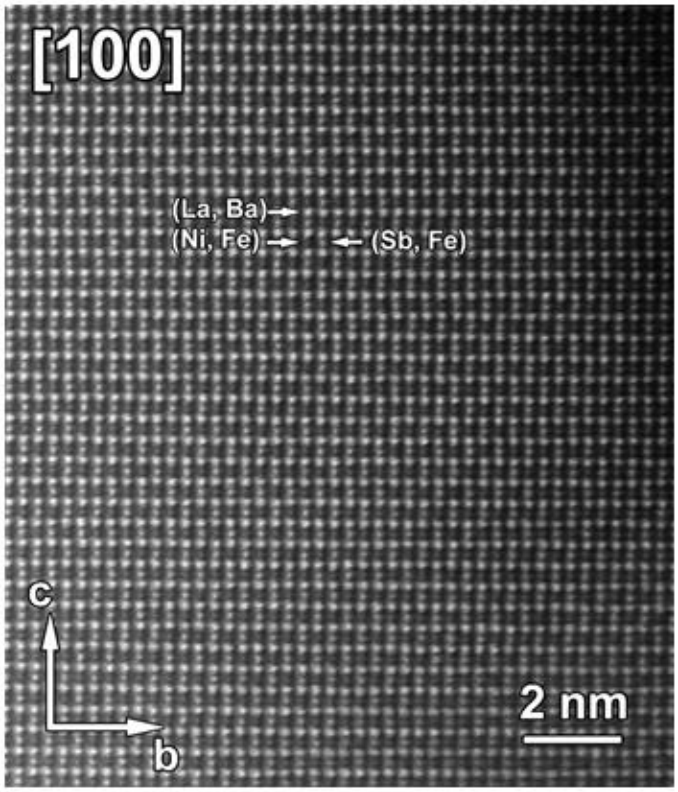

Figure 7.12 High resolution HAADF-STEM image of $BaLa_2FeNiSbO_9$ in $P2_1/n$ symmetry along the [100] zones axis, where the continuous rows of bright dots along the b-axis are occupied by both La and Ba. The rows with alternation of darker and brighter dots along the b-axis correspond to (Ni,Fe) and (Sb,Fe) atom columns, respectively.

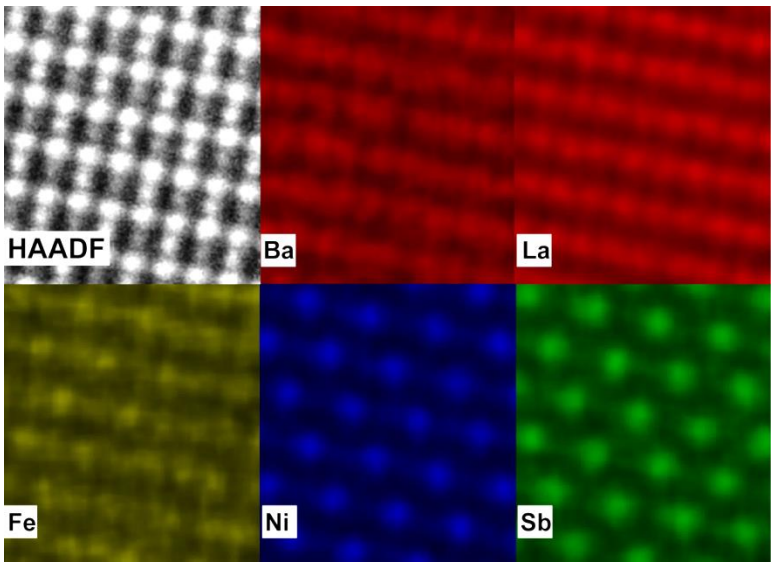

Figure 7.13 Top left: high resolution HAADF-STEM image of the $BaLa_2FeNiSbO_9$ sample along [010]. Ordering is present between Ni and Sb over B sites (Ni:Sb = 1:1), while Fe is present at both B sites with a preference for the Sb position.

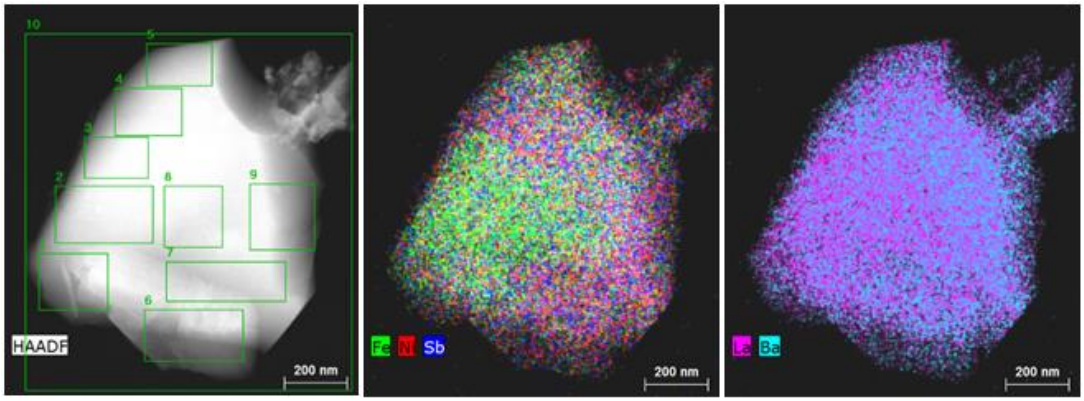

Figure 7.14 Left: HAADF-STEM image of $BaLa_2FeNiSbO_9$ in which regions are marked for composition analysis. Middle: mixed element map of Fe, Ni and Sb, where an inhomogeneous distribution can be seen. Right: mixed element map of La and Ba, also here the elements are inhomogeneously distributed.

Table 7.5 Element content of the sample $BaLa_2FeNiSbO_9$ derived from the regions studied by TEM. Values are present in atomic %.

	Ba	La	Fe	Ni	Sb
average	15.3	36.7	18.1	14.7	15.1
standard deviation	4.0	4.9	6.5	3.4	4.0

According to the EDX measurements presented above, we can conclude that the four samples discussed in this chapter are inhomogeneous, and we suggest decreasing homogeneity from left to right: $CaLa_2FeCoSbO_9$ – $SrLa_2FeNiSbO_9$ – $CaLa_2FeNiSbO_9$ – $BaLa_2FeNiSbO_9$. However, statistics from TEM are always poor. These samples show inhomogeneity within the crystals, while they also contain some entire crystals with a different composition, making the interpretation of their physical properties complicated.

$CaLa_2FeCoSbO_9$ was studied by Mössbauer spectroscopy at room temperature. The spectrum with a large velocity scale, see Figure 7.15, can be fitted with a simple quadrupole doublet, indicating the sample is paramagnetic at room temperature. However, one doublet is not sufficient to fit the high-resolution spectrum taken over a smaller velocity scale, and it is best fitted with two quadrupole doublets, which is consistent with the two crystallographically-distinct B sites partially occupied by Fe in the $P2_1/n$ model, see Figure 7.16. There was no evidence of magnetic hyperfine splitting.

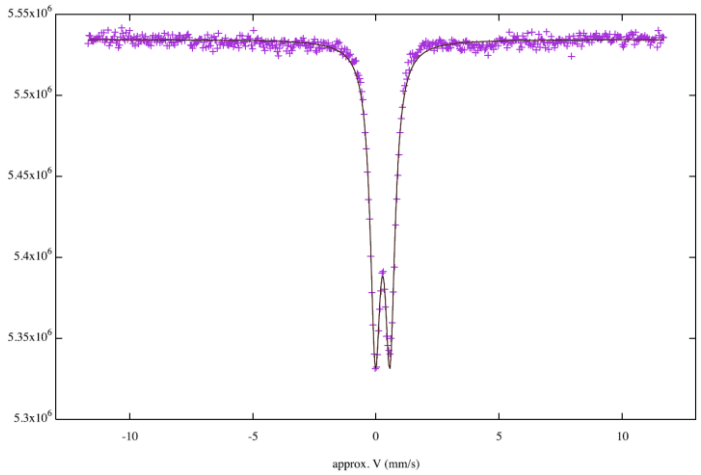

Figure 7.15 ^{57}Fe Mössbauer spectrum of $CaLa_2FeCoSbO_9$ acquired at room temperature on an extended velocity scale.

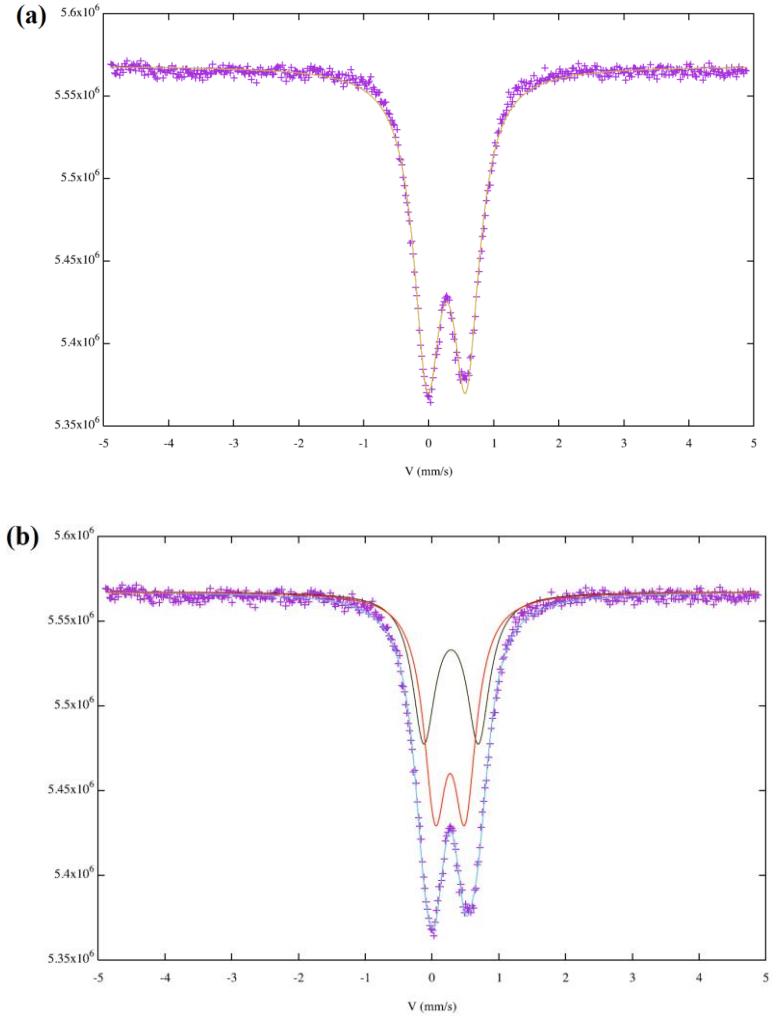

Figure 7.16 ^{57}Fe Mössbauer spectra of $CaLa_2FeCoSbO_9$ acquired at room temperature on a narrower velocity scale and fitted to (a) one doublet; (b) two doublets.

As it was not possible to identify the accurate compositions of the different phases detected by TEM, all the neutron diffraction data collected on these four compounds were analysed using a single-phase structural model in space group $P2_1/n$. In analysing the time-of-flight neutron diffraction pattern of $CaLa_2FeCoSbO_9$ collected at 300 K the distribution of cations was allowed to vary away from that determined by XRPD. It was necessary to refine the cation distribution because, in contrast to $SrLa_2FeCoSbO_9$, additional intensity was apparent in the (101) and (011) reflections in the neutron diffraction pattern collected at 300 K if we assumed the cation distribution was $CaLa_2(Fe_{0.5}Co)_{2d}(Fe_{0.5}Sb)_{2c}O_9$. Although this additional intensity can also be accounted for by magnetic scattering, the Mössbauer spectrum suggested that all the Fe^{3+} cations in the sample were paramagnetic, and it was therefore reasonable not to include a magnetic structure in this refinement. We were able to allow the distribution of cobalt and iron atoms over the 2*c* and 2*d* sites to vary, provided that the overall composition was held constant. The occupancy of cobalt on the *2c* site refined to zero, and the iron atoms were found to be distributed over the two sites. Consistent with the XRPD data, most of the antimony atoms were found to occupy the 2*c* site, with a minor amount occupying the 2*d* site. The final refined cation distribution from neutron diffraction data can be represented by the formula $CaLa_2(Fe_{0.32}CoSb_{0.18})_{2d}(Fe_{0.68}Sb_{0.82})_{2c}O_9$. The data collected at 5 K were analysed by holding the cation distribution fixed at that determined from the room-temperature data. The principal change on cooling was an increase in the intensity of the (101) and (011) reflections, and in order to model this increase in intensity it was necessary to allow for the presence of magnetic Bragg scattering. The extra intensity could be accounted for by the G-type magnetic structure shown in Figure 7.17, where the mean magnetic moment on each B site is coupled in an antiparallel manner to those of the six nearest-neighbour sites. The mean moments on the Fe/Co-containing 2*d* sites and the Fe/Sb-containing 2*c* sites refined to values of 2.56(3) and 0.94(2) μ_B per cation, respectively. Given that Sb^{5+} is diamagnetic, the former value and the latter value corresponds to a moment of 2.91(3) and 2.08(5) μ_B per Fe^{3+} cation, respectively. Analysis of the neutron data thus leads to a description of $CaLa_2FeCoSbO_9$ as a ferrimagnet at 5 K with a net moment of 2.43(5) μ_B per formula unit. The structural parameters derived from analysis of the data collected at both 300 and 5 K are listed in Table 7.6, with the bond lengths in Table 7.7. The fits to the data collected on banks 3 to 6 at both 300 K and 5 K are shown in Figure 7.18.

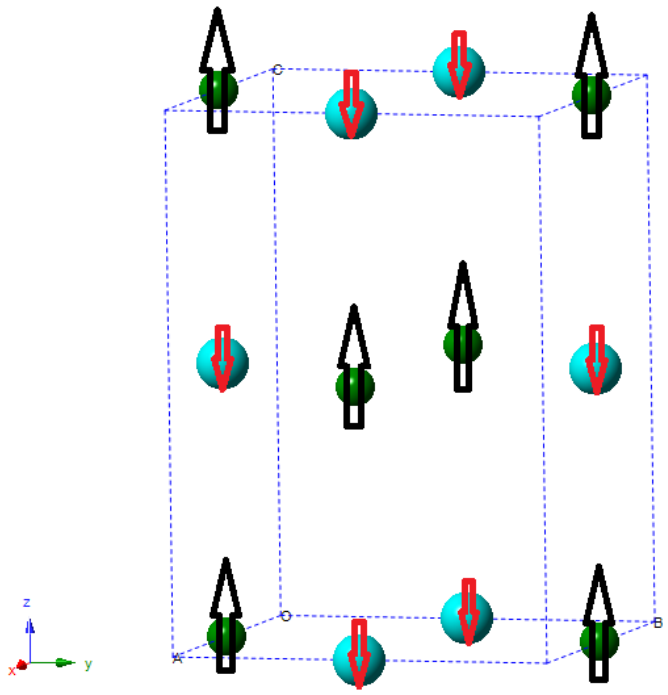

Figure 7.17 The G-type magnetic structure adopted by $CaLa_2FeCoSbO_9$. Arrows indicate the direction of ordered spins at the B sites. Green spheres represent the 2*d* sites and blue spheres represent the 2*c* sites.

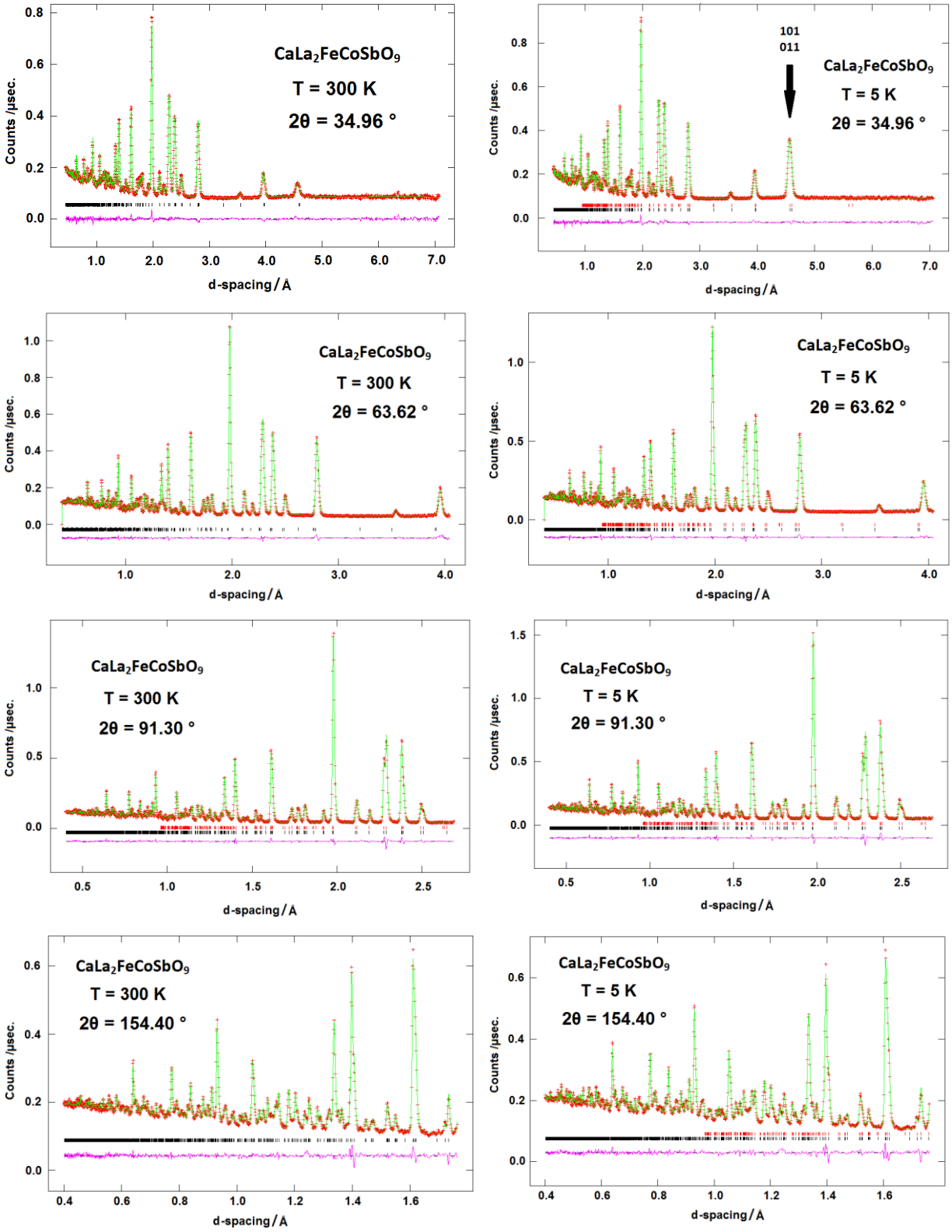

Figure 7.18 Observed (red), calculated (green) time-of-flight neutron diffraction patterns of $CaLa_2FeCoSbO_9$ at 300 K and 5 K collected at four banks. A difference curve (purple) is shown and reflection positions are marked. Black bars represent structural reflections and red bars represent magnetic reflections. An arrow indicates the peak with the strongest magnetic contribution.

Table 7.6 Refined structural parameters for $CaLa_2FeCoSbO_9$ at 300 and 5 K; space group $P2_1/n$

T (K)			300	5
a (Å)			5.5646(3)	5.5547(3)
b (Å)			5.6187(4)	5.6182(3)
c (Å)			7.8918(5)	7.8777(4)
β (°)			89.998(9)	89.996(8)
R_{wpr}			2.71%	2.72%
χ^2			1.66	3.29
Ca/La	4*e*	Occupancy	0.3333/0.6667	0.3333/0.6667
		x	0.4929(2)	0.4918(2)
		y	0.5371(1)	0.53940(9)
		z	0.2530(5)	0.2515(5)
		*Ui*so (Å^2)	0.0115(2)	0.0074(1)
Fe_1/Co/Sb_1	2*d*	Occupancy	0.215(8)/0.6667/0.119(8)	0.215/0.6667/0.119
		*U*iso (Å^2)	0.0027(6)	0.0011(5)
Fe_2/Sb_2	2*c*	Occupancy	0.452(8)/0.548(8)	0.452/0.548
		*U*iso (Å^2)	0.0055(4)	0.0038(3)
O_1	4*e*	*x*	0.2872(6)	0.2862(5)
		y	0.2935(6)	0.2950(5)
		z	0.0373(3)	0.0391(3)
		*U*iso (Å^2)	0.0093(8)	0.0060(5)
O_2	4*e*	*x*	0.2069(6)	0.2050(5)
		y	0.7873(6)	0.7861(5)
		z	0.0464(3)	0.0465(3)
		*U*iso (Å^2)	0.0098(8)	0.0061(5)
O_3	4*e*	*x*	0.5819(2)	0.5827(2)
		y	0.9793(2)	0.9786(1)
		z	0.2518(8)	0.2503(6)
		*U*iso (Å^2)	0.0115(2)	0.0087(2)

Table 7.7 Selected bond lengths (Å) and bond angles (degrees) in $CaLa_2FeCoSbO_9$ at 300 K and 5 K.

	300 K	5 K
$Ca/La – O_1$	2.466(4)	2.448(4)
$Ca/La– O_1$	2.692(4)	2.677(4)
$Ca/La – O_1$	2.766(5)	2.762(5)
$Ca/La – O_2$	2.677(5)	2.658(4)
$Ca/La – O_2$	2.390(4)	2.398(4)
$Ca/La – O_2$	2.785(5)	2.786(5)
$Ca/La – O_3$	2.533(1)	2.519(1)
$Ca/La – O_3$	2.389(2)	2.388(2)
$Fe_1/Co/Sb_1 – O_1$	2.052(3) * 2	2.062(2) * 2
$Fe_1/Co/Sb_1 – O_2$	2.055(3) * 2	2.065(2) * 2
$Fe_1/Co/Sb_1 – O_3$	2.042(6) * 2	2.029(5) * 2
$Fe_2/Sb_2 – O_1$	1.997(3) * 2	1.987(2) * 2
$Fe_2/Sb_2 – O_2$	2.017(3) * 2	2.004(2) * 2
$Fe_2/Sb_2 – O_3$	2.015(6) * 2	2.023(5) * 2
$O_1 – Fe_1/Co/Sb_1 – O_2$	89.1(2) * 2	89.1(2) * 2
$O_1 – Fe_1/Co/Sb_1 – O_3$	87.98(9) * 2	88.11(8) * 2
$O_2 – Fe_1/Co/Sb_1 – O_3$	88.31(9) * 2	88.44(8) * 2
$O_1 – Fe_2/Sb_2 – O_2$	88.9(2) * 2	89.0(2) * 2
$O_1 – Fe_2/Sb_2 – O_3$	89.76(9) * 2	89.81(9) * 2
$O_2 – Fe_2/Sb_2 – O_3$	89.94(9) * 2	89.94(8) * 2
$Fe_1/Co/Sb_1 – O_1 – Fe_2/Sb_2$	155.2(2)	154.6(1)
$Fe_1/Co/Sb_1 – O_2 – Fe_2/Sb_2$	152.4(2)	152.3(1)
$Fe_1/Co/Sb_1 – O_3 – Fe_2/Sb_2$	153.17(6)	152.88(5)

Neutron diffraction patterns for the nickel-containing series $ALa_2FeNiSbO_9$ (*A*=Ba, Sr, Ca) were acquired at 300 K and 5 K using a time-of-flight diffractometer in the case of $SrLa_2FeNiSbO_9$ and constant-wavelength instruments for the barium and calcium analogues. In each case extra intensity compared to that expected on the basis of the X-ray data was observed at high *d*-spacing at both temperatures. In contrast to the case of $CaLa_2FeCoSbO_9$, in the nickel-containing series this intensity could not be accounted for by varying the cation distribution, so it was necessary to assume that these compounds are ordered in a G-type

magnetic structure at 300 K. On the basis of preliminary refinements, in which the distribution of iron and nickel over the six-coordinate sites was allowed to vary, the cation distribution in $SrLa_2FeNiSbO_9$ was constrained to be $SrLa_2(Fe_{0.5}Ni)_{2d}(Fe_{0.5}Sb)_{2c}O_9$. There is less difference between the scattering lengths of iron and nickel than there is between those of iron and cobalt but the results of these preliminary refinements were nevertheless conclusive. The structural parameters refined from time-of-flight data collected at 300 and 5 K are presented in Tables 7.8 and 7.9, respectively. The fits to the data collected on four banks at 300 and 5 K are shown in Figure 7.19. The mean ordered moment on the 2*d* site at 300 K refined to a value of 0.6(2) μ_B per cation and that on the 2*c* site to 0.4(2) μ_B. These values increased to 0.68(8) and 1.5(1) per cation on cooling to 5 K, leading to a calculated net magnetisation of 1.2(2) μ_B per formula unit at the lower temperature. Constant-wavelength neutron diffraction patterns of $CaLa_2FeNiSbO_9$ and $BaLa_2FeNiSbO_9$ were collected on both D2b and D1b. The same data analysis strategy was used in each case. Firstly, the data collected at 300 K using D2b were analysed, principally to refine the crystal structure, although a G-type magnetic model was included in the analysis. During our refinements of the structure of $CaLa_2FeNiSbO_9$ the unit cell parameters were fixed at the values determined by X-ray diffraction and the wavelength of the neutron beam was allowed to vary. The value of the wavelength thus determined was used in the analysis of the data collected from $BaLa_2FeNiSbO_9$. Following preliminary refinements, all the Ni^{2+} cations were placed on the *2d* site and the overall cation distributions can thus be represented by the formula $ALa_2(Fe_{0.5}Ni)_{2d}(Fe_{0.5}Sb)_{2c}O_9$. The structural parameters determined in this way were then used to model the structural scattering present in the data collected at 300 K using D1b. Only the ordered magnetic moment and the instrumental parameters were varied during the analysis of these data. This procedure was then repeated in order to analyse the data collected at 5 K, although in this case the refined neutron wavelength was always held constant and the unit cell parameters were refined. The observed and calculated patterns for $CaLa_2FeNiSbO_9$ at 300 and 5 K are shown in Figure 7.20 and those for $BaLa_2FeNiSbO_9$ are shown in Figure 7.21. The structural parameters of both compounds at 300 K are listed in Table 7.8 and the values at 5 K in Table 7.9. The bond lengths for the calcium-, strontium- and barium-containing compounds at each temperature are listed in Tables 7.10, 7.11 and 7.12, respectively. The refined magnetic parameters of these compositions are presented in Table 7.13, which also includes the values reported above for the Co-containing compositions.

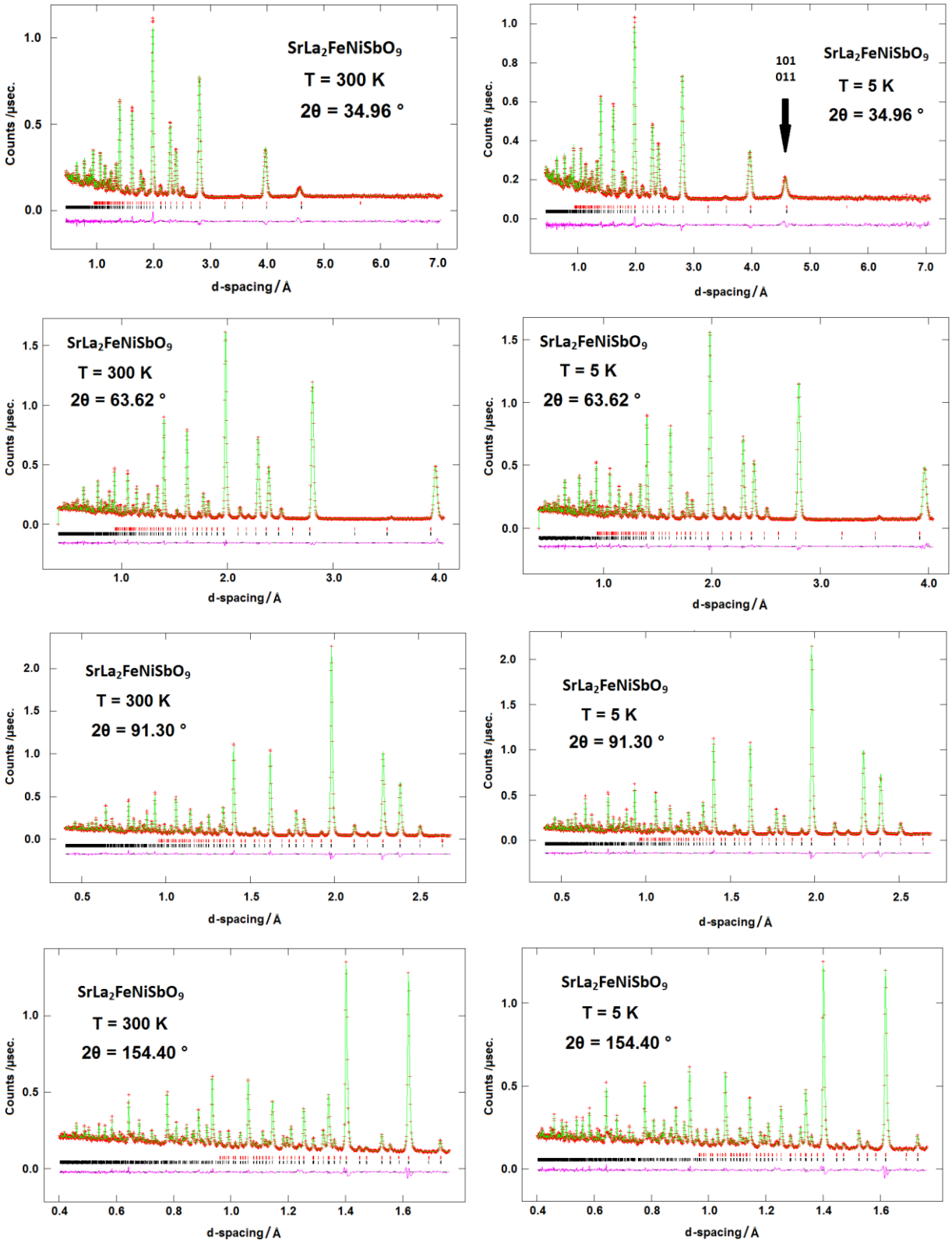

Figure 7.19 Observed (red), calculated (green) time-of-flight neutron diffraction patterns of $SrLa_2FeNiSbO_9$ at 300 K and 5 K collected at four banks. A difference curve (purple) is shown and reflection positions are marked. Black bars represent structural reflections and red bars represent magnetic reflections. An arrow indicates the peak with the strongest magnetic contribution.

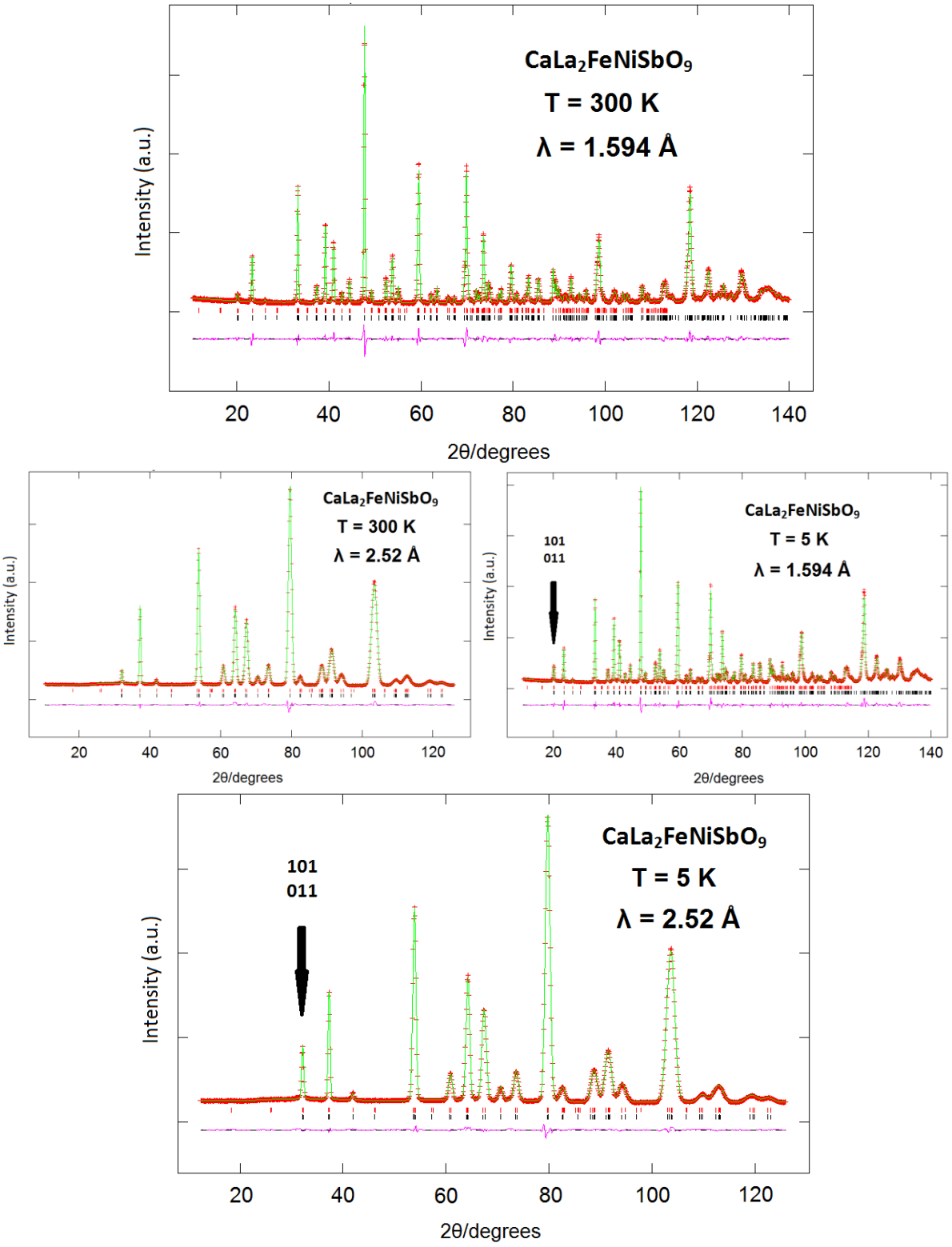

Figure 7.20 Observed (red), calculated (green) neutron diffraction patterns of $CaLa_2FeNiSbO_9$ at 300 K and 5 K collected using two wavelengths. A difference curve (purple) is shown and reflection positions are marked. Black bars represent structural reflections and red bars represent magnetic reflections. An arrow indicates the peak with the strongest magnetic contribution.

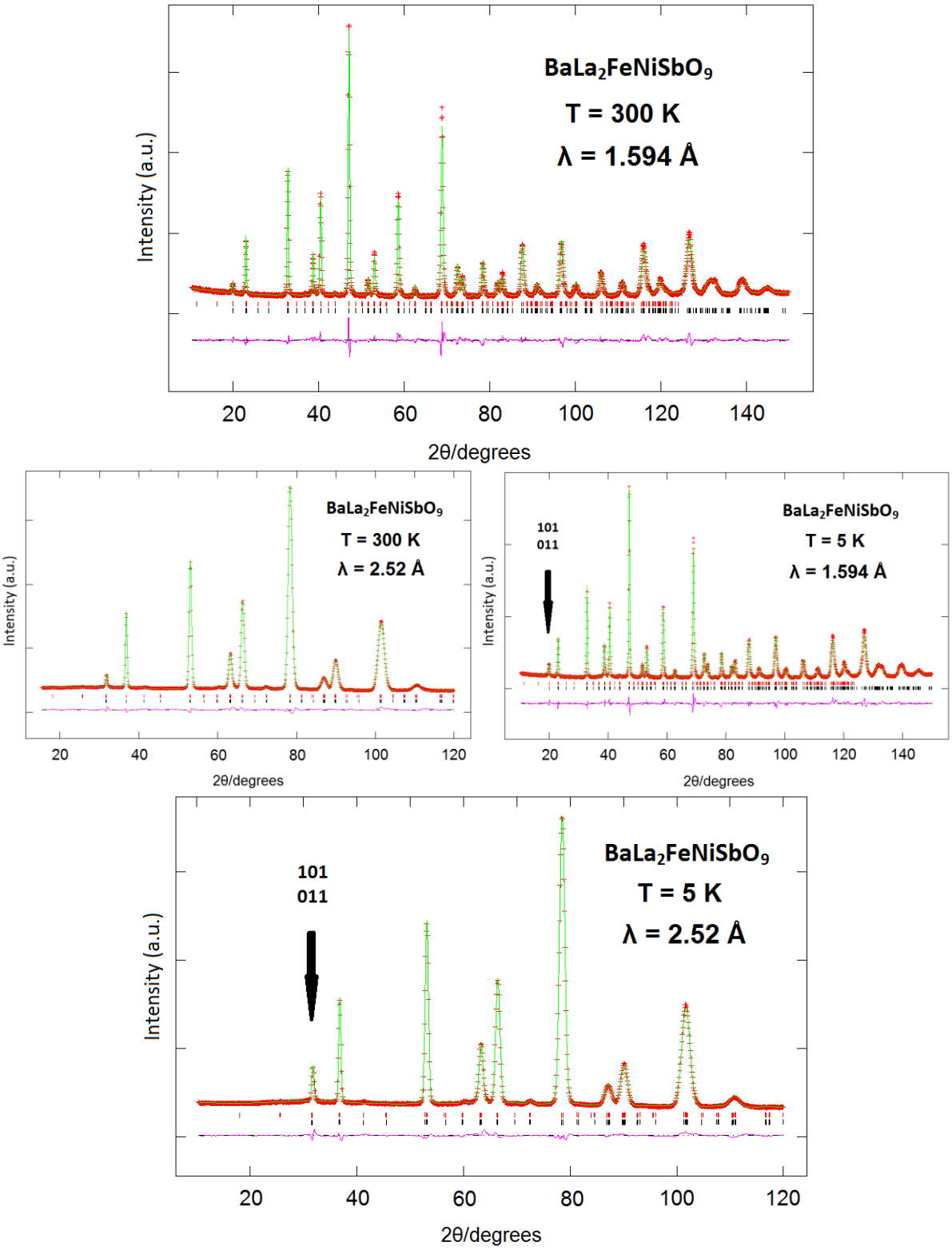

Figure 7.21 Observed (red), calculated (green) neutron diffraction patterns of $BaLa_2FeNiSbO_9$ at 300 K and 5 K collected using two wavelengths. A difference curve (purple) is shown and reflection positions are marked. Black bars represent structural reflections and red bars represent magnetic reflections. An arrow indicates the peak with the strongest magnetic contribution.

Table 7.8 Refined structural parameters of $ALa_2FeNiSbO_9$ (*A*=Ca, Sr, Ba) at 300 K.

A			Ca	Sr	Ba
a (Å)			5.5543	5.6091(3)	5.6588(4)
b (Å)			5.5976	5.6017(3)	5.6358(4)
c (Å)			7.8759	7.9204(4)	7.9648(5)
β (°)			89.99	89.98(1)	89.95(2)
R_{wpr}			5.76%	3.21%	4.73%
χ^2			7.20	2.57	7.19
A/La	*4e*	*x*	0.4934(6)	0.4952(4)	0.498(1)
		y	0.5346(3)	0.5241(2)	0.491(1)
		z	0.251(1)	0.2485(9)	0.250(2)
		Occupancy	0.3333/0.6667	0.3333/0.6667	0.3333/0.6667
		*U*iso (Å^2)	0.0116(4)	0.0118(2)	0.0123(4)
Fe_1/Ni	*2d*	Occupancy	0.3333/0.6667	0.3333/0.6667	0.3333/0.6667
		*U*iso (Å^2)	0.0011(2)	0.0045(3)	0.0005(3)
Fe_2/Sb	*2c*	Occupancy	0.3333/0.6667	0.3333/0.6667	0.3333/0.6667
		*U*iso (Å^2)	0.0011(2)	0.0028(4)	0.0005(3)
O_1	*4e*	*x*	0.289(1)	0.2793(7)	0.254(2)
		y	0.298(1)	0.2846(8)	0.256(2)
		z	0.0381(7)	0.0413(4)	0.9757(9)
		*U*iso (Å^2)	0.006(1)	0.0074(6)	0.016(2)
O_2	*4e*	*x*	0.212(1)	0.2216(8)	0.228(2)
		y	0.7821(9)	0.7753(8)	0.768(2)
		z	0.0473(7)	0.0296(3)	0.9600(7)
		*U*iso (Å^2)	0.006(1)	0.0094(6)	0.011(2)
O_3	*4e*	*x*	0.5733(5)	0.5705(4)	0.456(1)
		y	0.9812(4)	0.9895(3)	0.992(2)
		z	0.250(2)	0.253(1)	0.249(2)
		*U*iso (Å^2)	0.0102(6)	0.0089(3)	0.017(1)

Table 7.9 Refined structural parameters of $ALa_2FeNiSbO_9$ (*A*=Ca, Sr, Ba) at 5 K.

A			Ca	Sr	Ba
a (Å)			5.5454(1)	5.6021(3)	5.6529(3)
b (Å)			5.5924(1)	5.5985(2)	5.6256(3)
c (Å)			7.8614(2)	7.9107(3)	7.9497(4)
β (°)			89.99(1)	90.042(9)	90.02(2)
R_{wpr}			5.36%	2.95%	5.17%
χ^2			7.18	2.48	6.61
A/La	*4e*	Occupancy	0.3333/0.6667	0.3333/0.6667	0.3333/0.6667
		x	0.4924(5)	0.4943(4)	0.501(1)
		y	0.5366(2)	0.5273(1)	0.507(1)
		z	0.250(1)	0.2494(9)	0.250(2)
		*U*iso (Å^2)	0.0061(3)	0.0072(1)	0.0091(4)
Fe_1/Ni	*2d*	Occupancy	0.3333/0.6667	0.3333/0.6667	0.3333/0.6667
		*U*iso (Å^2)	0	0.0022(3)	0
Fe_2/Sb	*2c*	Occupancy	0.3333/0.6667	0.3333/0.6667	0.3333/0.6667
		*U*iso (Å^2)	0	0.0009(4)	0
O_1	*4e*	*x*	0.291(1)	0.2821(7)	0.253(2)
		y	0.2983(8)	0.2877(7)	0.255(2)
		z	0.0409(9)	0.0390(5)	0.0260(8)
		*U*iso (Å^2)	0.000(1)	0.0042(6)	0.014(2)
O_2	*4e*	*x*	0.213(1)	0.2219(7)	0.229(1)
		y	0.7815(9)	0.7743(7)	0.769(2)
		z	0.0450(9)	0.0336(5)	0.0395(7)
		*U*iso (Å^2)	0.005(1)	0.0065(7)	0.007(2)
O_3	*4e*	*x*	0.5769(5)	0.5717(4)	0.5481(8)
		y	0.9807(4)	0.9886(3)	0.003(2)
		z	0.251(1)	0.2533(8)	0.249(2)
		*U*iso (Å^2)	0.0056(5)	0.0053(3)	0.016(1)

Table 7.10 Selected bond lengths (Å) and bond angles (degrees) in $CaLa_2FeNiSbO_9$ at 300 and 5 K.

	300 K	5 K
Ca/La – O_1	2.42(1)	2.393(9)
Ca/La – O_1	2.716(9)	2.705(9)
Ca/La – O_1	2.75(1)	2.74(1)
Ca/La – O_2	2.63(1)	2.62(1)
Ca/La – O_2	2.413(9)	2.434(9)
Ca/La – O_2	2.82(1)	2.81(1)
Ca/La – O_3	2.539(3)	2.528(3)
Ca/La – O_3	2.425(4)	2.409(4)
Fe_1/Ni – O_1	2.060(6) * 2	2.056(5) * 2
Fe_1/Ni – O_2	2.045(6) * 2	2.039(6) * 2
Fe_1/Ni – O_3	2.02(1) * 2	2.02(1) * 2
Fe_2/Sb – O_1	1.986(7) * 2	1.996(6) * 2
Fe_2/Sb – O_2	2.005(6) * 2	1.998(5) * 2
Fe_2/Sb – O_3	2.01(1) * 2	2.01(1) * 2
O_1 – Fe_1/Ni – O_2	89.4(4)	88.9(4)
O_1 – Fe_1/Ni – O_3	89.2(2)	89.5(2)
O_2 – Fe_1/Ni – O_3	87.1(2)	87.9(2)
O_1 – Fe_2/Sb – O_2	86.9(4)	86.5(4)
O_1 – Fe_2/Sb – O_3	89.2(2)	89.1(2)
O_2 – Fe_2/Sb – O_3	88.8(2)	89.7(3)
Fe_1/Ni – O_1 – Fe_2/Sb	154.1(4)	152.8(4)
Fe_1/Ni – O_2 – Fe_2/Sb	153.5(4)	154.5(4)
Fe_1/Ni – O_3 – Fe_2/Sb	155.9(2)	154.8(2)

Table 7.11 Selected bond lengths (Å) and bond angles (degrees) in $SrLa_2FeNiSbO_9$ at 300 and 5 K.

	300 K	5 K
Sr/La – O_1	2.441(6)	2.445(5)
Sr/La – O_1	2.696(6)	2.707(6)
Sr/La – O_1	2.831(7)	2.802(7)
Sr/La – O_2	2.709(6)	2.674(5)
Sr/La – O_2	2.552(6)	2.534(6)
Sr/La – O_2	2.799(7)	2.812(6)
Sr/La – O_3	2.641(2)	2.619(2)
Sr/La – O_3	2.443(3)	2.441(3)
Fe_1/Ni – O_1	2.045(5) * 2	2.045(4) * 2
Fe_1/Ni – O_2	2.019(5) * 2	2.024(4) * 2
Fe_1/Ni – O_3	2.040(9) * 2	2.045(7) * 2
Fe_2/Sb – O_1	2.004(4) * 2	2.001(4) * 2
Fe_2/Sb – O_2	1.994(5) * 2	1.993(4) * 2
Fe_2/Sb – O_3	2.000(9) * 2	1.993(6) * 2
O_1 – Fe_1/Ni – O_2	90.0(2)	89.3(2)
O_1 – Fe_1/Ni – O_3	89.0(1)	89.6(1)
O_2 – Fe_1/Ni – O_3	89.0(1)	89.9(1)
O_1 – Fe_2/Sb – O_2	87.6(2)	86.8(2)
O_1 – Fe_2/Sb – O_3	88.7(1)	89.4(2)
O_2 – Fe_2/Sb – O_3	88.2(1)	88.8(1)
Fe_1/Ni – O_1 – Fe_2/Sb	156.4(2)	156.4(2)
Fe_1/Ni – O_2 – Fe_2/Sb	161.9(2)	160.7(2)
Fe_1/Ni – O_3 – Fe_2/Sb	157.2(1)	156.8(1)

Table 7.12 Selected bond lengths (Å) and bond angles (degrees) in $BaLa_2FeNiSbO_9$ at 300 and 5 K.

	300 K	5 K
Ba/La – O_1	2.91(1)	2.67(1)
Ba/La – O_1	2.69(1)	2.68(1)
Ba/La – O_1	2.70(1)	2.92(1)
Ba/La – O_2	2.93(2)	2.71(1)
Ba/La – O_2	2.71(1)	2.51(1)
Ba/La – O_2	2.52(2)	2.92(1)
Ba/La – O_3	2.83(2)	2.80(2)
Ba/La – O_3	2.569(8)	2.550(7)
Fe_1/Ni – O_1	2.02(1) * 2	2.01(1) * 2
Fe_1/Ni – O_2	2.04(1) * 2	2.035(8) * 2
Fe_1/Ni – O_3	2.00(2) * 2	2.00(2) * 2
Fe_2/Sb – O_1	2.00(1) * 2	2.00(1) * 2
Fe_2/Sb – O_2	2.01(1) * 2	2.015(8) * 2
Fe_2/Sb – O_3	2.02(2) * 2	2.01(2) * 2
O_1 – Fe_1/Ni – O_2	85.6(5)	85.3(4)
O_1 – Fe_1/Ni – O_3	88.5(4)	89.3(3)
O_2 – Fe_1/Ni – O_3	87.3(3)	87.4(3)
O_1 – Fe_2/Sb – O_2	87.7(5)	87.6(4)
O_1 – Fe_2/Sb – O_3	89.5(4)	90.0(4)
O_2 – Fe_2/Sb – O_3	84.6(4)	85.8(4)
Fe_1/Ni – O_1 – Fe_2/Sb	168.7(4)	168.0(4)
Fe_1/Ni – O_2 – Fe_2/Sb	159.8(3)	160.0(3)
Fe_1/Ni – O_3 – Fe_2/Sb	165.5(4)	164.4(3)

Table 7.13 Refined magnetic moment (μ_B) of per cation on the 2*d* and 2*c* sites and calculated net magnetisation per formula unit at 300 and 5 K in $CaLa_2FeCoSbO_9$ and $ALa_2FeNiSbO_9$ (*A*=Ca, Sr, Ba).

Compound	*2d* moment (μ_B)		*2c* moment (μ_B)		Net magnetisation (μ_B)	
	300 K	5 K	300 K	5 K	300 K	5 K
$CaLa_2FeCoSbO_9$	0	2.56(3)	0	0.94(2)	0	2.43(5)
$BaLa_2FeNiSbO_9$	0.8(3)	1.4(2)	0.4(3)	0.8(2)	0.6(6)	0.9(5)
$SrLa_2FeNiSbO_9$	0.6(2)	0.68(8)	0.4(2)	1.5(1)	0.3(5)	1.2(2)
$CaLa_2FeNiSbO_9$	0.8(1)	1.74(7)	0.4(1)	1.07(7)	0.6(2)	1.0(1)

7.4 Discussion

Judging from XRPD and neutron diffraction data alone, $CaLa_2FeCoSbO_9$ and $ALa_2FeNiSbO_9$ (*A*=Ba, Sr, Ca) all appear to adopt the same monoclinic crystal structure as their analogue $SrLa_2FeCoSbO_9$, which was discussed in Chapter 6. Refinement of the neutron diffraction data suggests that the four compounds have similar B site ordering patterns to that in $SrLa_2FeCoSbO_9$, where the Co/Ni and Sb atoms order in 1:1 ratio and Fe atoms are distributed equally over the two crystallographically-distinct B sites, although slight partial disorder is observed in the case of $CaLa_2FeCoSbO_9$. Ni^{2+} is similar to Co^{2+} in both size and charge, and consequently it is very common for analogous compounds containing these two cations to share the same crystal structure [9-12]. As stated in Chapter 6, Fe^{3+} is able to share one crystallographic site with Co^{2+} due to small difference in size and charge, and for the same reason Fe^{3+} can usually occupy the same site as Ni^{2+} as well[13, 14]. Again in contrast to $La_3Ni_2SbO_9$[9] and $La_3Co_2SbO_9$[10], where a portion of Co^{2+} or Ni^{2+} cations has to share one site with Sb^{5+}, in the perovskites described in this chapter the presence of an equal (or nearly equal) concentration over the B sites of Fe^{3+}, intermediate in both size and charge compared with Co^{2+} and Ni^{2+}, leads to the complete ordering pattern observed for the divalent metal cation and Sb^{5+}. In the cases of $CaLa_2FeCoSbO_9$, $CaLa_2FeNiSbO_9$ and $SrLa_2FeNiSbO_9$, the mean Fe/Co(Ni) – O bond lengths around the 2*d* sites are, as expected, significantly longer than the Fe/Sb – O bond lengths around the 2*c* sites. This effect caused by different

cation radii is the least obvious in $BaLa_2FeNiSbO_9$, which could be due to either the greater level of inhomogeneity observed in the sample by TEM or the relatively large standard deviation on the refined structural parameters from neutron diffraction, or both. Of course the inhomogeneity is like to increase the standard deviations. The Fe/Co – O bond lengths in the cobalt-containing compounds, including $SrLa_2FeCoSbO_9$, are slightly longer than the Fe/Ni – O bond lengths in the nickel-containing compounds. We note that at room temperature the mean Ni – O bond length around the octahedrally-coordinate cation sites in NiO is 2.089 Å[15], and the mean *M* – O bond lengths around the six-coordinate cation sites in Sb_2O_5, Fe_2O_3, and CoO are 1.992, 2.029 and 2.129 Å, respectively [12, 16, 17], which are in good agreement with our results. The mean Ca/La – O bond length in $CaLa_2FeCoSbO_9$ is 2.587 Å, slightly smaller than the mean Sr/La – O distance of 2.639 Å found in $SrLa_2FeCoSbO_9$ (see Chapter 6). The mean *M*/La – O bond lengths in $CaLa_2FeNiSbO_9$, $SrLa_2FeNiSbO_9$ and $BaLa_2FeNiSbO_9$ are 2.589 Å, 2.639 Å and 2.73 Å, respectively. The mean La – O bond length found in $La_3Ni_2SbO_9$ is 2.607 Å[9], which is larger than the Ca/La – O bond length but smaller than the Sr(Ba)/La – O bond lengths in these compounds, which is consistent with the trend (from small to large) of ionic radii of Ca^{2+}, La^{3+}, Sr^{2+} and Ba^{2+}.

However, the TEM data described above demonstrate that these samples are inhomogeneous in a way that $SrLa_2FeCoSbO_9$ was not. XRPD and NPD reveal the average structure of the material, but electron microscopy is able to probe shorter length scales and hence to reveal inhomogeneities within individual powder particles. In view of the variations in composition revealed in these studies, the parameters derived from our neutron data must be treated with some suspicion. This is most clearly illustrated in the case of $BaLa_2FeNiSbO_9$, where TEM clearly showed the presence of two different symmetries even though the neutron diffraction patterns were well fitted by a single-phase model. Indeed, the fact that the analysis of all our NPD data resulted in what would generally be regarded as "good fits" illustrates the importance of looking at the microstructure when studying particularly complex compositions. The cobalt-containing compounds are more homogenous than the nickel-containing analogues, which could be related to the different reaction rates of Co^{2+} and Ni^{2+}, as a d^8 cation possesses greater crystal field stabilisation energy than a d^7 cation, and thus tends to react more slowly. In general the strontium-containing compounds show relatively good homogeneity compared with their calcium and barium analogues, which could be due to a better size match between the A-cations and B-cations. These results are reminiscent of

$Sr_3Fe_2TeO_9$ discussed in Chapter 3, where TEM data also contradicted the original assignment of symmetry and provided a clear view of the true structure. However $Sr_3Fe_2TeO_9$ seems to be less complicated than the four compounds in this chapter. The tetragonal and trigonal phases contained in $Sr_3Fe_2TeO_9$ were very clearly seen by TEM with phase borders and well-defined crystal structures, with the former having previously been reported in the literature[18]. In contrast, the four compositions here have never been reported before. Recall that in Chapter 5 we discussed the compound $Sr_2LaFe_2SbO_9$, which appeared body-centred when studied by XRPD but showed weak peaks indicative of primitive structure in the neutron diffraction pattern. In that chapter we used a primitive triclinic space group, *P* -1, to account for the diffraction data, although this space group is of unusually low symmetry for such perovskites. Now we can propose an alternative explanation for the diffraction data: it is possible that the sample was not homogeneous, and actually have contained two phases. The dominant phase could be a body-centred triclinic phase in space group *I* -1 and the minor phase a primitive phase, possibly in space group $P2_1/n$, which gave rise to the additional weak peaks observed in neutron diffraction. However, in the GEM data that we presented in Chapter 5 there was no evidence for the existence of multiple phases, and consequently we obtained reasonably good fit using single-phase model. A study of $Sr_2LaFe_2SbO_9$ by TEM might resolve this issue.

The magnetometry data shown in Figure 7.1 suggest that $CaLa_2FeCoSbO_9$ and $ALa_2FeNiSbO_9$ (*A*=Ba, Sr, Ca) all show ferrimagnetic behaviour with a Curie temperature higher than that of $SrLa_2FeCoSbO_9$. $CaLa_2FeCoSbO_9$ is ferrimagnetic below 250 K, and the comparable transition temperatures of the three nickel-containing compounds are all very close to room temperature, which is partially due to the relatively large magnetic moment on Fe^{3+} besides the B-site ordering pattern. The presence of long-range magnetic ordering is clearly demonstrated by the presence of magnetic Bragg scattering in the neutron diffraction patterns collected at 5 K for all four compounds. The magnetic model used to account for the magnetic scattering is essentially the same antiferromagnetic G-type magnetic structure involving nearest-neighbour interactions as was assigned to $SrLa_2FeCoSbO_9$ and assumes that the samples are homogeneous. The difference in magnetic moment between the 2*d* and 2*c* sites results in a net ferrimagnetism, and the model is thus qualitatively consistent with the magnetometry data. For the nickel-containing ferrimagnets we would expect to see a mean ordered moment of $M_{Fe}/3$ on the 2*c* site and an antiparallel moment of $(M_{Fe} + 2M_{Ni})/3$ on the

2*d* site, resulting in a net magnetisation of M_{Ni} per formula unit, where M_{Fe} and M_{Ni} are the magnetic moments of Fe^{3+} and Ni^{2+} which would be expected to take values of ~5 and ~2 μ_B, respectively. The ordered moments determined by neutron diffraction and the magnetisation measured in 50 kOe are all lower than the values predicted by this simplistic model, and a possible reason for this has been proposed in Chapter 6. The nickel-containing compounds have a lower saturated moment per formula unit than the cobalt-containing compounds, which could partially result from the relatively large inhomogeneity besides the smaller moment of Ni^{2+} compared to Co^{2+}. This is consistent with the fact that $BaLa_2FeNiSbO_9$, which shows the greatest level of inhomogeneity, has the lowest susceptibility and saturated moment, while $CaLa_2FeNiSbO_9$ and $SrLa_2FeNiSbO_9$ are rather similar to each other. In the case of $CaLa_2FeCoSbO_9$, the expected net magnetisation per formula unit is not simply M_{Co} due to the minor amount of Sb^{5+} occupying the 2*d* site, but still the observed ordered moment and magnetisation are lower than the calculated values at 5 K. $M(H)$ is non-linear at room temperature although Mössbauer spectroscopy suggests the material is paramagnetic; the hysteresis seen in $\chi(T)$ above the Curie temperature could be caused by short-range spin ordering involving some of the magnetic cations.

We must emphasise that the discussion of the magnetic properties presented above is largely based on the assumption that our samples are homogeneous when they clearly are not. All the different particles have the perovskite structure and this allows us to model our neutron diffraction data to get an average structure, even when the cation distribution is inhomogeneous. However, the magnetic properties of each sample will be governed by local interactions. For example, a crystallite rich in lanthanum and iron might be expected to have magnetic properties similar to those of $LaFeO_3$ [19-21] and this might be the cause of some of the hysteresis observed above room temperature. $CaLa_2FeCoSbO_9$ has the lowest level of inhomogeneity of the four compounds discussed in this chapter and its magnetic behaviour is similar to that of homogeneous $SrLa_2FeCoSbO_9$, see Chapter 6. The magnetic transition is less marked, as judged by the difference between χ_{ZFC} and χ_{FC}, in the other compositions and the transition temperature is less well defined. The broadening of the susceptibility maximum is consistent with the presence of a range of compositions through the sample. It is likely that if another set of samples was prepared, then their magnetic properties would be similar to, but subtly different from, those described above because the level of inhomogeneity will be dependent on the details of the particular synthesis protocol. If reproducible data are to be

collected on these compounds it will probably be necessary to develop a solution-based synthesis that leads to a more homogeneous cation distribution in the early stages of the reaction.

7.5 Conclusions

In this study four perovskites: $CaLa_2FeCoSbO_9$ and $ALa_2FeNiSbO_9$ (*A*=Ba, Sr, Ca) have been prepared using standard solid-state reactions. X-ray and neutron diffraction data show that the four compounds all adopt the monoclinic crystal structure $P2_1/n$ with a 1:1 B-site ordering pattern where Co^{2+}/Ni^{2+} and Sb^{5+} tend to occupy distinct crystallographic sites while Fe^{3+} is distributed over the two B-sites, which is similar to the ordering pattern observed in $SrLa_2FeCoSbO_9$, see Chapter 6. TEM images have confirmed the B-site ordering, but also revealed the different levels of inhomogeneity that are present in these compounds. The inhomogeneity is least significant in $CaLa_2FeCoSbO_9$, while it is more significant in the nickel-containing species. $BaLa_2FeNiSbO_9$ is the most inhomogeneous compound among the four compositions, where both the primitive $P2_1/n$ phase and the body-centred $I2/m$ or $I4/m$ phase have been observed in the sample. Magnetometry data together with neutron diffraction data have shown that these perovskites are ferrimagnets with relatively high Curie temperatures, and their ferrimagnetism can be explained by a G-type magnetic structure model by assuming single-phase compositions. However, in contrast to homogeneous $SrLa_2FeCoSbO_9$, doubt has been cast on the interpretation of the diffraction data for these four compounds, and their magnetometry data are likely to be irreproducible under solid-state reaction conditions.

References

[1] N.P. Vyshatko, V.V. Kharton, A.L. Shaula, F.M.B. Marques, Powder Diffraction 18 (2003) 159.

[2] R.K. Gupta, C.M. Whang, Journal of Physics: Condensed Matter 19 (2007) 196209-1.

[3] H. Falcón, A.E. Goeta, G. Punte, R.E. Carbonio, Journal of Solid State Chemistry 133 (1997) 379.

[4] Y. Minet, V. Lefranc, N. Nguyen, B. Domengès, A. Maignan, B. Raveau, Journal of Solid State Chemistry 121 (1996) 158.

[5] Y. Tang, E.C. Hunter, P.D. Battle, R.P. Sena, J. Hadermann, M. Avdeev, J.M. Cadogan, Journal of Solid State Chemistry 242 (2016) 86.

[6] A.C. Larson, R.B. von Dreele, General Structural Analysis System (GSAS), Los Alamos National Laboratories, 1990.

[7] H.M. Rietveld, Journal of Applied Crystallography 2 (1969) 65.

[8] B. vanLaar, W.B. Yelon, J. Appl. Cryst. 17 (1984) 47.

[9] P.D. Battle, S.I. Evers, E.C. Hunter, M. Westwood, Inorg. Chem. 52 (2013) 6648.

[10] D.G. Franco, V.C. Fuertes, M.C. Blanco, M.T. Fernandez-Diaz, R.D. Sanchez, R.E. Carbonio, J. Solid State Chem. 194 (2012) 385.

[11] H.P. Rooksby, Acta Crystallographica 1 (1948) 226.

[12] N.C. Tombs, H.P. Rooksby, Nature 165 (1950) 442.

[13] A. della Giusta, F. Princivalle, S. Carbonin, Mineralogy and Petrology 37 (1987) 315.

[14] M.C. Blesa, U. Amador, E. Moran, N. Menendez, J.D. Tornero, J. Rodriguez Carvajal, Solid State Ionics 63 (1993) 429.

[15] S.D. Singh, A.K. Poswal, C. Kamal, P. Rajput, A. Chakrabarti, S.N. Jha, T. Ganguli, Solid State Communications 259 (2017) 40.

[16] M. Jansen, Angewandte Chemie-International Edition in English 17 (1978) 137.

[17] E.N. Maslen, V.A. Streltsov, N.R. Streltsova, N. Ishizawa, Acta Crystallographica Section B-Structural Science 50 (1994) 435.

[18] S.A. Ivanov, P. Nordblad, S.G. Eriksson, R. Tellgren, H. Rundlof, Mater. Res. Bull. 42 (2007) 776.

[19] S. Chanda, S. Saha, A. Dutta, B. Irfan, R. Chatterjee, T.P. Sinha, Journal of Alloys and Compounds 649 (2015) 1260.

[20] A.K. Azad, A. Mellergard, S.G. Eriksson, S.A. Ivanov, S.M. Yunus, F. Lindberg, G. Svensson, R. Mathieu, Materials Research Bulletin 40 (2005) 1633.

[21] A.K. Azad, S.G. Eriksson, J.T.S. Irvine, Materials Research Bulletin 44 (2009) 1451.

Chapter 8: Structural and Magnetic Properties of the Perovskites: $A_2LaFe_2NbO_9$ (*A*=Sr, Ca) and $Ca_2LaFe_2TaO_9$

8.1 Introduction

In the previous chapters we have discussed iron-containing perovskites with d^{10} cations on 33 % of the B sites; B-site ordering is induced by the difference in size and charge between the *p*-block cations and the transition metal cations. It can be seen that as the charge difference increases it becomes more likely that the B-cations will order in certain ways; the ordering can be either 1:1 or 2:1 and, either complete or partial. The resulting ordering largely controls the magnetism of the samples, and they can be antiferromagnetic, ferrimagnetic, or spin-glass like. As the d^{10} cations are diamagnetic, the magnetic properties of those compounds largely depend on the nature of the transition metal cations on the B sites.

Besides d^{10} cations from the *p*-block, some d^0 cations from the *d*-block, such as Nb^{5+} and Ta^{5+}, are also able to introduce B-site ordering into perovskites. For example, it has been reported that $La_3Mg_2NbO_9$ can adopt a monoclinic crystal structure with 1:1 B-site ordering[1, 2]. La_2NaTaO_6 exists in the same crystal structure with complete 1:1 ordering of Na^+ and Ta^{5+}[3], as the charge difference between the B-cations is significant. As this charge difference decreases to two, it is still possible for ordering to occur. Ba_2LaNbO_6 and Ba_2LaTaO_6 are both reported to have a body-centred monoclinic structure, displaying 1:1 ordering of La and Nb/Ta atoms over the two crystallographically-distinct B sites[4, 5]. Ca_2FeNbO_6 has a primitive monoclinic unit cell, with partial 1:1 ordering of Fe and Nb atoms on the B sites[6]; however, Pb_2FeNbO_6 is reported to adopt a disordered structure[7]. Sr_2FeTaO_6 can be either ordered or disordered, depending on the method of synthesis[8, 9]. When the charge difference between B-cations is small enough, such as in $Na_3LaTi_2Nb_2O_{12}$, the tendency to order vanishes and the B-cations are randomly distributed, although this particular compound shows unusual 1:1 cation ordering over the A sites[10].

The ordered perovskites containing Nb^{5+} and Ta^{5+} on the B sites show various magnetic properties, and as the pentavalent d^0 cations are diamagnetic, the magnetic cation species are usually responsible for the observed magnetism. For instance, antiferromagnetism is observed

in $LaCaCoNbO_6$ which results from the interactions between Co-sublattices[11]. In $La_3Co_2NbO_9$ and $La_3Co_2TaO_9$, competition between the antiferromagnetic Co^{2+}-O-Co^{2+} and the ferromagnetic Co^{2+}-O-M^{5+}-O-Co^{2+} couplings is proposed to occur[12]. Our group has previously studied three ordered perovskites $La_3Ni_2SbO_9$, $La_3Ni_2NbO_9$ and $La_3Ni_2TaO_9$, and the difference in their magnetic behaviours is striking, as they are isostructural compounds containing the same magnetic species[13-15]. Comparative studies of other pairs of d^0 and d^{10} compounds suggest that magnetic structures they adopt at low temperatures partly depend on whether the diamagnetic cation on the octahedrally-coordinate sites has empty *d* orbitals available to take part in the superexchange interactions[15-17]. This explanation accounts for the difference observed between the antimony-containing and niobium/tantalum-containing compounds. However, a discrepancy in magnetic properties between $La_3Ni_2NbO_9$ and $La_3Ni_2TaO_9$ is also noticeable, see Figure 8.1, and this has been explained by the difference in particle size and domain size within the samples. These facts illustrate that not only magnetic cations, but also diamagnetic cations can influence the crystal and local structures, and consequently physical properties of perovskites. In this chapter, in a continuation of our work on the iron-containing perovskites, we have focused on the Nb/Ta-containing species: $A_2LaFe_2NbO_9$ (*A*=Sr, Ca) and $Ca_2LaFe_2TaO_9$. We have undertaken an investigation of these compounds using X-ray and neutron diffraction and magnetometry measurements, and the results of this study are described below.

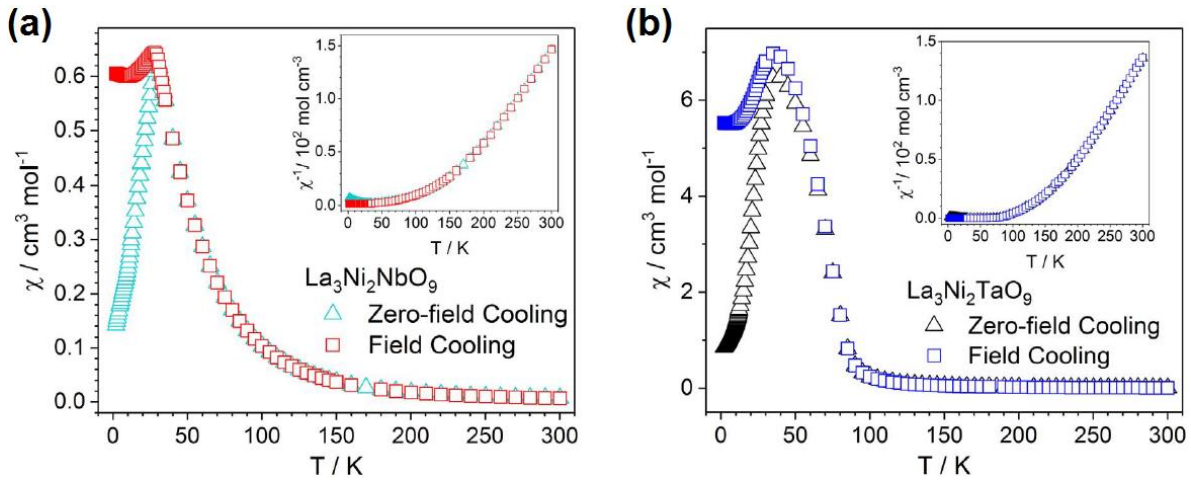

Figure 8.1 The dc molar susceptibility and (inset) inverse susceptibility of (a) $La_3Ni_2NbO_9$ and (b) $La_3Ni_2TaO_9$ measured in 100 Oe as a function of temperature[15].

8.2 Experimental methods

Polycrystalline samples of $A_2LaFe_2NbO_9$ (*A*=Sr, Ca) were prepared using the standard ceramic method. ACO_3(*A*=Sr, Ca), La_2O_3, Fe_2O_3 and Nb_2O_5 (purity >99.95%) were weighed out in the appropriate stoichiometric ratio and ground together in an agate mortar for 30 minutes to give a homogeneous mixture. La_2O_3 was heated at 800 °C for 24 hours prior to use to ensure it was completely dry. The mixture was then loaded into an alumina crucible and fired at 800 °C for 24 h. It was then quenched to room temperature, reground and pressed into a pellet which was fired in air at 1300 °C for 48 hours and subsequently annealed at 1300 °C for another 48 hours after further grinding. Finally, the furnace was allowed to cool to 800 °C and then the samples were quenched to room temperature. A polycrystalline sample of $Ca_2LaFe_2TaO_9$ was prepared under the same conditions with starting materials of $CaCO_3$, La_2O_3, Fe_2O_3 and Ta_2O_5 (purity >99.95%) in the appropriate stoichiometric ratio.

The brown-black reaction products were initially characterised by X-ray powder diffraction (XRPD) using Cu $K\alpha_1$ radiation. The data for $A_2LaFe_2NbO_9$ (*A*=Sr, Ca), collected at room temperature on a Panalytical X'Pert diffractometer, were analysed using the Rietveld method as implemented in the GSAS[18] program package. Neutron diffraction data were collected from the reaction products $A_2LaFe_2NbO_9$ (*A*=Sr, Ca) at 5K and 300K on the GEM time-of-flight diffractometer at the ISIS spallation source. The data collected on detector banks at scattering angles, 2θ, of 34.96°, 63.62°, 91.30° and 154.40° were refined simultaneously. Neutron diffraction data were collected from $Ca_2LaFe_2TaO_9$ on the diffractometer Echidna at the Bragg Institute, ANSTO, Australia by Dr. Maxim Avdeev. The angular region $10 < 2\theta/° < 147.5$ was scanned in steps of 0.05° at both 300 and 3.5 K using neutron wavelengths of 1.6215(5) and 2.4395(5) Å. In both cases data analysis was performed using the Rietveld method[19]. The peak shape was modelled using the function devised by van Laar and Yelon[20] and the background was fitted using a twelve-term Chebyschev polynomial.

The molar magnetic susceptibilities of these compounds were measured over the temperature range $2 < T/K < 300$ using a Quantum Design MPMS 5000 SQUID magnetometer. Data were collected on warming in a field of 100 Oe after cooling the samples both in the absence of an applied field (zero-field cooled, ZFC) and in the measuring field (field cooled, FC). The isothermal sample magnetisation of each sample was measured as a function of field over the range $-50 < H/kOe < 50$ at 300 and 5 K after cooling in a field of 50 kOe.

8.3 Results

The XRPD patterns of the reaction products $A_2LaFe_2NbO_9$ (*A*=Sr, Ca) suggested that the syntheses had produced phase-pure pseudo-cubic perovskites. However, the two compositions apparently deviate from the ideal primitive cubic symmetry in different ways. The XRPD pattern of $Ca_2LaFe_2NbO_9$ shown in Figure 8.2 was indexed using the monoclinic space group $P2_1/n$ with $a \sim\sqrt{2}a_p$, $b \sim\sim\sqrt{2}a_p$ and $c \sim 2a_p$, where a_p is the unit cell parameter of a primitive cubic perovskite. In this space group the structural model, see Figure 8.3, involves a 4*e* site that accommodates a disordered distribution of Ca and La, three further 4*e* sites that accommodate oxide anions and two independent B sites, *2d* (½, 0, 0) and *2c* (0, ½, 0) which accommodate the two cation species Fe^{3+} and Nb^{5+}. Refinements of the distribution of Fe and Nb over the crystallographically-distinct B sites suggested that in contrast to the $P2_1/n$ perovskites discussed in Chapter 5, the 2*c* sites are largely occupied by Fe and that the Nb and the remaining Fe atoms are randomly distributed over the 2*d* sites, leading to a 1:1 ordering of the B sites. However, in this case the swap of 2*c* and 2*d* sites is just due to the change of the origin of unit cell, and it is possible to obtain refinement with similar quality by fixing the occupancies at the 2*c* and 2*d* sites the other way round.

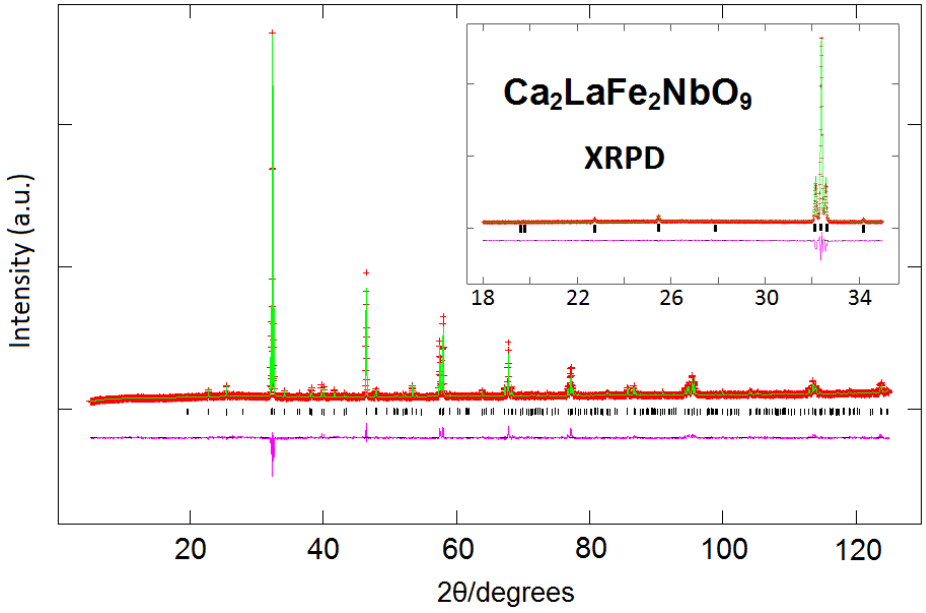

Figure 8.2 Observed (red), calculated (green) X-ray powder diffraction patterns of $Ca_2LaFe_2NbO_9$ at room temperature. A difference curve (purple) is shown and reflection positions are marked. The low angle region is magnified in the inset.

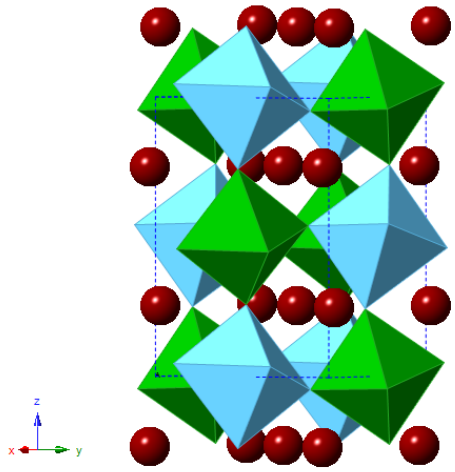

Figure 8.3 Crystal structure of $Ca_2LaFe_2NbO_9$. Blue octahedra are largely occupied by Fe, and green octahedra are occupied by approximately equal amounts of Fe and Nb. Red circles represent the Ca and La atoms at the A site.

As in the case of $Sr_2LaFe_2SbO_9$, described in Chapter 5, the peak distribution in the XRPD pattern of $Sr_2LaFe_2NbO_9$ could only be accounted for in a unit cell with $a \sim\sqrt{2}a_p$, $b \sim\sim\sqrt{2}a_p$ and $c \sim 2a_p$ if the symmetry was reduced to triclinic and the absence of reflections having $h + k + l = 2n + 1$ suggested that this cell was *I* centred, and thus X-ray diffraction data collected from this compound were first analysed in space group *I* -1. However as in the case of $Sr_2LaFe_2SbO_9$, the neutron diffraction data, which will be discussed below, showed the symmetry deduced from the X-ray data to be incorrect.

The XRPD pattern of the reaction product $CaLa_2Fe_2TaO_9$ shown in Figure 8.4 suggested that the synthesis had produced a phase-pure, pseudo-cubic perovskite. The pattern can be indexed using the monoclinic space group $P2_1/n$, as shown in Figure 8.3, and refinements of the distribution of Fe and Ta over the crystallographically-distinct B sites suggested that the 2*d* sites and 2*c* sites have different concentrations of Fe and Ta, but the difference is small compared with $Ca_2LaFe_2NbO_9$. In $CaLa_2Fe_2TaO_9$, Fe atoms slightly preferred occupying the 2*c* sites while Ta atoms had a preference for the 2*d* sites, which resulted in a less well-developed 1:1 B-site ordering pattern than in $Ca_2LaFe_2NbO_9$.

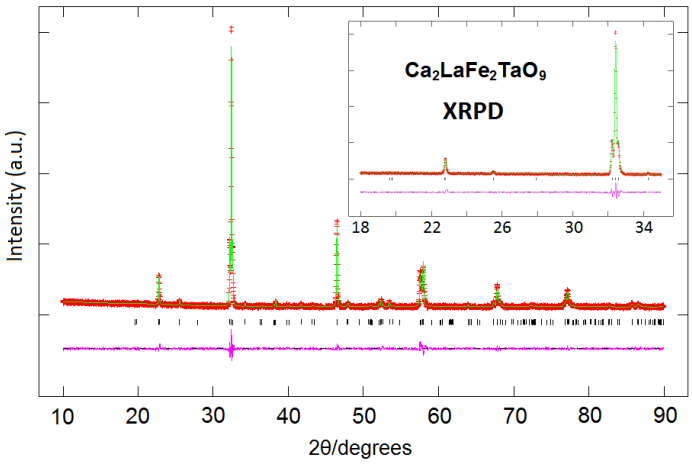

Figure 8.4 Observed (red), calculated (green) X-ray powder diffraction patterns of $Ca_2LaFe_2TaO_9$ at room temperature. A difference curve (purple) is shown and reflection positions are marked. The low angle region is magnified in the inset.

The temperature dependence of the dc molar magnetic susceptibilities of $A_2LaFe_2NbO_9$ (A=Sr, Ca) and $Ca_2LaFe_2TaO_9$ is shown in Figure 8.5, along with the field dependence of the magnetisation measured at 300 and 5 K. The susceptibility data collected on the three compositions are qualitatively similar, displaying a decrease in the FC susceptibilities with increasing temperature, a relatively large difference between the ZFC and FC curves and transition temperatures higher than room temperature. However, upon close inspection of the three $\chi(T)$ plots, the behaviours of the three compounds are not exactly the same. $Ca_2LaFe_2NbO_9$ shows the highest magnitude of susceptibility with a broad peak at ~220 K in ZFC, and below this temperature the ZFC curve is flattened, until it drops significantly at ~8 K. $Sr_2LaFe_2NbO_9$ shows a maximum at ~15 K in the ZFC, and below this temperature ZFC susceptibility drops rapidly. This compound has the lowest magnitude of susceptibility among the three compositions. $Ca_2LaFe_2TaO_9$ shows the smoothest ZFC curve, and its ZFC susceptibility decreases from ~20 K as temperature increases. The behaviours of ZFC and FC susceptibilities of the three perovskites, together with the non-linearity of the $M(H)$ curves collected at 300 K and the presence of a small remanent magnetisation shows that none of the three compounds is a simple paramagnet at that temperature. Differences are apparent in the three $M(H)$ curves recorded at 5 K. $Sr_2LaFe_2NbO_9$ and $Ca_2LaFe_2TaO_9$ both display clear hysteresis loops with relatively large coercive fields, while $Ca_2LaFe_2NbO_9$ exhibits a very narrow hysteresis loop with a smaller coercive field. None of the three samples is

approaching saturation under the measured fields. The coercive field and remanent magnetisation per formula unit of each compound at 5 K are listed in Table 8.1.

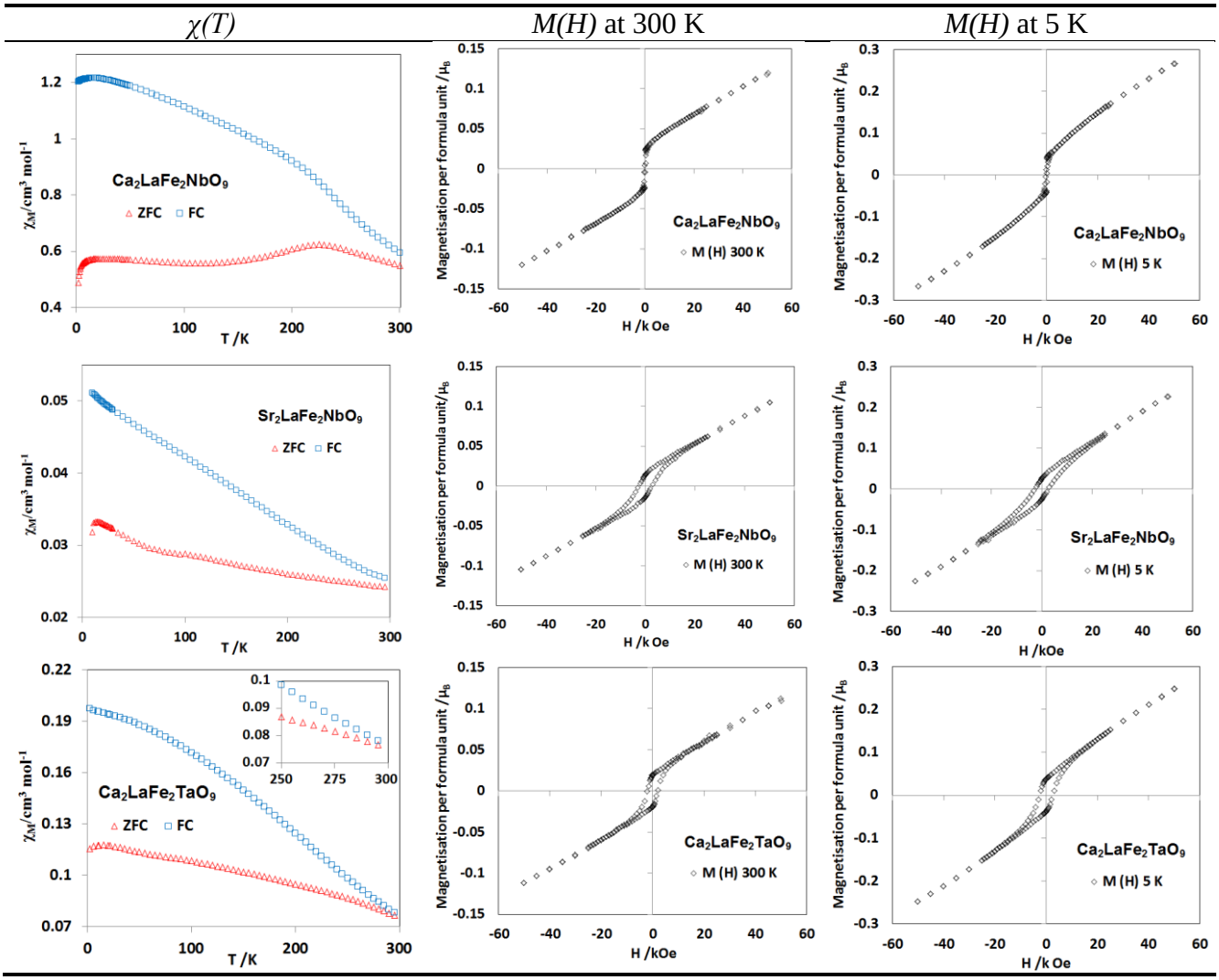

Figure 8.5 The temperature dependence of the dc molar magnetic susceptibilities and the field dependence of the magnetisation per formula unit of $A_2LaFe_2NbO_9$ (A=Ca, Sr) and $Ca_2LaFe_2TaO_9$ at 300 K and 5 K.

Table 8.1 Coercive field, H_c, and remanent magnetisation per formula unit, M_r, of $A_2LaFe_2NbO_9$ (A=Ca, Sr) and $Ca_2LaFe_2TaO_9$ at 5 K.

Compound	H_c (kOe)	M_r (μ_B)
$Ca_2LaFe_2NbO_9$	0.25	0.039
$Sr_2LaFe_2NbO_9$	3.0	0.027
$Ca_2LaFe_2TaO_9$	3.1	0.037

The time-of-flight neutron diffraction patterns collected from $Ca_2LaFe_2NbO_9$ at 300 K were analysed using the structural model derived from the XRPD data as a starting point. The magnetic data described above suggest that magnetic Bragg scattering might be present in these patterns and many of the reflections that might be expected to have a magnetic contribution are also sensitive to the degree of cation ordering over the two distinct six-coordinate sites in space group $P2_1/n$. In order to decouple these effects a combined refinement based on both the neutron pattern and the XRPD pattern was performed. The distribution of Fe and Nb across the 2*d* and 2*c* sites was allowed to vary, and the resulting cation distribution can be represented by the formula $Ca_2La(Fe_{0.85}Nb_{0.65})_{2d}(Fe_{1.15}Nb_{0.35})_{2c}O_9$. The neutron pattern did indeed contain additional intensity in the 101 and 011 reflections and in order to account for this intensity it was necessary to include a G-type magnetic structure, see Figure 8.6, in which the magnetic moment of Fe^{3+} on each B site is coupled in an antiparallel manner to those of the six nearest-neighbour sites. The refined structural parameters at 300 K are listed in Table 8.2. The fit to the patterns collected at the four detector banks can be seen in Figure 8.7. When we assumed that the Fe^{3+} cations on both sites have the same moment and that the moments on all the Fe^{3+} cations are ordered, then the moment per Fe^{3+} cation was refined to be 2.38(1) μ_B. Given that Nb^{5+} cation is diamagnetic and the occupancies of Fe on the 2*d* and 2*c* sites are 57(1) % and 77(1) % respectively, the mean moments per cation on the 2*d* and 2*c* sites were calculated to be 1.36(2) and 1.83(2) μ_B. Analysis of the neutron data thus leads to a description of $Ca_2LaFe_2NbO_9$ as a ferrimagnet at 300 K with a net moment of 0.71(4) μ_B per formula unit.

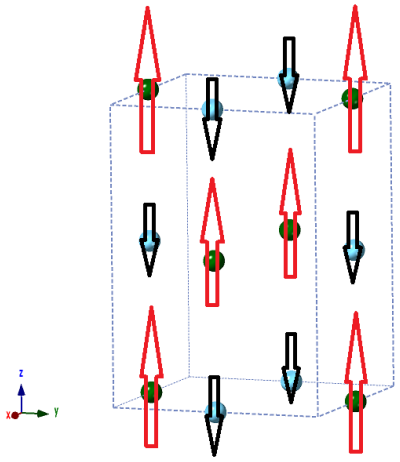

Figure 8.6 The G-type magnetic structure adopted by $Ca_2LaFe_2NbO_9$. Arrows indicate the direction of ordered spins at the B sites. Every magnetic ion in the cell is coupled in an antiferromagnetic manner to its six nearest neighbours.

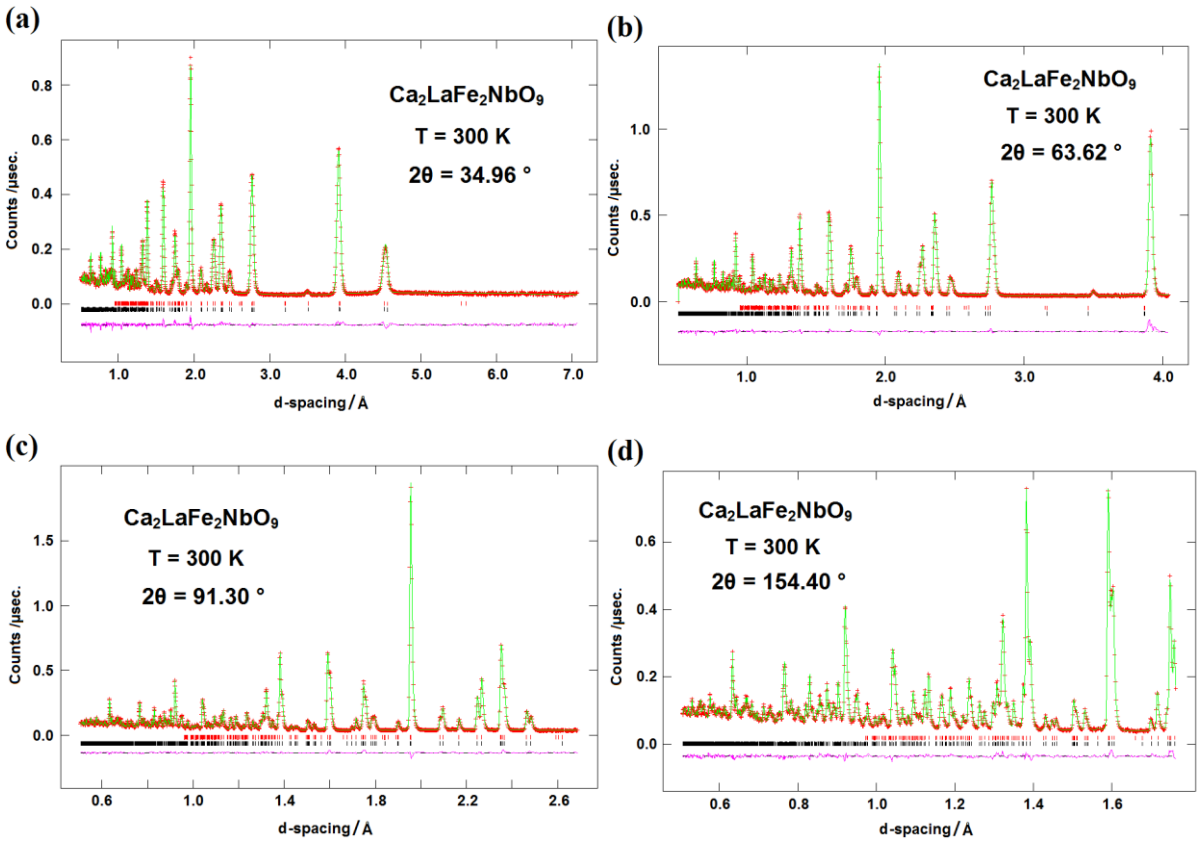

Figure 8.7 Observed (red), calculated (green) TOF neutron diffraction patterns of $Ca_2LaFe_2NbO_9$ at 300 K collected at four banks. A difference curve (purple) is shown and reflection positions are marked. Black bars represent structural reflections and red bars represent magnetic reflections.

Table 8.2 Structural parameters of $Ca_2LaFe_2NbO_9$ at 300 K.

Atom	Site	*x*	*y*	*z*	U_{iso}	fractional occupancy
Ca	4*e*	0.4925(2)	0.5358(1)	0.2521(6)	0.0100(2)	0.6667
La	4*e*	0.4925(2)	0.5358(1)	0.2521(6)	0.0100(2)	0.3333
Fe1	2*d*	0.5	0	0	0.0027(7)	0.57(1)
Fe2	2*c*	0	0.5	0	0.0062(8)	0.77(1)
Nb1	2*d*	0.5	0	0	0.0027(7)	0.43(1)
Nb2	2*c*	0	0.5	0	0.0062(8)	0.23(1)
O1	4*e*	0.2900(7)	0.2899(8)	0.0348(3)	0.0065(7)	1.0
O2	4*e*	0.2094(8)	0.7906(8)	0.0463(3)	0.0077(7)	1.0
O3	4*e*	0.5783(2)	0.9803(2)	0.250(1)	0.0084(2)	1.0

Space group $P2_1/n$, a = 5.49234(3) Å, b = 5.56403(3), c = 7.80590(4) Å, β = 89.999(6)°

R_{wp} = 4.09 %, χ^2=2.482

Analysis of the neutron patterns collected from $Ca_2LaFe_2NbO_9$ at 5 K was carried out using the structural model described above with the cation distribution over the B sites fixed to be the same as that determined from the room temperature data. The observed magnetic scattering was consistent with the G-type structure described above, with the principal change on cooling being an increase in the intensity of the magnetic scattering at higher *d*-spacings. The structural parameters derived from analysis of the data collected at 5 K are listed in Table 8.3, with the bond lengths and angles at both 300 K and 5 K in Table 8.4. The fits to the data collected on the four detector banks are shown in Figure 8.8. With the same assumptions as at 300 K, the mean ordered moment on the 2*d* site at 5 K increased to a value of 2.19(1) μ_B per cation and that on the 2*c* site to 2.96(1) μ_B, leading to a calculated net magnetisation of 1.16(2) μ_B per formula unit at the lower temperature.

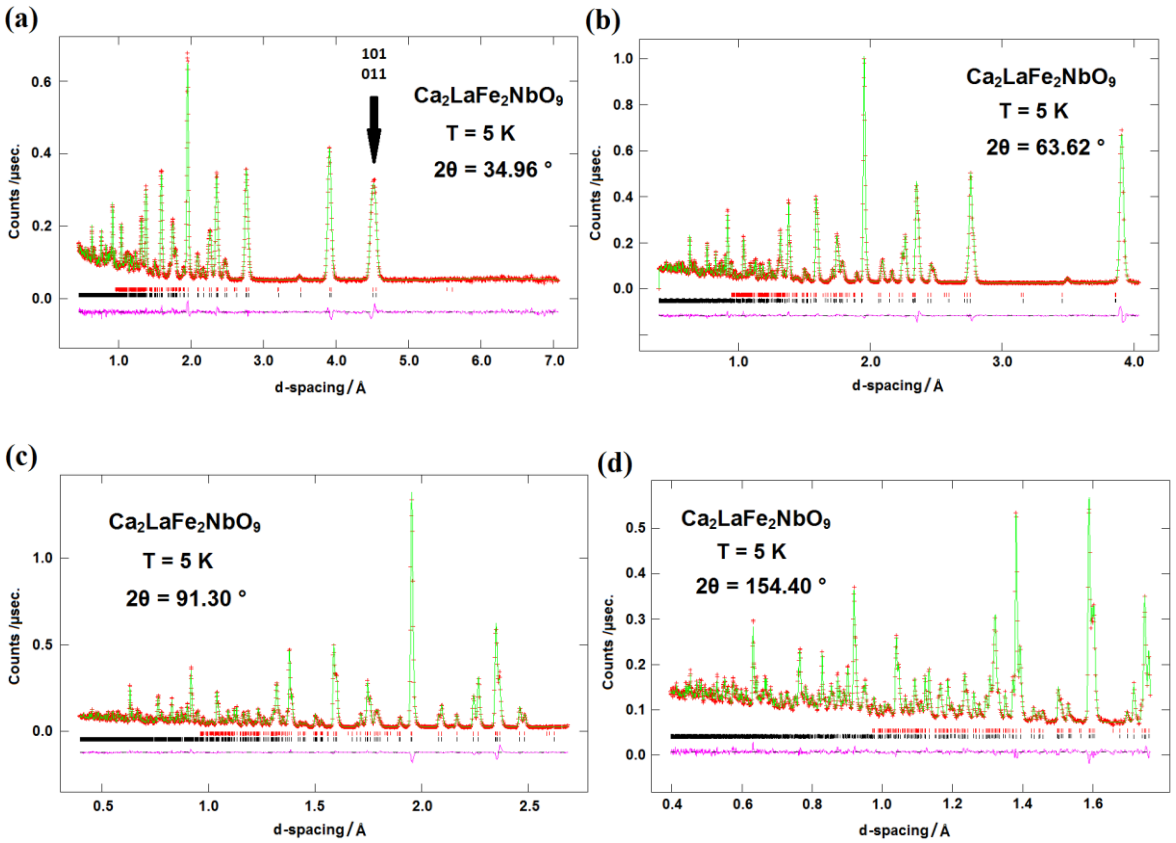

Figure 8.8 Observed (red), calculated (green) time-of-flight neutron diffraction patterns of $Ca_2LaFe_2NbO_9$ at 5 K collected at four banks. A difference curve (purple) is shown and reflection positions are marked. Black bars represent structural reflections and red bars represent magnetic reflections. An arrow indicates the peak with the strongest magnetic contribution.

Table 8.3 Structural parameters of $Ca_2LaFe_2NbO_9$ at 5 K.

Atom	Site	*x*	*y*	*z*	U_{iso}	fractional occupancy
Ca	4*e*	0.4927(2)	0.5387(1)	0.251(1)	0.0064(1)	0.6667
La	4*e*	0.4927(2)	0.5387(1)	0.251(1)	0.0064(1)	0.3333
Fe1	2*d*	0.5	0	0	0.0023(9)	0.57
Fe2	2*c*	0	0.5	0	0.0027(9)	0.77
Nb1	2*d*	0.5	0	0	0.0023(9)	0.43
Nb2	2*c*	0	0.5	0	0.0027(9)	0.23
O1	4*e*	0.2928(8)	0.2919(8)	0.0377(3)	0.0031(6)	1.0
O2	4*e*	0.2100(8)	0.7898(9)	0.0458(4)	0.0052(7)	1.0
O3	4*e*	0.5797(2)	0.9797(1)	0.251(1)	0.0047(2)	1.0

Space group $P2_1/n$, a = 5.482(1) Å, b = 5.564(1), c = 7.794(2) Å, β = 89.99(1)°

R_{wp} = 3.37 %, χ^2= 1.755

Table 8.4 Selected bond lengths (Å) and bond angles (degrees) in $Ca_2LaFe_2NbO_9$ at 300 and 5 K.

	300 K	5 K		300 K	5 K
Ca/La – O_1	2.447(4)	2.418(7)	O_1 – Fe_1/Nb_1 – O_2	89.2(2)	89.9(2)
Ca/La – O_1	2.678(4)	2.674(6)	O_1 – Fe_1/Nb_1 – O_3	87.98(8)	88.50(9)
Ca/La – O_1	2.718(5)	2.708(7)	O_2 – Fe_1/Nb_1 – O_3	87.9(1)	88.8(1)
Ca/La – O_2	2.648(5)	2.629(6)	O_1 – Fe_2/Nb_2 – O_2	89.4(2)	88.8(2)
Ca/La – O_2	2.359(4)	2.380(7)	O_1 – Fe_2/Nb_2 – O_3	89.62(9)	89.99(9)
Ca/La – O_2	2.761(5)	2.759(8)	O_2 – Fe_2/Nb_2 – O_3	89.53(8)	89.9(1)
Ca/La – O_3	2.518(1)	2.500(1)	Fe_1/Nb_1 – O_1 – Fe_2/Nb_2	156.1(2)	154.5(2)
Ca/La – O_3	2.377(2)	2.377(2)	Fe_1/Nb_1 – O_2 – Fe_2/Nb_2	152.3(1)	152.7(2)
Fe_1/Nb_1 – O_1	2.002(5) * 2	2.004(5) * 2	Fe_1/Nb_1 – O_3 – Fe_2/Nb_2	154.38(6)	153.91(5)
Fe_1/Nb_1 – O_2	2.009(5) * 2	2.006(5) * 2			
Fe_1/Nb_1– O_3	2.004(9) * 2	2.006(9) * 2			
Fe_2/Nb_2 – O_1	1.994(5) * 2	2.001(5) * 2			
Fe_2/Nb_2 – O_2	2.017(5) * 2	2.013(5) * 2			
Fe_2/Nb_2 – O_3	1.998(9) * 2	1.994(9) * 2			

Time-of-flight neutron diffraction patterns collected from $Sr_2LaFe_2NbO_9$ at 300 K were analysed using the same strategy. The triclinic space group *I* -1, which could account for the XRPD pattern, could not account for the NPD pattern because the weak peaks observed at d-spacings of ~2.1 Å and ~2.5 Å, see Figures 8.9(a), are forbidden for a body-centred structure. Hence the primitive triclinic space group *P* -1 was chosen to analyse the diffraction patterns and a combined refinement using NPD and XRPD data was carried out. In contrast to the monoclinic model described above, this triclinic model consists of four distinct B sites: 1*d* (½, 0, 0), 1*g* (0, ½, ½), 1*c* (0, ½, 0) and 1*f* (½, 0, ½). In order to stabilize the refinements, the cation occupancies at the 1*d* and 1*g* sites were fixed to be the same; as were those at the 1*c* and 1*f* sites. This assumption imposes a body-centred arrangement on the six-coordinate cations which is consistent with the absence of $h + k + l = 2n + 1$ reflections in the XRPD pattern. The refined cation distribution across the four B sites can then be written as $Sr_2La(Fe_{0.46}Nb_{0.29})_{1d}(Fe_{0.46}Nb_{0.29})_{1g}(Fe_{0.54}Nb_{0.21})_{1c}(Fe_{0.54}Nb_{0.21})_{1d}O_9$, which suggests partial B-site ordering. The additional intensity observed at higher d-spacings in the neutron pattern at

300 K could again be accounted for by a G-type magnetic model. Good agreement between the calculated and observed patterns was also achieved with the *P* -1 model when the XRPD data were re-analysed. The fits to the neutron and X-ray diffraction patterns are shown in Figure 8.9 and 8.10, respectively. The primitive triclinic crystal structure proposed for $Sr_2LaFe_2NbO_9$ is shown in Figure 8.11. The neutron data collected at 5 K showed an increase in the intensity of the magnetic scattering but could be fitted using the same triclinic structural model. The structural parameters at 300 K are listed in Table 8.5 and those at 5 K in Table 8.6. The most significant bond lengths and bond angles are presented in Table 8.7. The fits to the data collected at 5 K on the four detector banks are shown in Figure 8.12.

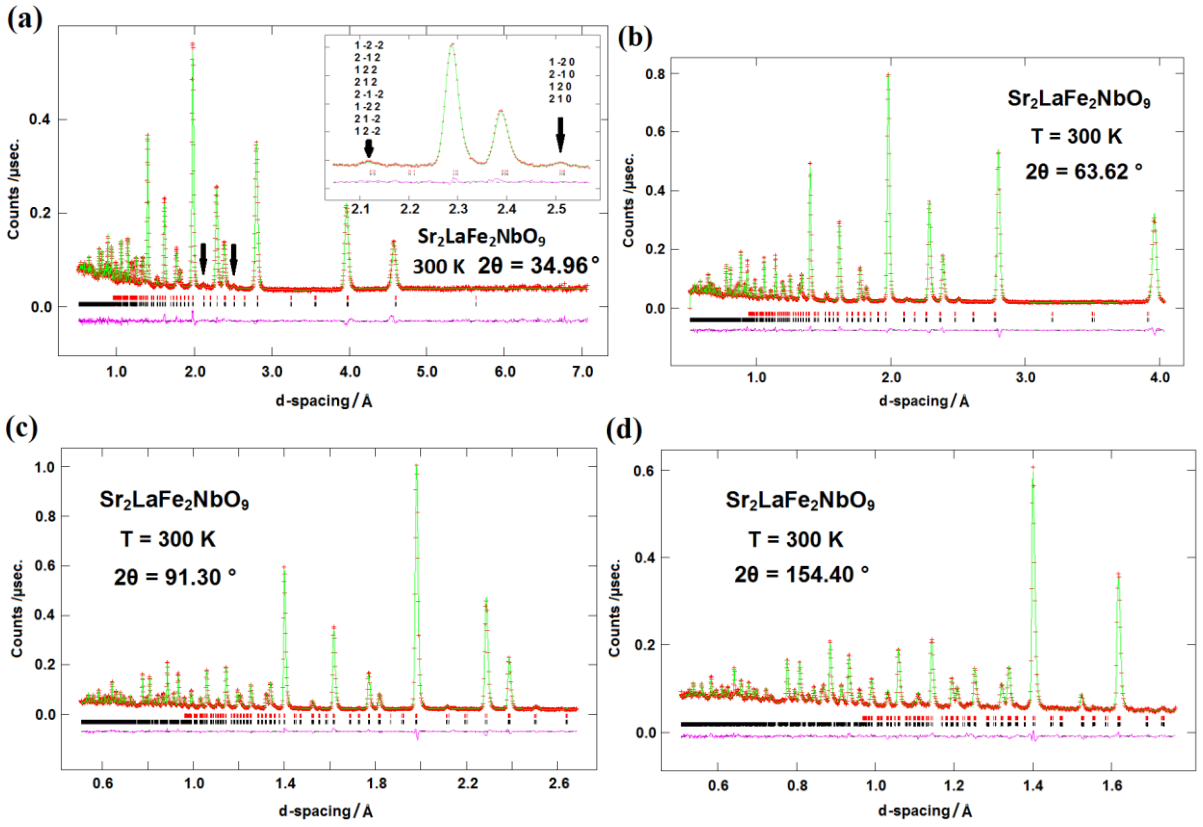

Figure 8.9 Observed (red), calculated (green) time-of-flight neutron diffraction patterns of $Sr_2LaFe_2NbO_9$ at 300 K collected at four banks. A difference curve (purple) is shown and reflection positions are marked. Black bars represent structural reflections and red bars represent magnetic reflections. Arrows indicate peaks that are forbidden in an *I*-centred cell.

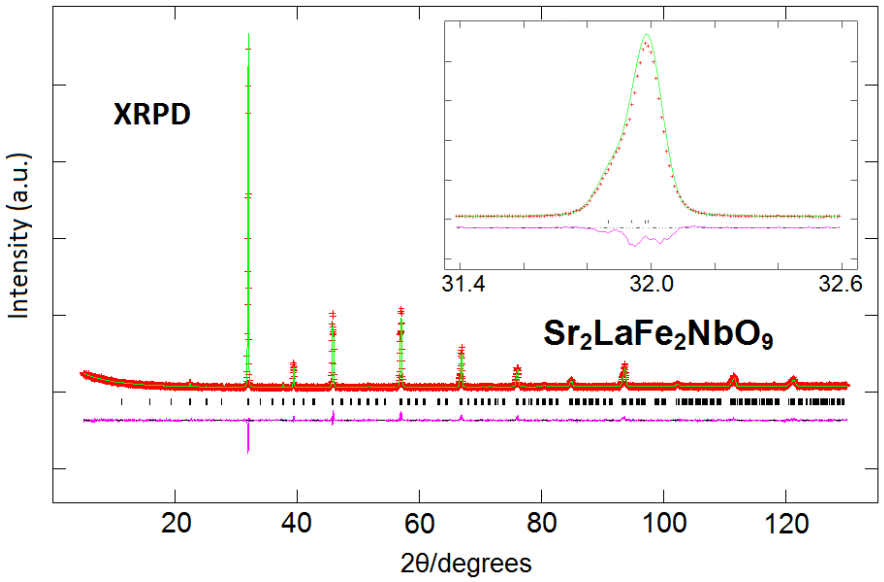

Figure 8.10 Observed (red), calculated (green) X-ray powder diffraction patterns of $Sr_2LaFe_2NbO_9$ at room temperature. A difference curve (purple) is shown and reflection positions are marked. The inset shows the splitting of the strongest peak.

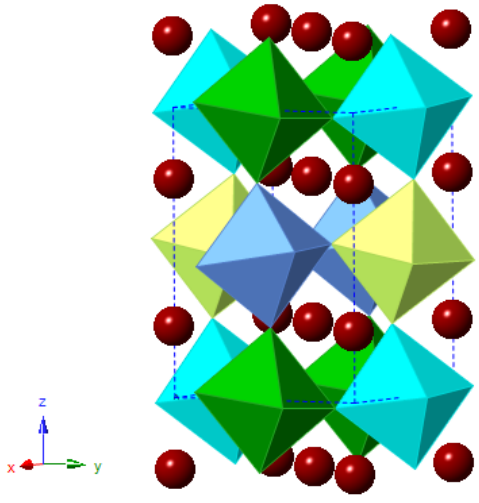

Figure 8.11 *P* -1 structure adopted by $Sr_2LaFe_2NbO_9$. Four distinct B sites are represented by octahedra in four different colours in the cell. Red circles represent the Sr and La atoms at the A site.

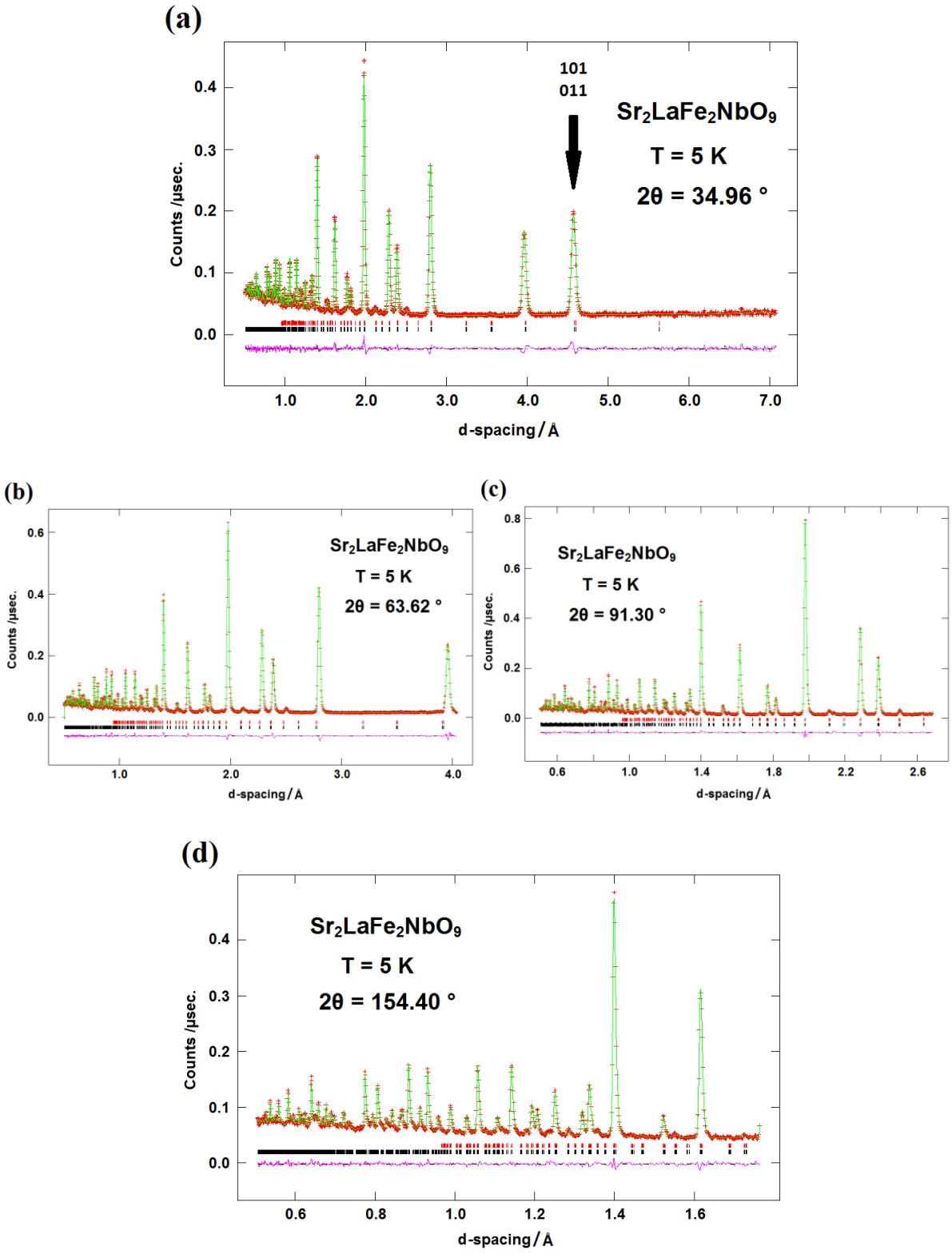

Figure 8.12 Observed (red), calculated (green) time-of-flight neutron diffraction patterns of $Sr_2LaFe_2NbO_9$ at 5 K collected at four banks. A difference curve (purple) is shown and reflection positions are marked. Black bars represent structural reflections and red bars represent magnetic reflections. An arrow indicates the peak with the strongest magnetic contribution.

Table 8.5 Structural parameters of $Sr_2LaFe_2NbO_9$ at 300 K.

Atom	Site	*x*	*y*	*z*	U_{iso}	fractional occupancy
Sr1	2*i*	0.006(2)	0.003(1)	0.250(1)	0.0112(9)	0.6667
Sr2	2*i*	0.503(2)	0.502(1)	0.2507(9)	0.0112(9)	0.6667
La1	2*i*	0.006(2)	0.003(1)	0.250(1)	0.0119(9)	0.3333
La2	2*i*	0.503(2)	0.502(1)	0.2507(9)	0.0119(9)	0.3333
Fe1	1*c*	0	0.5	0	0.00253(7)	0.72(2)
Fe2	1*f*	0.5	0	0.5	0.00253(7)	0.72(2)
Fe3	1*d*	0.5	0	0	0.00253(7)	0.61(2)
Fe4	1*g*	0	0.5	0.5	0.00253(7)	0.61(2)
Nb1	1*c*	0	0.5	0	0.00253(7)	0.28(2)
Nb2	1*f*	0.5	0	0.5	0.00253(7)	0.28(2)
Nb3	1*d*	0.5	0	0	0.00253(7)	0.39(2)
Nb4	1*g*	0	0.5	0.5	0.00253(7)	0.39(2)
O1	2*i*	0.258(1)	0.256(1)	0.0346(9)	0.0074(1)	1.0
O2	2*i*	0.261(2)	0.741(1)	0.9826(8)	0.0074(1)	1.0
O3	2*i*	0.277(2)	0.277(2)	0.4683(8)	0.0074(1)	1.0
O4	2*i*	0.215(1)	0.788(1)	0.528(1)	0.0074(1)	1.0
O5	2*i*	0.515(1)	0.947(1)	0.248(1)	0.0074(1)	1.0
O6	2*i*	0.984(1)	0.527(1)	0.251(1)	0.0074(1)	1.0

Space group *P* -1, a = 5.5990(2) Å, b = 5.5926(2), c = 7.9148(2) Å, α = 90.148(3)°, β = 90.170(3)°, γ = 89.790(1)°

R_{wp} = 4.93 %, χ^2= 1.765

Table 8.6 Structural parameters of $Sr_2LaFe_2NbO_9$ at 5 K.

Atom	Site	*x*	*y*	*z*	U_{iso}	fractional occupancy
Sr1	2*i*	0.015(2)	0.999(1)	0.250(1)	0.006(1)	0.6667
Sr2	2*i*	0.513(2)	0.497(1)	0.251(1)	0.006(1)	0.6667
La1	2*i*	0.015(2)	0.999(1)	0.250(1)	0.006(1)	0.3333
La2	2*i*	0.513(2)	0.497(1)	0.251(1)	0.006(1)	0.3333
Fe1	1*c*	0	0.5	0	0.00168(9)	0.72
Fe2	1*f*	0.5	0	0.5	0.00168(9)	0.72
Fe3	1*d*	0.5	0	0	0.00168(9)	0.61
Fe4	1*g*	0	0.5	0.5	0.00168(9)	0.61
Nb1	1*c*	0	0.5	0	0.00168(9)	0.28
Nb2	1*f*	0.5	0	0.5	0.00168(9)	0.28
Nb3	1*d*	0.5	0	0	0.00168(9)	0.39
Nb4	1*g*	0	0.5	0.5	0.00168(9)	0.39
O1	2*i*	0.265(2)	0.268(2)	0.026(1)	0.0036(1)	1.0
O2	2*i*	0.244(1)	0.758(1)	0.9780(8)	0.0036(1)	1.0
O3	2*i*	0.274(2)	0.273(2)	0.4713(9)	0.0036(1)	1.0
O4	2*i*	0.221(2)	0.783(1)	0.529(1)	0.0036(1)	1.0
O5	2*i*	0.5094(9)	0.944(1)	0.248(1)	0.0036(1)	1.0
O6	2*i*	0.9784(9)	0.566(1)	0.252(1)	0.0036(1)	1.0

Space group *P* -1, a = 5.589(2) Å, b = 5.593(2), c = 7.901(3) Å, α = 90.164(5)°, β = 90.120(5)°, γ = 89.820(2)°

R_{wp} = 3.55 %, χ^2= 2.186

Table 8.7 Selected bond lengths (Å) and bond angles (degrees) in $Sr_2LaFe_2NbO_9$ at 300 and 5 K.

	300 K	5 K		300 K	5 K
$Sr_1/La_1 – O_1$	2.630(7)	2.719(7)	$O_1 – Fe_1/Nb_1 – O_2$	86.7(3)	88.3(3)
$Sr_1/La_1 – O_1$	3.05(1)	3.07(1)	$O_1 – Fe_1/Nb_1 – O_6$	87.0(3)	86.5(3)
$Sr_1/La_1 – O_2$	2.942(7)	2.844(8)	$O_2 – Fe_1/Nb_1 – O_6$	86.9(3)	89.9(2)
$Sr_1/La_1 – O_2$	2.76(1)	2.68(1)	$O_3 – Fe_2/Nb_2 – O_4$	88.7(3)	89.2(3)
$Sr_1/La_1 – O_3$	2.77(1)	2.73(2)	$O_3 – Fe_2/Nb_2 – O_5$	89.1(3)	88.7(3)
$Sr_1/La_1 – O_3$	3.164(6)	3.134(7)	$O_4 – Fe_2/Nb_2 – O_5$	86.6(4)	87.5(3)
$Sr_1/La_1 – O_4$	2.77(1)	2.76(1)	$O_1 – Fe_3/Nb_3 – O_2$	85.7(3)	87.2(4)
$Sr_1/La_1 – O_4$	2.446(7)	2.498(8)	$O_1 – Fe_3/Nb_3 – O_5$	90.0(3)	88.0(3)
$Sr_1/La_1 – O_5$	2.77(1)	2.85(1)	$O_2 – Fe_3/Nb_3 – O_5$	89.1(3)	89.6(3)
$Sr_1/La_1 – O_5$	2.87(1)	2.78(1)	$O_3 – Fe_4/Nb_4 – O_4$	87.3(3)	87.7(3)
$Sr_1/La_1 – O_6$	2.667(6)	2.437(9)	$O_3 – Fe_4/Nb_4 – O_6$	87.5(3)	87.1(3)
$Sr_1/La_1 – O_6$	2.931(6)	3.172(8)	$O_4 – Fe_4/Nb_4 – O_6$	86.0(3)	89.9(4)
$Sr_2/La_2 – O_1$	2.59(1)	2.59(2)	$Fe_1/Nb_1 – O_1 – Fe_3/Nb_3$	163.9(4)	166.0(5)
$Sr_2/La_2 – O_1$	2.961(6)	2.845(8)	$Fe_1/Nb_1 – O_2 – Fe_3/Nb_3$	170.8(3)	169.5(4)
$Sr_2/La_2 – O_2$	2.85(1)	3.00(1)	$Fe_2/Nb_2 – O_3 – Fe_4/Nb_4$	161.0(3)	163.0(3)
$Sr_2/La_2 – O_2$	2.643(6)	2.670(8)	$Fe_2/Nb_2 – O_4 – Fe_4/Nb_4$	159.3(3)	160.7(3)
$Sr_2/La_2 – O_3$	2.489(7)	2.532(8)	$Fe_2/Nb_2 – O_5 – Fe_3/Nb_3$	162.3(3)	161.7(4)
$Sr_2/La_2 – O_3$	2.82(1)	2.81(2)	$Fe_1/Nb_1 – O_6 – Fe_4/Nb_4$	169.9(4)	157.9(3)
$Sr_2/La_2 – O_4$	3.155(8)	3.168(8)			
$Sr_2/La_2 – O_4$	2.86(1)	2.77(1)			
$Sr_2/La_2 – O_5$	3.105(6)	3.093(9)			
$Sr_2/La_2 – O_5$	2.489(6)	2.501(9)			
$Sr_2/La_2 – O_6$	2.91(1)	3.01(1)			
$Sr_2/La_2 – O_6$	2.70(1)	2.63(1)			
$Fe_1/Nb_1 – O_1$	2.00(1) * 2	1.98(1) * 2			
$Fe_1/Nb_1 – O_2$	1.995(9) * 2	1.996(9) * 2			
$Fe_1/Nb_1 – O_6$	2.00(1) * 2	2.03(1) * 2			
$Fe_2/Nb_2 – O_3$	2.00(1) * 2	1.99(2) * 2			
$Fe_2/Nb_2 – O_4$	2.006(8) * 2	2.00(1) * 2			
$Fe_2/Nb_2 – O_5$	2.01(1) * 2	2.01(1) * 2			
$Fe_3/Nb_3 – O_1$	1.99(1) * 2	2.00(1) * 2			
$Fe_3/Nb_3 – O_2$	1.982(9) * 2	1.981(9) * 2			
$Fe_3/Nb_3 – O_5$	1.99(1) * 2	1.99(1) * 2			
$Fe_4/Nb_4 – O_3$	2.00(1) * 2	2.00(2) * 2			
$Fe_4/Nb_4 – O_4$	2.024(8) * 2	2.02(1) * 2			
$Fe_4/Nb_4 – O_6$	1.98(1) * 2	2.00(1) * 2			

Constant-wavelength neutron diffraction patterns collected from $CaLa_2Fe_2TaO_9$ on Echidna at 300 K were analysed using the structural model derived from the XRPD data as a starting point. As in the above cases, a combined refinement based on both the neutron pattern and the XRPD pattern was performed. The distribution of Fe and Ta across the 2*d* and 2*c* sites was allowed to vary, and the resulting cation distribution can be represented by the formula $CaLa_2(Fe_{0.95}Ta_{0.55})_{2d}(Fe_{1.05}Ta_{0.45})_{2c}O_9$. It was clear that the neutron pattern contained significant additional intensity in the 101 and 011 reflections and in order to account for this intensity a G-type magnetic structure was included in the refinement. The fitted neutron profiles at 300 K are shown in Figure 8.13, and the refined structural parameters at 300 K are listed in Table 8.8. The neutron patterns collected from $CaLa_2Fe_2TaO_9$ at 3.5 K with both wavelengths 1.6215 and 2.4395 Å were analysed simultaneously. They can be indexed using the same $P2_1/n$ model with the cation distribution being held constant as in the room-temperature data, and the moment on the magnetic ions was allowed to vary. The principal change on cooling was an increase in the intensity of the magnetic scattering at higher d-spacings. The observed and calculated neutron patterns for $CaLa_2Fe_2TaO_9$ at 3.5 K are shown in Figure 8.14, and the refined structural parameters at 3.5 K are listed in Table 8.9. Selected bond lengths and bond angles at 300 K and 3.5 K are listed in Table 8.10. The refined magnetic parameters of all the compositions discussed above are presented in Table 8.11.

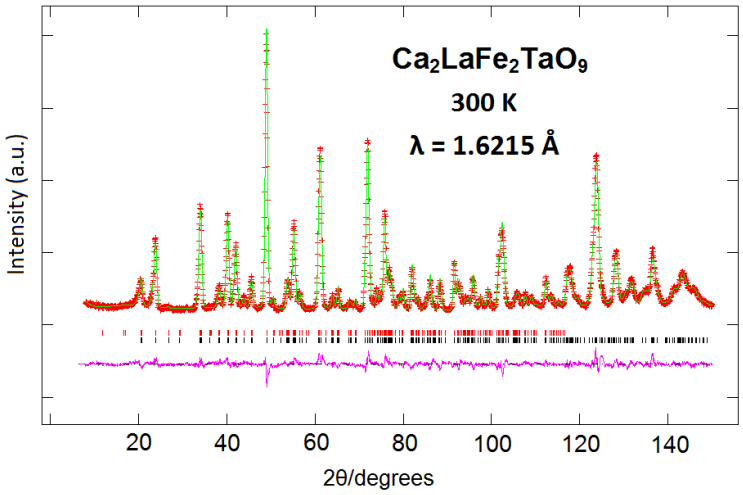

Figure 8.13 Observed (red), calculated (green) neutron diffraction patterns of $CaLaFe_2TaO_9$ at 300 K collected using wavelength of 1.6215 Å. A difference curve (purple) is shown and reflection positions are marked. Black bars represent structural reflections and red bars represent magnetic reflections.

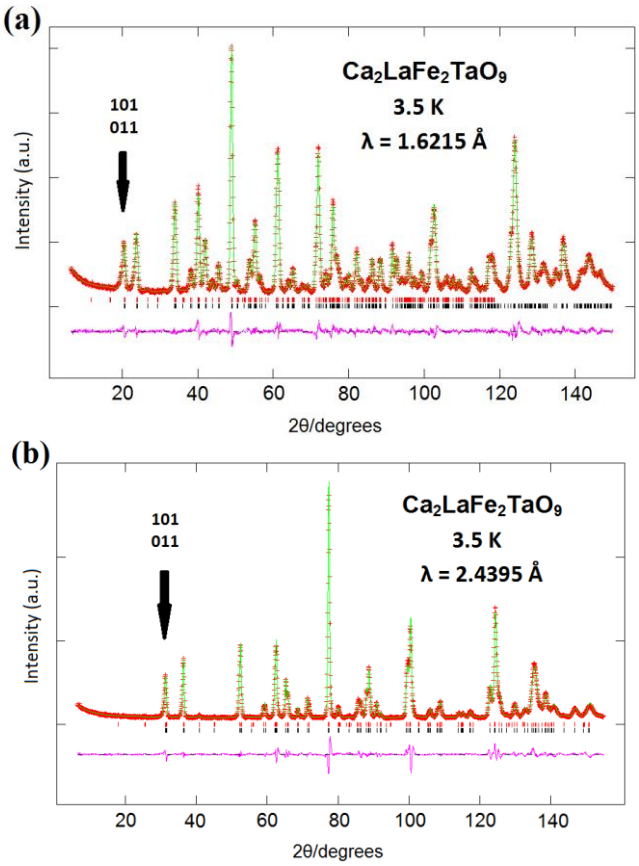

Figure 8.14 Observed (red), calculated (green) neutron diffraction patterns of $CaLaFe_2TaO_9$ at 3.5 K collected using wavelength of (a) 1.6215 Å and (b) 2.4395 Å. A difference curve (purple) is shown and reflection positions are marked. Black bars represent structural reflections and red bars represent magnetic reflections. An arrow indicates the peak with the strongest magnetic contribution.

Table 8.8 Structural parameters of $CaLa_2Fe_2TaO_9$ at 300 K.

Atom	Site	*x*	*y*	*z*	U_{iso}	fractional occupancy
Ca	4*e*	0.4921(6)	0.5344(3)	0.247(2)	0.0126(4)	0.6667
La	4*e*	0.4921(6)	0.5344(3)	0.247(2)	0.0126(4)	0.3333
Fe1	2*d*	0.5	0	0	0.0031(2)	0.63(1)
Fe2	2*c*	0	0.5	0	0.0031(2)	0.70(1)
Ta1	2*d*	0.5	0	0	0.0031(2)	0.37(1)
Ta2	2*c*	0	0.5	0	0.0031(2)	0.30(1)
O1	4*e*	0.285(1)	0.288(2)	0.042(1)	0.0084(3)	1.0
O2	4*e*	0.204(1)	0.794(4)	0.038(1)	0.0084(3)	1.0
O3	4*e*	0.5737(5)	0.9803(4)	0.250(3)	0.0084(3)	1.0

Space group $P2_1/n$, a = 5.4970(1) Å, b = 5.5575(1), c = 7.8080(2) Å, β = 90.02(2)°

R_{wp} = 6.74 %, χ^2= 2.146

Table 8.9 Structural parameters of $CaLa_2Fe_2TaO_9$ at 3.5 K.

Atom	Site	*x*	*y*	*z*	U_{iso}	fractional occupancy
Ca	4*e*	0.4916(5)	0.5384(3)	0.243(1)	0.0060(5)	0.6667
La	4*e*	0.4916(5)	0.5384(3)	0.243(1)	0.0060(5)	0.3333
Fe1	2*d*	0.5	0	0	0.0011(2)	0.63
Fe2	2*c*	0	0.5	0	0.0011(2)	0.70
Ta1	2*d*	0.5	0	0	0.0011(2)	0.37
Ta2	2*c*	0	0.5	0	0.0011(2)	0.30
O1	4*e*	0.284(1)	0.292(2)	0.0408(9)	0.0053(3)	1.0
O2	4*e*	0.200(1)	0.791(2)	0.0426(9)	0.0053(3)	1.0
O3	4*e*	0.5759(4)	0.9799(3)	0.248(2)	0.0053(3)	1.0

Space group $P2_1/n$, a = 5.4866(1) Å, b = 5.5558(1), c = 7.7957(2) Å, β = 89.963(9)°

R_{wp} = 6.75 %, χ^2= 4.256

Table 8.10 Selected bond lengths (Å) and bond angles (degrees) in $CaLa_2Fe_2TaO_9$ at 300 and 3.5 K.

	300 K	3.5 K		300 K	3.5 K
Ca/La – O_1	2.39(1)	2.379(9)	O_1 – Fe_1/Ta_1 – O_2	87.3(5)	87.6(4)
Ca/La – O_1	2.65(1)	2.67(1)	O_1 – Fe_1/Ta_1 – O_3	89.9(3)	89.1(2)
Ca/La – O_1	2.75(2)	2.70(1)	O_2 – Fe_1/Ta_1 – O_3	89.4(3)	88.8(2)
Ca/La – O_2	2.69(1)	2.642(9)	O_1 – Fe_2/Ta_2 – O_2	88.9(5)	89.2(4)
Ca/La – O_2	2.40(2)	2.404(9)	O_1 – Fe_2/Ta_2 – O_3	88.0(3)	88.5(2)
Ca/La – O_2	2.73(2)	2.77(1)	O_2 – Fe_2/Ta_2 – O_3	89.2(3)	89.8(2)
Ca/La – O_3	2.518(3)	2.496(2)	Fe_1/Ta_1 – O_1 – Fe_2/Ta_2	154.9(6)	154.9(4)
Ca/La – O_3	2.406(4)	2.396(3)	Fe_1/Ta_1 – O_2 – Fe_2/Ta_2	153.6(6)	152.0(4)
Fe_1/Ta_1 – O_1	2.016(9) * 2	2.032(8) * 2	Fe_1/Ta_1 – O_3 – Fe_2/Ta_2	155.7(1)	155.0(1)
Fe_1/Ta_1 – O_2	2.010(9) * 2	2.041(7) * 2			
Fe_1/Ta_1– O_3	2.00(2) * 2	1.98(1) * 2			
Fe_2/Ta_2 – O_1	1.989(8) * 2	1.968(7) * 2			
Fe_2/Ta_2 – O_2	2.00(1) * 2	1.983(8) * 2			
Fe_2/Ta_2 – O_3	2.00(2) * 2	2.01(1) * 2			

Table 8.11 Refined magnetic moment per cation and calculated net magnetisation per formula unit at 300 and 5 K in $A_2LaFe_2NbO_9$ (*A*=Ca, Sr), and at 300 and 3.5 K in $CaLa_2Fe_2TaO_9$.

Compound	Site / moment (μ_B)				Net magnetisation (μ_B)	
	300 K		3.5/5 K		300 K	3.5/5 K
$Ca_2LaFe_2NbO_9$	2*d*/1.36(2)	2*c*/1.83(2)	2*d*/2.19(1)	2*c*/2.96(1)	0.71(4)	1.16(2)
$Sr_2LaFe_2NbO_9$	1*c*,1*f*/1.77(5)	1*d*,1*g*/1.50(5)	1*c*,1*f*/2.63(1)	1*d*,1*g*/2.23(1)	0.4(1)	0.60(2)
$Ca_2LaFe_2TaO_9$	2*d*/1.79(3)	2*c*/1.99(4)	2*d*/2.41(2)	2*c*/2.68(2)	0.30(8)	0.41(4)

8.4 Discussion

Our diffraction data demonstrate that two different crystal structures apply to the three perovskites discussed in this chapter. $Ca_2LaFe_2NbO_9$ and $Ca_2LaFe_2TaO_9$ both have a $P2_1/n$ monoclinic unit cell with B-site ordering, which is comparable to their antimony analogue, see Chapter 5. As stated in section 8.1, it is known for Fe^{3+} to order over the B sites with both Nb^{5+} and Ta^{5+} in perovskites. However, as the radii of Nb^{5+} and Ta^{5+} are larger than the radius of Sb^{5+}, which leads to a fairly small difference in size between the diamagnetic B-cation and Fe^{3+}, cation ordering in these two niobium and tantalum compounds becomes less well-developed. It can be seen that the level of B-site ordering decreases from left to right along the series: $Ca_2LaFe_2SbO_9$ - $Ca_2LaFe_2NbO_9$ - $Ca_2LaFe_2TaO_9$, see Table 8.2 and 8.8. The cation-ordering levels of $Ca_2LaFe_2NbO_9$ and $Ca_2LaFe_2TaO_9$ are more similar to those in $CaLa_2Fe_2SnO_9$ than $Ca_2LaFe_2SbO_9$. In the case of $Ca_2LaFe_2TaO_9$ the errors on the occupancies of B-cations are considerable and the small difference in occupancy between 2*d* and 2*c* sites suggests that the arrangement of B-cations is most close to disordered in this compound. In $Ca_2LaFe_2NbO_9$ the octahedra at the two B sites are similar in size, see Table 8.4; while in $Ca_2LaFe_2TaO_9$ the 2*d* site seems to be larger in size and this difference in size between two B sites increases upon cooling, see Table 8.10. The mean Ca/La-O bond lengths in $Ca_2LaFe_2NbO_9$ and $Ca_2LaFe_2TaO_9$ at 300 K are 2.563 Å and 2.57 Å, respectively, and they are both close to the value of 2.565 Å observed in $Ca_2LaFe_2SbO_9$ at 300 K. The volumes of

the unit cells of $Ca_2LaFe_2NbO_9$ and $Ca_2LaFe_2TaO_9$ are very similar and are slightly larger than that of $Ca_2LaFe_2SbO_9$.

In contrast to its calcium analogue, $Sr_2LaFe_2NbO_9$ adopts the triclinic space group *P* -1, which was also observed in $Sr_2LaFe_2SbO_9$, see Chapter 5. As stated in Chapter 5, this space group is of unusually low symmetry for perovskites. As the size difference between the diamagnetic B-cation and Fe^{3+} decreases, B-site ordering in $Sr_2LaFe_2NbO_9$ becomes less well-developed than that in $Sr_2LaFe_2SbO_9$, see Table 8.5. Moreover, $Sr_2LaFe_2NbO_9$ displays a lower degree of B-site ordering than $Ca_2LaFe_2NbO_9$, reflecting the fact that A-cations with smaller radii tend to increase the level of B-site ordering, and the reason for this has been discussed in Chapter 5. Similar to $Sr_2LaFe_2SbO_9$, $Sr_2LaFe_2NbO_9$ exhibits no A-cation ordering, and the octahedra on different B sites have approximately the same average Fe-O bond length both at room temperature and 5 K, see Table 8.7. The mean Sr/La-O bond length at 300 K in $Sr_2LaFe_2NbO_9$ is 2.806 Å, which is close to the mean Sr/La-O bond length observed in $Sr_2LaFe_2SbO_9$ at 300 K. The unit cell volume of $Sr_2LaFe_2NbO_9$ is slightly larger than that of $Sr_2LaFe_2SbO_9$. While the triclinic distortion of the unit cell can be seen in the X-ray diffraction, it is neutron diffraction that shows the structure to be primitive, and we thus deduce that despite the displacement of oxygen atoms, the B-cations arrange themselves in a body-centred cell. However, as shown in Chapter 7, inhomogeneity could affect the determination of the crystal structure and provide an alternative explanation for the diffraction data. The weak peaks indicative of primitive structure in the neutron diffraction pattern could arise from a minor primitive phase, possibly in space group $P2_1/n$, while the dominant phase in the sample could be a body-centred triclinic phase in space group *I* -1. Perovskites containing strontium at the A site in space group *I* -1 have been previously reported in the literature, such as $Sr_2LaCr_2SbO_9$, $Sr_4Mg_2MoNbO_{12}$ and Sr_2FeIrO_6 [21-23]. In the GEM data that we presented for $Sr_2LaFe_2NbO_9$ there was no evidence for the existence of multiple phases, and consequently we obtained reasonably good fit using single-phase model. A study of $Sr_2LaFe_2NbO_9$ by TEM might resolve this issue.

Neutron diffraction has shown that the three samples with d^0 B-cations have a G-type magnetic structure both at room temperature and 5 K. Every Fe^{3+} is coupled in an antiparallel manner with its nearest neighbours, interacting through a superexchange mechanism. As iron is distributed over the crystallographically-distinct B-sites in different concentrations, the three compounds can be described as ferrimagnets. The room-temperature neutron-diffraction

data and the hysteresis observed in the susceptibility throughout the measured temperature range show that the ordering temperatures of our samples are higher than 300 K, which is similar to the case of the d^{10} compounds discussed in Chapter 5. However, these three samples with d^0 cations show very different susceptibility behaviour from those antimony and tin compounds. There is relatively large difference lying between ZFC and FC susceptibilities of these samples nearly throughout the measured temperature range, and there is no such clear and well-defined maximum observed in ZFC as seen in the antimony-containing compounds. Moreover, both the neutron data and hysteresis at room and low temperatures suggest the magnetic moment on Fe^{3+} in the three d^0 compounds grows significantly as temperature decreases. The refined moments on the Fe^{3+} cations are below the spin-only value, see Table 8.11, suggesting that not all the Fe^{3+} cations take part in the long-range magnetic ordering. This can be explained by the partial cation ordering pattern, which could result in some diamagnetic-cation-rich regions that disrupt the network of Fe-O-Fe interactions. The refined moment of the Fe^{3+} cations in the $Ca_2LaFe_2NbO_9$, which possesses the highest degree of B-site ordering and the lowest chance of the presence of d^0-O-d^0 nearest-neighbour environments, is the largest among the three compounds, but lower than what would have been predicted in a fully-ordered antiferromagnet. Besides, $Ca_2LaFe_2NbO_9$ and $Sr_2LaFe_2NbO_9$ both show a smaller calculated and observed net magnetisation per formula unit than their more ordered antimony-containing analogues. Although the d^0 compounds have relatively disordered structures, the variation of local composition is not as dominant as in the case of $La_3Ni_2SbO_9$ in determining the magnetic properties of these compounds, since neutron diffraction still detects magnetic Bragg peaks and overall long-range order must therefore persist over relatively large distances in the sample. In the $M(H)$ plots shown in Figure 8.5, we can see the observed net magnetisation per formula unit for the three compounds is lower than the calculated value based on the simple ferrimagnetic model. As stated previously, one possible reason is that the full magnetisation of the polycrystalline sample is not observed in the measured field range. Another explanation is that the presence of the diamagnetic Nb^{5+}/Ta^{5+} reduces the effectiveness and dominance of the NN antiferromagnetic Fe – O – Fe interaction and results in the competition between the NN and NNN 90 ° interactions along the Fe – O – O – Fe pathway. We note that $Ca_2LaFe_2NbO_9$ has significantly smaller coercive field than the other two compounds, suggesting that the domain size is different in these materials. In a previous study of $La_3Ni_2NbO_9$ and $La_3Ni_2TaO_9$,

variation of coercive field and domain size was also observed, and it was accounted for by the different particle size in their microstructures after TEM experiments were conducted[15].

The d^0 compounds discussed in this chapter show very different magnetic behaviour not only from the d^{10} compounds described in Chapter 5, but also from the antiferromagnet $LaCaCoNbO_6$[11] and the spin glass $La_3Ni_2NbO_9$. The ZFC and FC susceptibilities of the three compounds do not coincide below 300 K as they would in a simple Curie-Weiss paramagnet or antiferromagnet. The observation of hysteresis, together with the neutron diffraction data shows that long-range magnetic order is present in these compounds above 300 K. However, the low value of the moment measured by neutron diffraction shows that the order is incomplete. As in the case of $A_2LaFe_2SbO_9$, we propose that at 300 K a backbone of magnetically-ordered spins, large enough to be detected by neutron diffraction, exists within the structure, and as the sample is cooled further, more spins join the backbone and the average ordered moment detected by neutron diffraction increases. However this growth of the magnetic backbone develops much more slowly in these d^0 compounds, and the temperature for the remaining paramagnetic spins, isolated presumably in Nb^{5+}/Ta^{5+}-rich regions, to undergo spin-glass freezing is lowered below 20 K with enhanced magnetic frustration. This "freezing" temperature is much lower than that observed in antimony-containing compounds. The slow-down of the formation of the magnetic backbone could partially result from the increasing level of disorder in the crystal structure, but it could also arise from the different electronic configurations of d^0 and d^{10} cations at the B site, which might change the relative strengths of competitive interactions in the material. The fundamental difference between d^0 and d^{10} cations lies in whether there is an empty *d* orbital available for hybridisation. In a study of Sr_2CuTeO_6 and Sr_2CuWO_6[17], it was proposed that the open shell of W^{6+}, with a d^0 electronic configuration, allows the low-lying 5*d* orbital of W to hybridise and overlap strongly with the *p* orbital of oxygen, and consequently introduces the Cu electron hopping via the Cu – O – M^{6+} – O – Cu pathway. In contrast, the closed-shell d^{10} configuration does not permit virtual electron hopping via this pathway in Sr_2CuTeO_6. Recently Vasala *et al* observed the relatively strong magnetic interaction mediated through the Cu – O – W^{6+} – O – Cu pathway in Sr_2CuWO_6 again, whereas this interaction was reported to be weaker in Sr_2CuTeO_6[24]. Similar coupling interactions between magnetic cations mediated by d^0 diamagnetic cation were also reported in a study of $La_3Co_2NbO_9$ and $La_3Co_2TaO_9$[12]. It is thus reasonable to propose that in our d^0 compounds, the third-nearest-

neighbour interaction (J_3, distance ~$2a_p$) could also occur in the material and take part in the competition with the NN interaction (J_1, distance ~a_p) and NNN interaction (J_2, distance ~$\sqrt{2}a_p$), see Figure 8.15. In the J_3 interaction, partial electronic density is able to be transferred via the Fe^{3+} – O – Nb^{5+}/Ta^{5+} – O – Fe^{3+} pathway. This additional competitive interaction would hence further reduce the dominance of the NN interactions, and consequently have the effect of slowing down the building up of the ferrimagnetic backbone in the material as temperature decreases. However, it is clear that among all the competitive interactions potentially involved in the d^0 compounds discussed in this chapter, the antiferromagnetic NN interaction is still the dominant one, as indicated by the long-range G-type magnetic structure detected by neutron diffraction. It is also worth noting that the discussion of magnetism of these materials is based on a single-phase model; other factors such as variation in microstructure and inhomogeneity are not considered here.

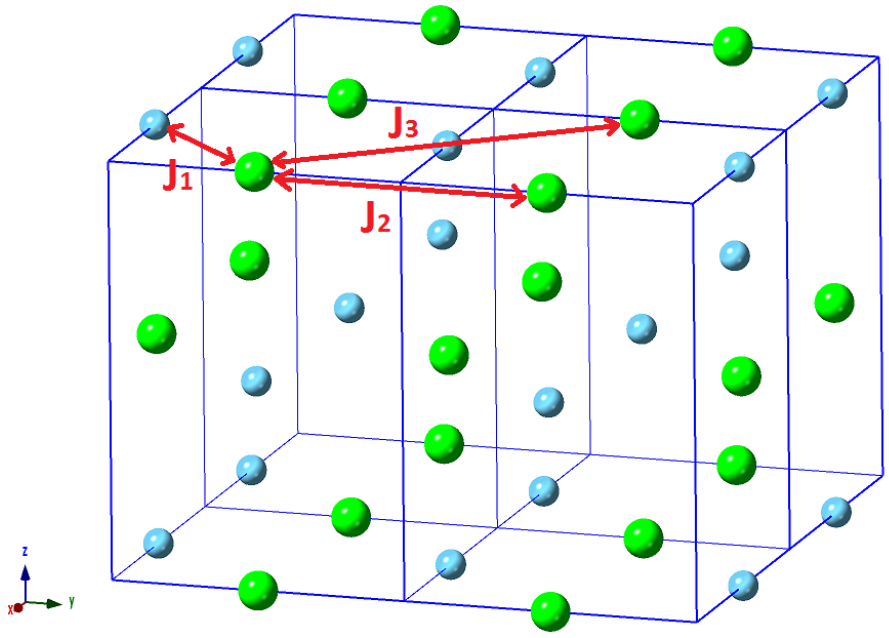

Figure 8.15 J_1, J_2 and J_3 interaction pathways in ordered pseudo-cubic perovskite unit cells. Spheres in different colours represent crystallographically-distinct B sites. Cations at the A sites and oxygen atoms are omitted for clarity.

8.5 Conclusions

In this study three perovskites containing d^0 B-cations: $A_2LaFe_2NbO_9$ (A=Sr, Ca) and $CaLa_2Fe_2TaO_9$ have been prepared using standard solid-state reactions. X-ray and neutron diffraction data show that $Ca_2LaFe_2NbO_9$ and $Sr_2LaFe_2NbO_9$ exhibit different levels of cation ordering, and like their antimony-containing analogues, the former adopts a monoclinic $P2_1/n$ structure and the latter adopts a triclinic P -1 structure. Compared to the antimony compounds in Chapter 5, $SrLa_2Fe_2NbO_9$ and $CaLa_2Fe_2NbO_9$ show a less well-developed cation ordering pattern due to the smaller difference in size of B-cations. $CaLa_2Fe_2TaO_9$ adopts the same crystal structure as $CaLa_2Fe_2NbO_9$ with the lowest level of B-cation ordering among the three compounds. Magnetometry data together with neutron diffraction data have shown that these perovskites are not simple paramagnets at room temperature, and they all adopt a G-type magnetic structure, which leads to long-range ferrimagnetic behaviour. However, magnetically these compounds behave very differently from their antimony analogues. The formation of a magnetic backbone is significantly slowed down, and the temperature at which the paramagnetic spins to freeze is lowered below 20 K. We propose that in these materials the J_3 interaction takes place to compete with the dominant J_1 interaction and the J_2 interaction. In the J_3 interaction, electronic density is able to be transferred via the Fe^{3+} – O – Nb^{5+}/Ta^{5+} – O – Fe^{3+} pathway as d^0 cations provide empty d orbitals available for hybridisation to occur.

References

[1] H. Park, H. Lee, Y. Cho, Journal of Materials Research 18 (2003) 1003.

[2] S.A. Ivanov, N.W. Thomas, S. Ananta, R. Tellgren, H. Rundlof, Journal of the European Ceramic Society 20 (2000) 2325.

[3] I.P. Roof, M.D. Smith, H.C. zur Loye, Journal of Crystal Growth 310 (2008) 240.

[4] W.T. Fu, D.J.W. Ijdo, Journal of Solid State Chemistry 179 (2006) 1022.

[5] P.J. Saines, J.R. Spencer, B.J. Kennedy, M. Avdeev, Journal of Solid State Chemistry 180 (2007) 2991.

[6] A.R. Chakhmouradian, R.H. Mitchell, Journal of Solid State Chemistry 138 (1998) 272.

[7] N. Lampis, P. Sciau, A. Geddo Lahmann, Journal of Physics: Condensed Matter 11 (1999) 3489.

[8] P.D. Battle, T.C. Gibb, A.J. Herod, S.-H. Kim, P.H. Munns, Journal of Materials Chemistry 5 (1995) 865.

[9] E.L. Rautama, T.S. Chan, R.S. Liu, J.M. Chen, H. Yamauchi, M. Karppinen, Journal of Solid State Chemistry 179 (2006) 111.

[10] S.V. Krivovichev, A.R. Chakhmouradian, R.H. Mitchell, S.K. Filatov, N.V. Chukanov, European Journal of Mineralogy 12 (2000) 597.

[11] J.G. Bos, J.P. Attfield, Physical Review B 70 (2004) 174434.

[12] V.C. Fuertes, M.C. Blanco, D.G. Franco, J.M. De Paoli, R.D. Sanchez, R.E. Carbonio, Materials Research Bulletin 46 (2011) 62.

[13] P.D. Battle, S.I. Evers, E.C. Hunter, M. Westwood, Inorg. Chem. 52 (2013) 6648.

[14] P.D. Battle, M. Avdeev, J. Hadermann, J. Solid State Chem. 220 (2014) 163.

[15] C. Chin, P.D. Battle, S. Blundell, E.C. Hunter, F. Lang, M. Hendrickx, R. Paria Sena, J. Hadermann, Journal of Solid State Chemistry 258 (2018) 825.

[16] D. Iwanaga, Y. Inaguma, M. Itoh, Materials Research Bulletin 35 (2000) 449.

[17] Y.H. Xu, S.S. Liu, N.R. Qu, Y.L. Cui, Q.Q. Gao, R.N. Chen, J. Wang, F.M. Gao, X.F. Hao, Journal of Physics: Condensed Matter 29 (2017) 105801.

[18] A.C. Larson, R.B. von Dreele, General Structural Analysis System (GSAS), Los Alamos National Laboratories, 1990.

[19] H.M. Rietveld, Journal of Applied Crystallography 2 (1969) 65.

[20] B. vanLaar, W.B. Yelon, J. Appl. Cryst. 17 (1984) 47.

[21] E.C. Hunter, P.D. Battle, R. Paria Sena, J. Hadermann, Journal of Solid State Chemistry 248 (2017) 96.

[22] S. Vasala, M. Lehtimaki, S.C. Haw, J.M. Chen, R.S. Liu, H. Yamauchi, M. Karppinen, Solid State Ionics 181 (2010) 754.

[23] P.D. Battle, G.R. Blake, T.C. Gibb, J.F. Vente, Journal of Solid State Chemistry 145 (1999) 541.

[24] S. Vasala, O. Mustonen, M. Karppinen, E. Baggio-Saitovitch, Acta Crystallographica Section A 70 (2017) C820.

Chapter 9: Summary

This research project was designed to investigate the crystal structures and magnetic properties of iron-containing perovskites with general formulae $A_3Fe_2B'O_9$, $A_2A'Fe_2B'O_9$ and $A_2A'FeB'B''O_9$. The main aspects studied include their crystal symmetry, cation ordering and the influence of the latter on their magnetic behaviour. Fourteen perovskites are described in detail in thesis. All the compounds discussed were synthesised using standard solid-state reactions under various conditions. A combination of techniques has been applied to characterise the samples, including X-ray diffraction, neutron diffraction, magnetometry measurements, transmission electron microscopy and ^{57}Fe Mössbauer spectroscopy, the latter two in collaboration with groups outside Oxford. All these techniques are complementary to each other, and consequently it has proved possible to obtain a more complete picture of each compound by analysing data collected using the different techniques.

We have shown for the first time that $Sr_3Fe_2TeO_9$ adopts a trigonal perovskite-like structure with the Fe^{3+} and Te^{6+} cations ordering in a 2:1 sequence that is compatible with both the chemical composition and the multiplicities of the crystallographically distinct six-coordinate sites in the trigonal space group. This trigonal phase of $Sr_3Fe_2TeO_9$ shows antiferromagnetism at room temperature. However, the trigonal structure is disrupted by both nano-twinning and regions in which the cations order in a 1:1 sequence. These disruptions prevent full antiferromagnetic ordering throughout the sample and the unordered spins form a spin-glass phase that coexists with the antiferromagnetic phase below 80 K. The complexity revealed by our study accounts for the inconsistencies between the results of previous studies.

The barium analogue of $Sr_3Fe_2TeO_9$, $Ba_3Fe_2TeO_9$ is a 6*H* perovskite in which the cation sites in the face-sharing octahedra are occupied randomly by Fe^{3+} and Te^{6+} in a ratio that is close to, but different from, 1:1. The sites in the vertex-sharing octahedra are occupied predominantly by Fe^{3+} although some Te^{6+} is also present. Our study constitutes the first account of long-range magnetic order in this compound. At a temperature close to 300 K the atomic moments begin to order in an antiferromagnetic manner. A backbone of ordered spins forms within the structure and on further cooling more spins join the backbone. Spins in locally iron-rich regions order before those in regions where the superexchange pathways are prevented from percolating by a local excess of Te^{6+}. The spins that are unable to take part in the long-range magnetic order form clusters that freeze to form a spin glass at 18 K. In the

series $Sr_xBa_{3-x}Fe_2TeO_9$ (x=2.5, 2.25, 2, 1.5, 1.25, 1), as x decreases the crystal structure switches from purely pseudo-cubic to purely hexagonal via a biphasic region, illustrating the effect of the radius ratio r_A/r_B on crystal structures of such double perovskites.

In the study of the perovskites $A_2LaFe_2SbO_9$ (A=Ba, Sr, Ca) and $CaLa_2Fe_2SnO_9$, disorder at the A site is introduced. X-ray and neutron diffraction data show that these compounds adopt different crystal structures. In $A_2LaFe_2SbO_9$ (A=Ba, Sr, Ca), the calcium and strontium analogues adopt monoclinic $P2_1/n$ structure and triclinic P -1 structures, respectively, which show different levels of cation ordering. The barium analogue has been shown by neutron diffraction to adopt a primitive orthorhombic structure *Pbnm* with disordered B sites. Magnetometry data together with neutron diffraction data have shown that these perovskites are not simple paramagnets at room temperature, and they all adopt a G-type magnetic structure, which leads to long-range ferrimagnetic or weak ferromagnetic behaviour, although these three compounds also contain a minor spin-glass-like phase below 50 K. Neutron diffraction data collected from $CaLa_2Fe_2SnO_9$ showed it to have a monoclinic $P2_1/n$ structure with cation ordering. In this case the B-site ordering is less complete than in the antimony-containing series, which is consistent with the smaller difference in charge between Fe^{3+} and Sn^{4+}. Magnetometry data together with neutron diffraction data suggest that $CaLa_2Fe_2SnO_9$ is a ferrimagnet with a Curie temperature above room temperature, and the moment on the Fe^{3+} cations in this compound drops relatively slowly as the sample is warmed up from 5 K to room temperature.

To examine the effect of the coexistence of three B-cation species, $SrLa_2FeCoSbO_9$ was synthesised. The six-coordinate cations in $SrLa_2FeCoSbO_9$ order, we believe, in a previously-unreported manner. Consequently, this compound shows clear evidence of long-range magnetic order when studied by neutron diffraction at low temperatures. The observed cation distribution, with diamagnetic Sb^{5+} and magnetic Co^{2+} each partially occupying only one of the six-coordinate sites, results in ferrimagnetism below the Curie temperature of 215 K. This ordering temperature is considerably higher than the temperature of the magnetic transitions observed in the other comparable perovskites such as $La_3Ni_2SbO_9$ and $La_3Co_2SbO_9$, perhaps as a result of the involvement of the strongly-magnetic Fe^{3+} cations.

Four perovskites, $CaLa_2FeCoSbO_9$ and $ALa_2FeNiSbO_9$ (A=Ba, Sr, Ca) were prepared as analogues of $SrLa_2FeCoSbO_9$. X-ray and neutron diffraction data show that the four compounds all adopt the monoclinic crystal structure $P2_1/n$ with a 1:1 B-site ordering pattern

where Co^{2+}/Ni^{2+} and Sb^{5+} tend to occupy distinct crystallographic sites while Fe^{3+} is distributed over the two B-sites, which is similar to the ordering pattern observed in $SrLa_2FeCoSbO_9$. TEM images have confirmed the B-site ordering, but also revealed the different levels of inhomogeneity that are present in these compounds. The inhomogeneity is least significant in $CaLa_2FeCoSbO_9$, while it is more significant in the nickel-containing species. $BaLa_2FeNiSbO_9$ is the most inhomogeneous compound among the four compositions, where both the primitive $P2_1/n$ phase and the body-centred $I2/m$ or $I4/m$ phase have been observed in the sample. Magnetometry data together with neutron diffraction data have shown that these perovskites are ferrimagnets with relatively high Curie temperatures, and their ferrimagnetism can be explained by a G-type magnetic structure model by assuming single-phase compositions. However, in contrast to homogeneous $SrLa_2FeCoSbO_9$, doubt has been cast on the interpretation of the diffraction data for these four compounds, and their magnetometry data are likely to be irreproducible under solid-state reaction conditions.

Three perovskites containing d^0 B-cations: $A_2LaFe_2NbO_9$ (A=Sr, Ca) and $CaLa_2Fe_2TaO_9$ were prepared for comparison with the perovskites containing d^{10} cations Te^{6+}, Sb^{5+} and Sn^{4+}. X-ray and neutron diffraction data show that $Ca_2LaFe_2NbO_9$ and $Sr_2LaFe_2NbO_9$ exhibit different levels of cation ordering, and the former adopts a monoclinic $P2_1/n$ structure and the latter a triclinic P -1 structure. Compared to their antimony analogues, $SrLa_2Fe_2NbO_9$ and $CaLa_2Fe_2NbO_9$ show less well-developed ordering pattern due to the smaller difference in size of B-cations. $CaLa_2Fe_2TaO_9$ adopts the same crystal structure as $CaLa_2Fe_2NbO_9$ with the lowest level of B-cation ordering among the three compounds. Magnetometry data together with neutron diffraction data have shown that these perovskites are not paramagnetic at room temperature, and they all adopt a G-type magnetic structure, which leads to long-range ferrimagnetic behaviour. However, these compounds behave very differently from their d^{10} analogues in their susceptibility. The formation of a magnetic backbone is significantly slowed down compared to the case of $A_2LaFe_2SbO_9$, and the temperature for the paramagnetic spins to freeze is lowered below 20 K. We propose that in these materials the third-nearest-neighbour J_3 interaction occurs to compete with the most dominant J_1 interaction, and potentially J_2 interaction as well. In the J_3 interaction, partial electronic density is able to be transferred via the $Fe^{3+} – O – Nb^{5+}/Ta^{5+} – O – Fe^{3+}$ pathway as d^0 cations provide empty d orbitals that can hybridise with the p orbital of oxygen.

In general, most of the perovskites discussed in this thesis show either complete or partial cation ordering at the B sites, except $Ba_2LaFe_2SbO_9$. The level of B-site ordering depends on

whether there is sufficient difference in size and/or charge between the B-cations, and the size of A-cations can sometimes influence the B-site ordering pattern as well. While nine out of fourteen perovskites in this thesis adopt the $P2_1/n$ crystal structure, it is worth noting that pseudo-cubic perovskites containing barium at the A-site tend to have higher crystal symmetry than calcium and strontium analogues, like the cases of disordered $Ba_2LaFe_2SbO_9$ and $BaLa_2FeNiSbO_9$, where a body-centred phase is present. Inhomogeneity plays an important role in the determination of crystal structure. TEM helped to identify the presence of both trigonal and tetragonal phases in $Sr_3Fe_2TeO_9$, as well as the different levels of inhomogeneity contained in the compounds described in Chapter 7. These facts reveal the limitation of diffraction techniques, as reasonably good refinements have been achieved with single-phase models. $Sr_2LaFe_2SbO_9$ and $Sr_2LaFe_2NbO_9$ are the two compounds that are most likely to exhibit similar inhomogeneity to that observed in $BaLa_2FeNiSbO_9$, and further TEM experiments in future might resolve this issue.

With the exception of 6*H* $Ba_3Fe_2TeO_9$, the perovskites discussed in this thesis all adopt the G-type magnetic structure, which is dominated by the strong superexchange interaction via the Fe^{3+} -O- Fe^{3+} NN pathway. However, different types of magnetic behaviour, including antiferromagnetism, ferrimagnetism, weak ferromagnetism and spin-glass behaviour have been observed. The various magnetic behaviours largely arise from the crystal structures and cation-ordering patterns adopted by these compounds. Moreover, competition between different magnetic interactions (J_1, J_2 and J_3) can occur to reduce the observed moment on Fe^{3+} from the spin-only value and the net magnetisation from the calculated value. However, in contrast to the relaxor ferromagnet $La_3Ni_2SbO_9$, all of the iron-containing perovskites are confirmed by neutron diffraction to show long-range magnetic order at low temperature, and in Chapter 6 and 7, relatively high ordering temperatures are reported for those perovskites containing 33% Fe^{3+} at the B site. These facts reflect the large moment on d^5Fe^{3+} and the strength of the Fe^{3+} -O- Fe^{3+} superexchange operating through both σ and π bonds. It has also been shown that apart from the magnetic B-cations, diamagnetic B-cations with different electronic configurations can affect the interaction pathways in the material. As stated before, inhomogeneity has been proved to be, or is likely to be, present in some of the compounds, and thus it will introduce complications, such as irreproducible data, to the interpretation of magnetic properties. At this stage the magnetism of these perovskites has been discussed by assuming a single-phase model. In the future if perovskites with similar compositions are to be made with better homogeneity, it will probably be necessary to develop a solution-based

synthesis that leads to a more homogeneous cation distribution in the early stages of the reaction.

Finally, we emphasise the importance of studying new materials with a variety of techniques that probe different length scales. This work has shown that it is easy to draw false conclusions when only one technique is used, just as we cannot get a good view of the full picture when only one piece of the puzzle is in place.

All the crystal structures and magnetic properties of the fourteen iron-containing perovskites discussed in detail in this thesis are listed in Table 9.1.



Figure 9.1 A bench full of samples in CG7, ICL, Department of Chemistry

Table 9.1 Crystal structures and magnetic properties of fourteen iron-containing perovskites

Compound	Crystal structure	Magnetic property
$Sr_3Fe_2TeO_6$	Two phases: *P*-3*c*1 with 2:1 B-site ordering and *I*4/*m* with 1:1 B-site ordering	Antiferromagnetic at 300 K, antiferromagnetism coexists with spin glass phase below 80 K
$Ba_3Fe_2TeO_6$	$P6_3/mmc$ with 2:1 B-site ordering	Antiferromagnetic below 300 K, antiferromagnetism coexists with spin glass phase below 18 K
$Ca_2LaFe_2SbO_9$	$P2_1/n$ with 1:1 B-site ordering	Ferrimagnetic at 300 K, G-type structure coexists with spin glass phase below 50 K
$Sr_2LaFe_2SbO_9$	*P* -1 with 1:1 B-site ordering	Ferrimagnetic at 300 K, G-type structure coexists with spin glass phase below 50 K
$Ba_2LaFe_2SbO_9$	*Pbnm* with no B-site ordering	Antiferromagnetic at 300 K with spin-canting, G-type structure coexists with spin glass phase below 50 K
$CaLa_2Fe_2SnO_9$	$P2_1/n$ with 1:1 B-site ordering	G-type ferrimagmetism at 300 K
$SrLa_2FeCoSbO_9$	$P2_1/n$ with 1:1 B-site ordering	G-type ferrimagmetism below 215 K
$CaLa_2FeCoSbO_9$	$P2_1/n$ with 1:1 B-site ordering, inhomogeneous	G-type ferrimagmetism below 250 K
$CaLa_2FeNiSbO_9$	$P2_1/n$ with 1:1 B-site ordering, inhomogeneous	G-type ferrimagmetism at 300 K
$SrLa_2FeNiSbO_9$	$P2_1/n$ with 1:1 B-site ordering, inhomogeneous	G-type ferrimagmetism at 300 K
$BaLa_2FeNiSbO_9$	$P2_1/n$ with 1:1 B-site ordering, inhomogeneous	G-type ferrimagmetism at 300 K
$Ca_2LaFe_2NbO_9$	$P2_1/n$ with 1:1 B-site ordering	Ferrimagnetic at 300 K, G-type structure coexists with spin glass phase below 20 K
$Sr_2LaFe_2NbO_9$	*P* -1 with 1:1 B-site ordering	Ferrimagnetic at 300 K, G-type structure coexists with spin glass phase below 20 K
$Ca_2LaFe_2TaO_9$	$P2_1/n$ with 1:1 B-site ordering	Ferrimagnetic at 300 K, G-type structure coexists with spin glass phase below 20 K

Appendix

Table A6.1 Sr, La, Fe, Co and Sb content of the $SrLa_2FeCoSbO_9$ sample from the regions marked in Figure 6.5. Values are given in atomic %.

	Region	Sr	La	Fe	Co	Sb
Figure 6.5: top	1	16.27	34.52	16.28	16.67	16.27
	2	18.52	33.85	15.08	15.65	16.91
	3	21.73	32.19	14.02	16.24	15.82
	4	20.96	32.49	13.75	16.7	16.1
	5	19.33	33.94	14.7	16.06	15.97
	6	20.38	31.72	13.97	16.89	17.04
	7	18.76	33.89	15.16	16.2	15.98
Figure 6.5: middle	1	20.05	32.95	14.57	16.32	16.11
	2	19.63	34.22	16.71	15.5	13.93
	3	20.42	33	14.35	16.4	15.83
	4	18.61	34.3	16.22	15.23	15.65
	5	18.7	32.44	15.72	16.78	16.35
Figure 6.5: bottom	1	16.97	34.34	15.27	15.59	17.84
	2	16.91	32.45	16.54	17.75	16.35
	3	18.45	34.2	15.03	16.51	15.82
	4	17.35	34.11	15.93	15.74	16.86
	5	17.73	33.51	16.03	16.45	16.27
	6	21.96	30.36	14.45	15.36	17.87
	7	16.48	35.84	15.28	16.29	16.12
	8	20.65	33.64	13.67	15.86	16.18
	9	18.96	33.23	18.39	14.59	14.82
	10	18.87	33.19	15.33	16.07	16.53

Table A6.2 Element content of the sample $SrLa_2FeCoSbO_9$ derived from the regions studied by TEM. Values are present in atomic %.

	Sr	La	Fe	Co	Sb
Average	19.0	33.4	15.3	16.1	16.2
Standard deviation	1.6	1.2	1.1	0.7	0.9

Table A7.1 Ca, La, Fe, Ni and Sb content of the $CaLa_2FeNiSbO_9$ sample from the regions marked in Figure 7.5. Values are given in atomic %.

Region	Ca	La	Fe	Ni	Sb
1	16.59	35.27	14.74	15.94	17.46
2	17.49	33.39	17.17	16.16	15.79
3	20.01	33.95	12.89	15.74	17.41
4	19.72	33.15	11.62	17.63	17.87
5	19.82	34.47	13.58	14.55	17.58
6	17.82	33.71	15.39	15.82	17.26
7	19.96	33.03	13.99	16.40	16.62
8	17.94	35.29	15.49	14.55	16.73
9	18.89	35.26	13.62	15.53	16.70
10	18.64	34.30	15.32	15.00	16.75
11	24.82	27.44	4.51	19.95	23.28
12	24.88	27.39	6.83	19.52	21.37
13	24.31	28.60	6.41	19.36	21.32
14	18.07	34.43	13.94	16.24	17.31
15	19.76	32.80	10.42	19.44	17.58
16	16.84	35.88	13.78	16.62	16.88
17	17.91	34.87	15.71	15.93	15.58
18	18.25	33.96	15.01	15.87	16.92
19	19.04	34.05	13.50	15.49	17.92
20	18.13	34.62	14.51	16.08	16.66

Table A7.2 Sr, La, Fe, Ni and Sb content of the $SrLa_2FeNiSbO_9$ sample from the regions marked in Figure 7.9. Values are given in atomic %.

Region	Sr	La	Fe	Ni	Sb
1	16.4	34.5	14.2	16.8	18.2
2	15.0	34.4	21.0	13.4	16.2
3	15.8	37.7	17.9	12.6	16.0
4	12.4	25.6	37.9	12.2	11.9
5	15.7	35.4	16.1	15.0	17.9
6	13.1	36.8	20.1	14.2	15.9
7	10.8	41.2	35.8	4.9	7.3
8	10.9	45.5	29.5	5.6	8.5
9	19.2	31.6	10.7	19.0	19.6
10	16.8	34.4	16.2	15.1	17.5
11	15.0	35.0	15.7	15.7	18.6
12	15.9	35.3	13.9	15.1	19.8

Table A7.3 Ba, La, Fe, Ni and Sb content of the $BaLa_2FeNiSbO_9$ sample from the regions marked in Figure 7.14. Values are given in atomic %.

Region	Ba	La	Fe	Ni	Sb
1	14.7	37.5	22.2	11.7	13.9
2	14.1	37.2	27.4	9.7	11.6
3	14.8	37.2	25.0	10.8	12.3
4	18.8	33.2	17.5	13.9	16.7
5	15.8	35.8	22.4	12.2	13.8
6	19.0	32.5	15.1	15.2	18.2
7	18.2	33.5	16.1	15.3	17.0
8	15.3	37.2	24.3	10.2	13.0
9	20.5	31.2	16.4	14.2	17.7
10	17.4	34.5	20.5	12.6	15.0

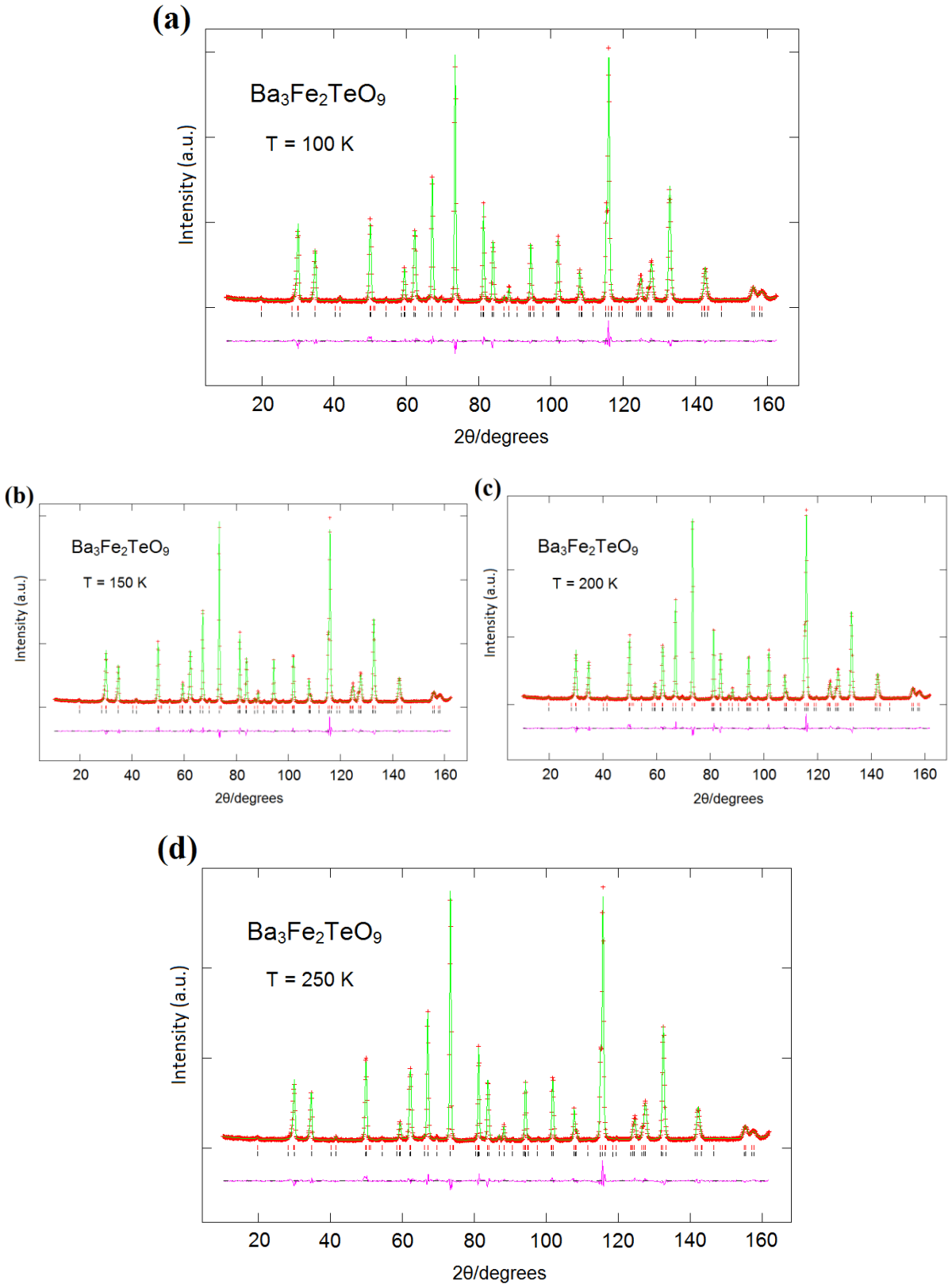

Figure A4.1 Observed (red), calculated (green) neutron diffraction patterns of $Ba_3Fe_2TeO_9$ at (a)100 K, (b) 150 K, (c) 200 K and (d) 250 K (λ = 2.4395 Å). A difference curve (purple) is shown and reflection positions are marked.